Universität Hamburg
DER FORSCHUNG | DER LEHRE | DER BILDUNG

Smarter Routes to “Smart” Polymers: Application of Experimental Design in Polymer Chemistry

Dissertation

in conformity with the requirements for the degree of
Doctor rerum naturalium (Dr. rer. nat)
submitted to the University of Hamburg
—
Faculty of Mathematics, Informatics, and Natural Sciences
—
Department of Chemistry

submitted by
Tilman Eckert

Hamburg, 2022

Supervisor: Prof. Dr. Volker Abetz
1st Referee: Prof. Dr. Volker Abetz
2nd Referee: Prof. Dr. Horst Weller
Date of Disputation and Print Release: July 1st, 2022

This dissertation was created under the supervision of Prof. Dr. Volker Abetz at the Institute of Physical Chemistry (Department of Chemistry, Faculty of Mathematics, Informatics, and Natural Sciences) of the University of Hamburg. The work was started in October 2018 and the dissertation was submitted in April 2022.

Publications

Parts of this work have already been published in scientific journals. The respective articles are listed in the following:

1) Polymethacrylamide – An underrated and easily accessible upper critical solution temperature polymer: Green synthesis *via* photoiniferter reversible addition–fragmentation chain transfer polymerization and analysis of solution behavior in water/ethanol mixtures.
Tilman Eckert, Volker Abetz
J. Polym. Sci. **2020**, *58*, 3050-3060.
DOI: 10.1002/pol.20200566

2) Experimental Design in Polymer Chemistry – A Guide towards True Optimization of a RAFT Polymerization Using Design of Experiments (DoE).
Tilman Eckert, Florian Klein, Piet Frieler, Oliver Thunich, Volker Abetz
Polymers **2021**, *13*, 3147.
DOI: 10.3390/polym13183147

Contents

Abbreviations

ACVA	4,4'-azobis(4-cyanovaleric acid)
ANOVA	analysis of variance
CCD	central composite design
$CDCl_3$	deuterated chloroform
CI	confidence interval
CPDT	2-cyano-2-propyl dodecyl trithiocarbonate
CRP	controlled radical polymerization
CTCA	4-(([2-carboxyethyl]thio)carbonothioyl) thio-4-cyanopentanoic acid
CTCPA	4-cyano-4-(((propylthio)carbonothioyl)thio)pentanoic acid
df	degrees of freedom
DLS	dynamic light scattering
DMF	*N*,*N*-dimethylformamide
DMSO	dimethylsulfoxide
DoE	design of experiments
DSC	differential scanning calorimetry
EtOH	ethanol
FC-CCD	face-centered central composite design
FHS	Flory–Huggins–Staverman
FI	factor intercation
HB	hydrogen bonding
IQ	intelligence quotient
LCST	lower critical solution temperature
MAAm	methacrylamide
MMA	methyl methacrylate
NaCl	sodium chloride
NAGA	*N*-acryloyl glycinamide
$NaHCO_3$	sodium hydrocarbonate
PDMA	poly(*N*,*N*-dimethyl acrylamide)
PEG	poly(ethylene glycol)
PISA	polymerization-induced self-assembly
PMAAm	poly(methacrylamide)
PMAAm-*b*-PMMA	poly(methacrylamide-*b*-methyl methacrylate)

PMAAm-*b*-PS	poly(methacrylamide-*b*-styrene)
PMMA	poly(methyl methacrylate)
PNAGA	poly(*N*-acryloyl glycinamide)
PS	poly(styrene)
PT	phase transition
PTT	phase transition temperature
RAFT	reversible addition-fragmentation chain transfer
RSM	response surface methodology
SEC	size exclusion chromatography
UCST	upper critical solution temperature

Constants and Variables

The following constants and variables are ordered according to their occurrence in the text.

$\Delta_{\mathrm{mix}}G$	Gibbs energy of mixing
$\Delta_{\mathrm{mix}}H$	enthalpy of mixing
$\Delta_{\mathrm{mix}}S$	entropy of mixing
T	temperature
ϕ_{s}	volume fraction of solvent
ϕ_{p}	volume fraction of polymer repeating unit
k_{B}	Boltzmann constant
N	number of lattice sizes occupied by polymer chain
$Đ$	dispersity
E_{sp}	cross-interaction energy between solvent and polymer
E_{ss}	self-interaction energy between solvent molecules
E_{pp}	self-interaction energy between polymer repeating units
χ	interaction parameter
$\bar{M}_{\mathrm{n,th}}$	number–averaged theoretical molecular weight
p	monomer conversion
$[\mathrm{M}]_0$	initial monomer concentration (prior to polymerization)
$[\mathrm{I}]_0$	initial initiator concentration (prior to polymerization)
M_{M}	molecular weight of the monomer
M_{RAFT}	molecular weight of the RAFT agent
$[\mathrm{RAFT}]_0$	initial concentration of RAFT agent
[I•]	concentration of growing species introduced by initiator
L	chain end livingness
M_{I}	molecular weight of initiator radical
R_{M}	ratio of $[\mathrm{M}]_0$ and $[\mathrm{RAFT}]_0$
R_{I}	ratio of $[\mathrm{I}]_0$ and $[\mathrm{RAFT}]_0$
w_{s}	combined weight content of all polymerization solids
E_x	effect of factor x
Y_+ and Y_-	response at the high (+) and low (−) factor level

n_+ and n_-	number of runs at the high (+) and low (−) factor level
β	factor coefficient of prediction model term
n_{Run}	number of runs in experimental design
n_f	number of examined factors in full factorial design
n_p	fraction order reducing the full factorial design
μ	expected value of normal distribution
σ	standard deviation of normal distribution
SS	sums of squares
R^2	squared Pearson correlation coefficient
$\mathrm{R}^2_{\mathrm{adj}}$	adjusted-R^2
n_{s}	number of data points used generation of prediction model
n_{t}	number of model terms included in prediction model
$\mathrm{R}^2_{\mathrm{pred}}$	predicted-R^2
$\overline{M}_{\mathrm{n,app}}$	apparent number–averaged molecular weight from SEC
R_{h}	hydrodynamic radius
t	time
Đ	dispersity
w_{EtOH}	weight fraction of ethanol
w_{NaCl}	weight fraction of NaCl
w_{NaHCO3}	weight fraction of $NaHCO_3$
w_{PMAAm}	weight fraction of PMAAm
η	viscosity
D	diffusion coefficient

1 Zusammenfassung

Polymere mit *upper critical solution temperature* (UCST) weisen einzigartige Eigenschaften und großes Potenzial für die Entwicklung von sogenannten "smarten" Polymermaterialien auf. Nichtsdestotrotz sind UCST-Polymere bis zum heutigen Tage noch relativ wenig erforscht – vermutlich aufgrund ihrer ausgesprochenen Empfindlichkeit gegenüber ionischen Verunreinigungen und äußerst teurer Monomere. Im ersten Teil dieser Arbeit wird deshalb eine umweltfreundliche und einfache Synthese des kostengünstigen UCST-Polymers Poly(methacrylamid) (PMAAm) mittels photoiniferter *reversible addition-fragmentation chain transfer* (RAFT)-Polymerisation entwickelt. Die hochgradig gut kontrollierte Polymerisation ergibt eng verteiltes PMAAm ($Đ$ < 1.1), welches scharfe und ausgeprägte thermoreversible UCST-Phasenübergänge in Wasser/Ethanol-Gemischen aufweist, die durch temperaturabhängige Messungen mittels dynamischer Lichtstreuung (DLS) gründlich untersucht werden. Die Phasenübergangstemperatur (engl. *phase transition temperature*, PTT) nimmt mit wachsender Kettenlänge sowie steigenden Gewichtsanteilen von Ethanol (Nichtlösungsmittel) und PMAAm stark zu und liegt zwischen 10 °C und 80 °C. Es wurde außerdem festgestellt, dass die PTT kontinuierlich abnimmt, wenn die Lösung über mehrere Stunden auf Temperaturen von 70 °C oder höher erhitzt wird. Aufgrund der extremen Empfindlichkeit der UCST-Phasenübergänge können selbst stöchiometrisch vernachlässigbare Mengen an irreversibel hydrolysierten Amidseitengruppen die PTT innerhalb von Stunden deutlich reduzieren. Bei niedrigeren Temperaturen von 40 °C bleiben die PTTs der PMAAm-Lösungen allerdings mindestens drei Tage lang stabil, was darauf hindeutet, dass bei niedrigeren Temperaturen keine irreversible Hydrolyse stattfindet. Diese generelle Neigung von nichtionischen, zumeist aus Acrylamideinheiten aufgebauten UCST-Polymeren zur Amidhydrolyse der Seitengruppen stellt eine Herausforderung für potenzielle Anwendungen von "smarten" UCST-Materialien dar, da hierdurch das UCST-Lösungsverhalten instabil wird. Trotz alldem ist diese Empfindlichkeit gegenüber der Amidhydrolyse eine einzigartige Eigenschaft der UCST-Polymere, die sich beispielweise in biomedizinischen Anwendungen als vorteilhaft erweisen könnte, da eine kontinuierliche Hydrolyse von aggregierten Partikeln die Nierensekretion stetig erleichtern kann.

Obwohl die RAFT-Technik in der Polymerchemie gut etabliert ist, ist die Optimierung der Polymerisation im Hinblick auf Parameter wie Molekulargewicht, Dispersität oder sogar „Lebendigkeit“ der Kettenenden mit konventionellen Versuchsverfahren kaum möglich. Eine Methode zur zuverlässigen und präzisen Identifizierung von „Sweetspots“ der Polymerisation ist die sogenannte statistische Versuchsplanung (engl. *Design of Experiments*, DoE). Richtig angewandt, ist DoE effizienter, planbarer und reproduzierbarer als herkömmliche Versuchsreihen. Darüber hinaus kann DoE einen größeren Wissenszuwachs ermöglichen, da es auch Faktorwechselwirkungen erkennt, weshalb DoE in industriellen Forschungseinrichtungen längst fest etabliert ist. In der akademischen Forschung hingegen ist die DoE-Methode noch weitgehend unbekannt. Der zweite Schwerpunkt dieser Arbeit besteht daher darin, das Potenzial von DoE in der akademischen Forschung zu demonstrieren und zu zeigen, dass die Methode auch für komplexere Reaktionssysteme wie die RAFT Polymerisation eingesetzt werden kann. Diese Arbeit bietet hierbei eine umfassende Anleitung, wie RAFT Polymerisationen mittels DoE optimiert werden können. Dies wird exemplarisch für die thermisch initiierte RAFT Lösungspolymerisation von Methacrylamid (MAAm) gezeigt. Der in der Anleitung Schritt-für-Schritt aufgearbeitete Arbeitsablauf ermöglicht die Adaptierung für praktisch jede andere Polymerisation. Die Optimierung der RAFT Polymerisation von MAAm erfolgte mittels r*esponse surface methodology* (RSM) unter Verwendung eines flächenzentrierten *central composite design* (FC CCD). Hiermit wurden durch polynomiale Regression der experimentellen Daten hochpräzise Vorhersagemodelle für die Zielgrößen Monomerumsatz, Dispersität sowie theoretische und experimentelle zahlenmittlere Molmassen generiert. Diese Modelle ermöglichen ein umfassendes Systemverständnis, da jeder Term der Gleichungen einzeln interpretiert werden kann und Faktorinteraktionen identifiziert werden, welche mit herkömmlichen experimentellen Ansätzen normalerweise unentdeckt bleiben. Darüber hinaus ermöglichen die Vorhersagegleichungen eine echte Polymerisationsoptimierung, da für alle möglichen synthetischen Ziele die optimale Kombination der Faktoreinstellungen berechnet werden kann. Dieser Teil der Arbeit zeigt das große Potential von DoE im Bereich der akademischen Forschung. Kolleginnen und Kollegen (auch aus anderen Fachgebieten) werden so ermutigt, DoE in ihren täglichen Arbeitsablauf einzubauen.

Im letzten Teil dieser Arbeit liegt der Schwerpunkt auf der Kettenverlängerung von PMAAm, um "smarte" Diblockcopolymere mit UCST-Löslichkeitsverhalten herzustellen. Poly(methacrylamid-*b*-methylmethacrylat) (PMAAm-*b*-PMMA) wird erfolgreich durch tensidfreie photoiniferter RAFT Dispersionspolymerisation synthetisiert. Methylmethacrylat (MMA) kann hierbei in weniger als 150 min zu ca. 98 % umgesetzt werden. Temperaturabhängige DLS-Messungen der

PMAAm-*b*-PMMA-Dispersionen zeigen ein bemerkenswertes thermosensitives und -reversibles UCST-Löslichkeitsverhalten der stabilisierenden PMAAm-Schale in Wasser/Ethanol-Gemischen. Die selbstangeordneten Partikel zeigen einen allmählichen, UCST-artigen Quellprozess der PMAAm-Hülle beim Erhitzen und scheinen beim Abkühlen von etwa 30 °C auf 10 °C kleine Aggregate zu bilden. Im Gegensatz zum PMAAm-Homopolymer wird jedoch kein makroskopischer Phasenübergang beobachtet, was vermutlich durch die stark repulsiven Kräfte der Carboxylgruppen an den PMAAm-Kettenenden bedingt ist. Änderungen der Dispersionskonzentration, der PMMA-Blocklänge und sogar der Partikelgröße haben keinen signifikanten Einfluss auf das beobachtete UCST-Löslichkeitsverhalten, welches augenscheinlich unter den richtigen Umständen recht robust sein kann. UCST-Löslichkeitsverhalten bleibt somit ein vielversprechendes Attribut für künftige Anwendungen in "intelligenten" Polymermaterialien.

2 Abstract

Upper critical solution temperature (UCST) polymers feature unique characteristics and great potential for the generation of "smart" polymeric materials. Yet, arguably due to very costly monomers and high sensitivity towards ionic impurities, they remain rather sparsely investigated. In the first part of this work, an eco-friendly synthesis of the easily accessible and inexpensive UCST polymer poly(methacrylamide) (PMAAm) *via* photoiniferter reversible addition-fragmentation chain transfer (RAFT) polymerization is developed. The well-controlled polymerization yields narrowly distributed PMAAm ($Đ < 1.1$) with distinct and pronounced thermoreversible UCST-type phase transitions (PTs) in water/ethanol mixtures which are thoroughly investigated *via* temperature-dependent dynamic light scattering (DLS) measurements. The phase transition temperature (PTT) strongly increases with increasing chain length as well as with rising weight fractions of ethanol (non-solvent) and PMAAm and ranges between 10 °C and 80 °C. It was found that the UCST-type PTT decreases over time if the solution is heated to temperatures of 70 °C or higher. Due to the extreme sensitivity of UCST-type PTs, even stoichiometrically negligible events of irreversible amide side group hydrolysis can significantly suppress the PTT within hours. At lower temperatures of 40 °C, the PTTs of the PMAAm solutions remain stable over at least three days implying the absence of irreversible hydrolysis. This general propensity of non-ionic, acrylamide-based UCST polymers towards side group hydrolysis constitutes another challenge for potential applications of "smart" UCST-based materials. Nonetheless, it is also a rather unique feature which could potentially even be beneficial in, for instance, biomedical applications as continuous hydrolysis of aggregated particles can swiftly facilitate renal secretion.

While the RAFT technique is well-established in polymer chemistry, optimization of the polymerization with respect to several different quantities like molecular weight, dispersity or even chain end livingness is rarely achievable with conventional experimentation procedures. A method for reliable and precise identification of the polymerization "sweet spots" is experimentation *via* design of experiments (DoE). If applied correctly, DoE boasts greater efficiency, plannability and reproducibility than conventional experimentation approaches. On top of that, DoE can facilitate greater knowledge generation as it will reveal even factor interactions. For all these reasons, DoE is already firmly established in industrial research facilities.

In academic research, however, its concept remains widely unknown. The second focus of this work was thus to introduce its potential to polymer chemists and to demonstrate that it can even be used for complex reaction systems such as a RAFT polymerization. This work thus provides a comprehensive step-by-step guide on how to optimize a RAFT polymerization *via* DoE. This is exemplarily shown for the thermally initiated RAFT solution polymerization of methacrylamide (MAAm). The presented workflow facilitates adaptation for virtually any other polymerization. The optimization of the RAFT polymerization of MAAm was achieved *via* response surface methodology (RSM) using a face-centered central composite design (FC-CCD). Through polynomial regression of the experimentally observed data, highly accurate prediction models for the four responses monomer conversion, dispersity and theoretical as well as apparent number-averaged molecular weights are generated. These equations enable a thorough system comprehension as each model term can be interpreted individually and several factor interactions – which are usually not detected *via* conventional experimentation approaches – are revealed. Furthermore, the prediction equations allow for true polymerization optimization as the optimal combination of factor settings will be disclosed for virtually any synthetic goal. This part of this work successfully shows the huge potential of DoE for academic research purposes. Fellow colleague (even from other fields) are thus encouraged to implement DoE into their everyday workflow.

In the last part of this work, the focus lies on chain extension of PMAAm in order to produce polymeric "smart" diblock copolymers with UCST-type behavior. Poly(methacrylamide-*b*-methyl methacrylate) (PMAAm-*b*-PMMA) is successfully synthesized *via* photoiniferter surfactant-free RAFT dispersion polymerization. Methyl methacrylate (MMA) conversions of around 98 % are achievable within less than 150 min. Characterization *via* size exclusion chromatography (SEC) analyses was, however, unfeasible as no eluent is able to dissolve both the highly polar PMAAm-block and the non-polar PMMA-block. Temperature-dependent DLS measurements of the PMAAm-*b*-PMMA-dispersions show peculiar thermosensitive and reversible UCST-behavior of the stabilizing PMAAm-shell in water/ethanol mixtures. The self-assembled particles show a gradual UCST-type swelling process of the PMAAm-shell upon heating and appear to form small aggregates upon cooling from around 30 °C to 10 °C. Unlike the PMAAm homopolymer, however, no macroscopic PT is observed – most likely due to the repulsive forces of the carboxylic groups located at the PMAAm chain ends. Changes of concentration of the dispersion, PMMA-block length and even particle size did not affect this peculiar solution behavior. Apparently, UCST-"smartness" can, under the right circumstances, be more robust than sometimes credited for and remains a promising candidate for future applications of “smart” materials.

3 Introduction

As the work presented in this dissertation was conducted within a time span from late 2018 to early 2022, it should come as no surprise it was heavily affected by the Covid-19 pandemic. Due to the necessity of social distancing, the author of this work (just as many other colleagues around the world) isolated himself in his home office for several months. These stints away from laboratory facilities made a more efficient approach towards experimentation – once the laboratory work could be resumed – more worthwhile than ever. Similar to the excellent dissertation of Felix Lauterbach – which (amongst many other things) criticized the outdated workflow in the typical chemistry lab[1] – this work thus tries to provide a modernized approach towards experimentation. Hence, this work offers an “entrance card” into the realms of the so-called Design of Experiments (DoE). Apart from the high plannability, efficiency and statistical reliability of DoE, system investigation *via* an experimental design also allows for great information gain which is why it is already firmly established in industrial research facilities.[2,3] However, probably due to missing courses within chemistry studies at university, DoE remains widely unused (and even unknown) in academic research. This work thus provides simplified and application-oriented theoretical background of DoE (section 3.4) and aspires to pave the way for other scientists to adapt the experimental technique into their workflow. Additionally included is a step-by-step DoE-application guide (section 6.1) for the optimization of a RAFT polymerization – a controlled radical polymerization that enjoys increasing relevance in industry.[4]

RAFT polymerizations are a highly versatile technique that can be utilized in a multitude of solvents for a broad set of different monomer species.[5–11] Additionally, RAFT also embodies a “living” polymerization character due to the thiocarbonylthio moiety at the omega chain end (more on the theory behind RAFT is presented in section 3.3). Due to these polymerization traits, RAFT also facilitates the generation of complex multiblock polymer architectures. When so-called stimuli-response blocks are incorporated in such architectures, highly interesting “smart” materials can be generated which are used for drug delivery systems for biomedical applications[12–14], surfaces that can change between hydrophobic and hydrophilic[15–17] or filtration devices with switchable permeability.[18–22] Stimuli-responsive or, in more plain English, “smart” polymers owe this description to their ability to undergo rapid changes as a response to just small variations in their physical or chemical surroundings. Within the group of “smart” polymers, the group of thermoresponsive polymers are arguably the most famous representative. In aqueous solutions, for instance, these polymers can swiftly change their solubility and cause a temperature-induced phase separation. During such a phase separation, well-dissolved polymer coils in homogenous solution turn into interchain associated aggregates resulting in a polymer rich and polymer poor phase.[23] When this occurs upon heating, this process is called a lower critical solution temperature (LCST)-type PT; when phase separation is caused by cooling, it is due to a UCST-type PT (the thermodynamic background of these phenomena will be described in detail in section 3.1). While LCST polymers have been intensively studied over the last years, astonishingly few research articles have been attributed towards investigation of UCST polymers. Considering the exclusive features of UCST polymers such as their ability to encapsulate hydrophilic substances *via* different polar and non-polar interactions – which is difficult to achieve with LCST polymers due to their emerging hydrophobicity above the PTT – the low coverage of UCST polymers is rather surprising.[24–26] Hence, one of this work’s major focusses lied in investigation of the potential of different UCST polymers concerning synthesis, solution behavior and utilization in “smart” applications.

There are, however, certain predicaments accompanied with UCST polymers like high sensitivity of the UCST-type PTT towards chain incorporation of ionic groups, a limited selection of potent polymer solvents and even the degradation of the UCST-type PTT due to irreversible hydrolysis events (see section 3.2).[27–29] Particularly in zwitterionic UCST-polymers, also called polybetaines, the UCST-type PTT depends strongly on the concentration of salt.[30] Non-ionic UCST polymers – which are typically acrylamide-based – are, on the other hand, usually very costly due to monomers requiring elaborate syntheses.

Apart from the implementation of DoE in the experimental workflow (see section 6), one of the main focusses of this work is thus to find an easily accessible and affordable RAFT polymer that shows UCST solution behavior and can be synthesized quickly and reliably – even by less experienced scientists (see section 5). In combination with acquired expertise in UCST polymer synthesis and solution behavior, this work additionally aspires to provide new insights into the development of “smart” UCST-based materials (section 7) *via* polymerization-induced self-assembly (PISA). The morphologies built by a self-assembly process typically generate very high effective local concentrations of the UCST polymer block as well as spatial proximity to the block inducing the self-assembly (in membranes with switchable pore size, for instance, the “smart” pore-forming block is confined by the membrane majority component). The last part of this work was thus to investigate if these PISA-effects cause noticeable changes of the UCST-type solution behavior.

3.1 The Phase Behavior of UCST Polymer Solutions

A solvent and a solute mix spontaneously when the Gibbs energy of mixing $\Delta_{\mathrm{mix}}G$ is negative:

$$\Delta_{\mathrm{mix}}G = \Delta_{\mathrm{mix}}H - T\,\Delta_{\mathrm{mix}}S \tag{1}$$

In a binary mixture that solely features dispersive forces, the existence of two separate phases is enthalpically favored (the enthalpy of mixing $\Delta_{\mathrm{mix}}H$ is positive) as the interaction between alike molecules is stronger than between unlike molecules. If not for the second term of equation (1) – which contains the entropy of mixing $\Delta_{\mathrm{mix}}S$ – such a solution would always remain separated. Due to the strong increase in combinatorial entropy upon changing from a phase separated to a homogenous solution, $\Delta_{\mathrm{mix}}S$ will be positive as well. If, upon increasing the temperature T of the solution, the entropic contribution overpowers $\Delta_{\mathrm{mix}}H$, $\Delta_{\mathrm{mix}}G$ will turn negative and the binary solution homogenizes. This temperature, at which the mixture transitions from binary a unary (or *vice versa*) is called a PTT.[31]

In polymer solutions, however, other contributions to $\Delta_{\mathrm{mix}}H$ and $\Delta_{\mathrm{mix}}S$ come into play as it gets a bit more complex. The main characteristic of UCST polymers, for instance, is their ability to form very strong intra- and intermolecular polymer–polymer interactions. These can come in form of Coulomb interactions in polybetaines or in form of hydrogen bonding (HB).[32,33] Due to these strong polymer–polymer interactions, $\Delta_{\mathrm{mix}}H$ is positive as well promoting a binary solution with a polymer-rich and a polymer-poor phase. Although the anisotropy of these polymer–polymer interactions complicates $\Delta_{\mathrm{mix}}S$ by introduction of the so-called orientational entropy, $\Delta_{\mathrm{mix}}S$ of UCST polymers remains positive and thus facilitates a transition into a unary solution when reaching the PTT (upon heating).

A more sophisticated approach towards the qualitative explanation of UCST-type PTs is provided by the Flory–Huggins–Staverman (FHS) theory which is provided in equation (2):[34–38]

$$\frac{\Delta_{\mathrm{mix}}G}{k_{\mathrm{B}}T} = \underbrace{\phi_{\mathrm{s}}\,\phi_{\mathrm{p}}\,\chi}_{=\frac{\Delta_{\mathrm{mix}}H}{k_{\mathrm{B}}T}} + \underbrace{\phi_{\mathrm{s}}\ln\phi_{\mathrm{s}} + \frac{\phi_{\mathrm{p}}}{N}\ln\phi_{\mathrm{p}}}_{=-\frac{\Delta_{\mathrm{mix}}S}{k_{\mathrm{B}}}} \tag{2}$$

The FHS theory assumes a lattice model with equally sized lattice sites that are either occupied by a solvent molecule or a polymer repeating unit. Equation (2), provides the Gibbs energy of mixing per lattice site (*i.e.*, per solute or polymer repeating unit) by normalization with thermal energy $k_{\mathrm{B}}T$. The occupied volume fractions of both species are represented by ϕ_{s} and ϕ_{p}, respectively ($\phi_{\mathrm{s}} + \phi_{\mathrm{p}} = 1$). A polymer chain occupies N lattice sites. Through simple mathematic evaluation of this equation, it becomes evident that the entropy terms will always favor mixing as they portray the ideal combinatorial entropy of mixing. Also, the entropy of mixing will decrease with increasing values of N (*i.e.*, a measure of chain length). The enthalpic term includes the interaction parameter χ which is provides an estimate of the interactions between solvent and solute (polymer repeating unit):

$$\chi = \frac{z\,(E_{\mathrm{sp}} - \frac{E_{\mathrm{ss}} + E_{\mathrm{pp}}}{2})}{k_{\mathrm{B}}T} \tag{3}$$

As long as they are attractive, the cross-interaction energy (E_{sp}) as well as self-interaction energies (E_{ss} and E_{pp}) are negative. It thus follows that if E_{sp} is lower than the average self-interaction energy – as is the case for UCST polymers – χ will be positive and linearly depends on the inverse temperature and the lattice coordination number z (*i.e.*, the number of neighboring lattice sites). At this point it must be mentioned that χ can show strong concentration dependence – especially in poor solvents – which is not included in the original FHS theory. In fact, if the FHS theory wants to adequately model LCST-type PTs, the expression for χ must be augmented by terms which additionally attribute the orientational entropy. As this is thoroughly described elsewhere and is not required for qualitative explanation of UCST polymer PTs, however, it is continued with the simplified expression in equation (3).[31] Although a negative $\Delta_{\mathrm{mix}}G$ denotes spontaneous mixing, it is not a guarantee for only one mixed phase as a $\Delta_{\mathrm{mix}}G < 0$ only implies that the mixture will not separate into two phases of pure components. This will become more apparent when looking at all implications that can be drawn from equation (2). Figure 1 schematically shows the entropic (graph A) and enthalpic contribution to $\Delta_{\mathrm{mix}}G$.

The entropic term of equation (2) is, in fact, independent of temperature and always favors mixing of solute and solvent (remember that it only accounts for combinatorial entropy). When the size of the solute equals the solvent size ($N = 1$), the $\Delta_{\mathrm{mix}}S$ function is symmetrical at a ϕ_{p} of 0.5. In polymer solutions, however, the entropic contribution to $\Delta_{\mathrm{mix}}G$ will be asymmetrical due to the solute populating N lattice sites. As the interaction parameter $\chi \sim T^{-1}$, the enthalpic contribution (which will always favor phase separation) will gradually decrease with increasing temperatures.

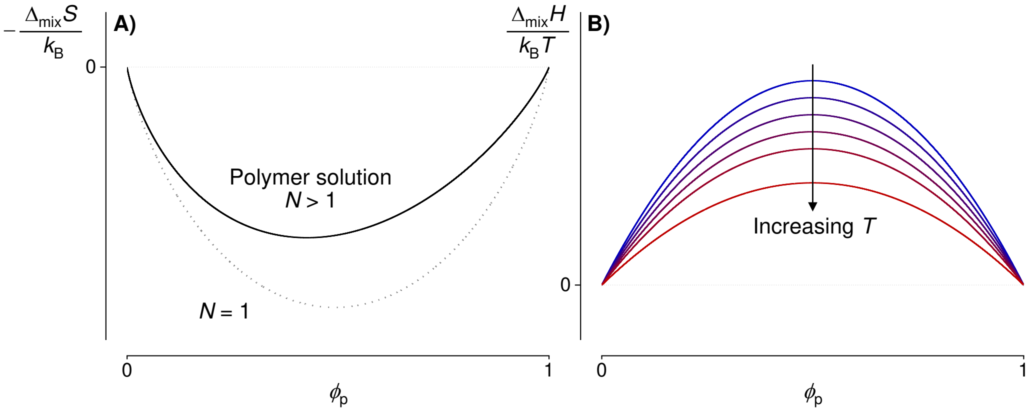

Figure 1: Schematical predictions of the entropy (graph A) and enthalpy (graph B) of mixing. The enthalpic contribution to the Gibbs energy of mixing decreases with rising temperature as indicated by the color gradient.

A separation of phases will occur, when the system can lower its Gibbs energy of mixing by division into two phases.[31] Figure 2 schematically shows the predicted Gibbs energy of mixing for a polymer solution (note the slight asymmetry caused by $N > 1$) at a high temperature (graph A) and a low temperature (graph B). At the high temperature – where the enthalpic contribution is comparably low – a one-phase solution will always be favored for any value of ϕ_{p} (*i.e.*, a measure for the polymer concentration). This can be demonstrated best by an exemplary scenario with a polymer solution with $\phi_{\mathrm{p}} = \phi_{\mathrm{A}}$. Any polymer solution will exhibit small, local phase separations at any time due to spontaneous fluctuations of polymer concentration. If, however, these fluctuations lead to an overall increase of the Gibbs energy of mixing, these infinitesimal phase separations will be revoked and the initial "polymer concentration" ϕ_{A} will always be re-established. Whether a phase separation into a polymer-poorer phase ϕ_A' and a polymer-richer phase ϕ_A'' (red circles) will be favored becomes apparent by simply drawing a straight (dotted) line that connects both volume fractions on the $\Delta_{\text{mix}}G$-curve. This line represents the change of Gibbs energy associated with the phase separation process from ϕ_A to ϕ_A' and ϕ_A'' which is the vertical difference between the $\Delta_{\text{mix}}G$-curve and the straight line at ϕ_A. It becomes evident that as long as the course of the Gibbs energy is "concave up" – or, in other words, shows a left-hand bend – phase separation will always be unfavored:

$$\text{solution stable if:} \qquad \left(\frac{\partial^2 \Delta_{\text{mix}}G}{\partial \phi_p^2}\right)_{T,p} > 0 \tag{4}$$

At lower temperatures, however, the enthalpic contribution to the Gibbs energy becomes larger and $\Delta_{\text{mix}}G$ can show a local maximum (graph B). Close to the local Gibbs energy maximum, the curve is "concave down" which implies that a unary solution is unstable and favors phase separation. In a concave down-region, any small concentration fluctuation (and subsequent phase separation into $\phi_p + \delta\phi_p$ and $\phi_p - \delta\phi_p$) will thus actually decrease $\Delta_{\text{mix}}G$. These fluctuations will promote further phase separation until $\Delta_{\text{mix}}G$ is minimized and the solution is thermally equilibrated (note that for thermal equilibration, the chemical potentials – *i.e.*, the partial derivative of $\Delta_{\text{mix}}G$ with respect to ϕ_p – of both solute and solvent must be equal in both phases). For instance, a polymer solution with a volume fraction of $\phi_p = \phi_B$ that is close to the local maximum (black circle) will reduce $\Delta_{\text{mix}}G$ until thermal equilibration has been achieved by phase separation into the so-called binodal compositions ϕ_B' and ϕ_B'' (green circles) as indicated by the tangent line connecting both points.

To sum things up, polymer solutions are unstable and favor phase separation if the $\Delta_{\text{mix}}G$ is concave down and stable when $\Delta_{\text{mix}}G$ is concave up. But what if neither is the case, as demonstrated in equation (5):

$$\left(\frac{\partial^2 \Delta_{\text{mix}}G}{\partial \phi_p^2}\right)_{T,p} = 0 \tag{5}$$

Such inflection points are called “stability limits” and denote the so-called spinodal point with the compositions ϕ'_{sp} and ϕ''_{sp}. At a given temperature (and pressure), a homogenous polymer solution is metastable between the binodal and spinodal composition: although $\Delta_{\mathrm{mix}}G$ is concave up in this ϕ_{p}-region, phase separation to the binodal compositions will occur if the energy barrier of the local maximum can be overcome.

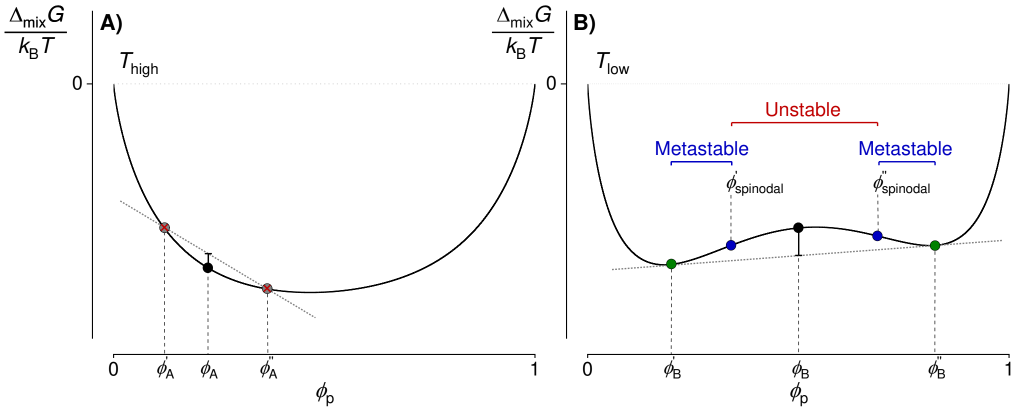

Figure 2: Schematical predictions of the Gibbs energy of mixing at high (graph A) and low (graph B) temperatures. Graph A) The course of $\Delta_{\mathrm{mix}}G$ is concave. Phase separation is thus always unfavored as the Gibbs energy associated with the phase separation process from, for instance, ϕ_{A} to ϕ'_{A} and ϕ''_{A} (represented by the dotted line) will always be higher than the unary composition ϕ_{A}. Graph B) At lower temperatures, the enthalpic contribution is larger and $\Delta_{\mathrm{mix}}G$ can exhibit a local maximum. In the concave down-region a solution with the composition ϕ_{B} (black circle) close to this local maximum, a unary, homogenous polymer solution is unstable and will phase separate into the two thermally equilibrated binodal compositions ϕ'_{B} and ϕ''_{B} (green circles). The ϕ_{p}-regions between the binodal and spinodal (*i.e.*, the curve’s inflection points) compositions are metastable. Phase separation to the binodal compositions will only occur if the energy barrier of the local maximum is overcome.

At comparably low temperatures, $\Delta_{\mathrm{mix}}H$ causes a broad local maximum in the $\Delta_{\mathrm{mix}}G$-curve that gets less and less pronounced with increasing temperature. Exactly this is shown in graph A of Figure 3. The binodal (green circles) as well as spinodal (blue circles) compositions will thus converge and eventually all meet at the critical temperature (black dashed line). This critical temperature – in this case a UCST – is the first temperature whose corresponding $\Delta_{\mathrm{mix}}G$-curve does not exhibit inflection points and can be understood as the zero of the third derivative of $\Delta_{\text{mix}}G$:

$$\left(\frac{\partial^3 \Delta_{\text{mix}} G}{\partial \phi_{\text{p}}^3}\right)_{T,p} = 0 \tag{6}$$

The conclusions of the temperature dependent $\Delta_{\text{mix}}G$-curves can be translated into a phase diagram (graph B of Figure 3) which plots the (green) binodal and (blue) spinodal curve in a temperature–composition plot. The two domes meet at the critical point – the UCST. Above this temperature (and above the binodal curve), homogenous polymer solutions are stable. For instance, a homogenous polymer solution with the composition ϕ_{C} will be stable at the comparably high temperature T_3 (green circle). Upon cooling of the solution to T_2 (blue circle), the solution will become metastable and will remain homogenous. If, however, the energy barrier of the corresponding $\Delta_{\text{mix}}G$ maximum could be overcome, phase separation into the two according binodal compositions (small blue circles) would occur. By further cooling to temperature T_3 (red circle), a homogenous polymer solution will become unstable (upon crossing the spinodal curve). Spontaneous phase separation into the two corresponding binodal compositions (small red circles) will take place.

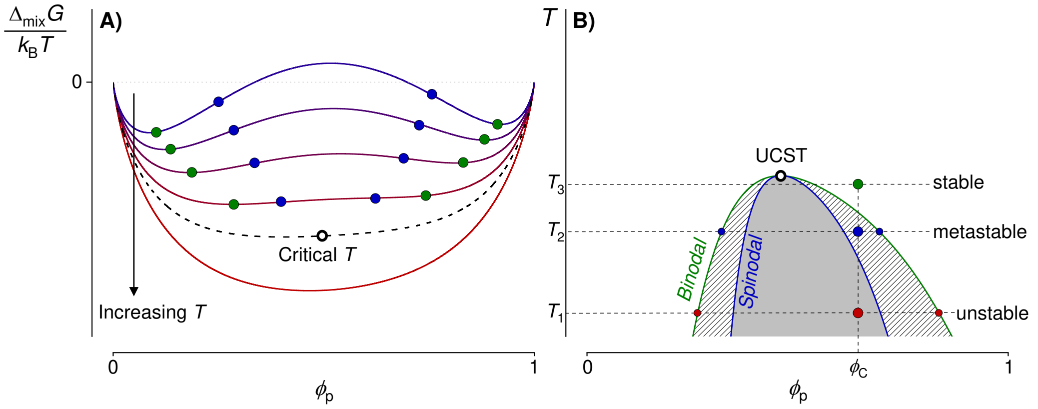

Figure 3: Graph A) Schematical predictions of the Gibbs energy of mixing at multiple temperatures. With increasing temperature, the binodal (green circles) and spinodal (blue circles) will converge and coincide at the critical temperature (dashed line, unfilled circle denotes UCST). Graph B) The associated phase diagram plots the (green) binodal and (blue) spinodal curve in a temperature–composition plot. A homogenous polymer concentration with composition ϕ_{C} will be stable above the binodal at temperature T_3 (green circle), metastable at temperature T_2 between binodal and spinodal (blue circle) and unstable within the binodal at temperature T_1 (red circle).

Graph B of Figure 3 allows for another conclusion: when investigating the PT of a UCST polymer solution, the measurement is typically started above the UCST-type PT in a homogenous and stable solution. Measurable increases in particle size upon cooling (due to polymer aggregation after surpassing the PTT) will only denote the spinodal decomposition.

3.2 Non-Ionic UCST Polymers

The peculiar solution behavior of UCST polymers stems from their ability to establish strong intra- and intermolecular interactions in water. In non-ionic UCST polymers, these interaction stem from strong HB typically facilitated by amide functionalities in the side groups. In contrast to potential LCST polymers, though, the number of UCST homopolymers with observable PTTs between 0 °C and 100 °C is fairly small. Figure 4 shows a library of some non-ionic UCST homopolymers listed according to their observed PTT (note that these PTTs are only rough approximations as they strongly depend on concentration and chain length). All the listed polymers share an acryl- or methacrylamide functionality. Lutz *et al.*, for instance, showed that poly(*N*-acryloylasparagine amide) synthesized *via* RAFT polymerization showed relatively sharp, yet strongly concentration-dependent PTTs in pure water.[39] Higher UCST-type PTTs were observed for poly(6-acryloyloxymethyl uracil) and polyureido-derivatives.[16,40] The most extensively investigated UCST polymer, however, most likely is poly(*N*-acryloyl glycinamide) (PNAGA) which shows UCST-type PTs when synthesized both from conventional free-radical as well as RAFT polymerization and has already been subject of several excellent research articles.[23,41–43] When looking at the structural complexity of all the respective repeating units, however, it comes as no surprise that these polymers are very hard to obtain as they are either very costly or require elaborate syntheses. Compared to the easy accessibility of LCST-"smartness" which can be facilitated by rather inexpensive poly(*N*-isopropylacrylamide), a polymeric material with UCST-behavior is thus much harder to come by. The only obvious exception from this is PMAAm which was found to exhibit a UCST-type PT in pure water at approximately 40 °C by Agarwal *et al.* if synthesized *via* conventional free-radical polymerization.[28] Due to these promising findings, the synthesis of PMAAm *via* a controlled radical pathway (RAFT) was intensively investigated within this work as it was expected to offer an easily accessible route towards UCST-"smartness" in multiblock architectures (see section 5.2).

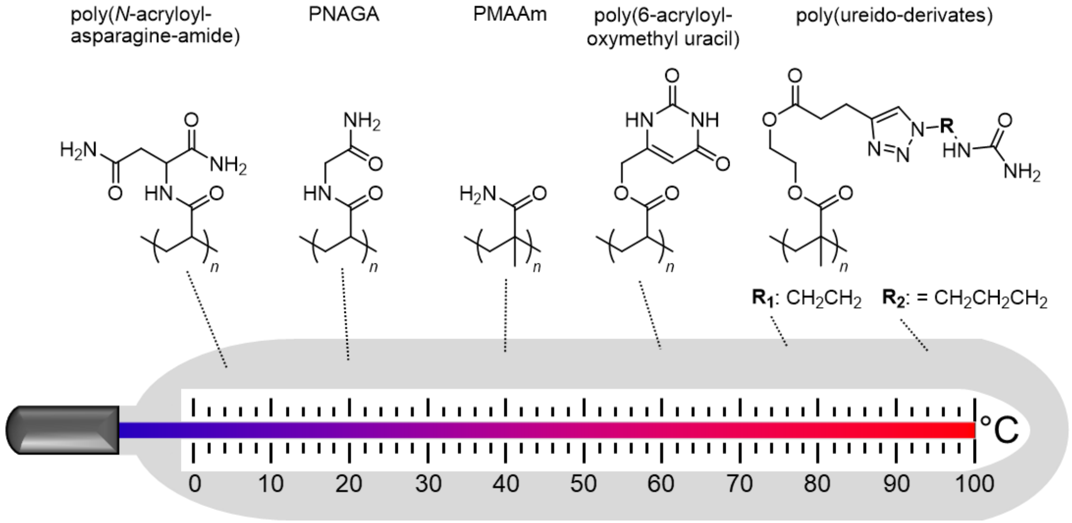

Figure 4: Library of non-ionic UCST-type homopolymers with UCST-type PTTs in aqueous solution. It has to be stated that these PTTs are strongly influenced by polymer concentration and architecture, chain length, molecular weight distribution, ionic impurities and polymer end groups and the indications of PTTs are thus only rough approximations. The polymers share an acryl- or methacrylamide functionality in the repeating unit and require elaborate monomer syntheses – with the exception of PMAAm.[16,39,40]

Despite the undeniable potential of UCST polymers, surprisingly few articles addressing them have been published. From the author's point of view, this might be due to some challenging features, owned by all non-ionic UCST polymers. It is, for instance, commonly known that UCST-type PTs are extremely sensitive towards ionic groups incorporated into the chain. Agarwal *et al.*, for example, found that just traces of acrylic acid repeating units (around 0.2 wt%) incorporated into a PNAGA chain suppress the PT below 0 °C and thus make it unobservable.[27] Also, incorporation of ionic end groups through ionic chain transfer agents or initiators were found to severely suppress UCST-type PTs.[44] Due to this strong sensitivity, the UCST-type PTTs in aqueous solution are even known to decrease over time (if the solution is kept at elevated temperatures of over 70 °C) due to irreversible amide side group hydrolysis into carboxylic groups.[27] Although this reaction only occurs on stoichiometrically negligible scales, the resulting carboxylic groups increase the polymer–solvent interactions so strongly that the PT can even disappear completely. Although being beneficial for certain applications – such as gradually improved renal secretion in biomedical applications due to the hydrolysis-induced increased solubility – polymer chemists should always be aware of the challenges of working with UCST polymers.

3.3 The RAFT Polymerization

The RAFT polymerization is a controlled radical polymerization. As such, it boasts great potential and versatility as it allows for polymerization of a large variety of double bond-containing monomers in virtually any solvent,[5–11] in bulk as well as in heterogenous chain growth reactions such as RAFT emulsion and RAFT dispersion polymerizations.[45–47] A well-controlled RAFT polymerization is essential for the building of polymer blocks with highly similar chain length and composition – especially when tailored (co)polymers with narrow dispersity are required.[48] The great versatility and control of a RAFT polymerization stems from the utilization of the proper chain transfer agent – also commonly called a RAFT agent – that is suitable for the used monomer species. A RAFT agent is typically comprised of a thiocarbonylthio moiety that is covalently linked to the stabilizing group Z as well as the so-called leaving group R. Figure 5 shows the characteristic chemical structure of a RAFT agent consisting of a thioether stabilizing group and a leaving group that will form a tertiary radical. Such trithiocarbonate RAFT agents are an optimal fit for many different monomer species such as most (meth)acrylates and (meth)acrylamides. Even styrene can be successfully polymerized *via* trithiocarbonate RAFT agents.[49]

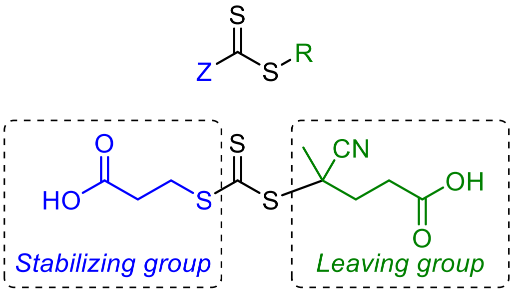

Figure 5: Chemical structure of a RAFT agent. The thiocarbonylthio moiety is attached to a leaving group R as well as a stabilizing group Z.

Depending on the atom of the Z-group attached to the thiocarbonyl moiety, many other RAFT agents like xanthates (oxygen), dithiocarbamates (nitrogen) or dithioesters (carbon) can be constructed. In this work, though, only trithiocarbonates are utilized as they offer great control for the used UCST-type monomer species. The following section will present the underlying fundamentals of the mechanism that facilitates the famous control of the RAFT polymerization.

3.3.1 The Mechanism of the RAFT Polymerization

As any (controlled) radical polymerization, a RAFT polymerization can only be initiated by generation of radicals. The initiation by an initiator radical (which can, for instance, be generated by decomposition of a thermal initiator) is achieved by addition to the double bond of the monomer species. As shown in Figure 6 which shows the reaction scheme of the RAFT mechanism, the newly formed active growing species P_n• can add to other monomer units. These chain growth reactions, however, are largely suppressed by addition of the RAFT agent which produces an intermediary radical. In the so-called preequilibrium, this intermediary radical can either fragment back into the two original components or into a so-called macroRAFT agent (which contains a dormant growing polymer chain) and the leaving group radical R•. At this point, the complexity of choosing the right RAFT agent becomes apparent: on the one hand, R• has to be stable enough for intermediate radical to fragment into its direction, as otherwise the RAFT mechanism will be halted. On the other hand, the radical needs to be sufficiently reactive to facilitate quick reinitiation by addition to monomer. As soon as all leaving group radicals have reinitiated new growing species, the preequilibrium is completed and the main equilibrium is established. Herein, the RAFT intermediate radical exclusively facilitates chain transfer between energetically equivalent growing species with equal fragmentation and addition rates. In a wisely chosen RAFT system, the rates of addition and fragmentation are both significantly larger than the rate of propagation. All growing species thus will be provided equally short active time periods for propagation steps before renewed deactivation by addition to a macroRAFT agent which results in similar molecular weights that are rising linearly with the monomer conversion.

As the RAFT polymerization is a radical polymerization, irreversible termination events *via* combination or disproportionation are unavoidable. This is why RAFT polymerizations are not declared as living by IUPAC definition which states that “chain termination is absent from living polymerizations”.[50] Nonetheless, RAFT polymerizations are inherently of a certain living character as all chains that preserve their thiocarbonylthio moiety can be extended enabling generation of complex multiblock architectures.

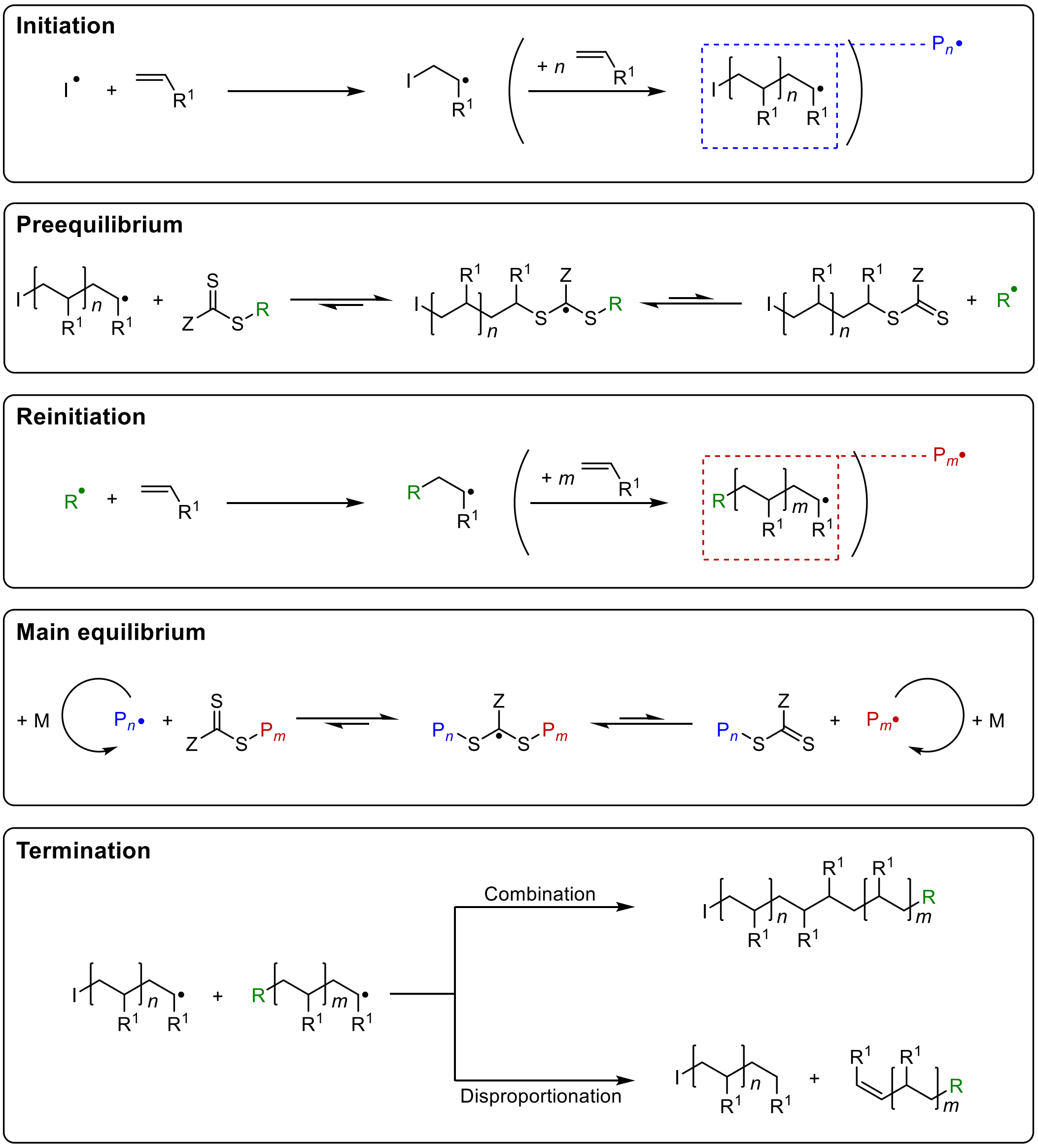

Figure 6: Schematic mechanism of the RAFT polymerization. The reaction is initiated by addition of initiator-derived radical (I•) to a monomer generating a growing species P_n•. In the preequilibrium, such a growing species can add to the RAFT agent resulting in an intermediary radical which can fragment into a macroRAFT agent and the leaving group R• (highlighted in green). After quantitative reinitiation of R•, the main equilibrium of the RAFT polymerization is established. Herein, all active growing species have equally short time periods to propagate by addition to monomer units (M). As the RAFT polymerization is a radical polymerization, irreversible termination events are inevitable. Two active growing species can either terminate *via* disproportionation or combination.

As mentioned previously, a RAFT polymerization will be well-controlled when the rates of addition and fragmentation are significantly higher than the propagation rate and when the leaving group radical reinitiates efficiently so the preequilibrium can quickly be overcome. Also, the concentration of the RAFT (and later macroRAFT) agent needs to be significantly higher than the concentration of the radical species so that all growing species can participate in the chain transfer and are quickly transferred into their dormant state after each active cycle. While too high concentrations of the RAFT agents can lead to rate retardation as the active time-period of the radicals will be vanishingly low, too low concentrations will lead to a more uncontrolled, conventional polymerization process with enhanced likelihood of termination events.

Besides the polymerization control, RAFT also allows for precise tailoring of the molecular weight. This is due to the fact that the number of generated macromolecules should theoretically equal the sum of RAFT agents and initiator derived radicals (if termination *via* combination is neglected). This may sound trivial at first, yet oftentimes constitutes a hard-to-conceive reality for RAFT-newbies. To be fair, the fact that one initiator radical can, theoretically, produce an unlimited amount of polymer chains is counterintuitive when thinking of a conventional chain growth process. Figure 7 illustrates how the chain transfer of a RAFT polymerization facilitates this peculiarity. Herein, we assume an arbitrary polymerization solution that contains 20 monomers (blue spheres), four RAFT agents (with four leaving groups represented by the green spheres) and one initiator radical (red sphere). After chain initiation, the “activity” is transferred to a leaving group radical (resulting in a macroRAFT agent). The leaving group radical can, subsequently, form a new growing species by reinitiation which, in turn, can add to a RAFT agent. This way, just one single radical can successively turn all four RAFT agents into macroRAFT agents containing a dormant chain instead of a leaving group. The thereby established main equilibrium functions analogously: after the short time an active growing species has for a propagation step, it adds to a macroRAFT agent forming an intermediate thiyl radical holding two dormant polymer chains. Through repeated random fragmentation and subsequent random addition to (perhaps) another macroRAFT agent, just this one radical can, theoretically, cause five chains (one initiator radical plus four RAFT agents) to grow – piece by piece. As, once activated by fragmentation from the intermediate radical, each growing species has equal time periods before becoming dormant again. This way, equally long polymer chains will be produced.

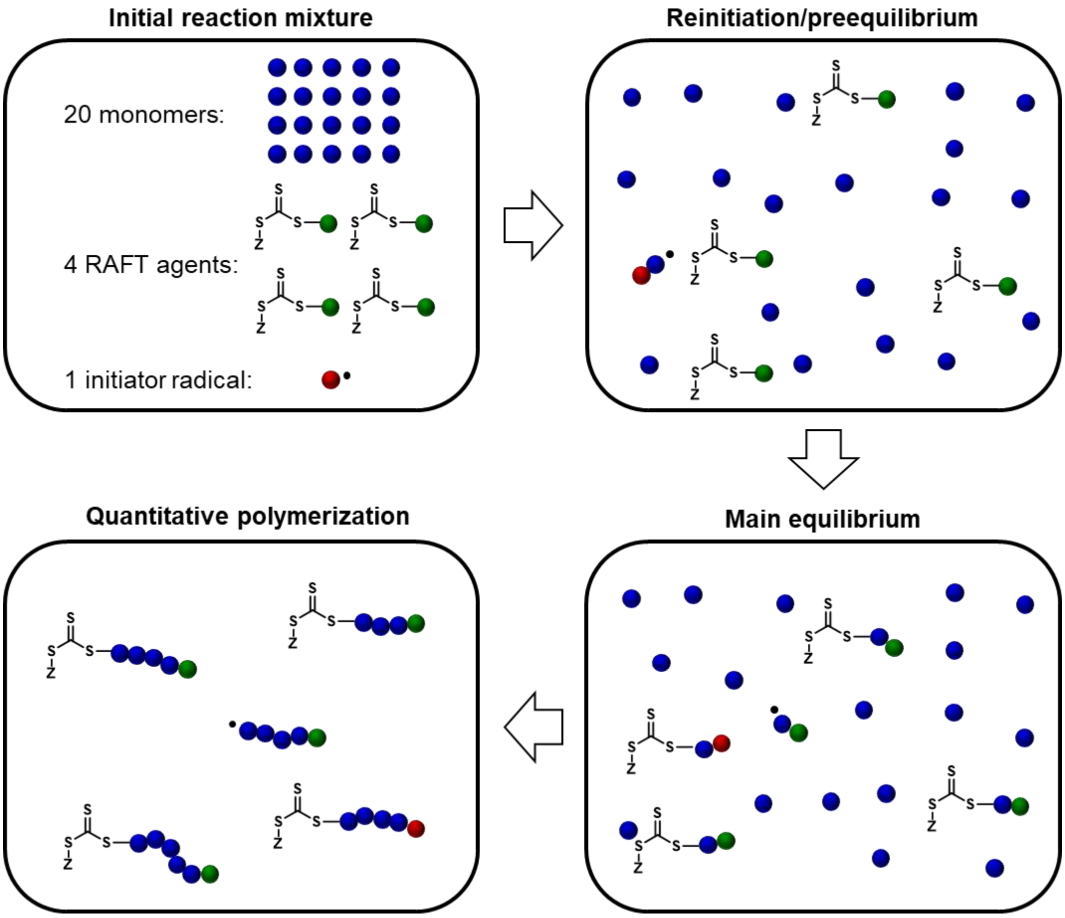

Figure 7: Schematic illustration of the RAFT process. The amount of chains is determined by the sum of growing chains introduced by the initiator radicals and the number of RAFT agents. The chain transfer mechanism of the preequilibrium and main equilibrium enables a controlled, step-by-step chain growth of all growing species.

The even distribution of monomer units between the growing species facilitates precise tailoring of the theoretical number-averaged molecular weight $\overline{M}_{\mathrm{n,th}}$ by adjustment of the ratio between the initial concentrations of monomer and RAFT agent ($[\mathrm{M}]_0$ and $[\mathrm{RAFT}]_0$, respectively). This commonly conducted *via* the following equation:[51,52]

$$\overline{M}_{\mathrm{n,th}} = \frac{p\,[\mathrm{M}]_0 M_{\mathrm{M}}}{[\mathrm{RAFT}]_0 + [\mathrm{I}\bullet]} + M_{\mathrm{RAFT}} \qquad (7)$$

In equation (7), p is the monomer conversion, M_{M} and M_{RAFT} are the molecular weights for the monomer and RAFT agent, respectively. The concentration of growing species introduced by the thermal initiator [I•] adds to the overall number of chains (simple decomposition kinetics for [I•] are available in literature).[49,51,52] As already implied by Figure 7, the chain end livingness L – *i.e.*, the proportion of polymer chains carrying the RAFT-characteristic thiocarbonyl moiety – solely depends on the number of growing species generated from the initiator according to equation (8):

$$L = \frac{[\mathrm{RAFT}]_0}{[\mathrm{RAFT}]_0 + [\mathrm{I}\bullet]} \tag{8}$$

If, as in the arbitrary example of Figure 7, five chains emerge from one initiator radical and four RAFT agents, the maximum chain end livingness will, for instance, amount to 80%. For a well-controlled polymerization with maximum livingness (which is of fundamental importance for construction of multiblock architectures), it is thus usually aimed for the lowest possible initiator concentration that still facilitates reasonably quick polymerization rates.

At this point, the attentive reader might have already seen the error of equation (7): by addition of M_{RAFT} to $\overline{M}_{\mathrm{n,th}}$, the equation assumes that every chain still carries the “full weight” of the RAFT agent – the thiocarbonylthio- and Z-group at one end and the R-group at the other end. This, however, stands in direct opposition to the fact that the number of chains is enlarged by [I•]. To be fair, as the impact of [I•] to $\overline{M}_{\mathrm{n,th}}$ is typically negligibly small, this mistake does not carry a lot of “weight” (pun intended). However, if its impact is included into the $\overline{M}_{\mathrm{n,th}}$-calculation, it should be done correctly as in equation (9) which also accounts for the molecular weight of the initiator radical M_{I}:

$$\overline{M}_{\mathrm{n,th}} = \frac{p\,[\mathrm{M}]_0 M_{\mathrm{M}}}{[\mathrm{RAFT}]_0 + [\mathrm{I}\bullet]} + L\cdot M_{\mathrm{RAFT}} + (1 - L)\,M_{\mathrm{I}} \tag{9}$$

As just stated, the impact of [I•] is usually negligibly small as typically $[\mathrm{RAFT}]_0 >> [\mathrm{I}]_0$. Hence, $\overline{M}_{\mathrm{n,th}}$ is most-often computed *via* the simplified expression of equation (10):

$$\overline{M}_{\mathrm{n,th}} = \frac{p\,[\mathrm{M}]_0 M_{\mathrm{M}}}{[\mathrm{RAFT}]_0} + M_{\mathrm{RAFT}} \tag{10}$$

This simplified computation is usually reasonably accurate which is why it was also used for all $\overline{M}_{\mathrm{n,th}}$-calculations in this work (for more information on this matter see section 10.1, Appendix).

3.3.2 Radical Generation *via* Photoiniferter RAFT

There are several different methods to generate radicals for a RAFT polymerization like redox initiation,[53–55] photoactivation *via* usage of a photoinitiator[56,57] or photo-induced electron transfer[58–60] and even electrochemical initiation.[61,62] The most elegant way of radical generation stems from direct photolysis of the thiocarbonylthio moiety (mechanism illustrated in Figure 8) as it makes the usage of an additional initiator species redundant. This way, no initiator derived impurities or altered alpha chain ends will be obtained. Through absorption of UV- or visible light, the bond between leaving group (or propagating chain) and the thiocarbonylthio compound is reversibly cleaved generating a highly stabilized thiyl radical and an active radical that can enter the pre- or main equilibrium.[49] A polymerization that is initiated in this manner is called a photoiniferter RAFT as the RAFT agent thus facilitates *ini*tiation, chain trans*fer* as well as reversible *ter*mination (*iniferter*).[63–69]

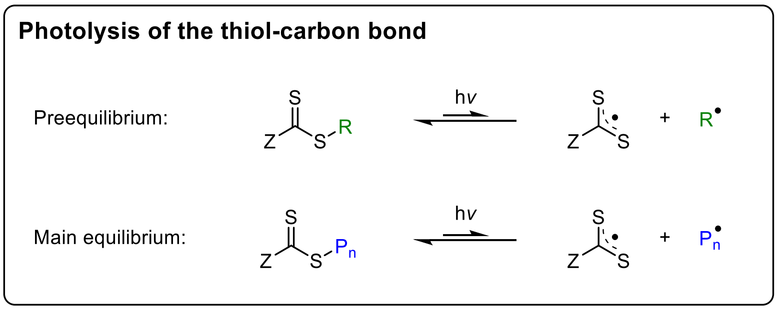

Figure 8: Light-absorption facilitates the reversible cleavage of the carbon–sulfur bond between the leaving group (or growing species) and the thiocarbonylthio moiety. The emerging radical can participate in the typical RAFT equilibria or reversibly recombine with the concomitantly emerging stabilized thiyl radical.

As previously mentioned, photoiniferter RAFT enables a controlled polymerization without the need of a potentially contaminating initiator species. The number of polymer chains derived from a photoiniferter RAFT polymerization should thus theoretically equal the number of RAFT agents. Another big asset of the photoiniferter process becomes evident when looking at the limitations of the conventional, thermal initiation method: unlike the decomposition of thermal initiator, radical generation *via* photolysis of the thiocarbonylthio group will remain constant throughout the whole polymerization process and independent of the reaction temperature. Especially the latter feature boasts great advantages as it allows for polymerization at comparably low temperatures.[66]

3.3.3 Chain Extension *via* Heterogenous RAFT Polymerizations

As the RAFT polymerization has a “living” character, the produced polymer chains can – if they still carry the thiocarbonylthio moiety – be extended. When using another monomer species in such a chain extension, block copolymers can be built in a controlled fashion. In the special case that the polymerization solvent exclusively dissolved the first block, chain growth of the solvophobic second block induces the formation of highly interesting nanoobjects (typically spherical micelles) stabilized by the first, solvophilic block. This PISA can be achieved *via* heterogenous RAFT which can be carried out in an emulsion as well as in a dispersion polymerization process. These polymerizations can be carried out in water (or aqueous cosolvents) enabling an environment-friendly, cheap as well as efficient reaction medium with excellent heat transfer.[70] Typically, RAFT emulsion and dispersion polymerizations require more or less the same ingredients: a dispersing solvent medium, monomer, an emulsifier (for example a surfactant which is a compound that lowers the surface tension between two phases) and an initiator for the generation of radicals. In a chain extension of a soluble block *via* RAFT, however, things can become even more efficient: the stabilization of the particles formed by PISA is accomplished by the first block allowing for a “surfactant-free” process. As surfactants can imply significant disadvantages for biomedical applications or in film formations due to their propensity towards migration and, additionally, are usually difficult and expensive to remove, their redundancy is a great asset of the surfactant-free RAFT approach. If, furthermore, the polymerization can be conducted *via* photoiniferter radical generation, the required ingredients become even more minimalistic as only solvent, macroRAFT agent and monomer will be required.

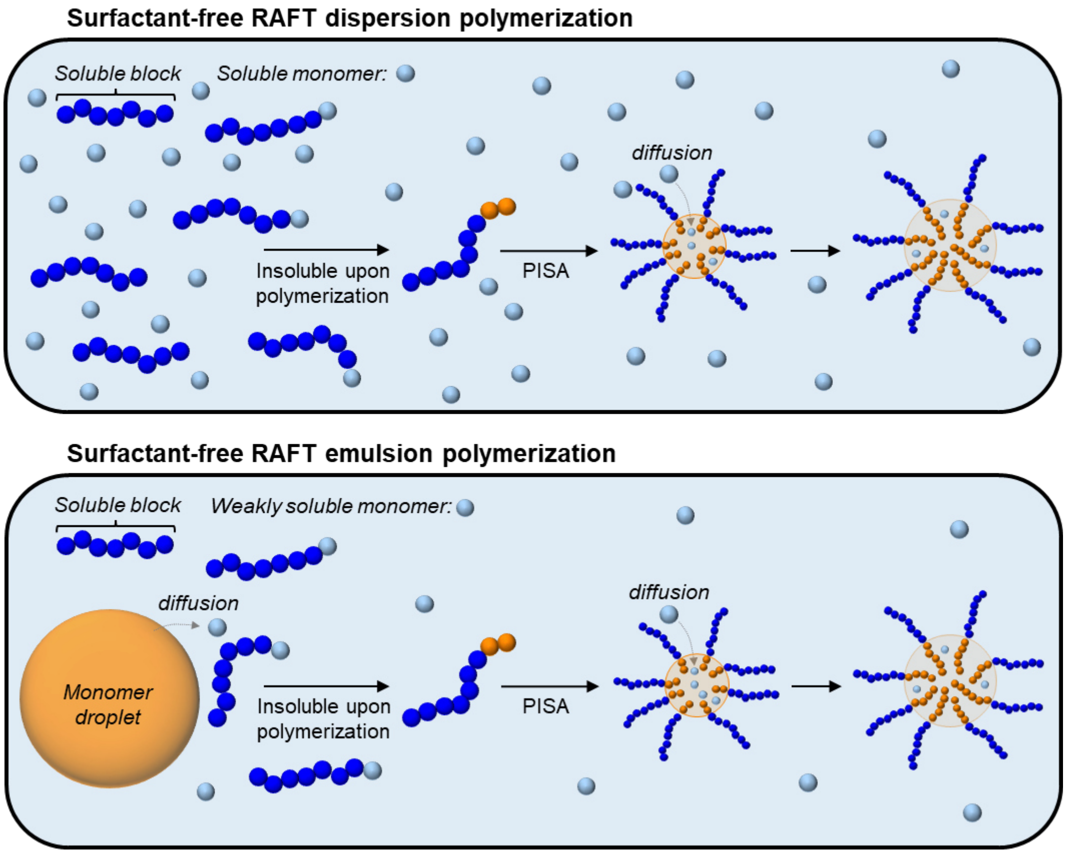

Figure 9: Schematical presentation of surfactant-free RAFT dispersion (top) and emulsion (bottom) polymerization. In both mechanisms, the solvophobic second block collapses into micelles formed by PISA after reaching a critical chain length. This solvophobicity (of the second polymer block, the micelle core as well as the monomer units and droplets) is denoted by the orange color. The soluble first block as well as the dissolved monomer units are colored in deep and light blue, respectively. The polymerization proceeds within these nanoparticles converting the monomer units with drastically enhanced rates. The micelles are thus continuously "fed" with monomer by diffusion and continuously grow in size.

Figure 9 shows the schematical polymerization course of both the surfactant-free RAFT dispersion (top scheme) and emulsion (bottom scheme) process. The main difference between the two polymerizations is the solubility of the monomer in the continuous phase: while being soluble in dispersion, the monomer is insoluble in emulsion polymerizations (the latter thus comprises large, phase-separated monomer droplets and only a very small fraction of dissolved monomer). In the chain extension of the solvophilic first block, monomer units will be added to the growing species. Upon reaching a critical chain length, the second, solvophobic block collapses forming stabilized micelles *via* PISA. From this point on, the polymerization proceeds within the confined dimensions of the micelle-cores which drastically enhances the polymerization rate compared to typical solution polymerizations.[66] Due to the rapid monomer consumption within the micelles, a concentration gradient between the continuous phase and the micelle-cores permanently forces monomer to diffuse into the stabilized particles which, in turn, steadily grow throughout the polymerization.

Due to PISA, the active growing species in RAFT emulsion and dispersion polymerization are compartmentalized which drastically enhances the conversion of monomer to polymer.[70] Hence, these heterogenous RAFT polymerizations are especially fruitful for the polymerization of slowly propagating monomers. As in-depth explanations on the peculiarities of heterogenous RAFT polymerizations would go beyond the scope of this work, the reader is referred to excellent, more specific literature.[71–76]

3.3.4 Reproducibility of RAFT Polymerizations

When scanning a freshly published scientific article for details on a RAFT polymerization, the polymer scientist will typically be interested in several parameters. Apart from the physical (*e.g.*, temperature, light intensity, etc.) and categoric parameters (initiation method, choice of solvent and reactants), also the concentrations of and ratios between the reactants (monomer, RAFT agent, initiator) are fundamentally important. The latter specifications, however, can sometimes get a little chaotic. Concentrations, for instance, are oftentimes provided in the unit "moles per liter" which can be misleading and difficult to reproduce due to changes of volume upon mixing (and temperature). It is hence, in general, more precise (or less ambiguous) to work in weight percentages. At a given mass of polymerization solvent, RAFT polymerization solutions can be precisely reproduced knowing just three (or even just two in case of a photoiniferter RAFT polymerization) parameters:

R_M: The initial ratio of monomer concentration to the concentration of RAFT – or macroRAFT – agent ($[\mathrm{M}]_0/[\mathrm{RAFT}]_0$).

R_I: The initial ratio of initiator concentration to the concentration of RAFT – or macroRAFT – agent ($[\mathrm{I}]_0/[\mathrm{RAFT}]_0$). This quantity is omitted for photoiniferter RAFT polymerizations.

w_S: The combined weight content of the polymerization solids monomer, RAFT agent and – if applied – initiator of the polymerization solution.

The advantages of these three parameters become obvious when contemplating a fictional RAFT polymerization as an example. At a given mass of solvent (which will determine the scale of the polymerization), the mere specification of $R_M = 100$, $R_I = 0.01$ and $w_s = 10$ wt% will provide sufficient information for preparation of the reaction solution. The reader will instantly understand that 10 wt% of the polymerization solution will be monomer, RAFT agent and a minor amount of initiator. Additionally, R_M discloses the theoretical polymerization degree at 100 % monomer conversion while R_I reveals the ratio between initiator and RAFT agent – two highly relevant pieces of information for RAFT experts.

In this work, the three parameters R_M, R_I and w_s will be used consistently to specify on experimental details and relevant reaction conditions of the conducted RAFT polymerizations. Within this context, the influence of w_s on the reactant solutions is rather straightforward as it determines the total mass to be occupied by monomer, RAFT agent and initiator. The interplay of R_M and R_I, though, is a tad more complex: while $[M]_0$ and $[RAFT]_0$ stay largely unaffected by R_I (since the weight content of the initiator will always be negligibly low), $[I]_0$ strongly depends on both R_M and R_I (high values of $[I]_0$ are obtained at low R_M-values and high R_I-values). Using just these three variables R_M, R_I, and w_s, the author aspires to provide synthetic information in a more efficient, precise and informative manner.

3.4 Design of Experiments

As a statistical and planned approach towards experimentation, DoE is a powerful tool for reproducible and efficient process optimization and is firmly established in various fields of industry.[2,3,77–79] Despite highly promising recent surveying articles,[80–84] however, DoE remains widely unknown in academic research as it is simply not part of the typical chemistry university education. From the author's perspective, this can mean missing out on a great opportunity. If performed correctly, DoE can provide various benefits for the academic scientist like more efficient laboratory workflow, more reliable results and even greater knowledge generation compared to conventional experimentation.

DoE can be applied in various ways and for various goals with greatly varying experimental effort. Within a DoE, the effect of parameters (*i.e.*, "factors" in DoE-terminology) on measurable quantities (*i.e.*, "responses") is investigated in a planned approach. These factors – or, to put it more precisely, these factor effects – will be tested for statistical significance. Additionally, the factors can be – if an appropriately comprehensive plan was performed – mathematically linked to the measured response(s) which ultimately yields mathematical equations (*i.e.*, prediction models or prediction equations) which forecast the experiment outcome for any factor combinations. As a result, application of DoE is applicable for versatile purposes being able to unveil different scientific challenges:

1. Identification of significant and insignificant factors
2. Quantification of factor effects
3. Revelation of factor interactions (FIs)
4. Complete modelling of monitored responses *via* prediction equations

In the following chapters, an overview of the fundamentals of DoE is provided addressing all four mentioned points as well as the required know-how for adaptation.

3.4.1 The Perks of DoE

At this point, the reader might be wondering why and how DoE can be superior to conventional experimentation. This section will focus on answering this question by providing appropriate examples and addressing the four points mentioned in the last section.

3.4.1.1 Identification of Significant and Insignificant Factor Effects

Identifying significant and insignificant factors can be very straightforward: In a RAFT polymerization, for instance, the polymerization temperature (factor) is undoubtedly significant for the monomer conversion (response). When a scientist truly wants to be aware every facet of the examined system, however, other more unimposing factors might be worth testing as well. In case of a typical RAFT polymerization these might be the stirring speed, the overall reaction volume, the content of added internal standard (usually DMF) or even the time of N_2-bubbling prior to the polymerization. Testing factors for significance or insignificance is (just) one of the great skills of a DoE.

When a factor is changed to another value (or “level” in DoE-terminology) and another experiment (called “run”) is performed, the measured response will not attain the exact same value. The response-discrepancy can either be caused by statistical error of the system (and typically be small) or by the factor exerting a significant impact (which is called a “factor effect”) on the response. Within the scope of a DoE, appropriate statistical methods (more on that in section 3.4.3) are applied comparing the factor effect with the system error and, thereby, providing a statistical probability for the factor to be significant.

Figure 10 illustrates two exemplary scenarios with highly different system error (which obviously can only be determined if sufficient runs are performed). In both graphs the arbitrary responses 1 and 2 are plotted against each other with each circle representing one run. The color of the circle symbolizes the setting of the factor. In scenario A, 8 runs with the exact same factor setting (black circles) are performed. The scattering of the responses must thus be attributed to system error. Upon setting the factor to another level (red circle), the change of responses is in the same order of magnitude as the system error. Statistical analysis will result in a high probability that the factor is insignificant. Scenario B, on the other hand, shows a factor effect that is markedly higher than the system error. The probability that the factor is significant is very high. Naturally, the experimental effort – or, in other words, the required amounts of runs – are very important for the scientist as well. Fortunately, certain minimal-effort DoE-plans (called “screenings”) are available for mere assessment of factor significance (for more information see section 3.4.2). It should also be stated that DoE-efficiency generally increases with the number of examined factors.

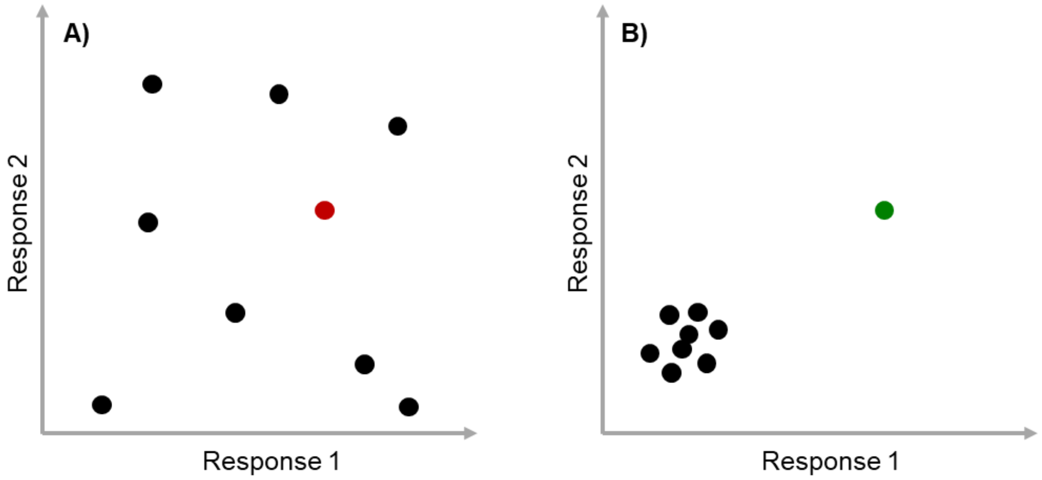

Figure 10: Two exemplary scenarios with highly different system error. Two arbitrary responses 1 and 2 are plotted against one another while each circle represents one run and the circle color represents the setting of one arbitrary factor. Graph A) System error is very high. Changing the factor level (red circle) results in a factor effect that is in the same order of magnitude as the system error. The factor is probably insignificant. Graph B) System error is low. The effect of changing the factor to a different level (green circle) is notedly higher than the system error. The factor is probably significant.

It becomes evident that DoE also solves another problem that typically arises in conventional experimentation: the statistical security of the obtained results. It can become very tempting to just accept a single experiment that might support an assumed – or even desired – theory. In order to provide an example, it is assumed that a polymer scientist wants to prove that elevating the temperature of a RAFT emulsion polymerization leads to an increase of average size of the latex particles. The scientist conducts two polymerizations at different temperatures, analyzes the size of the latex particles and obtains the desired result: at the lower polymerization temperature the particles possess an R_h-value of 50 nm while 60 nm are measured for the particles from the higher temperature synthesis. Obviously, it still is completely unknown what caused this size deviation – system error, inaccuracies of the analytic device or, in fact, the polymerization temperature. All this is easily solved with an appropriate DoE.

3.4.1.2 Quantification of Factor Effects

Apart from the sheer distinction between significant and insignificant factors, quantification of the factor effects is, for obvious reasons, important as well. It is vital to know the impact a change of factor level exerts on the measured response.

Figure 11 illustrates the geometry of a so-called two-level full factorial design for three factors. Each factor will be tested on two different levels (coded by “–“ and “+”) resulting in a total of 8 runs (illustration A) which form a so-called experimental space. Later modelling *via* prediction equations will only be reliable within this experimental space as extrapolation can be erroneous.

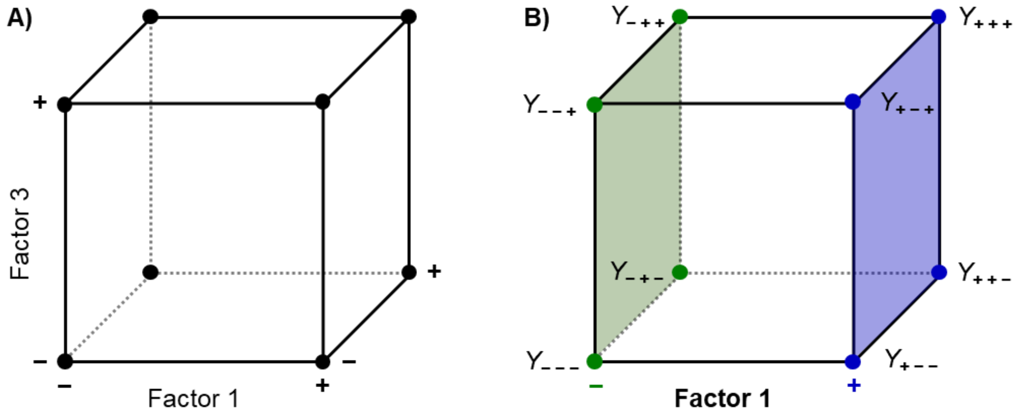

Figure 11: Illustration A) Experimental geometry of a two-level full factorial plan with three factors. Each circle represents one run. The low and high levels of each factor are coded with “–” and “+”, respectively. In illustration B, the effect of Factor 1 is determined by mean comparison of an arbitrary response Y at low and high level.

For each run, at least one response (in theory there is no response limit) is measured. As indicated in the exemplary scenario of illustration B, the factor effect of Factor 1 ($E_{\text{Factor 1}}$) is determined comparing the response means at low (Y_-) and high (Y_+) level (n_+ and n_- denote the number of runs performed at the respective factor’s high and low level):

$$E_{\text{Factor 1}} = \frac{\Sigma Y_+}{n_+} - \frac{\Sigma Y_-}{n_-}. \tag{11}$$

If, for instance, the effect of a factor is negative, the respective response decreases when changing the factor from its low to its high level. As long the different runs cause at least some deviations in the response, naturally every factor and every factor interaction (FI) will possess an effect. Depending on the effect size and the statistical error of the examined system, appropriate statistical tools will assess the factors’ (and the interactions’) significance (see section 3.4.3.2).

3.4.1.3 Revelation of Factor Interactions

Let us assume a relatively simple and comprehensible system in which an exemplary response Y_1 depends on just two factors (A and B). What would be your approach towards investigation of the influences factors A and B exert on Y_1?

In conventional experimentation, system examination is usually performed with the OFAT (one-factor-at-a-time) approach. Herein, just one factor is varied (to investigate its influence on Y_1) while all other factors (in our exemplary scenario only factor B) are kept at a constant level. If, for instance, Y_1 is required to attain a peak value, factor A would then presumably be set to the level where the highest value of Y_1 was obtained and factor B would be varied in subsequent tests – while keeping factor A at the "optimized" level. This OFAT approach, however, has a major drawback: in scientific reality, the effect of a factor A can, naturally, drastically depend on the setting of another factor B (and *vice versa*). This FI AB might not only lead to missing out on finding the true peak value for Y_1, it might also lead to inferior understanding of the examined system.

Fortunately, as already subtly foreshadowed in the previous section, DoE is not only apt to investigate and assess the influence of changing factor levels on a response but will also reveal potential FIs. The potential impact of a two-factor interaction (2FI) AB on the exemplary response Y_1 is illustrated in Figure 12 which plots the response surface of Y_1 versus the factors A and B. Here, the evolution of Y_1 differs completely for the low and high level of B. As in a DoE, the whole experimental space (meaning the square formed by the two levels of each factors) will be examined, the FI AB will be revealed, the optimum will be found and a greater understanding of the system will be achieved.

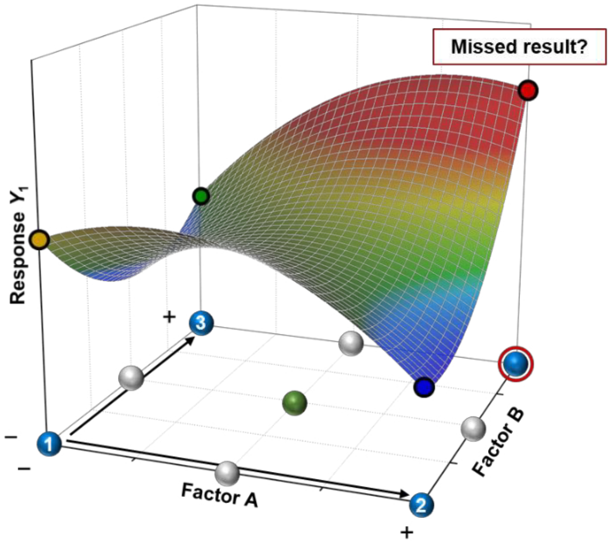

Figure 12: OFAT (one-factor-at-a-time) approach towards experimentation. As indicated by the response surface of the exemplary response Y_1 which shows a strong 2FI AB, this experimental approach might lead to missing out on a potential optimum and true understanding of the examined system.

With the OFAT approach, on the other hand, the workflow might be the following: after completion of the starting experiment (in this scenario factors are set to A^- and B^-, superscripts represent the high "+" or low "–" level), factor A is increased to A^+ while B^- stays constant yielding a lower Y_1-value. As the goal is a maximization of Y_1, the next run would likely performed with the factor settings A^- and B^+ which, in this example, again would not yield a higher value of Y_1. Arguably not every researcher would now go the extra mile and test the factor settings A^+ and B^+ – a reasonable decision that might, however, lead to missing out on the true optimum of Y_1 within the observed experimental space.

3.4.1.4 Complete Modelling of Monitored Responses via Prediction Equations

Finding the factor settings that achieve the optimal system response is a highly difficult task. With the OFAT approach it is, in fact, arguably impossible as the only way to resolve response surfaces (like the one in Figure 12) would be an impracticable multitude of runs. While the only way to find an actual optimum *via* the OFAT method is sheer luck and good faith, DoE actually provides a planned approach towards it. By addition of more runs in the experimental space – and thus providing more than just two levels per factor – non-linear relationships can be detected.

Addition of so-called center points and axial points (green and grey spheres, respectively in the experimental space of Figure 12) facilitates – in this case – three levels per factor. These more complex and sophisticated designs which are apt to adequately portray non-linear factor-response relationship are commonly called response surface methodology (RSM) designs which allow for higher order polynomial regression. To put this in other words: true optimization is achieved through mathematical fits which are called prediction equations. Utilization of these prediction equations will easily reveal the ideal factor settings for every desired response-target.

An exemplary prediction model for response Y_1 depending on two factors x_1 and x_2 is shown in equation (12). Usually, these prediction equations are presented in "coded" form. This means that the factors do not possess their actual values (*e.g.*, a certain mass or temperature) but are converted into coded values that range from −1 (the low level) to +1 (the high level). This way the prediction models provide more information and are easily comprehensible: the intercept β_0, for instance, represents the average of all responses and is thus (logically) obtained when all factors are set to their center (0) level. Additionally, as in the coded form all factors possess the same range, the factor coefficients β provide insight on the extent of the terms impact on the response. These terms can be linear (as in $\beta_1 x_1$ or $\beta_2 x_2$), but they can also represent FIs ($\beta_{12} x_1 x_2$) or non-linear factor-response relationships ($\beta_{11} x_1^2$).

$$Y_1 = \beta_0 + \beta_1 x_1 + \beta_2 x_2 + \beta_{12} x_1 x_2 + \beta_{11} x_1^2 + \dots \tag{12}$$

An adequate prediction equation that contains all factors that significantly influence the response provides all the information necessary for optimization and thorough system understanding. Thorough understanding of DoE, however, requires knowledge over the generation of the design plans as well as a certain statistical background which will be provided in the following sections

3.4.2 DoE – The Experimental Plan

One of the major attributes of DoE is its efficiency and plannability. Depending on the target of the scientist or potential practical restrictions it is advisable to choose the experimental plan with minimal effort and concurrent maximal information generation. Besides the most basic plans like two-level factorial designs which are commonly used for screening purposes (and will be illustrated in the following section), there are a multitude of different options for a multitude of different scientific challenges. In the following, the basic principles of experimental design plans, the concept and meaning of design plan resolution (section 3.4.2.2) as well as options to detect non-linear relationships (section 3.4.2.3) and to fully optimize (and predict) complex system *via* RSM (section 3.4.1.4) will be presented. The following sections are intended as an accessible introduction into the basics of DoE and will thus be presented in "plain" English. For highly detailed and elaborate statistical background it is referred elsewhere.[85,86]

3.4.2.1 Two-Level Factorial Design

The biggest difference in experimentation between DoE and the conventional OFAT-approach is that DoE allows for variation of multiple factors simultaneously. The simplest experimental design involves two factors which are both tested at two levels. The resulting experimental space can be illustrated as a square (see Figure 13, illustration A) whose four vertices represent the four required runs. These runs are additionally listed in the respective design plan which provides the coded factor levels required for each individual run. In two-level full factorial designs, the number of required runs n_{Run} scales with the amount of examined factors n_f according to:

$$n_{\mathrm{Run}} = 2^{n_f} \tag{13}$$

As the number of factors increases, the experimental effort increases exponentially. The experimental space of a two-level three factor design, for instance, can thus – as one dimension is added – be depicted as a cube (Figure 13, illustration B). The resulting experimental plan consists of eight runs. Self-evidently, the experimental effort for higher amounts of factors quickly becomes impracticable. With the invention of fractional factorial designs, however, there fortunately is a method to drastically reduce the amount of runs while maintaining optimal knowledge generation (see section 3.4.2.2).

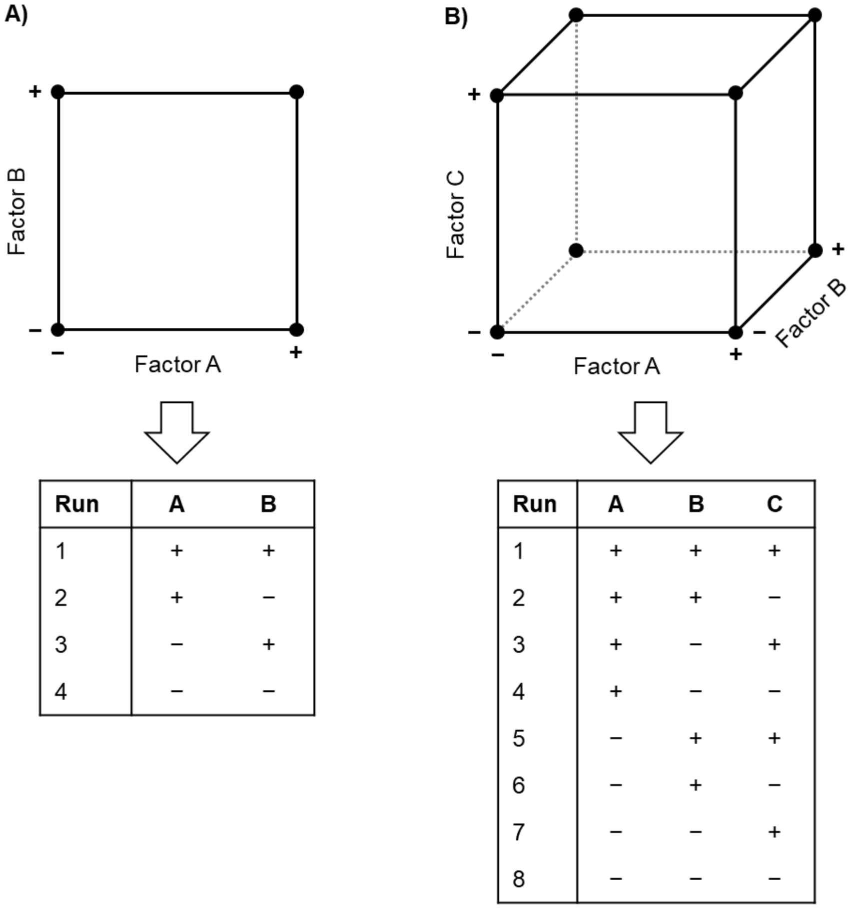

Run	A	B
1	+	+
2	+	−
3	−	+
4	−	−

Run	A	B	C
1	+	+	+
2	+	+	−
3	+	−	+
4	+	−	−
5	−	+	+
6	−	+	−
7	−	−	+
8	−	−	−

Figure 13: Illustration of two-level full factorial designs and the respective design plans for investigation of two factors (A) and three factors (B).

In order to process all this information in a more easily comprehensible fashion, a fictional two-level factorial design for three factors will be presented as demonstration example. In this scenario, the yield (*i.e.*, the response) of a thermally labile molecule in a chemical reaction is monitored in dependence of the factors reaction temperature T, reaction time t and stirring speed v_S whose levels were varied from 50−80 °C, 1−5 h and 400–800 rpm (low level to high level), respectively. The corresponding design plan is shown in Figure 15. In here, the factor levels of the eight required runs are shown in coded form. As full factorial designs allow for estimation of all interactions, also provides the interaction columns AB, AC, BC as well as the three-factor interaction (3FI) ABC. The plus and minus pattern of the interaction results from multiplication of the respective “parent” terms (multiplication of −A with −B, for instance, will yield a +AB). The effects of interactions can be computed in the same way as the main effects (as is shown in equation (11)).

Before this is further elaborated, it is worth mentioning a decisive DoE-fundamental: despite the fact that all design plans in Figure 13 and Figure 15 are well-ordered, random execution order of the runs is mandatory. Otherwise, potentially time-lurking effects – within our current DoE example this might be degradation of reaction educts – can be mistaken for an actual factor effect. By conducting the runs in random order, the risk of such time-lurking influences will be greatly reduced.

Run	**A**	**B**	**C**	**AB**	**AC**	**BC**	**ABC**
1	+	+	+	+	+	+	+
2	+	+	−	+	−	−	−
3	+	−	+	−	+	−	−
4	+	−	−	−	−	+	+
5	−	+	+	−	−	+	−
6	−	+	−	−	+	−	+
7	−	−	+	+	−	−	+
8	−	−	−	+	+	+	−

Figure 14: Ordered experimental plan of a two-level full factorial design with three factors A, B and C. The factor settings required for each run are provided in coded form ("−" for low and "+" for high level). The three two-factor and the one 3FI are highlighted in green. Their coded values are obtained by multiplication of the respective parent terms.

Figure 15 shows the design plan with the actual factor settings and provides the fictional experimental values for the only response of the DoE – the yield of the thermally labile compound. With the eight responses – which have an estimated systematical error of ± 2 % – the main and interaction effects can be determined (according to equation (11)). Already at first glance, some of those effects appear to be negligibly small while others seem to have a big impact on the observed yield. The yield seems to rise with increasing reaction time ($E_t = +7.8$) and to decrease with growing reaction temperature ($E_T = -15.3$) whereas the effect of the stirring speed ($E_{v_s} = +1.3$) is in the same magnitude of the systematical error (statistical evaluation of factor significance is provided in 3.4.3.2). Equally small effects are obtained for all interactions except one: strikingly, the strongest effect belongs to the interaction of reaction temperature and time ($E_{T\cdot t} = -37.7$). But what does this tell us?

Run	***T* / °C**	***t* / h**	**v_s / rpm**	$T \cdot t$	$T \cdot v_s$	$t \cdot v_s$	$T \cdot t \cdot v_s$	***Yield* / %**
1	80	5	800	-	-	-	-	43
2	80	5	500	-	-	-	-	40
3	80	1	800	-	-	-	-	72
4	80	1	500	-	-	-	-	70
5	50	5	800	-	-	-	-	93
6	50	5	500	-	-	-	-	95
7	50	1	800	-	-	-	-	50
8	50	1	500	-	-	-	-	48
Effect	−15.3	+7.8	+1.25	−37.7	+1.3	−0.8	+1.2	-

Main effects

Interactions

Figure 15: Ordered, fictional experimental plan of a two-level full factorial design with three factors reaction temperature T, reaction time t and stirring speed v_s with the actual factor level-values and the obtained experimental results (the response). The so-called main effects of the three factors as well as the interaction effects are additionally provided.

A FI between two factors means that the individual main effects depend on the factor level of the other. In order to illustrate this, the $T\cdot t$-interaction plot is provided in Figure 16. A negative interaction effect AB implies that both factors A and B exert an opposing effect on the measured response when switching the factor level of the interaction counterpart. Exactly this is displayed in the $T\cdot t$-interaction plot (Figure 16): while the yield increases drastically within the time window of 1–5 h at the low temperature level of 50 °C (blue symbols), the opposite effect is observed at the high temperature level (80 °C, red symbols). While after only 1 h, higher yields are obtained at 80 °C, the thermally labile compound thereafter appears to decompose resulting in a greatly reduced yield after 5 h of reaction time.

Interactions like these can easily stay undetected with conventional OFAT-experimentation – especially when the examined system is more complex than this simple, fictional example. As interactions, oftentimes also accommodate the most valuable information to gain comprehensive knowledge about the examined system, missing out on their detection can thus greatly be a great omission.

Interpretation of FIs can lead to highly interesting findings and, perhaps, a completely newfound system understanding.

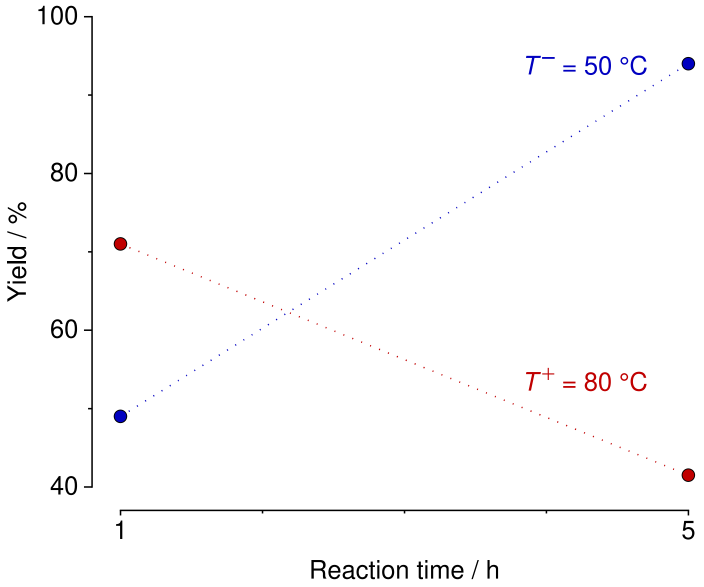

Figure 16: Interaction plot of reaction temperature and time. The yield of the thermally labile compound is plotted against the reaction time for the low level (50 °C, blue symbols) and for the high level (80 °C, blue symbols) of reaction temperature. The dashed lines are added as a guide to the eye.

Full factorial designs offer a possibility to unambiguously identify all main and interaction effects. With an increasing number of factors, though, the experimental effort increases exponentially and becomes untenable. A method to reduce the experimental effort without the necessity of losing system-information is presented in the following section.

3.4.2.2 Two-Level Fractional Factorial Designs

In two-level full factorial plan with three factors, three main effects, three 2FIs and one 3FI will be revealed. Ramping it up to five factors would already lead to resolution of five main effects, ten 2FIs, ten 3FIs five 4FIs and one 5FI. Full factorial designs can unambiguously cover every main and interaction effect. In the great majority of cases, however, 3FIs (and especially even larger interaction terms) have no significant influence on the examined response. The number of insignificant facts – which are only used for estimation of the system error – can amount far more than necessary.

It can thus be very wise and efficient to reduce the amount of runs with so-called fractional factorial designs. A proper fractional factorial will unambiguously reveal all main effects and 2FIs while interactions between more than two factors will be mathematically confounded – the price that must be paid for reducing the number of runs. The number of runs n_{Run} for a two-level fractional factorial is computed according to equation (14) in which n_f and n_p are the number of examined factors and the fraction number by which the full factorial is reduced, respectively.

$$n_{\mathrm{Run}} = 2^{n_f - n_p} \tag{14}$$

The way an exemplary two-level full factorial design with three factors is reduced to a fractional factorial design by reducing the number by 50 % ($n_p = 1$) is shown in Figure 17. The top part of this figure depicts the full factorial design matrix consisting of eight runs and the respective experimental space (which forms a cube). If we would assume, that the 3FI ABC had no significant effect – an oftentimes reasonable assumption – its investigation can be omitted by reduction of all runs resulting in ABC$^-$ (or ABC$^+$, the respective run columns and vertices of the cube are highlighted in red). In the resulting 2^{3-1}-fractional factorial, the ABC-interaction can thus not the estimated, as it is only investigated on one level (as indicated by the red coloring). The main effects and 2FIs are estimated based on two runs on their low and high level each. Unfortunately, though, each column has one column with identical coding. Factor A, for instance, is confounded with the 2FI BC (the confounding effect of each column is listed below the column header in italic letters). To put this in simpler words: if we observe an effect of factor A, it could easily stem from the confounding 2FI. It is mathematically impossible to distinguish between confounded terms. Fractional factorials that confound main effects with 2FIs have a so-called resolution of III (commonly provided in roman numerals) and are considered to be inapt designs – even for the simplest screening purposes. When we look at the resulting experimental "space" – if that description is even appropriate – that is spanned from just four vertices it does not come as a surprise that a 2^{3-1}-fractional factorial is a rather poor design.

Run	A	B	C	AB	AC	BC	ABC
1	+	+	+	+	+	+	+
2	+	+	−	+	−	−	−
3	+	−	+	−	+	−	−
4	+	−	−	−	−	+	+
5	−	+	+	−	−	+	−
6	−	+	−	−	+	−	+
7	−	−	+	+	−	−	+
8	−	−	−	+	+	+	−

Run	A *BC*	B *AC*	C *AB*	AB *C*	AC *B*	BC *A*	ABC
1	+	+	+	+	+	+	+
4	+	−	−	−	−	+	+
6	−	+	−	−	+	−	+
7	−	−	+	+	−	−	+

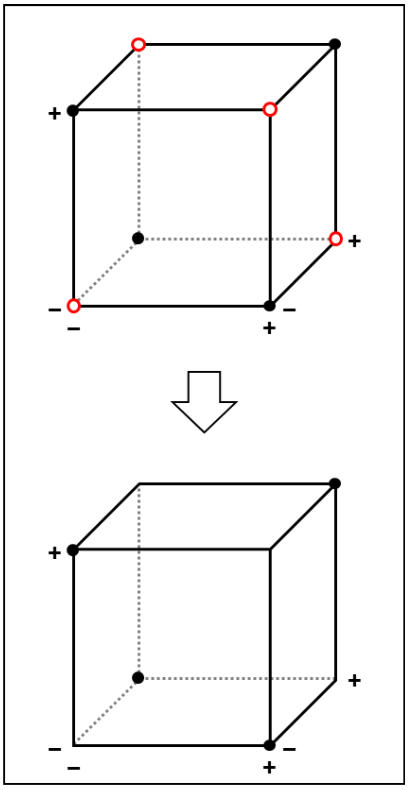

Figure 17: Reduction of a two-level full factorial design with three factors (A, B and C) into a 2^{3-1}-fractional factorial design by omission of all runs resulting in ABC^- (highlighted red). The experimental space is illustrated by a cube which is formed through 3 factors at two levels each. When the red vertices (*i.e.*, the runs resulting in ABC^-) are excluded, the experimental space is greatly reduced resulting in confounding of main effects and 2FIs.

A more reliable and better engineered design is the 2^{4-1}-fractional factorial which examines four factors with just eight runs. The full factorial 2^4-design matrix is depicted in the top table of Figure 18. This design results in four main effects, six 2FIs, four 3FIs and one 4FI. As resolution of the 4FI is – nearly always – superfluous, all runs resulting in a coding of $ABCD^-$ (highlighted in red) can be expurgated. As is shown in the emerging fractional factorial design matrix below, each column has one identical counterpart. Each main effect is confounded with a 3FI and the 2FIs are confounded with one another. As 3FIs are highly unlikely, this fractional factorial is able to unambiguously identify main effects – the main purpose of smaller screening designs.

Run	A	B	C	D	AB	AC	AD	BC	BD	CD	ABC	ABD	ACD	BCD	ABCD
1	+	+	+	+	+	+	+	+	+	+	+	+	+	+	+
2	+	+	+	−	+	+	−	+	−	−	+	−	−	−	−
3	+	+	−	+	+	−	+	−	+	−	−	+	−	−	−
4	+	+	−	−	+	−	−	−	−	+	−	−	+	+	+
5	+	−	+	+	−	+	+	−	−	+	−	−	+	−	−
6	+	−	+	−	−	+	−	−	+	−	−	+	−	+	+
7	+	−	−	+	−	−	+	+	−	−	+	−	−	+	+
8	+	−	−	−	−	−	−	+	+	+	+	+	+	−	−
9	−	+	+	+	−	−	−	+	+	+	−	−	−	+	−
10	−	+	+	−	−	−	+	+	−	−	−	+	+	−	+
11	−	+	−	+	−	+	−	−	+	−	+	−	+	−	+
12	−	+	−	−	−	+	+	−	−	+	+	+	−	+	−
13	−	−	+	+	+	−	−	−	−	+	+	+	−	−	+
14	−	−	+	−	+	−	+	−	+	−	+	−	+	+	−
15	−	−	−	+	+	+	−	+	−	−	−	+	+	+	−
16	−	−	−	−	+	+	+	+	+	+	−	−	−	−	+

Run	A *BCD*	B *ACD*	C *ABD*	D *ABC*	AB *CD*	AC *BD*	AD *BC*	BC *AD*	BD *AC*	CD *AB*	ABC *D*	ABD *C*	ACD *B*	BCD *A*	ABCD
1	+	+	+	+	+	+	+	+	+	+	+	+	+	+	+
4	+	+	−	−	+	−	−	−	−	+	−	−	+	+	+
6	+	−	+	−	−	+	−	−	+	−	−	+	−	+	+
7	+	−	−	+	−	−	+	+	−	−	+	−	−	+	+
10	−	+	+	−	−	−	+	+	−	−	−	+	+	−	+
11	−	+	−	+	−	+	−	−	+	−	+	−	+	−	+
13	−	−	+	+	+	−	−	−	−	+	+	+	−	−	+
16	−	−	−	−	+	+	+	+	+	+	−	−	−	−	+

Figure 18: Reduction of a two-level full factorial design of four factors (A, B, C and D) into a fractional factorial 2^{4-1}-design. The omitted columns (which represent $ABCD^{-}$) are highlighted in red. As a consequence, the 4FI effect cannot be identified (as it is only tested on one level). Although fractioning of the full factorial leads to confounded 2FIs, the main effects are only confounded with 3FIs and can thus be identified unambiguously.

Fractional factorials that lead to confounding of main effects with 3FIs and, coincidently, 2FIs with each other have a resolution of IV. Resolution IV-designs are a reasonable compromise between minimal experimental effort and sufficient knowledge generation and are commonly used for speedy screening purposes.

Resolution V-designs confound main effects with 4FIs and 2FIs with 3FIs and are thus even capable of unequivocal identification of 2FI effects. Table 1 provides the design resolutions of various two-level fractional factorial designs depending on the number of required runs and investigated factors. The diagonal of the full factorial designs is colored white as it provides full resolution of every main and interaction effect. Full factorial designs can be fractioned by cutting the required runs in half ($n_p = 1$) and even further reduction (*e.g.*, a 75 %-reduction of required runs with $n_p = 2$). Naturally, however, with increased fractioning, the design resolution will decrease. The red coloring of resolution III design symbolizes their inaptitude for identification of neither main nor 2FI effects as they are mathematically confounded. The yellow highlighting of resolution IV designs highlights the very delicate balance between minimal practical effort and knowledge generation (2FIs are confounded with each other). Resolution V (and higher resolution) designs are colored in green as they are capable of unambiguous identification of both main and interaction effects.

Table 1: Resolution of various two-level full and fractional factorials as well as the required amount of runs versus the number of examined factors.

Runs	**Factors**						
	2	**3**	**4**	**5**	**6**	**7**	**8**
4	2^2	2^{3-1} (III)					
8		2^3	2^{4-1} (IV)	2^{5-2} (III)	2^{6-3} (III)	2^{7-4} (III)	
16			2^4	2^{5-1} (V)	2^{6-2} (IV)	2^{7-3} (IV)	2^{8-4} (IV)
32				2^5	2^{6-1} (VI)	2^{7-2} (IV)	2^{8-3} (IV)
64					2^6	2^{7-1} (VII)	2^{8-2} (V)
128						2^7	2^{8-1} (VIII)
256							2^8

Depending on the scientist's goal, there will be more and less suitable designs. A typical DoE route would, for instance, look as follows:

For mere investigation of the main effects – which is then intended to be succeeded by a more comprehensive design that investigates only the significant factors – resolution IV designs typically suffice. This, however, comes with a certain risk: in the (very) rare case that a significant interaction effect (E_{AB}) stems from two factors with insignificant main effects (E_A and E_B), E_{AB} might be mistaken for E_{BC} (in a 2^{4-1}-design). In resolution V (and higher resolution) designs, this (rather low) risk can be eliminated as 2FIs are only confounded with 3FIs. For more information about design matrices, design resolution and confounding effects it is referred to excellent textbooks with more detailed elaborations.[85,87]

3.4.2.3 Detection of Non-Linear Relationships via Center Points

As a general rule of thumb, one should not overestimate non-linear effects. Very often, the observed relationships between factors and responses will be adequately described by a linear model (based on only two levels per factor). More complex systems, however, can show highly interesting non-linear effects which definitely cannot be identified with simple two-level factorial designs. Figure 19 shows different potential non-linear factor-response-relationships. When only a two-level factorial design is conducted, experimental values (the Y-mean at x^{-} and x^{+}, black circles) are observed exclusively at two levels per factor (unfilled circles). This may lead to missing out on a strong non-linear effect – or even a response maximum as shown by the black line in graph A. Graph B shows the rare case in which a factor with no (or minimal) main effect exhibits a response maximum between the examined factor levels due to a strong non-linear effect. Despite having a great impact on the response, this factor would likely be assessed as insignificant and ditched in later, more comprehensive investigations. The easiest and most efficient solution to this problem is the addition of so-called center points (factor level coded with a “0”, orange circles in Figure 19). The center point is always located in the middle of the low and high factor level and will – with great probability – be able to detect non-linearities. In extremely rare cases, a factor-response-relationship can even possess multiple maxima within the observed factor range. A particularly unfortunate representative of this case is shown in graph C, in which the observed response at the center level coincidently falls perfectly in line with the low-and high-level response. Here, the factor-response-relationship would erroneously be identified as linear (orange dashed line).

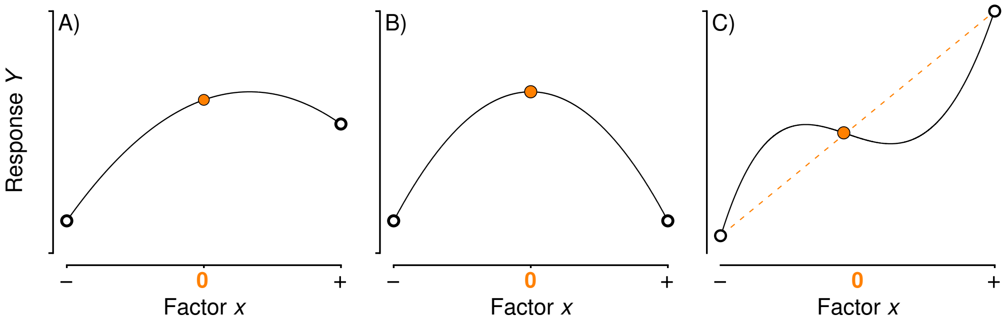

Figure 19: Display of different fictional factor-response-relationships. Performing a two-level factorial design provides experimental data at the low and high factor levels (unfilled circles). Potential non-linear factor-response-relationships (black line) would not be detected. Addition of so-called center points in the middle of the low and high factor level (orange circles, coded with a "0") can lead to detection of non-linear effects (graphs A and B). In rare cases of even more complex factor-response-relationships (graph C), three factor levels will not suffice for adequate modelling. In particularly unfortunate cases, this can even lead to erroneous identification of a linear factor-response-relationship (dotted orange line).

3.4.2.4 Modelling of Non-Linear Systems via RSM Designs

Center points lie in the center of the design geometry and always possess a (coded) level of 0 for all factors (see Figure 20, illustration A). Due to its prominent location within the design, the observed response at the center point has a stronger influence on the analytic findings of the DoE than the responses of the vertices. This so-called leverage might be a familiar phenomenon from simple linear regression: a data point that is located in a distance to the majority of the other data points, it exerts a much stronger influence on the linear fit than the average data point. Measuring errors will thus drastically corrupt the quality of the fit. A simple way to reduce data point leverage is run repitition. Hence, it is strongly advised to perform replicate runs of the center points.

While addition of center points allows for detection of non-linear effects, the generated knowledge is limited. As at the center point all factors are set to their respective midlevel, it is impossible to attribute these non-linearities to the individual factors. For appropriate assignment of non-linear effects every factor requires (at least) three distinct levels. The most intuitive way to achieve this might be a three-level full factorial design. The geometry of such a design (for three factors) is shown in illustration B of Figure 20. Although three-level factorials allow for modelling of non-linear factor-response-relationships (*i.e.*, generation of quadratic prediction equations), their major drawback instantly catches the eye: the experimental effort becomes unrealistic very fast. The established route towards modelling of non-linear systems is thus to augment the two-level factorial frame with specifically located data points and thereby turning them into so-called response surface methodology (RSM) designs. The design geometry of, arguably, the most famous RSM representative is shown in illustration C. In this so-called central composite design (CCD), the two-level full factorial is augmented by a center point (orange circle) and "axial" points (green circles). At axial points, all factors except one are at their midlevels (0). The axial factor levels (−a and +a) are located at a specific distance outside of the original factor ranges providing a total of five levels per factor. Occasionally, however, practical execution of these axial runs becomes unfeasible due to extreme – or even inaccessible – factor levels. In this case, a viable solution is to locate these axial points at the center of each "face" of the experimental space (−a = −, +a = +). This CCD-subspecies is hence called a face-centered central composite design (FC-CCD).

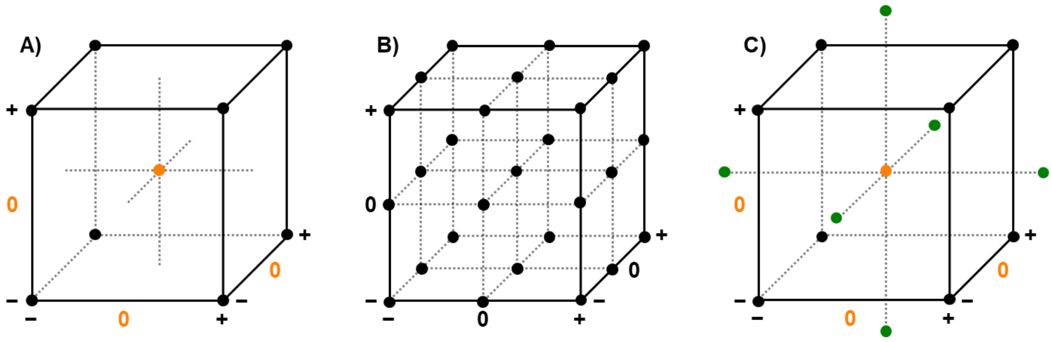

Figure 20: Display of design geometry for different experimental designs examining three factors. A) Two-level full factorial with added center point. This design can identify main effects and factor interactions. Non-linearities are detected, however, cannot be assigned to individual factors. B) Three-level full factorial designs will unveil even quadratic terms. The accompanied experimental effort is usually unrealistically high. C) The CCD is a result of augmentation of a full-factorial two-level design (illustration A). CCDs allow for identification of non-linear terms as well, yet, in a markedly more efficient manner than a three-level full factorial design.

CCDs are able to generate prediction models that will unveil main effects, factor interactions and non-linear factor-response relationships. In the rare case that quadratic fitting is insufficient, there are options available to augment the design for resolution of cubic terms and even higher. At this point, it is worth mentioning that other RSM designs like the so-called Box-Behnken and computer-generated optimal designs can lead to success as well. Especially the latter have proven to be highly efficient. Despite a less intuitive run arrangement – factor levels will be distributed scattered and disordered within the experimental space – than in CCDs, computer-generated optimal designs combine minimal practical effort with maximum prediction accuracy. For interested readers, detailed elucidation of computer generated optimal designs are provided elsewhere.[88,89]

While this section (3.4.2) provided sufficient know-how on the generation of design plans and their resolution of main effects, interactions and non-linearities, the next section will serve as an introduction into the statistical fundamentals surrounding DoE.

3.4.3 Statistical Fundamentals for DoE

In the following the most important statistical fundamentals for DoE will be presented in a simplified manner. At first, the basics behind normal distributions (section 3.4.3.1) and quantification of effect significance *via* analysis of variance (ANOVA, section 3.4.3.2) will be covered. After that, the most relevant and DoE-standard diagnostical tools are presented in section 3.4.3.3.

3.4.3.1 The Normal Distribution

The probability density function $\Phi_{\sigma,\mu}$ of a (real-valued random) variable is distributed symmetrically around its expected value μ (with the standard deviation σ) according to the following equation:

$$\Phi_{\sigma,\mu} = \frac{1}{\sqrt{2\pi}\,\sigma}\exp\left(-\frac{1}{2}\left(\frac{x-\mu}{\sigma}\right)^2\right) \tag{15}$$

Normally distributed events occur commonly in in our everyday life – may that be in physical, biological or technical processes, a classic board game (e.g, the sum of two dices) or the repetition of a measurement with a certain systematic error. The plot of a normally distributed variable (see Figure 21) shows a symmetrical distribution around the expected value which naturally grows broader if the standard deviation increases. The absolute $\Phi_{\sigma,\mu}$-values do not possess great information. It is the integral $\int_{x_2}^{x_1} \Phi_{\sigma,\mu}\,\mathrm{d}x$ – that is the area beneath the function from the between the variable values x_1 and x_2 – that will provide the probability of the variable to fall within that value-interval. As the probability density functions are normalized, the area between $x_1 = \infty$ and $x_1 = -\infty$ will equal a probability of 1. The integral $\int_{-\sigma}^{\sigma} \Phi_{\sigma,\mu}\,\mathrm{d}x$ – that spans from $x_1 = \sigma$ to $x_1 = -\sigma$ – represents a 68 % probability

($\int_{-2\sigma}^{2\sigma} \Phi_{\sigma,\mu}\,\mathrm{d}x = 95\ \%$, $\int_{-3\sigma}^{3\sigma} \Phi_{\sigma,\mu}\,\mathrm{d}x = 99.7\ \%$). When presenting the mean of a normally distributed measured parameter together with a so-called confidence interval (CI), the typical scientific consensus is to provide a CI that equals $2{\cdot}\sigma$.

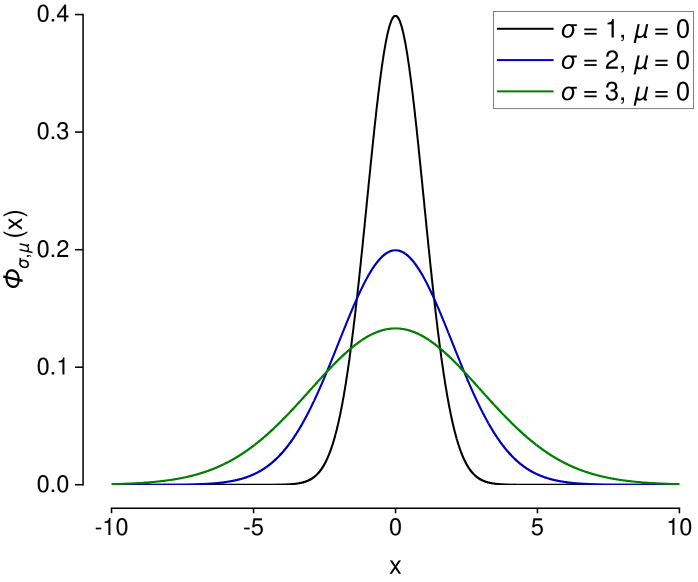

Figure 21: Display of three arbitrary probability density functions with different standard deviation.

3.4.3.1.1 The Normal Plot

In a DoE, the influence of (usually more than two) factors on (usually more than one) response is investigated. A two-level full factorial design, for instance, will produce 15 effects (composed of main effects and various factor interactions, see section 3.4.2.2). The normal plot is a great way to gain a visual impression on data that is normally distributed and data that departs from normality. Or, within the context of a DoE, it serves as a quick tool to assess which effects are significant or insignificant.

As normally distributed data varies symmetrically around a mean value, naturally, bigger and smaller effects will be obtained. If normally distributed, a plot of the effect sizes against the so-called cumulative probability of the normal distribution should be approximately linear. The cumulative probability of the normal distribution signifies the probability that a measurement (in our case an effect size) falls below a certain value Y. This is perhaps best explained by providing an example: the intelligence quotient-(IQ)-value is a normally distributed quantity with a mean value of – by definition – 100. The normal IQ-distribution (with a standard deviation σ of 15, $\mu = 100$) is illustrated in Figure 22 (graph A). With increasing IQ, naturally, the cumulative probability increases. IQs below 55 are incredibly rare (around 0.1 %) while the chance of testing a random person with an IQ below 100 amounts to 50 %. Around 68 % of people possess an IQ between 85 and 115.

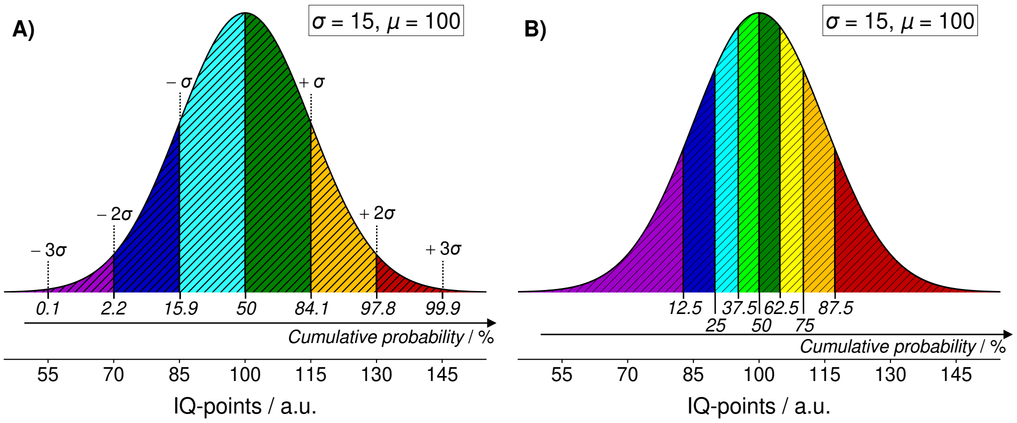

Figure 22: Display of the IQ-normal distribution. Graph A) The cumulative probability to measure an IQ below 100 amounts to 50 %. Around 68 % of people possess an IQ between 85 and 115 (± 1σ) and around 95 % fall within the IQ-range of 70 and 130 (± 2σ). Graph B) The same normal distribution is cut into quantiles which are intervals with equal probability.

If – for whatever dystopic reason – it would be required to sort people by their IQ while building equally sized groups, the disparities would differ greatly depending on the group's location under the normal distribution. In other words, the number of people with an IQ between 0 and 82.7 would be equal to the number of people with an IQ between 100 and 104.8. In statistical terminology, these groups (continuous probability intervals) are called quantiles. These quantiles – which become narrower the closer they are to the normal distribution's mean – are shown in graph B of Figure 22. Exactly these quantiles play a major role in the normal plot.

For creation of a normal plot, the data – like the observed effects from a DoE – are first ranked in size. Then, the Y-axis – which is the cumulative probability scale – is divided into as many quantiles as there is data. Finally, the sorted data is plotted in the midpoint of each quantile. In graph A of Figure 23, the IQ measurements of 100 fictional people (generated by computer with $\sigma = 15$ and $\mu = 100$) is plotted accordingly. Unsurprisingly, the plot suggests normality as indicated by the black line which falls in reasonable agreement with the data.

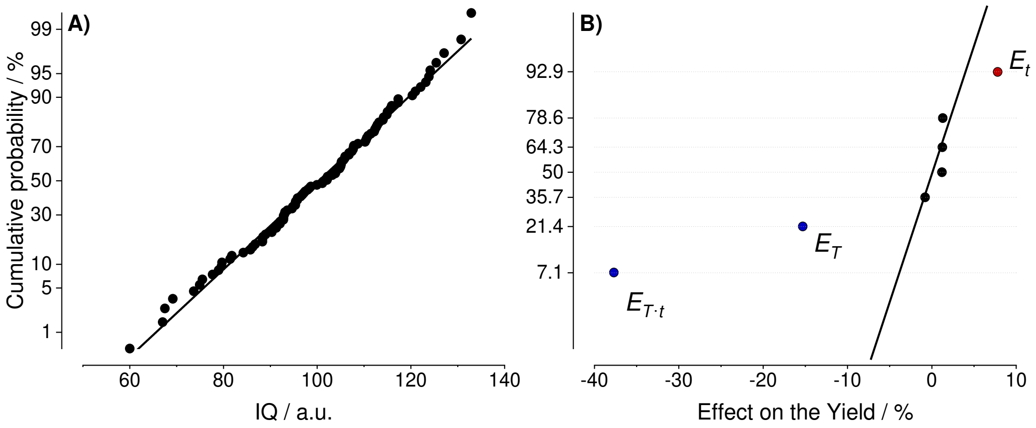

Figure 23: Display of two normal probability plots. Graph A) Fictional normally distributed data (data randomly generated with $\sigma = 15$ and $\mu = 100$) of IQ-measurements from 100 people. As expected, the normally distributed data falls in reasonable agreement with the black line. Graph B) Normal plot of the seven main and interaction effects from the fictional two-level full factorial design that tested the influence of reaction time, reaction temperature and stirring speed on the reaction yield of a thermally instable compound. The strong negative (blue circles) effects E_T and $E_{T \cdot t}$ as well as the less imposing positive (red circle) effect E_t deviate from the line that is spanned by the weak and most likely insignificant effects (black circles). There is a high probability that these three effects are significant.

In DoE, normal plots are commonly used as first indicators for effect significance (or insignificance). The significant few (main and interaction) effects will diverge from the linear array of the insignificant many. Within the fictional example of the two-level full factorial design provided in section 3.4.2.1 (for the design plan see Figure 15), the influence of reaction time, reaction temperature and stirring speed on the reaction yield of a thermally instable compound was tested. The seven respective observed effects (which induce 7 quantiles of slightly above 14 %) are displayed in a normal plot (graph B, Figure 23). Especially the two negative effects (blue symbols) E_T and $E_{T \cdot t}$ deviate strongly from the black line that is indicated from the lesser effects. The deviation of the positive effect (red symbol) E_T is less evident. At this point, the conclusiveness of normal plots shows its limit: although offering a valuable visual tool for assessment of effect significance, these plots cannot provide quantification of significance.

3.4.3.2 Quantification of Effect Significance: Analysis of Variance

A quantifiable assessment of effect significance is of fundamental importance for the scientist. The statistical significance of main or interaction effects determines if the accompanied factors will be further investigated in more comprehensive RSM designs and if they will be included in the prediction model. Quantification of effect significance can be achieved by the so-called ANOVA (analysis of variance). The ANOVA compares the variance between means (remember that every effect is a mean according to equation (11)). ANOVA can become mathematically complex very quickly (*e.g.*, for RSM designs) and are well-explained in many textbooks about statistics.[85,87,90–92] Luckily, though, ANOVA can be computed automatically by DoE software (in this work DesignExpert was used). As ANOVA is fundamental to every DoE, it is, nonetheless, highly valuable to understand what ANOVA brings to the table. This section presents a relatively simple ANOVA which analyzes the effect significances of, once again, the fictional example of the two-level full factorial design provided in section 3.4.2.1 (see Figure 15).

ANOVAs work with the so-called sums of squares (SS) as a measure for variance. The SS of a main effect of factor A ($\mathrm{SS_A}$) is computed as follows:

$$\mathrm{SS_A} = \mathrm{SS_{A^+}} + \mathrm{SS_{A^-}} = \frac{n_\mathrm{Run}}{2}\left({}^1\!/_2\, E_\mathrm{A}\right)^2 + \frac{n_\mathrm{Run}}{2}\left({}^1\!/_2\, E_\mathrm{A}\right)^2 = \frac{n_\mathrm{Run}}{4}(E_\mathrm{A})^2 \qquad (16)$$

In equation (16), $\mathrm{SS_{A^+}}$ and $\mathrm{SS_{A^-}}$ are the sums of squares from the $\mathrm{A^+}$-level and the $\mathrm{A^-}$-level mean to the overall experimental response mean. In a simple two-level full factorial design, $\mathrm{SS_{A^+}}$ and $\mathrm{SS_{A^-}}$ thus stem from exactly half of the conducted measurements (*i.e.*, the $\frac{n_\mathrm{Run}}{2}$-term) and their respective effects each amount to exactly half of the total main effect of A ($\frac{E_\mathrm{A}}{2}$). The SS for all other main and interaction effects can be computed analogously. The ANOVA for the two-level full factorial design provided in section 3.4.2.1 (see Figure 15) is listed in Table 2. The SS for each main and interaction effect are shown in the second column. In this ANOVA, only the three effects E_T, E_t and $E_{T\cdot t}$ are investigated by variance comparison with the so-called residuals. All lesser, insignificant effects are thrown in the residual pool and serve as an estimate of error. Similar to the residual pool, the SS of the so-called model is computed by addition of the individual examined effect-SS.

The third column provides the so-called (statistical) degrees of freedom (df). This rather inconceivable quantity usually amounts to the number of the sample data minus one (df = $n - 1$). However, it might be better understood as the number of independent information used for determination of an estimate. Think of it this way: when choosing three random numbers with a mean value of 100, only two of these numbers are independent. No matter what you do – once the first two numbers are picked, the third one is fixed. As all effect in Table 2 derives from two averages (high level versus low level, see equation (11)), they possess 1 df each.

The actual variance of an estimate is called the mean square (fourth column) is calculated by dividing the respective SS through the df. Subsequent division of the estimates mean square through the mean square of the residual generates the so-called *F*-value (fifth column) which is named in honor of the famous statistician Sir Ronald Fisher. Depending on the df of the investigated estimate (*e.g.*, an effect) and the df of the residual, the computed F-value corresponds with a specific probability that is the p-value (sixth column, for more information about the F-value and the associated F-distribution see elsewhere).[93] Putting it very simply – and that is the objective of this chapter – the p-value of an effect is the probability to observe that same effect (or a bigger one) purely as a result of system error. Insignificant effects, which stem from system error, will have a comparably high p-values while significant effects will result in relatively low p-values. The smaller the p-value of an effect is, the lower is the probability of it being caused by system error. By definition, an effect is significant if its p-value is smaller than 0.05. The ANOVA in Table 2 thus quantifies the three investigated effects E_T, E_t and $E_{T \cdot t}$ as significant – their variance differs significantly from the variance of the residuals. The last row of an ANOVA table is the so-called “Corr. Total” which is the total SS corrected for the response mean. It thus represents the total variance of the system and is the sum of the model- and the residual-SS.

Table 2: ANOVA table for the fictional two-level full factorial design that analyzes the influence of reaction temperature T, reaction time t and stirring speed v_s on the reaction yield of a thermally instable compound.

Source	**SS**	**df**	**Mean square**	**F-value**	**p-value**
Model	**3360**	**3**	**1120**	**427**	**< 0.0001**
A: *T*	465	1	465	177	0.0002
B: *t*	120	1	120	46	0.0025
AB: *T·t*	2775	1	2775	1057	< 0.0001
Residual	**10.50**	**4**	**2.625**		
C	3.125	1	3.125		
AC	3.125	1	3.125		
BC	1.125	1	1.125		
ABC	3.125	1	3.125		
Corr. total	**3371**	**7**			

The actual model (*i.e.*, the prediction equation) is performed easily by standard statistical software. In our example, the model includes the three effects E_T, E_t and $E_{T\cdot t}$. But how do we know if we can trust a prediction equation? Stemming from a two-level full factorial design, the prediction model will, naturally, not include non-linear terms. However, unless center points are added to the designs it is impossible to be certain that only linear effects describe the system adequately.

If, however, non-linear factor-response-relationships are detected (by a more complex design with implemented center points), non-linear – usually quadratic – terms need to be added to the prediction equation. In the following, an exemplary, arbitrary system with several non-linear effects will be contemplated. Herein, the relevant aspects of the ANOVA (which analyzes the significance of each equation term) as well as other quantities which are crucial for the trustworthiness of the prediction equation will be discussed. Table 3 shows an exemplary ANOVA of an exemplary RSM design with 5 investigated factors (A, B, C, D, E). Seven effects are included into the model: four main effects (A, C, D, E), one interaction (AB) and three non-linear effects (A^2, D^2, E^2). Apparently, investigation of factor B was superfluous which means a lot of practical effort could have been avoided with an adequate screening plan. All other model terms possess highly significant effects (p-value < 0.0001).

Compared to the ANOVA in Table 2, Table 3 shows two new residual rows. The so-called “lack of fit” provides information whether the prediction model describes the examined system. If a seemingly insignificant effect is mistakenly thrown into the residual pool, the lack of fit will reveal that at least one more term should be added to the prediction model. This revelation is achieved by comparison of the residual variance (*i.e.*, the mean square) with the so-called "pure error" variance. The pure error stems from the deviation of replicate runs as only those will disclose the "pure" experimental error (in this case the pure error is calculated from six center point runs which lead to 5 df). If all the effects in the residual pool (which are not included in the model) are truly insignificant – meaning they do not exert a significant influence on the measured response – the variance of the residuals and the pure error should not differ significantly. An insignificant (p-value > 0.05) lack of fit is thus a desirable result.

Table 3: Exemplary, arbitrary ANOVA table of an RSM design investigating 5 factors (A, B, C, D, E). Non-linear effects are detected. The residuals do not contain any significant effects as shown by the insignificant (p > 0.05) lack of fit.

Source	**SS**	**df**	**Mean square**	**F-value**	**p-value**
Model	5050.1	7	721.44	762.51	< 0.0001
A	882.83	1	882.83	933.10	< 0.0001
C	20.59	1	20.59	21.76	< 0.0001
D	2995.1	1	2995.1	3165.6	< 0.0001
E	918.70	1	918.70	971.00	< 0.0001
A^2	108.62	1	108.62	114.81	< 0.0001
D^2	55.57	1	55.57	58.73	< 0.0001
E^2	38.53	1	38.53	40.72	< 0.0001
Residuals	35.95	38	0.9461		
Lack of fit	33.26	33	1.01	1.87	0.2520
Pure error	2.70	5	0.5394		
Corr. total	5086.0	45			

Unfortunately, significant model terms and insignificant lack of fit are not sufficient evidences for the "fitness" of a prediction equation. The following section will present tools to "diagnose" statistical diseases which might adulterate the generated model.

3.4.3.3 Prediction Model Diagnostics

There is a great variety of different diagnostics for DoE prediction equation. The most relevant ones, at least from the author's perspective, are the so-called normal plot of residuals, the residuals versus predicted plot and the residuals versus runs plot. If these plots imply no danger signal and the ANOVA determined a significant model with an insignificant lack of fit, there is a great chance the predictions are trustworthy and will reliably predict the observed response.

3.4.3.3.1 The Normal Plot of Residuals

It might be rather confusing for the DoE-newbie that the term "residual" is diversely used. As mentioned in the previous section, the ANOVA combines all insignificant effects in the "residual" pool. However, the word has another meaning in the field of statistics. A residual is the difference of the actual, experimentally observed value and the respective predicted value generated by the prediction model. If the model predicts with equal accuracy over the whole experimental space, the residuals should thus be normally distributed. The number of plotted residuals equals the number of runs. Figure 24 illustrates two normal plots of factorials from two fictional arbitrary experimental designs. Graph A illustrates residuals which array reasonably linear on a normal plot – the deviation of predicted and actual, experimentally observed responses is normally distributed over the whole experimental space. Generally speaking, the DoE expert should not be too painstaking about linearity in the normal plot. It is no coincidence that statisticians speak of the so-called "pencil test": if a pencil is placed on your normal plot and covers all the data, consider it a line.[85]

If, on the other hand, distinct deviations from normality in form of S-shapes trends (Graph B) are visible, the prediction model probably does not predict with equal accuracy over the whole experimental space. Non-normally distributed residuals are oftentimes observed when the measured responses differ by orders of magnitude (*e.g.*, $Y_{\mathrm{Run1}} = 1.7$ and $Y_{\mathrm{Run2}} = 113$). In such cases, the DoE expert should consider data transformation – a topic that goes beyond the scope of this work and is comprehensively explained elsewhere.[87]

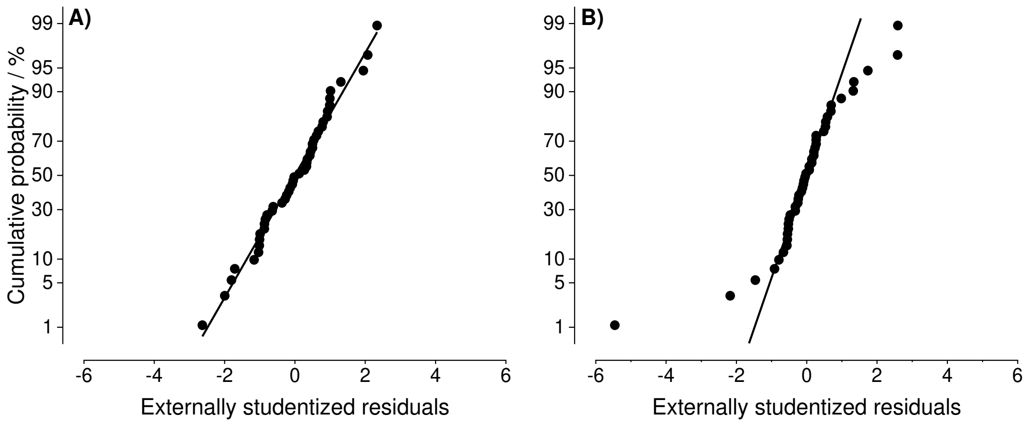

Figure 24: Display of two normal probability plots of the externally studentized residuals of two fictional arbitrary experimental designs. Graph A) The residuals are linearly which suggests normality. Graph B) The residual show trends that diverge from linearity. Data transformation might be required.[87]

In most standard statistical or DoE-specific software, the normal probability plots are generated automatically. However, rather than plotting the ordinary residuals, it is common to program the plotting of so-called externally studentized residuals. External studentization of residuals is an elegant method of accounting for varying leverage of the design points. This is achieved by deleting each observed response successively, re-establishing the respective and individual prediction model for each deleted response and, finally, calculating the externally studentized residual (*i.e.*, the difference of the predicted and the deleted, observed response).[89]

3.4.3.3.2 The Residuals versus Predicted Plot

Another commonly used diagnostic tool is the so-called residuals versus predicted plot. As the name suggests, the (externally studentized) residuals are plotted against the responses predicted by the model. Two exemplary, fictional representatives of the residuals versus predicted plot are illustrated in Figure 25. Herein, the exemplary response is dimensionless and ranges between values of 20 and 100. Normally distributed (externally studentized) residuals should vary randomly around a value of 0 (black horizontal line). The red lines signify the so-called Bonferroni-corrected confidence limits.[86] These are typically provided automatically by statistical software; for particularly interested readers, thorough information about the determination of these limits is provided elsewhere.[94] In plain English, residuals that fall outside of these limits are very likely to stem from outliers (red circle, graph A) and it is highly recommended to repeat these runs. This is, in fact, another highly welcome feature of DoE: outliers that might heavily alter the outcome and knowledge generation of conventional OFAT experimentation, will be detected *via* simple statistical diagnostics. Apart from an outlier, graph A of Figure 25 provides a desirable outcome: the residuals are evenly spread throughout the whole predictive range of the model implying equal variance or, in statistical terminology, homoscedasticity. Graph B, on the contrary, shows an increasing variance towards the higher values of the predicted exemplary response. Such a “megaphone” pattern implies heteroscedasticity and is a sign that a data transformation might be required.

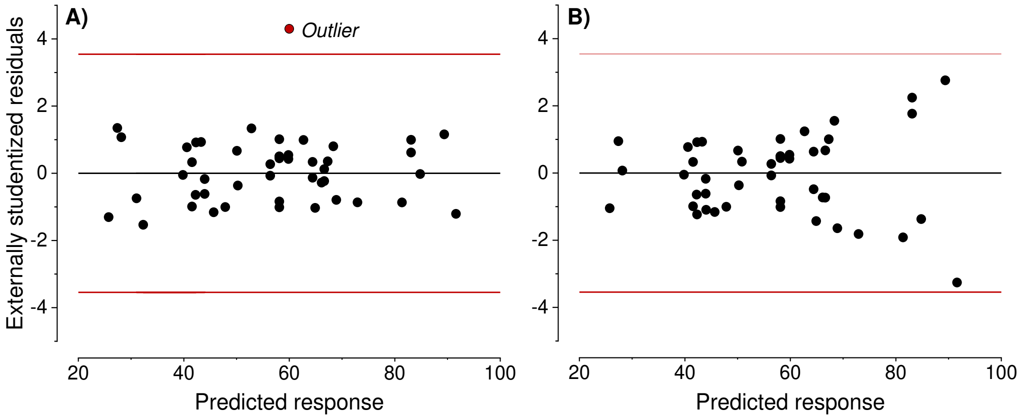

Figure 25: Two exemplary residuals versus predicted plot showing fictional residual data plotted against an arbitrary dimensionless response. Normally distributed data should vary randomly around a value of 0 (black line). If the residuals do not fall inside the Bonferroni-corrected confidence limits (red lines), they are likely to stem from outliers. Graph A) One residual is, most likely, and outlier (red symbol). The other residuals imply homoscedasticity as they are evenly spread throughout the whole predictive range of the model. Graph B) The residuals imply heteroscedasticity as the variance grows larger towards the higher values of the exemplary predicted response. A data transformation might be required.

3.4.3.3.3 The Residuals Versus Runs Plot

The so-called residuals versus runs plot looks similar to the residuals versus predicted plot. The x-axis, however, does not represent a type of response but simply the number of runs (in conducted order). The plot will reveal time-related and hidden influences that might have been lurking in the background. Graph A of Figure 26 shows the ideal case when no time-related variable influences the response throughout the conduction of the design plan. Herein, the residuals should scatter randomly around a value of 0 (outliers can be detected in this plot also). Graph B shows the opposite and undesirable case. After around half of the conducted runs (in our exemplary scenario 46 runs were performed), the residuals show an increasing trend. Apparently, an unexpected, time related variable exerted an influence on the response at the later stages of performing the design plan. Such a result is undesired for the scientist as it worsens the accuracy of the prediction model. However, it also provides a novel information that might – as so often is the case in conventional experimentation – otherwise stay unrevealed. Was one reactant contaminated or lose functionality during conduction of the design plan? Has a lamp lost light intensity or were the columns of a chromatographic analytic device damaged? Such questions can all be answered when looking at the residuals versus runs plot.

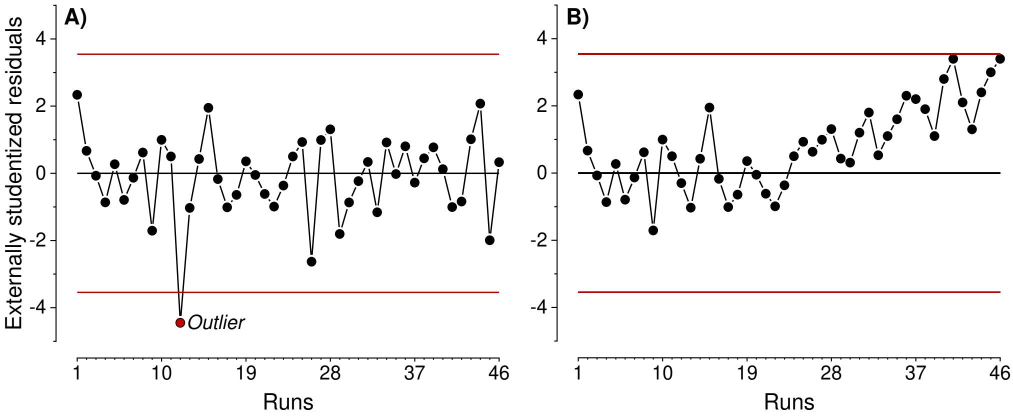

Figure 26: Display of two residuals versus runs plots (showing fictional data) which can reveal time-related and hidden influences on the measured response. Graph A) No time-related influence is implied as the residuals scatter randomly around a value of 0 (black line). Residuals outside of the Bonferroni-corrected confidence limits (red lines) identify outliers (red symbol). Graph B) Time-related effects are implied by residual-trends that deviate from the black line. In this case, the residuals noticeably increase after around half of the conducted runs. Apparently, an unquantifiable, time-related variable has exerted an influence on the response.

As you would probably expect, there are a myriad of different statistical tools that are useful for diagnoses of your DoE – each providing a slightly different message. Understanding the fundamentals of the normal plot of residuals and the residuals versus predicted/runs plot, however, is a great basis which is usually sufficient to assess if your obtained prediction model is trustworthy. In the next section, one last set of quantities – the "so-called goodness of fit" statistics – which are essential to assess the trustworthiness of the obtained prediction models will be presented.

3.4.3.4 Final “Diagnosis” via Fit Statistics

Every scientist who has ever performed a linear regression most likely has already seen a fit statistics: herein, the “R^2” (which is the square of the Pearson correlation coefficient) provides a measure of how well the regression line fits the data points. The R^2-value will always range between 0 and 1. In linear regression, a great fit is implied by an R^2 very close to a value of 1. In more complex polynomial regression (as is required in RSM), however, the simple R^2 can be very misleading: here, R^2 denotes the ratio of variance (SS_{Model}) of the model and the corrected total around the mean value ($SS_{Corr.Total}$, see equation (17)).

$$R^2 = {}^{SS_{Model}}\!/_{SS_{Corr.Total}} \tag{17}$$

To put this in simpler words, R^2 describes the portion of the total variance of the examined system that is described by the model. It becomes evident, that R^2 is biased as it can only increase the more predictors (*i.e.*, mode terms) are included into the model. Even completely insignificant 4FIs can never make R^2 worse. Only looking at R^2 thus puts the scientist at acute risk of over-fitting.

Fortunately, cunning statisticians came up with very helpful statistic quantities to solve this problem: the so-called adjusted-R^2 (R^2_{adj}) and the predicted-R^2 (R^2_{pred}). The former quantity (R^2_{adj}) provides a more accurate measure of fit “goodness” than the raw R^2 as it includes a “penalty” for each added model term (predictor) n_t fitting any number of data points n_s according to equation (18):

$$R^2_{adj} = 1 - \frac{n_s - 1}{n_s - n_t}\,(1 - R^2) \tag{18}$$

In equation (18), a certain rivalry between the term-penalty and the raw R^2 arises: only if inclusion of a model term significantly improves R^2, the penalty will be outweighed. If a model term insignificant, R^2_{adj} will fall far below R^2 implying an over-fitting of the observed data.

The other goodness of fit measure R^2_{pred} indicates how well a regression model (*i.e.*, a prediction equation of a DoE) predicts response-values for new observations and is thus a very important statistic for RSM. For the calculation of R^2_{pred}, each measured response will be removed individually from the data set, the prediction equation will be re-estimated to the remaining data and the residuals will be calculated for all observed data points. Summing up all squared residuals generates the so-called “predicted residual sum of squares” (SS_{PRESS}).[95] Although this quantity is usually only referred to as “PRESS”, this work will use the term SS_{PRESS} to clarify what it actually is – a sum of squares. When a model predicts accurately, the SS_{PRESS} will be low compared to the $SS_{Corr.Total}$ (the variation of all data around the mean value) and a R^2_{pred} close to a value of 1 will be obtained according to equation (19).

$$R^2_{pred} = 1 - \frac{SS_{PRESS}}{SS_{Corr.Total}} \tag{19}$$

When the data is extremely overfit and the models are thus extremely poor at prediction, the SS_{PRESS} can, in fact, exceed the $SS_{Corr.Total}$ resulting in negative R^2_{pred}-values. In this case, the “mean prediction” (*i.e.*, simply predicting the average response) actually works better than the complex overfit model. In contrast to R^2_{adj} – which only detects unnecessary terms added to the prediction model – R^2_{pred} will alert the scientist when a fit artificially connects the data and finds relationships were there really are none. As a rule of thumb, R^2_{adj} should attain a maximum value while still being in reasonable agreement with the R^2_{pred} (< 0.2 difference).

The previous sections 3.4.2 and 3.4.3 provided a lot of statistic and DoE-related theory. Assessment of the trustworthiness of an established prediction model is ideally achieved by a combination of it all: if the ANOVA-results implies significant model terms (and an insignificant lack of fit), the diagnostic tools show no sign of heteroscedasticity or non-normality and the fit statistics neither suggest over-fitting nor bad prediction accuracy, then the model should be rock-solid. A way to apply all this knowledge within a typical DoE-experimentation workflow will be shown in section 6.1. Herein, a step-by-step application guide of a RAFT optimization via DoE is presented highlighting the typical challenges along the way.

4 Objectives of this Work

Applications of "smart" polymeric materials have gained immense popularity over the last decades. The polymers' "smartness" stems from their stimuli-responsiveness which describes their ability to show drastic and rapid changes – such as solubility – in response to just small external variations of physical or chemical conditions. The most thoroughly investigated and perhaps most auspicious representative of these "smart" polymers are thermoresponsive polymers which respond towards changes of temperature. These polymers enjoy great potential for application in the fields of drug delivery,[29,96] surface modification systems[15,17,97] or switchable filtration devices (just to mention a few).[98–103] Herein, the vast majority of research has been dedicated to LCST polymers which change from a fully dissolved into a collapsed, hydrophobic state upon surpassing the LCST-type PT. UCST polymers, on the contrary, still remain rather unexplored as they are comparably rare, expensive or require elaborate monomer syntheses.

This work, thus, strives to shine light on the potential and the challenges of UCST polymers regarding easy accessibility, synthesis, solution behavior and "smartness" in multiblock architectures. These issues are addressed in three major parts which will be presented in the following:

In Search of a Suitable UCST Polymer:

In this part (section 5), the focus lies on finding an easily accessible (in terms of cost of synthetic effort) and non-health-hazardous monomer to synthesize a single polymer block with UCST-type solution behavior. Also, polymer synthesis – which was conducted *via* RAFT polymerization as a living character is highly adjuvant for later synthesis of multiblock architectures which can exhibit "smart" features – was targeted to be as easily feasible and reproducible as possible, even for less specialized chemists. On top of the synthetic findings, this part aims to reveal the peculiarities and complexity of the UCST-type solution behavior also highlighting the challenges that come with the synthesis *via* a controlled-radical polymerization. This way, it was tried to understand and assess the UCST-type thermoresponsive behavior of only the homopolymer which will be fundamental for later evaluation of the "smart" UCST-based behavior of more complex polymer architectures.

DoE in the Life of a Polymer Chemist

In order to save valuable resources and time, practical efficiency in the laboratory is carries great importance. One highly auspicious way to improve the efficiency of the typical chemist's workflow is facilitated through the concept of experimental design (*i.e.*, DoE). Thus, this part (section 6) aims to provide the practical know-how for other chemists to adapt DoE into their working routines. The foundation for this is provided in form of simplified and example-oriented theoretical background (section 3.4) as well as a step-by-step practical guide on how to utilize DoE for the optimization of a RAFT polymerization of a UCST-type monomer (section 6.1).

Generation of "Smart" UCST-Materials

Synthesis and, in particular, characterization of UCST type polymers is challenging as they possess very peculiar solubility. This becomes especially challenging when synthesizing, for instance, a diblock copolymer for the application in switchable filtration devices which require a large hydrophobic majority component usually provided by a poly(styrene) (PS) or PMMA block. Nonetheless, this part aims to show a synthetic route towards diblock copolymers with one UCST polymer block. Apart from the synthetic findings and challenges, also the solution behavior of the resulting diblock copolymers is required to be investigated. Herein, it was tried to reveal potential influences of the second block on the solution behavior of the UCST block. For the development of switchable filtration devices with tailored properties, for instance, these findings are crucial as the "smart", pore-forming UCST-block will be confined by the PS or PMMA membrane matrix. The third and final part of this work (section 7) thus also strives to provide first insights into the influences of proximity to typical membrane majority component blocks as well as the influence of very high effective local polymer concentrations on the solution behavior of the UCST block.

5 In Search of Suitable UCST Polymer Blocks

Non-ionic UCST-type polymers synthesized *via* a controlled radical pathway still remain a rather rare sight in academic research. Most polymers or copolymers that exhibit a UCST-type PT in aqueous solution either comprise severe health hazards or are difficult to obtain due to high prices or the necessity of elaborate syntheses.[69]

This section presents synthetic RAFT polymerization routes to the UCST-type polymers PNAGA (section 5.1) and PMAAm (section 5.2) which are built from less harmful and more easily accessible monomers. Herein, both polymers' suitability for further application in diblock copolymer synthesis and development of "smart" multiblock copolymer architectures will be assessed.

5.1 Poly(*N*-Acryloyl glycinamide)

Presumably, PNAGA is the most famous representative of the non-ionic UCST polymer family. Its UCST-type solution behavior was first reported by Agarwal *et al.* in 2010.[42] Its PTT was found to strongly depend on the polymerization method (RAFT or free–radical polymerization),[28] molecular weight[41] and polymer end groups.[43] Moreover, the UCST-type PT was observed to be strongly suppressed by only traces of ionic impurities, ionic groups incorporated in the chain by RAFT agent or initiator and even by the type of glass of the solution container.[27] At elevated temperatures (> 70°C), the latter was found to catalyze the hydrolysis of amide side chains into carboxylic groups leading to strongly enhanced polymer–water interactions.[27]

Due to all these difficulties, it is mandatory to work with highly pure chemicals. Within this context, especially the monomer *N*-acryloyl glycinamide (NAGA) needs to be purified meticulously in order to avoid impurities of acrylic acid. In the next section, the synthesis of PNAGA and amendments applied to a synthetic route by Agarwal *et al.* is described.[27]

5.1.1 Synthesis of *N*-Acryloyl glycinamide

The schematic display of the chemical equation of the synthesis of NAGA is illustrated in Scheme 1. NAGA is obtained through nucleophilic addition of the free electron pair of the primary amine of the glycinamide to the carbonyl group of the acryloyl chloride. Accruing hydrochloric acid is converted by an excess of potassium carbonate.

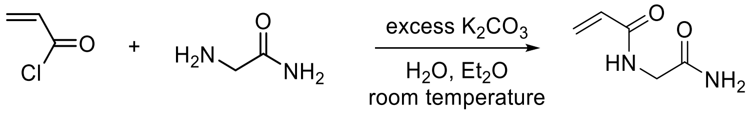

Scheme 1: Reaction equation of acryloyl chloride and *N*-glycinamide yielding NAGA.[27]

Due to the emerging byproducts of potassium salts and potassium acrylate – which will lead to incorporation of acrylic acid during the polymerization of NAGA – Argawal *et al.* explicitly point out the necessity of column chromatography of the crude product.[27] In combination with a subsequent recrystallization from a mixture of methanol and acetone (1/2, *v*/*v*), highly pure (< 5 ppm of potassium content) NAGA was obtained. Here, a very suitable method to assess the NAGA purity was differential scanning calorimetry (DSC). Synthesis without column chromatography yielded NAGA with 9700 ppm of potassium salt content that had a melting point of 132 °C, while the removal of the impurities notedly increased the melting point to a temperature of 143 °C.[27]

While most of the suggested synthetic route was adopted, slight adjustments were applied. The exact synthetic route can be found in section 8.2.1, however, the biggest differences in the synthetic route are listed in Table 4.

Table 4: Comparison of procedure of Argawal *et al.* and the procedure applied in this work for the synthesis of NAGA.[27]

Procedure by Argawal *et al.*	**Adapted procedure**
Water removed from crude product by lyophilization	Water removed by rotary evaporation (40 °C)
Reflux in methanol/dichloromethane (1/4, *v*/*v*) and subsequent filtration to remove polymeric impurities	Step was dismissed
Application of column chromatography	Crude product was only “filtrated” through short silica column

Procedure by Argawal *et al.*	**Adapted procedure**
Recrystallization from mixture of methanol and acetone (1/2, *v*/*v*)	Recrystallization from mixture of methanol

Although a negligibly lower yield was obtained *via* the altered procedure, the DSC measurement displayed in Figure 27 suggest a slightly more pure end product as the melting point of 144 °C is even higher than the one reported by Agarwal *et al.*[27]

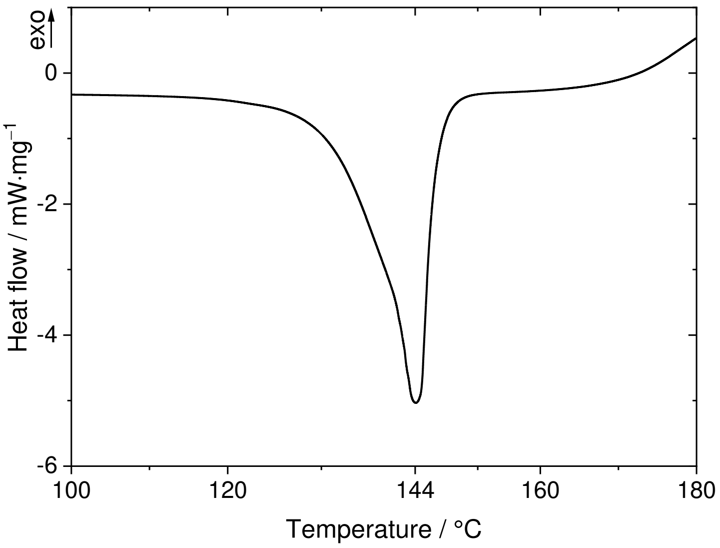

Figure 27: Determination of the melting point (144 °C) of NAGA *via* DSC.

Ultimately, the adapted synthetic route provides comparable yields, higher purity of the end product and a faster, less time-consuming procedure. The obtained NAGA was then applied for the synthesis of PNAGA *via* RAFT homopolymerization which will be presented in the following section.

5.1.2 Photoiniferter RAFT Polymerization of NAGA

PNAGA was synthesized *via* photoiniferter RAFT solution polymerization in dimethylsulfoxide (DMSO). The applied trithiocarbonate RAFT agent 2-cyano-2-propyl dodecyl trithiocarbonate (CPDT) served as RAFT agent and as radical source for the chain growth. The reaction equation is provided in Scheme 2.

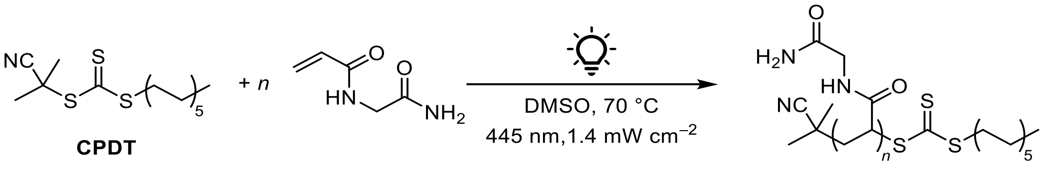

Scheme 2: Photoiniferter RAFT solution polymerization of NAGA in DMSO using a blue LED light source and CPDT as RAFT agent.

The polymerization (conducted with an R_M-value of 100 and a w_s of 20 wt%) facilitates monomer conversions of over 60 % in around 3 h with low dispersity-values ($Đ$-values, for kinetic study and SEC-measurement see Figure A2, Appendix) below 1.25. This implies a reasonably good control of the reaction and yielded PNAGA$^{7.89}$ (superscripts denote $\overline{M}_{\mathrm{n,th}}$-value in kDa determined *via* NMR spectroscopy)

As previously mentioned, PNAGA probably is the most famous, non-ionic UCST polymer. In order to assess its aptitude for a later usage in “smart” materials, the temperature–dependent behavior in aqueous solution of PNAGA$^{7.89}$ was investigated *via* DLS which will be presented in the following section.

5.1.3 Analysis of Aqueous Solutions of PNAGA *via* DLS

In order to analyze a potential UCST-type PT in water, aqueous PNAGA$^{7.89}$ solutions were prepared and analyzed *via* temperature-dependent DLS measurements. Figure 28 illustrates the evolution of the hydrodynamic radius (R_h) versus the temperature of a 1.0 wt% (top) and a 0.10 wt% (bottom) aqueous PNAGA solution. The measurements were started at 70 °C, cooled down to 10 °C (blue circles) and reheated back to 70 °C (red circles). Appropriate fitting of the intensity correlation functions suggested only one particle species which, interestingly, possess R_h-values of around 70 nm and 55 nm for the 1.0 wt% and the 0.10 wt% PNAGA solution, respectively. This implies that the PNAGA chains are not fully dissolved coils but form, most likely, spherical micelles (which grow with increasing polymer concentration) due to their dodecyl stabilizing group at the ω-end.

It is well-reported that when using an ionic initiator, the UCST of PNAGA will be suppressed below 0 °C. When using a non-ionic initiator and RAFT agent, though, a cloud point (CP) in pure water (0.2 wt% PNAGA solution) was observable for low-dispersity PNAGA chains ($Đ < 1.20$) with $\overline{M}_{\mathrm{n,th}}$-values below 5 kDa have been reported.[27] Despite working without any kind of potentially ionintroducing reactant, it becomes evident from Figure 28 that PNAGA$^{7.89}$ shows no UCST-type PT in water – either for a 0.10 wt% or 1.0 wt% aqueous solution. The fact, that a UCST-type PT of PNAGA reported by Agarwal *et al.* was not reproducible seems rather surprising as the only synthetic difference lied in the choice of a different initiator and a differing leaving group radical. Perhaps, the thus different α-chain end may have had a significant effect. Unfortunately, Agarwal *et al.* did not conduct DLS analyses of their PNAGA solutions (but only performed turbidity measurements) which could have provided sufficient information to understand the PT on a molecular level.

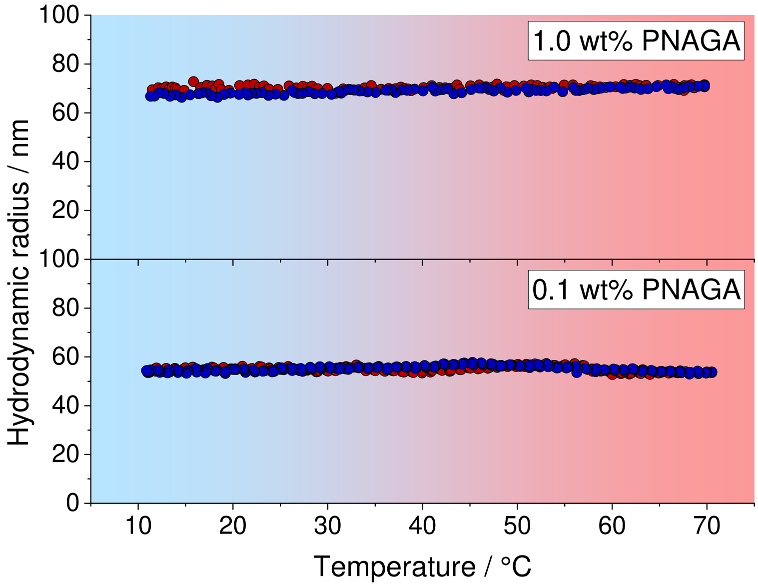

Figure 28: Evolution of the hydrodynamic radius with the temperature of an aqueous 1.0 wt% (top graph) and 0.10 wt% (bottom graph) PNAGA$^{7.89}$ solution. The measurement was started at 70 °C, cooled to 10 °C (blue circles) and reheated to 70 °C (red circles). PNAGA$^{7.89}$ shows no sign of a UCST-type solution behavior.

PNAGA$^{7.89}$ shows no UCST-type PT in aqueous solution (that is at least below 1.0 wt%). As a consequence, the elaborate monomer synthesis was deemed unreasonable. The focus of the following section was thus to find a suitable monomer alternative.

5.2 Poly(methacrylamide)

The library of monomers and monomer combinations leading to non-ionic UCST homo- and copolymers is limited in size. Copolymers like poly(acrylamide-*co*-acrylonitrile),[104] poly(NAGA-*co*-diacetone acrylamide)[105] or poly(acrylamide-*co*-styrene)[106] all require either highly toxic and hazardous, commercially unavailable or highly expensive (due to elaborate synthesis) monomers. Non-ionic UCST-type homopolymers remain a rarity. Apart from their acryl- or methacrylamide structure, repeating units like NAGA,[42] *N*-acryloylasparaginamide,[107] 6-acryloyloxymethyl uracil[16] or ureido-based derivatives[40] all share a very low accessibility – due to the required elaborate syntheses or high prices (see Figure 4). To the best of the author's knowledge, the only exemption is MAAm which is commercially available in large quantities and for comparably low prices. PMAAm shows a UCST-type PT in aqueous solution at 40.5 °C (onset cooling) when polymerized *via* conventional free–radical polymerization.[28]

As future potential "smart" applications require multiblock architectures, however, controlled polymerizations with a living character are expedient. To the best of the author's knowledge such a polymerization technique had, prior to this work, not been reported for the synthesis of PMAAm. The following sections will focus on PMAAm as a highly auspicious and heavily undervalued UCST-type polymer.

5.2.1 RAFT Polymerization of MAAm: RAFT Agent Solubility

In order to synthesize PMAAm successfully in a RAFT solution polymerization one has to consider the challenges of solubility of all polymerization ingredients. As PMAAm is exclusively soluble in water (above the UCST) or aqueous cosolvent mixtures (with water as major component), a RAFT agent that is soluble in these solvents is mandatory. However, the selection of non-ionic water soluble RAFT agents is very limited. The only two RAFT agents that were soluble in water or water/cosolvent-mixtures are 4-(([2-carboxyethyl]thio)carbonothioyl) thio-4-cyanopentanoic acid (CTCA) and 4-cyano-4-(((propylthio)carbonothioyl)thio)pentanoic acid (CTCPA). Scheme 3 shows the chemical structures of CTCA and CTCPA as well as their solubility in aqueous solutions. Both RAFT agents share the same leaving group but possess greatly different polarities regarding their stabilizing group: while CTCA carries a second terminal carboxylic moiety, CTCPA carries only an unipolar propyl group. Due to these differences, CTCA is completely water soluble while CTCPA is soluble only with the addition of organic cosolvent. At a temperature of 75 °C, 0.10 wt% of CTCPA are soluble in H_2O/*N*,*N*-dimethylformamide (7/3, *w*/*w*), H_2O/ethanol (8/2, *w*/*w*) or H_2O/dioxane (65/35, *w*/*w*).

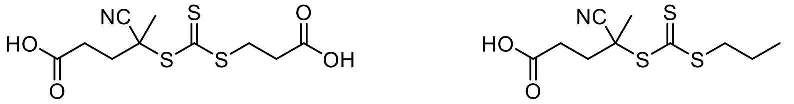

CTCA

water soluble

CTCPA

soluble in:
H_2O/DMF (7/3, *w*/*w*, at 75 °C)
H_2O/EtOH (8/2, *w*/*w*, at 75 °C)
H_2O/dioxane (65/35, *w*/*w*, at 75 °C)

Scheme 3: Chemical structures of the RAFT agents CTCA and CTCPA and their solubility in water and different water/cosolvent-mixtures, respectively.

Unfortunately, CTCPA appeared to be incapable of facilitating a controlled radical polymerization in each of the mentioned cosolvent mixtures as the elugrams recorded by SEC analyses were extremely broad and did not shift to lower elution volumes with increasing monomer conversion (for a more detailed presentation of the RAFT polymerization of MAAm using CTCPA as RAFT agents see section 10.3, Appendix).

CTCA, on the contrary, showed very different results which will be presented in the following section. However, at this point, a dilemma of RAFT solution polymerization-derived UCST becomes evident: strongly hydrophilic groups – like in this case carboxylic moieties – are necessary to dissolve the RAFT agent and to facilitate a controlled polymerization with a living character. Yet, these groups cause strong polymer–solvent interactions which are known to strongly suppress the UCST-type PTT.[27]

5.2.2 Photoiniferter UV-Induced RAFT Polymerization of MAAm

Using CTCA, a well-controlled photoiniferter RAFT solution polymerization of MAAm in water was successfully conducted *via* irradiation with UV-light. A schematic display of the chain growth reaction is shown in Scheme 4.

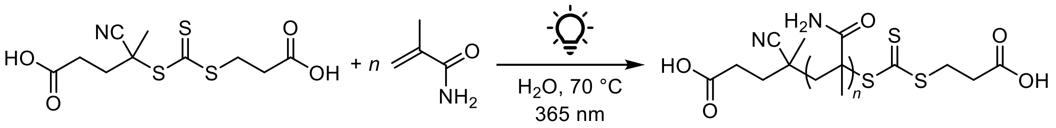

Scheme 4: Photoiniferter RAFT solution polymerization of MAAm in water using UV-light and CTCA for radical generation.

In order to facilitate a well-controlled and predictable polymerization and to gain overall insights on the reaction system, in-depth kinetic studies were conducted with varying R_M-values (*i.e.*, the theoretical degree of polymerization at 100% conversion of monomer which equals $[MAAm]_0/[CTCA]_0$), light intensities and temperatures were conducted. In Figure 29, the courses of monomer conversion versus the reaction time for the aqueous solution RAFT polymerization of MAAm at 70 °C and a constant w_s of 15 wt% are displayed. Here, graph A shows three kinetic studies with R_M-values at a constant light intensity. In theory, the polymerization rate of RAFT polymerization follows the same kinetics as conventional free–radical polymerizations. Hence, the polymerization rate should be directly proportional to the concentration of the active growing species ($[P_n^\bullet]$), the monomer concentration ($[M^\bullet]$) and the propagation rate coefficient (k_p). While $[M^\bullet]$ is equal for all polymerizations, higher values of R_M imply lower concentrations of the radical-generating species CTCA ([CTCA]).[49] It is thus rather striking to see that, at least within the ranges of 200–800, R_M appears to have no influence on the polymerization rate (despite [CTCA] varying by a factor of 4). Keeping in mind that lower [CTCA]-values (*i.e.*, higher R_M-values) also lead to higher degrees of polymerization – which in turn are known to notably reduce k_p[108,109] – this finding seems even more remarkable. Unfortunately, as no advanced analytical methods like electron spin resonance spectroscopy were available, the approach for explanation is highly speculative: photoiniferter RAFT polymerizations are known for a constant recombination/dissociation equilibrium of the active radical (which is the leaving group radical or the growing chain) and the highly stabilized RAFT thiyl radical (see Figure 6, section 3.3).[110,111] Under the given reaction conditions, the effective radical concentration might thus not be apt to surpass a certain value due to accumulation of recombination events. In other words, the recombination/dissociation equilibrium – which is solely responsible for generation of radical species – might lead to a maximum concentration of active growing species. After reaching this concentration maximum, no higher concentrations of CTCA or higher light intensities should be able to further accelerate the polymerization rate.

This speculative argumentation is backed by graph B of Figure 29 which shows three courses of monomer conversion versus the polymerization time for varying UV-light intensities at a constant R_{M}-value of 400. In here, the red circles (that appear in graph A and B) derive from the same experiment (at a light intensity of 0.38 mW cm^{-2}). Although elevation of the light intensity to 0.61 mW cm^{-2} will certainly accelerate sulfur–carbon homolysis (*i.e.*, generation of radicals), the overall rate of polymerization is not higher than at the lower light intensity of 0.38 mW cm^{-2}. Apparently, the polymerization rate has attained a certain limit which, most likely, has been caused by a concomitantly enhanced rate of reversible recombination events. Lowering the light intensity to 0.30 mW cm^{-2}, however, results in a significant reduction of the polymerization rate implying that the intensity of 0.38 mW cm^{-2} was only just facilitating the apparent [$P_n^{\bullet}$]-limit.

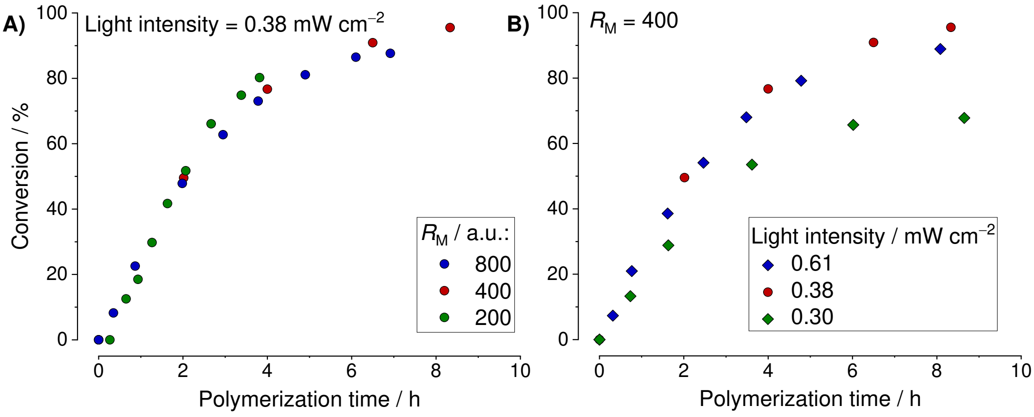

Figure 29: Monomer conversion versus the reaction time for the photoiniferter RAFT solution polymerization of MAAm in water at 70 °C and a w_s of 15 wt% using CTCA as RAFT agent. Graph A) The polymerization was conducted at a constant light intensity of 0.38 mW cm^{-2} while the R_{M}-value (*i.e.*, the theoretical degree of polymerization at 100% monomer conversion $[\mathrm{MAAm}]_0/[\mathrm{CTCA}]_0$) was varied. Graph B) The polymerization was conducted at a constant R_{M}-value of 400 while the light intensity was varied.

The temperature showed a more intuitive influence on the polymerization rate than [CTCA] and the intensity of the UV-light. When the polymerization is performed at 60 °C (rather than 70 °C), the polymerization rate is strongly decelerated reaching only 40 % conversion after over 7 h (see Figure A7, Appendix). This reduction is, of course, explained by the comparatively lower propagation rate coefficient which lowers with temperature according to Arrhenius law.

Despite these rather anomalous findings, the observed kinetics offer the scientist a certain convenience: under the studied parameter settings, at least, the polymerization seems to be extremely robust. Within light intensities of 0.38–0.61 mW cm^{-2}, the monomer conversion will be straightforwardly adjustable allowing for accurate chain length tailoring.

The evolution of SEC traces with increasing monomer conversion – which is directly proportional to $\overline{M}_{\mathrm{n,th}}$ – from the polymerization with the mid-parameters ($R_{\mathrm{M}} = 400$, 0.38 mW cm^{-2}) is illustrated in Figure 30.

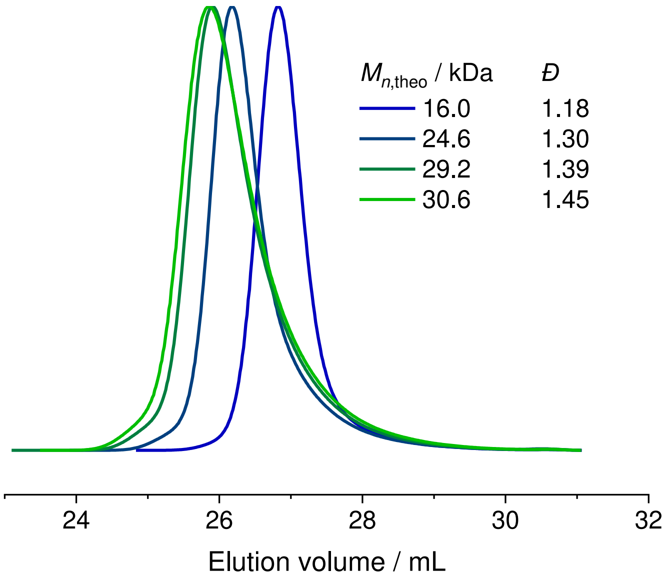

Figure 30: Evolution of SEC traces with increasing monomer conversion (directly proportional to $\overline{M}_{\mathrm{n,th}}$) of the photoiniferter RAFT polymerization of MAAm using CTCA as RAFT agent (70 °C, $R_{\mathrm{M}} = 400$, $w_{\mathrm{s}} = 15$ wt%, 0.38 mW cm^{-2}). Values of $\overline{M}_{\mathrm{n,th}}$ and $Đ$ are additionally provided.

Like in all other kinetic studies presented in Figure 29, the elugrams clearly shift towards lower elution volumes with increasing monomer conversion – a clear indicator for a well-controlled radical polymerization. Also, the $Đ$-values are very low ($Đ < 1.20$) and the traces appear very symmetrical. With increasing monomer conversion – and thus average chain length – the distributions start to broaden. These exact same trends are also observable in SEC experiments of all the other conducted kinetic studies (see Figure A8, Appendix). The broadening of the SEC traces can be caused by the increasing likelihood of irreversible termination compared to propagation events when the monomer concentration diminishes. Another phenomenon that can strongly contribute to broader weight distributions is the gradual photolytic decomposition of the trithiocarbonate moiety of the RAFT agent.[112] It was, however, found that no decomposition occurred within the first 3 h of the polymerization (4 % decomposition after 6 h and 14 % decomposition after 9 h, for more information see section 10.4.3 and Figure A10, Appendix).

The narrowest elugrams for likewise reasonably long polymer chains were obtained with an R_M-value of 400 and a light intensity of 0.38 mW cm^{-2}. These optimized reaction conditions were applied on a larger scale (5.53 g of MAAm were used for the polymerization) to obtain two PMAAm samples with differing chain lengths. Table 5 provides the sample codes (superscripts represent the $\overline{M}_{n,th}$-values in kDa) as well as the analytical and experimental data of these polymers.

Table 5 Experimental and analytical data of the photoiniferter RAFT polymerization of MAAm using CTCA as RAFT agent (70 °C, 0.38 mW cm^{-2}, R_M = 400, w_s = 15 wt%).

Sample Code[a]	**R_M**[b]	**t / min**	**Conversion**[c] **/ %**	**$\overline{M}_{n,th}$**[c] **/ kDa**	**$\overline{M}_{n,e\text{-}xp}$**[d] **/ kDa**	**Đ**[d]
PMAAm$^{11.7}$	400	174	33.2	11.7	6.87	1.08
PMAAm$^{20.1}$	400	300	58.1	20.1	9.64	1.11

[a]Superscripts represent $\overline{M}_{n,th}$. [b]R_M equals the ratio of initial concentrations of MAAm and CTCA. [c]Quantities determined *via* ^{1}H NMR spectroscopy and referencing to DMF. [d]Measured by SEC at 50 °Cin an 0.1 M $NaNO_3$ aqueous (Milli-Q quality) solution with an added 0.05 wt% of NaN_3. Calibration was performed applying PEG standards.

The polymerization yielded the two polymers PMAAm$^{11.7}$ and PMAAm$^{20.1}$ which both exhibit excellently low Đ-values of 1.08 and 1.11, respectively, as well as highly symmetric and narrow elution chromatograms (for SEC measurements see Figure A9, Appendix). Compared to the Đ-values of the kinetic studies, the dispersities of the scaled-up polymerization were even lower. While the small-scale kinetic studies were performed in screw-capped glass vials (see Experimental Section), this larger scale polymerization was performed in a 50 mL flask. In comparison to the small-scale kinetic studies, the now larger scale polymerization exhibited significantly lower rates of polymerization (compare conversion values of Figure 29 with Table 5). This might be explained by the different irradiation surface of the bigger reaction vessel which seems to have improved the polymerization control even further.

As the purpose of PMAAm syntheses ultimately is the analysis of its UCST-type solution behavior, in-depth DLS analyses of both PMAAm$^{11.7}$ and PMAAm$^{20.1}$-solutions were conducted and will be presented in the following.

5.2.3 UCST-Type Solution Behavior of PMAAm in Water/Ethanol Mixtures

Despite the fact, that a UCST-type PT at roughly 40 °C is observable for PMAAm synthesized *via* conventional free–radical polymerization, unfortunately, no UCST-type PT was observable for PMAAm synthesized *via* the applied RAFT route.[28] This is, most likely, due to two reasons: polymers synthesized *via* conventional free–radical polymerization reach markedly higher molecular weights which are accompanied by a significant loss of mixing entropy – the driving force of a UCST transition.[30,34] Hence, the UCST-type PTT will be higher for polymers with longer chains (and lower for lower-molecular-weight-polymers like PMAAm$^{11.7}$ or PMAAm$^{20.1}$ deriving from a controlled radical polymerization). The second factor which surely contributes to the non-observable UCST-type PT in water are the two carboxylic moieties introduced by the utilized RAFT agent CTCA due to their strong polymer–solvent interactions.

The absence of a UCST-type PT in pure water is illustrated in Figure 31 which shows the evolution of R_h against the temperature (70–14–70 °C) of a 1.0 wt% PMAAm$^{20.1}$-solution. The experiment is started at 70 °C and cooled down to roughly 14 °C (blue circles) before reheating the solution back to 70 °C (red symbols). Although any form of UCST-type behavior is missing, another quite interesting observation is made: in contrast to aqueous solutions of PNAGA, appropriate fitting of the intensity correlation functions indicates the coexistence of two different particle species (symbol area represents the relative scattering intensity of the particular species). Despite being completely dissolved and thermally equilibrated (see Figure A11 in section 10.5.1, Appendix), both unimer coils (R_h < 10 nm) and bigger polymer aggregates (R_h ~ 150 nm) appear to coexist in the solution. However, neither the size nor the relative scattering intensity of each particle species (both at around 50 %) seem to be affected by temperature.

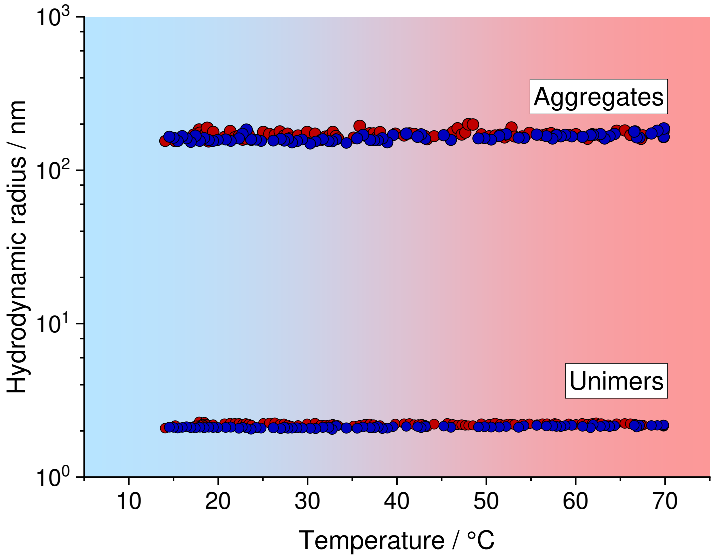

Figure 31: Temperature-dependent R_h-evolution of a 1.0 wt% aqueous solution of PMAAm$^{20.1}$. The measurement was started at 70 °C and cooled down to 14 °C (blue circles). Afterwards, the solution was reheated to 70 °C (red circles). The intensity correlation function indicates the coexistence of fully dissolved unimer coils and aggregate species (relative scattering intensity of both species is denoted by the symbol area). The colored background indicates the temperature transition from high (red) to low (blue) and serves as a guide to the eye.

To obtain a UCST-type PT – and to gain further insight into the UCST-type solution behavior of PMAAm – varying amounts of ethanol as cosolvent can be added. As a pure non-solvent for PMAAm, ethanol theoretically should decrease the polymer's solubility in aqueous solution.

As can be taken from Figure 32, a 0.5 wt% PMAAm$^{20.1}$-solution in a water/ethanol (75/25, *w*/*w*) mixture clearly exhibits a macroscopic UCST-type PT. Here, the R_h-is illustrated in a temperature range of 31–43 °C. At the start of the measurement, the two coexisting species are fully dissolved in a homogenous polymer solution (~36-43 °C). Interestingly, the relative scattering intensity of the unimer species (indicated by the smaller symbol areas) is significantly lower than in pure water (around 20 % compared to 50 %, respectively). At this point, it has to be stated that these percentages are intensity weighted (see section 8.3.3) and do not reveal actual number or mass fractions as these intensity weighted fractions scale with R^6 (R is the radius of the scattering particle). Nonetheless, keeping these facts in mind, they can provide valuable comparative insights into the polymer's solution behavior.

The markedly lower relative scattering intensity of the unimer species observed from Figure 31 might be due to the addition of ethanol – a non-solvent for PMAAm

– which might energetically favor increased aggregation due to intermolecular polymer–polymer interactions. Upon cooling (blue circles), however, the unimer species suddenly disappear at a UCST-type PTT of 36.5 °C as the R_h-value of the aggregate species rapidly increases by an order of magnitude ($R_h > 1000$ nm) while the solution turns completely turbid. Intra- and intermolecular polymer–polymer interactions are energetically favored over polymer–solvent interactions in this temperature-region. The reason why the smaller unimer species vanishes completely (*i.e.*, the intensity correlation function only shows a single exponential decay) might be due to enthalpy-driven agglomeration. However, as the scattering intensity scales with R_h^6, the alleged disappearing of the unimer species might be a mere result of the superimposition of the overwhelmingly intense signal of the significantly larger aggregate particles.

Upon reheating, the turbid solution redissolves, the unimer signals reappear and the aggregate species shrink into their initial, thermally equilibrated state. The UCST-type PT of PMAAm in mixtures of water and ethanol seem to be remarkably thermoreversible.

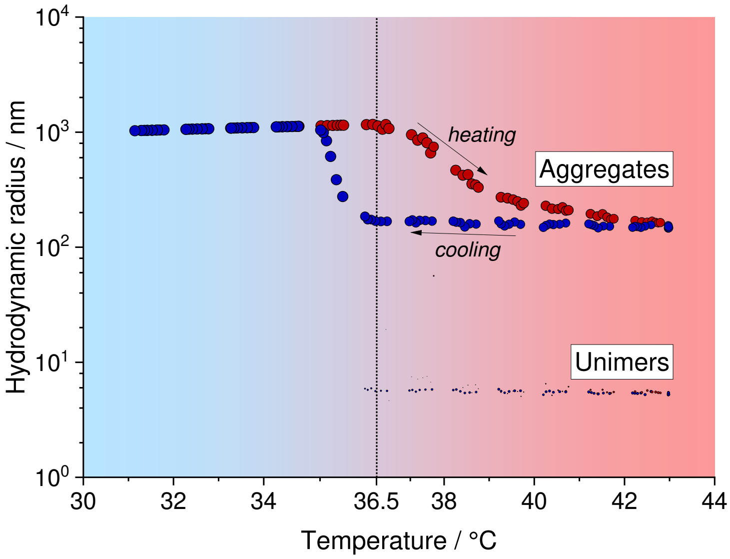

Figure 32: Temperature-dependent R_h-evolution of a 0.5 wt% aqueous solution of PMAAm$^{20.1}$ in a water/ethanol mixture (75/25, *w*/*w*). The measurement was started at 43 °C and cooled down to 14 °C (blue circles). Afterwards, the solution was reheated to 70 °C (red circles). The intensity correlation function indicates the coexistence of fully dissolved unimer coils and aggregate species (relative scattering intensity of both species is denoted by the symbol area). The dotted line signals the PTT (onset upon cooling). The colored background indicates the temperature transition from high (red) to low (blue) and serves as a guide to the eye.

When observing a UCST-type PT, the coexistence of two particle species, the distinct macroscopic phase separation as well as the thermoreversibility were observed analogously for both PMAAm$^{11.7}$ and PMAAm$^{20.1}$ – at all ethanol and polymer mass fractions. The temperature of the PT, though, was found to be strongly dependent on both these weight fractions as well as the polymer chain length. In Figure 33, the evolutions of the PTTs of PMAAm$^{11.7}$ (rhombuses) and PMAAm$^{20.1}$ (circles) at different ethanol weight fractions (17–35 wt%, denoted by different colors) are plotted versus the polymer weight fraction (0.1–10 wt%, logarithmic scale). Evidently, the PTT markedly increases with the content of the non-solvent ethanol: exemplarily, a 1.0 wt% solution of PMAAm$^{20.1}$ boasts PTTs of 23 °C and 82 °C at ethanol weight fractions of 17 wt% and 35 wt%, respectively. As ethanol is a non-solvent for PMAAm this result seems to be rather intuitive. The PTT of PMAAm$^{20.1}$ at 35 wt% ethanol could not be measured for concentrations higher than 82 °C due to the boiling point of ethanol.

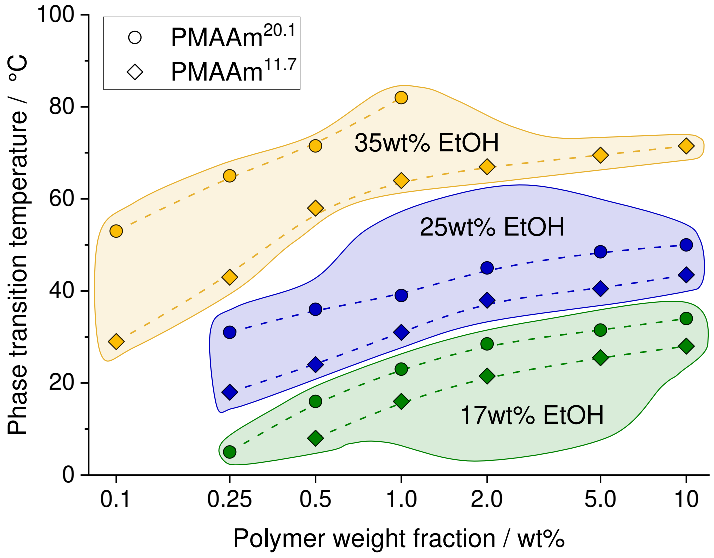

Figure 33: Display of PTTs for PMAAm$^{11.7}$ (rhombuses) and PMAAm$^{20.1}$ (circles) at different ethanol weight fractions (17–35 wt%, denoted by different colors) versus the polymer weight fraction. The dashed lines are added as a guide to the eye.

Apart from the distinct impact of the ethanol weight fraction, two other conclusions can be drawn from Figure 33: the PTT increases significantly with both polymer mass fraction and chain length. Since strong intra- and intermolecular interactions – in this case HB – are responsible for the UCST-type PTs, an increase of the PTT with polymer concentration (*i.e.*, the polymer weight fraction) seems plausible. Higher concentrations of polymer grant each HB donor or acceptor a higher chance of meeting their interaction-counterpart which ultimately leads to more intermolecular interactions.[44] At equal mass fractions of ethanol and polymer, the effect of chain length is also clearly visible: the PTT of PMAAm$^{20.1}$ is consistently, and without exception, significantly higher (6–24 °C) than the PTT of PMAAm$^{11.7}$. This is explained by the fact that higher the polymer chain lengths lead to a loss of mixing entropy.[30,34] Since PMAAm$^{20.1}$ has a higher chain length than PMAAm$^{11.7}$, its mixing entropy is lower which thus causes the entropy-driven breaking of the intra- and intermolecular HBs to occur at higher temperatures (see equation (2)).

It is likely, however, that the PTT-elevating effect of growing polymer chain lengths is further enhanced by the carboxylic moieties at the polymer end groups as equal polymer mass fractions result in higher amounts of substance – and thus a higher concentration of carboxylic groups – for the shorter PMAAm$^{11.7}$. Despite the fact that these groups only dissociate weakly in aqueous solution, they strongly increase the polymer–solvent interactions and hence drastically lower the PTT.

Apart from the weight content of a non-solvent, the polymer concentration or the chain length, there is another factor that can strongly influence a PTT of non-ionic UCST polymers. It is well-reported that irreversible hydrolysis of the amide side chains leads to a strong decrease of the UCST-type PTT as it will also introduce carboxylic moieties into the chain.[27,30,113–115] Although this feature boasts a major challenge for applications which require long-term reusability, this extraordinary trait – that causes gradual increase of solubility over time – can offer certain advantages. In biomedical applications, for instance, hydrolysis of the polymer could, after a targeted drug delivery process, theoretically lead to an over-time redissolution and renal secretion.[29,96] Due to both the challenging and potentially promising influence of hydrolysis on the PTT of non-ionic UCST polymers, the following section will present thorough investigations *via* temperature-dependent DLS analyses regarding the stability of the observed UCST-type PTTs of PMAAm in water/ethanol mixtures.

5.2.4 Effect of Side Group Hydrolysis on the PTT of PMAAm

The rates of irreversible amide side group hydrolysis will most certainly increase with temperature. In order to examine the influence of this reaction on the UCST-type PT on PMAAm, temperature-dependent DLS measurements of different PMAAm solutions in water/ethanol mixtures were conducted. This was achieved by testing the temperature stability of the PT over time while tempering the different PMAAm solutions to selected elevated temperatures. The blue circles in graph A of Figure 34 show the R_h-evolution of the cooling ramp (data points of heating ramp omitted for reasons of lucidity) of an exemplary 0.25 wt% PMAAm$^{20.1}$ solution in a water/ethanol mixture (65/35, *w*/*w*). The first cooling ramp of the measurement was started immediately after thermal equilibration at 70 °C and a macroscopic PTT of 65.5 °C was detected (and also expected; see Figure 33). After reheating to 70 °C, the solution was kept at this temperature for 4 h before the measurement was conducted for a second time (green circles). This procedure was then repeated a third time (yellow circles) and it becomes evident that the UCST-type PTT shows a significant decrease of around 3–4 °C each measurement just due to elongated exposition to elevated temperatures. Apparently, these conditions are sufficient to facilitate some degree of amide side group hydrolysis. It must be explicitly stated, however, that amide hydrolysis is extremely slow and was never detected *via* ^{1}H NMR spectroscopy – which is just another affirmation of how extremely UCST-type PTT are suppressed by even stoichiometrically negligible amounts of carboxylic groups incorporated into the chain.

These results are reproducible for other concentrations and PMAAm chain lengths as well: analogous results are obtained when examining a 1.0 wt% PMAAm$^{11.7}$ solution in a water/ethanol mixture (65/35, *w*/*w*) in equal manner (graph B). Expectedly, the UCST-type PTT will keep decreasing even further with heating time. Graph C of Figure 34 shows the PTTs of a 0.25 wt% PMAAm$^{20.1}$ solution in a water/ethanol mixture (75/25, *w*/*w*) versus the accumulated heating time at 70 °C that succeeds each cooling–heating cycle. The first three data points (at 0 h, 4 h and 8 h) stem from the same experiment that is shown in graph A. The PTT continuously decreases over time and, in a matter of 36 h, sinks as low as 44.2 °C – over 20 °C lower than the initial PTT at 65.5 °C. It is very likely that this hydrolysis induced PTT decrease might continue with additional heating time until it will eventually be suppressed below 0 °C.

Temperatures as high as 70 °C should, under normal circumstances, not be physiologically relevant. In order to investigate the PMAAm PTT in water/ethanol mixtures at temperatures close to body temperature, a 0.25 wt% PMAAm$^{20.1}$ solution in a water/ethanol mixture (75/25, *w*/*w*) was prepared. According to Figure 33, a PT is expected in a close to body temperature range of 35–40 °C. A temperature-dependent DLS measurement was conducted starting at a temperature of 40 °C. It was only cooled slightly below the macroscopic PTT of 32.4 °C (blue circles) in order to avoid agglomerate precipitation and quickly reheated (red circles) to 40 °C. The solution was then kept at a constant temperature of 40 °C for 72 h before repeating the whole experiment (white circles in background). As indicated by the almost congruent R_h-evolutions of the first and second measurement, no significant degradation of the PTT is observed. Apparently, PMAAm solutions do not undergo significant amounts of irreversible amide side chain hydrolysis events at 40 °C for a minimum of 72 h.

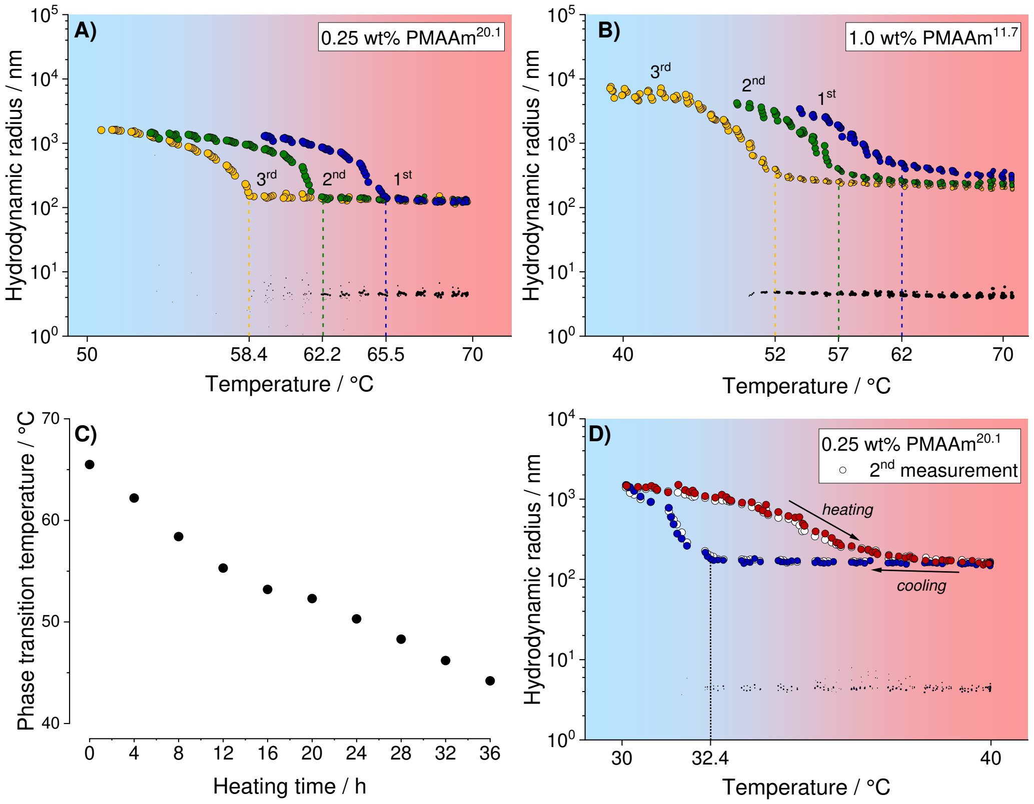

Figure 34: Analysis of the influence of hydrolysis on the PTT of PMAAm in mixtures of water and ethanol. In graphs A, B and D, the dotted horizontal lines highlight the onset of the UCST-type PT upon cooling and the area of the symbols represents the relative scattering intensity of the particular particle species (unimers and aggregates). Graph A) Display of the R_h-value for three cooling ramps of a 0.25 wt% PMAAm$^{20.1}$ solution in a water/ethanol mixture (65/35, *w*/*w*). After each cooling ramp, the solution was reheated back to 70 °C and kept at that temperature for 4 h prior to the next cooling ramp. Graph B) The same measurement as in graph A was conducted for a 1.0 wt% PMAAm$^{11.7}$ solution in a water/ethanol mixture (65/35, *w*/*w*). Graph C) The measurements of graph A were pursued seven more times. The PTT (onset of cooling) is plotted versus the accumulated heating time at 70 °C. Graph D) R_h-evolution of a 0.25 wt% PMAAm$^{20.1}$ solution in a water/ethanol mixture (75/25, *w*/*w*). The experiment was conducted in a more physiologically relevant temperature range. After completion of the first cooling (blue circles) and heating (red circles) cycle, the solution was tempered kept at a constant temperature of 40 °C for 72 h before the measurement was repeated (white circles).

5.2.5 Conclusion

This chapter presents an easily feasible and well-controlled photoiniferter RAFT polymerization of MAAm – a low-price and highly accessible monomer. The synthesis of the UCST-polymer PMAAm is highly robust due to an apparent "limit" of the polymerization rate making molecular weight targets precisely tailorable. Additionally, the polymerization is eco-friendly since the reaction is conducted in water. PMAAm shows highly thermoreversible UCST-type PTs in different water/ethanol mixtures with a pronounced hysteresis upon reheating. These PTTs ranged from 10–80 °C and showed to rise significantly with increasing ethanol weight fraction, chain length and with polymer concentration. With the presented results, it should thus be possible to prepare solutions of narrowly distributed PMAAm and adjust the thermoreversible UCST-type PT within that range.

As already reported for other UCST-type polymers,[27] the amide side chains of PMAAm can undergo irreversible amide side chain hydrolysis which strongly suppresses the UCST-type PTT. Although the PTT is stable for at least 72 h at 40 °C, higher temperatures (70 °C) will lead to significant decrease of the PTT over time.

In summary, PMAAm is a highly auspicious polymer and was thus found to be a promising UCST-block for syntheses of "smart" diblock copolymer architectures which will be presented in section 7.

6 DoE in the Life of a Polymer Chemist

Optimization of polymerizations and thorough kinetic studies are every polymer chemist's bread and butter – especially for controlled radical polymerizations such as RAFT. Herein, the polymer chemists could, for instance, require a certain polymer chain length and thus perform a kinetic study with an according R_M-value. Knowing the course of monomer conversion versus the reaction time for a given value of R_M, the way towards the originally targeted polymer chain length is paved. But what about other relevant quantities for RAFT polymers like $Đ$ or the chain end fidelity? Being able to target chain length while simultaneously striving for an optimal value of $Đ$ is hardly achievable with conventional experimentation. In the following, a step-by-step guide for application of DoE for the optimization of the thermally initiated RAFT polymerization of MAAm is presented. As found in the previous section, the resulting polymer PMAAm is a highly auspicious UCST-polymer. Synthetic optimization *via* DoE is thus greatly beneficial for purposes of later production of more complex, "smart" polymer architectures.

6.1 A Guide towards True Optimization of a RAFT Polymerization Using DoE

From the author's point of view, a RAFT polymerization is only "truly" optimized if all relations between the significant factors and responses are revealed in form of prediction equations (one for each response). In RAFT polymerizations, interesting responses obviously are the monomer conversion, an expression for the polymer chain length, the dispersity and the chain end fidelity (unfortunately, the latter quantity was not determined in this work since it is highly difficult to obtain analytically in a reliable and precise fashion). Only when mathematical expressions (*i.e.*, the prediction models) accurately predict the outcome of a polymerization depending on the input of the factors, the optimal conditions for any given goal of the polymerization can be obtained. In the following, the step-by-step route towards such a systematic optimization using DoE is provided. Although this route portrays a specific system, the basic steps are equal for all DoEs. The author hence also strongly encourages scientists of other research fields to have a go with DoE and try to implement it into their working routine.

6.1.1 Starting off: Finding the Significant Factors

The first step of any DoE is usually very simple and straightforward. The scientist needs to specify on the responses of interest. Typically, it is rather obvious which responses are required to be examined. However, as the DoE will examine (and fit) each response individually, the theoretical number of responses is unlimited. So if, besides the obvious ones, there is a quantity that might potentially be interesting as well, it can easily be included into the design. Apart from the work that goes into the response measurements, additional responses do not imply additional practical effort.

In the RAFT polymerization of MAAm, the monitored responses were the theoretical and apparent number-averaged molecular weights ($\boldsymbol{\bar{M}}_{\mathbf{n,th}}$ and $\boldsymbol{\bar{M}}_{\mathbf{n,app}}$, the latter quantity was measured by SEC using poly(ethylene glycol) (PEG) calibration standards), the molecular weight distribution (which is represented by $\boldsymbol{Đ}$) and, of course, the monomer conversion $\boldsymbol{p}$. In the context of this DoE guide for true optimization of a RAFT polymerization, all the responses (and the factors) are highlighted in bold letters. Although $\boldsymbol{\bar{M}}_{\mathbf{n,th}}$ and $\boldsymbol{p}$ are proportional (see to equation (A2), Appendix), it is worth to contemplate them individually as both have different meanings.

At this point, the DoE expert – or, ideally, a group of them – will start brainstorming which factors might potentially influence at least one the responses that will be monitored. As it was decided to initiate the polymerizations thermally utilizing the azo-initiator ACVA, two factors that certainly will influence at least one response are $\boldsymbol{R}_{\mathbf{M}}$ and $\boldsymbol{R}_{\mathbf{I}}$ (which are thoroughly explained in section 3.3.4). As any polymer chemist knows, there are three more factors that are – without the necessity of proving it in a screening design – undoubtedly significant: the polymerization time $\boldsymbol{t}$, polymerization temperature $\boldsymbol{T}$ and total solid content $\boldsymbol{w}_{\mathbf{S}}$. It would be unwise to waste valuable time and resources on proving the significance of these factors within a small screening design. In fact, the wise scientist already knows that an RSM design will be required to build accurate prediction models since at least one of the factors will definitely exert a non-linear effect on at least one of the responses. For instance, $\boldsymbol{p}$ will not increase linearly with $\boldsymbol{t}$ as the polymerization rate will decrease with receding monomer concentration.

There are, however, a few more unimposing factors like solvent mass $\boldsymbol{m}_{\mathbf{H_2O}}$ (which is an unambiguous measure for the reaction volume), the weight content of the added internal standard DMF $\boldsymbol{w}_{\mathbf{DMF}}$, the stirring rate $\boldsymbol{v}_{\mathbf{s}}$ and the time of N_2-purging $\boldsymbol{t}_{\mathbf{N_2}}$. Naturally, all these factors will drastically alter the polymerization if set to extreme values. Within reasonable ranges, however, it is commonly assumed that their influence is negligible. A highly beneficial feature of DoE is that these assumptions can easily be confirmed (or refuted) with statistical security by performing a minimal effort screening design. Table 6 shows the design plan (remember that the actual order of run execution is randomized in order to minimize potential time-lurking influences) of a two-level fractional factorial (2^{4-1}) design with four additional center points investigating the potential influence of $\boldsymbol{m}_{\mathbf{H_2O}}$ (1.00−5.00 g), $\boldsymbol{w}_{\mathbf{DMF}}$ (2.0−5.0 wt%), $\boldsymbol{v}_{\mathbf{s}}$ (400−800 rpm) and $\boldsymbol{t}_{\mathbf{N_2}}$ (5−15 min) on the responses $\boldsymbol{p}$, $\overline{\boldsymbol{M}}_{\mathbf{n,th}}$, $\boldsymbol{Đ}$ and $\overline{\boldsymbol{M}}_{\mathbf{n,app}}$. Notice how the certainly significant five factors were excluded from the design. These factors were conveniently set at constant levels ($\boldsymbol{T}$ = 80 °C, $\boldsymbol{t}$ = 260 min, $\boldsymbol{R}_{\mathbf{M}}$ = 350, $\boldsymbol{R}_{\mathbf{I}}$ = 0.0625, $\boldsymbol{w}_{\mathbf{s}}$ = 15 wt%) and the twelve RAFT polymerizations were conducted varying only $\boldsymbol{m}_{\mathbf{H_2O}}$, $\boldsymbol{w}_{\mathbf{DMF}}$, $\boldsymbol{v}_{\mathbf{s}}$ and $\boldsymbol{t}_{\mathbf{N_2}}$. As already insinuated by the very low response variations, not a single significant effect was detected. The four respective ANOVA tables (shown in Table A1, Appendix) did not compute a single effect with a significant p-value (< 0.05). The four less imposing factors are all insignificant and do not need to be added to the RSM design – a highly welcome finding as more factors are always accompanied by greater experimental effort. In hindsight, this screening might appear redundant as the insignificance of the factors was – within the examined, reasonable factor ranges – already expected. However, although the theoretical expertise of the scientist is, of course, fundamental, only "trusting your gut" when it comes to choosing the factors can potentially backfire. It is thus strongly recommended to statistically affirm factor insignificance with appropriate screening before elimination from the RSM design.

For all following RAFT polymerizations, the insignificant factors were set to their respective midlevels ($\boldsymbol{m}_{\mathbf{H_2O}}$ = 3.0 g, $\boldsymbol{v}_{\mathbf{s}}$ = 600 rpm, $\boldsymbol{t}_{\mathbf{N^2}}$ = 10 min). Only $\boldsymbol{w}_{\mathbf{DMF}}$ was set to its high level of 5.0 wt% as a higher concentration allowed for more accurate determination of $\boldsymbol{p}$ (due to a more pronounced reference signal in the ^{1}H NMR spectra).

Table 6: Two-level fractional factorial screening design (2^{4-1}) with four added center points. Display of the actual factor values as well as the observed responses.

Run	**Factors**				**Responses**			
	$m_{\mathrm{H_2O}}$ / **g**	w_{DMF} / **wt%**	v_{s} / **rpm**	$t_{\mathrm{N_2}}$ / **min**	p^{a} / %	$\bar{M}_{\mathrm{n,th}}{}^{a}$ / **kDa**	$Đ^{b}$	$\bar{M}_{\mathrm{n,app}}{}^{b}$ / **kDa**
1	1.00	2.0	400	5	45.2	11.9	1.20	6.4
2	5.00	2.0	400	15	46.7	12.1	1.16	6.4
3	1.00	5.0	400	15	40.2	10.5	1.17	5.6
4	5.00	5.0	400	5	43.3	11.3	1.17	6.4
5	1.00	2.0	800	15	42.3	11.0	1.18	5.7
6	5.00	2.0	800	5	41	10.8	1.15	7.4
7	1.00	5.0	800	5	41.4	10.4	1.20	6.6
8	5.00	5.0	800	15	44.3	11.6	1.19	6.1
9	3.00	3.5	600	10	44.9	11.8	1.2	6.7
10	3.00	3.5	600	10	44	11.6	1.18	6
11	3.00	3.5	600	10	42.7	11.4	1.15	6.8
12	3.00	3.5	600	10	46.8	12.3	1.16	6.1

[a] Determined *via* ^{1}H NMR spectroscopy and referencing to DMF. [b]Measured by SEC at 50 °C in an 0.1 M $NaNO_3$ aqueous (Milli-Q quality) solution with an added 0.05 wt% NaN_3 and calibration with PEG.

The successful screening allowed for the complacent conclusion that only the five factors $\boldsymbol{T}$, $\boldsymbol{t}$, $\boldsymbol{R}_{\mathbf{M}}$, $\boldsymbol{R}_{\mathbf{I}}$ and $\boldsymbol{w}_{\mathbf{S}}$ – which the author *ex ante* knew to be significant – are required to be investigated in an RSM design. A reaction scheme of the examined RAFT polymerization as well as all investigated significant factors and measured responses are displayed in Figure 35.

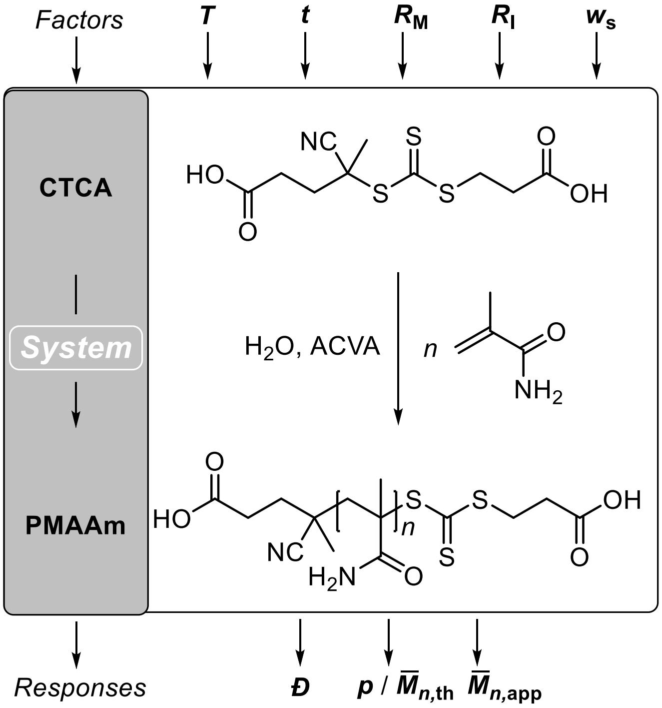

Figure 35: Schematical display of the aqueous RAFT solution polymerization of MAAm using CTCA as RAFT agent and ACVA as thermal initiator. The influences of the factors $\boldsymbol{T}$, $\boldsymbol{t}$, $\boldsymbol{R}_{\mathbf{M}}$, $\boldsymbol{R}_{\mathbf{I}}$ and $\boldsymbol{w}_{\mathbf{s}}$ on the responses $\boldsymbol{p}$, $\overline{\boldsymbol{M}}_{\mathbf{n,th}}$, $\boldsymbol{Đ}$ and $\overline{\boldsymbol{M}}_{\mathbf{n,app}}$ are investigated within an RSM design.

At this point, the responses of interest as well as the significant factors were successfully identified. Before starting an RSM design, however, some other steps are vital for the success of the optimization *via* DoE. In the following, these indispensable steps will be discussed in detail.

6.1.2 Choosing the RSM Design and Setting Factor Levels

Choosing the factor levels – or, in other words, the factor ranges that will be examined within the DoE – is no trivial task. Exactly this step can, in fact, pose one of the biggest challenges of the DoE-workflow. Wider factor ranges will grant a bigger experimental space and thus more knowledge generation about the examined system (remember that DoE only allows for prediction within the examined factor ranges). However, optimal prediction accuracy and unambiguous effect identification is only achievable when a quantifiable result is obtainable for each individual response in every single run – even when setting the factors at their most "extreme" combination. Within the examined RAFT system, for instance, the lowest response for p is expected at the factor levels (T^-, t^-, R_{M}^+, R_{I}^-, w_{S}^-): the combination of R_{M}^+, R_{I}^- and w_{S}^- facilitates minimal ACVA concentration. Combined with the low levels of T and t, the lowest p-value of the whole design will, most likely, be obtained. As a consequence, the polymer chain length might be so low that parts of the molecular weight distribution could fall out of the permeation limit of the SEC columns. This would lead to a corrupt (or even completely missing) response. Summing things up, searching (and finding) a reasonable balance between a large experimental space and guaranteeing run feasibility is another essential part of any DoE. The prudent DoE expert will thus conduct appropriate preliminary tests. This way, sudden unpleasant surprises during the execution of the design plan can be avoided.

Run feasibility of a design, however, is not exclusively depending on the factor ranges. Another essential aspect is the choice of the RSM design, which can have different geometries with differing point locations. The geometry of a Box-Behnken design, for instance, (displayed in part A of Figure 36) shows that no run points will be located at the edges of the experimental space (*i.e.*, the factorial points). At least one factor level will always be at its center. In some cases, this allows for wider factor ranges, however, it comes with a cost: Box-Behnken designs offer comparably poor precision when it comes to estimating interaction effects. The FC-CCD, which is shown in part B, is superior in that regard. Like the Box-Behnken, it only requires three levels per factor, yet, offers higher prediction accuracy. Hence, the FC-CCD was chosen as the RSM design to optimize the RAFT polymerization of MAAm.

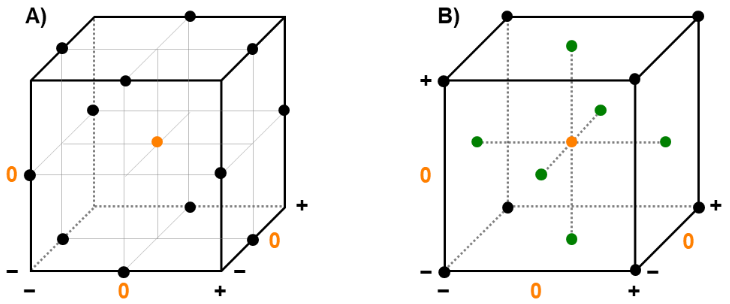

Figure 36: Display of design geometry for different two different RSM designs examining three factors. A) Box-Behnken design. B) Face-centered central composite design.

Being aware of the design geometry of the FC-CCD as well as the feasibility limits of the reaction and subsequent response measuring, appropriate preliminary tests were performed (see Figure A13, Appendix). The factor ranges were successfully determined and are listed in Table 7.

Table 7: Low (−), center (0) and high (+) level for each factor examined within the FC-CCD for the optimization of the RAFT polymerization of MAAm.

	T / °C	t / min	R_M	R_I	w_S
−	75	120	200	0.025	10.0
0	80	260	350	0.0625	15.0
+	85	400	500	0.1	20.0

As soon as the RSM design has been chosen, the factor ranges have been set and preliminary test assured the feasibility of all runs, the respective experimental plan can be executed. The ordered experimental plan is listed in Table A2 showing all factor levels as well as responses (remember that the actual order of execution was randomized to minimize potential time-lurking effects). At this point, prediction models for all individual responses can be generated by polynomial regression and revised by ANOVA as well as appropriate model diagnostic tools which will be presented in the following section.

6.1.3 Generation and Interpretation of Prediction Models

The prediction models for each individual response are generated by simple polynomial regression. Typically, this is conducted automatically by standard DoE software (DesignExpert was used in this work). As described in section 3.4.2.4, the maximum applicable polynomial order for the prediction models depends on the type of RSM design that was used. The FC-CCD allows for establishment of quadratic equations while higher ordered terms – *e.g.*, t^3 – will be confounded and thus cannot be estimated unambiguously. The challenge of finding the significant model terms (and excluding the insignificant ones) is achieved by an ANOVA as well as through contemplation of the fit statistics R^2_{adj} and R^2_{pred} (see section 3.4.3).

The resulting prediction models for p, $\overline{M}_{n,app}$ and $Đ$ are shown in equations (20), (21) and (22) (due to proportionality of p and $\overline{M}_{n,th}$, both models are highly similar and the $\overline{M}_{n,th}$-model is only shown in section 10.6.1.4, Appendix). The respective ANOVA tables and relevant fit statistics (also shown in section 10.6.1.4, Appendix) imply high prediction accuracy and model significance without a sign of over-fitting. As all prediction models are presented in coded form, the first term of each equation signifies the response mean or, in other words, the predicted response when all factors are set to their midlevel (0). For instance, if all factors are set to their midlevel, the $\boldsymbol{p}$-model predicts a monomer conversion of 42.3 %. Moreover, the coded form of the equation allows for straightforward assessment of each effects' size: lowering the temperature to its low level (−1) of 75 °C will reduce the conversion to 37.1 % (also mind the $\boldsymbol{T}^2$-term). Within the examined factor ranges, the prediction models will forecast the respective response for any set of factor combination.

$$\begin{gathered}\boldsymbol{p}\;/\;\% = 42.3 + 3.10\,T + 12.7\,t - 6.31\,R_\mathrm{M} + 9.59\,R_\mathrm{I} + 4.78\,w_\mathrm{s} - 2.06\,T\,t + 0.719\,T\,R_\mathrm{I} + \\ 0.275\,T\,w_\mathrm{s} - 1.74\,t\,R_\mathrm{M} + 1.28\,t\,R_\mathrm{I} + 1.52\,t\,w_\mathrm{s} - 1.09\,R_\mathrm{M}\,R_\mathrm{I} - 2.08\,T^2 - 4.28\,t^2 + 2.62\,R_\mathrm{M}^2 - \\ 2.88\,R_\mathrm{I}^2 - 1.17\,T\,t\,R_\mathrm{I} - 0.725\,T\,t\,w_s\end{gathered} \tag{20}$$

$$\begin{gathered}\boldsymbol{\bar{M}}_\mathbf{n,app}\;/\;\mathrm{kDa} = 6.23 + 0.259\,T + 1.25\,t - 1.06\,R_\mathrm{M} + 0.927\,R_\mathrm{I} + 0.488\,w_\mathrm{s} - 0.259\,T\,t + \\ 0.209\,T\,R_\mathrm{M} + 0.053\,T\,w_\mathrm{s} + 0.453\,t\,R_\mathrm{M} + 0.109\,t\,R_\mathrm{I} + 0.322\,t\,w_\mathrm{s} + 0.278\,R_\mathrm{M}\,R_\mathrm{I} + 0.278\,R_\mathrm{M}\,w_s \\ + 0.047\,R_\mathrm{I}\,w_s - 0.366\,T^2 - 0.766\,t^2 - 0.134\,T\,t\,w_s - 0.303\,t\,R_\mathrm{I}\,w_s\end{gathered} \tag{21}$$

$$\begin{gathered}\boldsymbol{Đ} = 1.26 + 0.04\,T + 0.0194\,t + 0.0135\,R_\mathrm{M} - 0.0194\,R_\mathrm{I} - 0.0297\,w_\mathrm{s} + 0.025\,T\,t - \\ 0.0144\,T\,R_\mathrm{I} - 0.0025\,T\,w_\mathrm{s} + 0.0188\,t\,w_\mathrm{s} + 0.0131\,R_\mathrm{I}\,w_\mathrm{s} + 0.0307\,t^2 + 0.0212\,t\,R_\mathrm{I}\,w_s\end{gathered} \tag{22}$$

It becomes evident that prediction models facilitate much more than just simple factor-dependent predictions. Although they may, at first glance, seem rather bulky, they boast highly valuable information about the examined system as each model term can theoretically be interpreted individually. This way, they also provide great potential for academic research goals and general qualitative understanding of the examined system. This becomes especially apparent interpreting the FIs. In order to demonstrate this, two randomly chosen interaction terms will be exemplarily interpreted: Figure 37 plots the prediction of the $\boldsymbol{T \cdot t}$-interaction terms of the $\boldsymbol{p}$- and **Đ**-prediction model. In interaction plots, all other factors are standardly set to their midlevel (0) which drastically simplifies both the $\boldsymbol{p}$- and **Đ**-prediction model which are shown in graph A and B, respectively. In both graphs, the respective response is plotted against $\boldsymbol{t}$ for the temperatures of 75 °C ($\boldsymbol{T}^-$, blue lines) and 85 °C ($\boldsymbol{T}^+$, red lines). Obviously, the two plots of graph A show two saturation curves typical for chain growth polymerizations. What is more interesting, however, is that the model terms can be interpreted individually: the model coefficients of the main effects β_T and β_t, for instance, possess values above 0 ($\beta_T = 3.10$, $\beta_t = 12.7$) connoting that $\boldsymbol{p}$ will increase along with $\boldsymbol{t}$ and $\boldsymbol{T}$. As monomer is, naturally, consumed throughout the reaction and elevated values of $\boldsymbol{T}$ facilitate quicker reaction rates according to

Arrhenius law, this is a rather expected finding. The negative coefficients of the quadratic terms ($\beta_{T^2} = -2.08$, $\beta_{t^2} = -4.28$) which cause the positive slope of $\boldsymbol{p}$ to recede are easily understood as well (whether plotted against $\boldsymbol{T}$ or $\boldsymbol{t}$) as the polymerization rate is directly proportional to the monomer concentration.[116] The 2FI-term of $\boldsymbol{T}$ and $\boldsymbol{t}$, on the contrary, reveals less trivial insights – as interaction terms so often do. As already described in detail in section 3.4, an interaction between factors $\boldsymbol{T}$ and $\boldsymbol{t}$ implies that the influence of $\boldsymbol{T}$ on the response $\boldsymbol{p}$ will vary for different values of $\boldsymbol{t}$ and *vice versa* – or, more simply put, the $\boldsymbol{p}$-prediction versus $\boldsymbol{t}$ for different values of $\boldsymbol{T}$ will not be parallel. Inside the factor ranges (75–85 °C), the negative interaction coefficient ($\beta_{T\cdot t} = -2.06$) implies a rather unexpected result. Apparently, the average polymerization rate (*i.e.*, the average slope of the plot) is higher at 75 °C which strongly suggests a suppression of the polymerization rate at 85 °C. This may either have been a cause of a lower monomer concentration to start with (at $\boldsymbol{t}^{-} = 120$ min, $\boldsymbol{p}$ is already higher at 85 °C). Another plausible explanation might be insufficient radical generation at 85 °C as around 98 % of the initial $[\text{ACVA}]_0$ composes in only 260 min. This might have lead to a significantly lower concentration of active growing species – especially in the later stages of the reaction (calculation of initiator decomposition is shown in section 10.6.2, Appendix).[117]

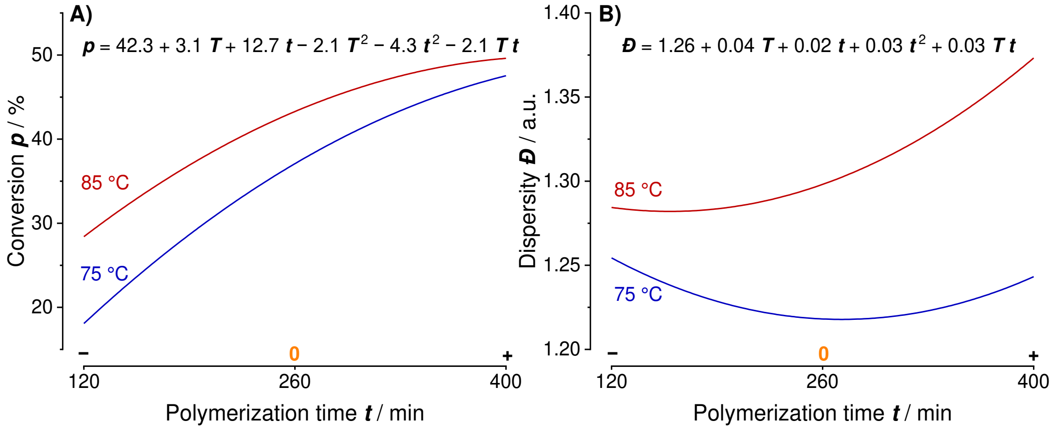

Figure 37: Exemplary illustration of the $\boldsymbol{T}\cdot\boldsymbol{t}$-interaction plots for the responses $\boldsymbol{p}$ (graph A) and $\boldsymbol{Đ}$ (graph B). Both responses are plotted against $\boldsymbol{t}$ for the two temperatures of 75 °C ($\boldsymbol{T}^{-}$, blue lines) and 85 °C ($\boldsymbol{T}^{+}$, red lines). The respective coded prediction models are provided additionally (factors $\boldsymbol{R}_{\mathrm{M}}$, $\boldsymbol{R}_{\mathrm{I}}$ and $\boldsymbol{w}_{\mathrm{s}}$ are set to their center (0) level).

Graph B shows the $\boldsymbol{T}\cdot\boldsymbol{t}$-interaction plot for the $\boldsymbol{Đ}$-prediction model. Herein, the predicted course of $\boldsymbol{Đ}$ versus $\boldsymbol{t}$ is, again, plotted for the temperatures of 75 °C ($\boldsymbol{T}^{-}$, blue lines) and 85 °C (***T***$^+$, red lines). Evidently, higher ***Đ***-values are obtained at higher temperatures due to a positive coefficient of ***T*** ($\beta_T = 0.04$). At the low level of ***T*** (75 °C), on the contrary, the ***Đ***-course shows a decrease with ***t***. Although graph A shows that they are not linearly dependent, it is fair to assume for controlled radical polymerizations (CRPs) that higher values of ***t*** always correlate with higher values of ***p*** and thus higher average chain length. This is not an unexpected result, as in CRPs, higher chain lengths are theoretically expected to lead to lower ***Đ***-values as they follow the Poisson distribution.[31] After the initial decline of ***Đ***, however, the course begins to increase resulting in a local minimum close to the midlevel of ***t***. Apparently, irreversible termination reactions and/or thermal decomposition of the RAFT functionality (thiocarbonylthio moiety) broaden the molecular weight distributions of PMAAm. While it is well-reported that both phenomena can increase the ***Đ***-value of polymer samples, it seems that especially the latter has exerted a big impact.[118,119] The two facts that trithiocarbonates attached to acrylate growing species – like a growing PMAAm – are particularly prone to thermal decomposition and that the ascent of ***Đ*** is more pronounced at ***T***$^+$ ($\beta_{T \cdot t} = +0.03$) give this interpretation further plausibility.

As implied earlier, interpretation of the ***T·t***-interactions shown in Figure 37 served the purpose to show exemplarily how the prediction equations can be extremely auspicious for the qualitative understanding of the examined system. This can be highly beneficial for academic research purposes as all factor-response-relationships will be safely revealed. With conventional OFAT-experimentation, on the contrary, some of these relationships – especially the FIs which are usually the most interesting ones – will likely be missed. Although it is easy to dwell in canticles about the potential of DoE in academic research, the other – and oftentimes considerable – DoE asset is the applicability of the prediction equations: using simple derivatization methods or desirability algorithms, the optimal factor settings for every possible response-goal can be easily obtained.[120] Within the context of the FC-CCD performed here, this means no matter what is desired – *e.g.*, a certain chain length with minimal (or a target) ***Đ***-value while striving for minimum monomer wastage – the ideal combination of factor levels will be revealed. Exactly this DoE-feature will be presented in the following section.

6.1.4 True System Optimization

The prediction models for responses $\boldsymbol{p}$, $\boldsymbol{\bar{M}}_{\mathbf{n,th}}$, $\boldsymbol{Đ}$ and $\boldsymbol{\bar{M}}_{\mathbf{n,app}}$ allow for revelation of the ideal combination of factor settings for any synthetic goal. Depending on these goals, different "desires" can be defined for each response and each factor:

- "Find an optimum": minimizing or maximizing of factors and/or responses
- "Keep it in range": factor and/or response must stay in a selectable interval
- "Attain a target value": factor and/or response must attain a selectable value

The scientist can have as many desires as he or she wishes – the prediction models and the so-called desirability algorithm will deliver the ideal factor combination within the examined experimental space. This desirability algorithm even allows for importance ranking of each individual "desire" (usually this is achieved by distributing measures of importance, like 5 stars for "very important" and one star for "less important").

Within the specific examined system of this work, another pleasant feature for RAFT experts arises: the prediction models even allow for optimization of a range of different chain lengths (*i.e.*, $\boldsymbol{\bar{M}}_{\mathbf{n,th}}$, in the FC-CCD values between 2.1 kDa and 25.1 kDa were obtained). Although this might sound obvious to a statistician, this is all but natural for the RAFT chemist utilizing the conventional OFAT-approach towards optimizing a RAFT polymerization for a $\boldsymbol{\bar{M}}_{\mathbf{n,th}}$-target. Herein, the typical procedure would likely be to pick a fixed suitable value of $\boldsymbol{R}_{\mathrm{M}}$ and polymerize up to the according value of $\boldsymbol{p}$ (for relationship between $\boldsymbol{R}_{\mathrm{M}}$ and $\boldsymbol{p}$, see equation (A2), Appendix) which always necessitates the execution of prior kinetic studies. If, however, the resulting polymer possesses an unsatisfyingly high value of $\boldsymbol{Đ}$, optimizations will only be achievable varying the other reaction parameters (factors $\boldsymbol{T}$, $\boldsymbol{w}_{\mathrm{S}}$ and the initiator concentration). Unfortunately though, in a complex reaction such as the RAFT polymerization all of these factors will influence the reaction kinetics which, again, will necessitate another kinetic study in order to precisely score the right $\boldsymbol{p}$ that corresponds with the given $\boldsymbol{\bar{M}}_{\mathbf{n,th}}$-target. No matter how much effort the RAFT scientist puts into these kinetic studies, "true" optimization – *i.e.*, reliable and comprehensive revelation of all factor interactions and the whole response surface – is unrealistic (if not unachievable) *via* conventional OFAT-experimentation.

In order to demonstrate how the prediction models find the ideal factors settings for any specific goal, three arbitrarily picked targets are listed in the following:

1. $\boldsymbol{\bar{M}_{\mathrm{n,th}}}$ = 8.0 kDa , $\boldsymbol{Đ}$ shall be minimized
2. $\boldsymbol{\bar{M}_{\mathrm{n,th}}}$ = 13.1 kDa, $\boldsymbol{Đ}$ = 1.25
3. $\boldsymbol{\bar{M}_{\mathrm{n,th}}}$ = 23.0 kDa, $\boldsymbol{Đ}$ = 1.32

Each of the three arbitrarily picked goals has two desires: one for $\boldsymbol{\bar{M}_{\mathrm{n,th}}}$ and one for $\boldsymbol{Đ}$. At this point, the prediction models will compute all combinations of factor settings that will yield a polymer possessing values for $\boldsymbol{\bar{M}_{\mathrm{n,th}}}$ and $\boldsymbol{Đ}$ that are as close as possible to the demanded desires. The resulting, “truly” optimal factor settings for the specific desires of the three arbitrarily picked goals are listed in Table 8.

Table 8: Three arbitrarily picked polymerization goals with specific $\boldsymbol{\bar{M}_{\mathrm{n,th}}}$- and $\boldsymbol{Đ}$-desires as well as the respective optimal factor settings (computed by the prediction equations).

Goal	***Optimal factor settings***					***Desired responses***	
	T / °C	t / min	R_{M}	R_{I}	w_{S}	$\bar{M}_{\mathrm{n,th}}{}^{a}$ / kDa	$Đ^{b}$
1	75	186	200	0.1	20	8.0	Minimize
2	80	321	256	0.091	13.6	13.1	1.25
3	82	390	466	0.1	19.95	23.0	1.32

[a] Determined *via* ^{1}H NMR spectroscopy and referencing to DMF. [b] Measured by SEC at 50 °C in an 0.1 M $NaNO_3$ aqueous (Milli-Q quality) solution with an added 0.05 wt% NaN_3 and calibration with PEG.

In these three arbitrarily picked, exemplary goals, no specific desire was demanded for the other two responses $\boldsymbol{p}$ and $\boldsymbol{\bar{M}_{\mathrm{n,app}}}$. Their values (corresponding with the computed optimal factor settings) will nonetheless be predicted by the respective models.

6.1.5 Validation of the Prediction Models

Although the prediction models are built from a foundation of experimental observations and are expected to accurately predict new data, it is strongly advised to validate them. This is achieved by conducting validation runs applying the computed optimal factor settings and comparing the observed and predicted responses. By definition, the prediction models are empirically validated when the observed responses all fall inside so-called 95 % prediction intervals. These intervals are estimated response ranges (based on the examined system’s systematical error) in which 95 % of new data should fall. Table 9 lists the predicted and observed responses for each exemplarily picked goal (see previous section) as well as the respective low and high borders of the 95 % prediction intervals.

Table 9: Predicted and observed responses for the three exemplary goals as well as the respective high and low border of the 95 % prediction intervals.

Goal	Response	Predicted	95 % PI low	95 % PI high	Observed
1	p^{a} / %	45.2211	41.0956	49.3466	45.7
	$\bar{M}_{\mathrm{n,th}}{}^{\mathrm{a}}$ / kDa	7.95615	5.80495	10.1073	8.10
	$Đ^{\mathrm{b}}$	1.16585	1.11668	1.21502	1.17
	$\bar{M}_{\mathrm{n,app}}{}^{\mathrm{b}}$ / kDa	4.70198	3.78601	5.61796	4.60
2	p^{a} / %	57.4723	53.8000	61.1445	56.7
	$\bar{M}_{\mathrm{n,th}}{}^{\mathrm{a}}$ / kDa	13.0571	11.1422	14.9719	12.6
	$Đ^{\mathrm{b}}$	1.25242	1.20764	1.29719	1.25
	$\bar{M}_{\mathrm{n,app}}{}^{\mathrm{b}}$ / kDa	6.3472	5.55299	7.14141	6.40
3	p^{a} / %	58.8018	54.7417	62.8618	57.8
	$\bar{M}_{\mathrm{n,th}}{}^{\mathrm{a}}$ / kDa	23.0066	20.8895	25.1237	22.9
	$Đ^{\mathrm{b}}$	1.32145	1.27417	1.36874	1.32
	$\bar{M}_{\mathrm{n,app}}{}^{\mathrm{b}}$ / kDa	9.86659	8.96695	10.7662	10.1

$^{\mathrm{a}}$ Determined *via* ^{1}H NMR spectroscopy and referencing to DMF. $^{\mathrm{b}}$Measured by SEC at 50 °C in an 0.1 M $NaNO_3$ aqueous (Milli-Q quality) solution with an added 0.05 wt% NaN_3 and calibration with PEG.

As all predicted responses clearly fall within the 95 % prediction intervals, the models are validated. However, the extreme accuracy facilitated by the prediction equations is best demonstrated graphically. Figure 38 shows the predicted (black spheres) and observed (blue spheres) responses as well as the respective 95 % prediction intervals for all three exemplary goals ($\boldsymbol{p}$ is left out due to redundancy with $\bar{\boldsymbol{M}}_{\mathbf{n,th}}$ and the difficulties of four-dimensional illustration). Clearly, the models work excellently: the prediction models are validated.

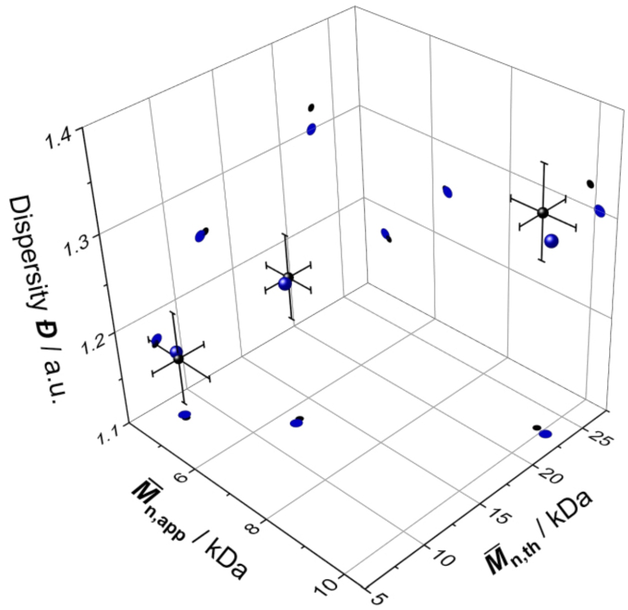

Figure 38: Three-dimensional display of the predicted (black spheres) and observed (blue spheres) responses of the three exemplarily picked polymerization goals. The prediction equations are validated as the observed responses all fall within the 95 % prediction intervals.

6.1.6 Conclusion

Although the examined system within the performed FC-CCD is a rather specific one, it served excellently for the demonstration of the academic potential of DoE. RSM showed to be extremely well-suited for revelation of all factor-response-relationships of a complex system such as a RAFT polymerization. Herein, highly accurate prediction equations for each observed responses ($\boldsymbol{p}$, $\bar{\boldsymbol{M}}_{\mathbf{n,th}}$, $\boldsymbol{Đ}$ and $\bar{\boldsymbol{M}}_{\mathbf{n,app}}$) were obtained *via* polynomial regression, ANOVA and appropriate model diagnostics (performed by the software DesignExpert). These equations mathematically link the factors $\boldsymbol{T}$, $\boldsymbol{t}$, $\boldsymbol{R}_{\mathrm{M}}$, $\boldsymbol{R}_{\mathrm{I}}$ and $\boldsymbol{w}_{\mathrm{S}}$ with the responses and allow for comprehensive portraying of the whole system (within the examined factor ranges).

RSM was shown to not only find potential system optima but also to boast great potential for academic research purposes as it also facilitates knowledge generation and qualitative understanding. Within this context, especially the FIs – which are easily missed with conventional OFAT-experimentation – reveal decisive information.

Most certainly, scientists of many different fields could greatly benefit from the perks of DoE. This work thus strives to encourage colleagues to go the extra mile and implement DoE into their workflow. Although DoE will not be the answer to every scientific question, it truly stands out when it comes to system optimization and systematic testing of relationships between parameters and measurable quantities. While the general DoE-route presented in this work will stay similar, there might be other RSM designs or omittable steps for other examined systems. Perhaps a different design could be more efficient (especially computer-generated optimal designs have gained attention recently). In some cases, RSM can even be superfluous when no non-linearities are observed in prior screening designs. Either way, for every specific demand, there will always be an ideal experimental design.

6.2 Advanced PTT-Analysis of PMAAm Solutions

As already reported in-depth in section 5.1.3, PMAAm exhibits a UCST-type PT in water/ethanol mixtures. The exact PTT strongly depends on polymer and ethanol weight fraction as well as on the polymer chain length.[69] These dependencies were tested meticulously and are best described by Figure 33. In hindsight, exactly a systematical study like this – with the PTT as response and three significant factors – would have been predestined for a DoE. Apart from the polymer and ethanol weight fraction and the polymer weight – which in the following will be referred to as w_{EtOH}, w_{PMAAm} and $\overline{M}_{\mathrm{n,th}}$ – there are, however, additional potential influences. For instance, the strong influence of salts – with a generally stronger anionic than cationic influence – on the solution behavior of LCST and UCST polymers according to the Hofmeister series is already well-reported.[30,121–123] As, for instance, in potential future biomedical application of "smart" UCST-type polymeric materials salts will naturally be present, potential effects of salt on the UCST-type PTT of PMAAm were investigated as well. The two anions with the highest concentration in human blood are chloride ($103\,\mathrm{mmol\cdot L^{-1}}$) and hydrocarbonate ($27\,\mathrm{mmol\cdot L^{-1}}$).[124] Thus, in the following, the results of an RSM design – more precisely a Box-Behnken design – investigating the influence of w_{EtOH}, w_{PMAAm} and $\overline{M}_{\mathrm{n,th}}$ and the concentrations of the salts sodium chloride and sodium hydrocarbonate (w_{NaCl} and $w_{\mathrm{NaHCO_3}}$, respectively) on the PTT of PMAAm in different water/ethanol mixtures will be presented. However, it must be stated before that, despite presenting it secondly, this was the first DoE conducted throughout the doctorate work. Hence, the analyzed PMAAm samples were still synthesized photochemically (and not with the optimized system presented in section 6.1). Also, the route to the RSM prediction models was rather inefficient as another design may have been more suitable (more on this matter will be discussed in the conclusive section 6.2.4).

6.2.1 Preparing for the Experimental Design: Polymer Synthesis

In order to perform a sophisticated screening design investigating the factors w_{EtOH}, w_{PMAAm}, $\overline{M}_{\mathrm{n,th}}$, w_{NaCl} and $w_{\mathrm{NaHCO_3}}$ that also screens for non-linearity, center points will be required. Here, the only factor that is not easily adjustable is $\overline{M}_{\mathrm{n,th}}$. In order to be set at three levels (−, 0 and +), three PMAAm samples with equidistant values of $\overline{M}_{\mathrm{n,th}}$ were required and successfully obtained by tailored synthesis (synthetic details are provided in section 10.6.3.1, Appendix). Table 10 lists their experimental as well as analytical data: the $\overline{M}_{\mathrm{n,th}}$ of 40.3 kDa precisely forms the midlevel (0) between the two factorial levels of 26.7 kDa (−) and 53.9 kDa (+).

Table 10 Experimental and analytical data of three PMAAm samples used for an experimental design.

Sample Code[a]	**T / °C**	**t / min**	**R_M**[b]	**Conversion**[b] **/ %**	**$\overline{M}_{n,\mathrm{th}}$**[c] **/ kDa**	**$Đ$**[d]
PMAAm$^{26.7}$	70	105	1000	31.0	26.7	1.15
PMAAm$^{40.3}$	70	165	1000	47.0	40.3	1.20
PMAAm$^{53.9}$	70	238	1000	63.0	53.9	1.27

[a]Superscripts represent $\overline{M}_{\mathrm{n,th}}$. [b]$R_M$ equals the ratio of initial concentrations of MAAm and CTCA. [c]Quantities determined *via* ^{1}H NMR spectroscopy and referencing to DMF. [d]Measured by SEC at 50 °C in an 0.1 M $NaNO_3$ aqueous (Milli-Q quality) solution with an added 0.05 wt% of NaN_3. Calibration was performed applying PEG standards.

In the succeeding screening design, the significance of the salt concentrations was tested. Although it was already known, that the other factors (w_{EtOH}, w_{PMAAm} and $\overline{M}_{\mathrm{n,th}}$) exert a significant impact on the PTT of the PMAAm solutions, they were included into the fractional factorial screening design – which will be presented in the following section – in order to detect potential FIs with w_{NaCl} and $w_{\mathrm{NaHCO_3}}$.

6.2.2 Screening: Testing the Salt Significance

The five factors were examined with a fractional factorial design (2^{5-1}) and augmented with five center points to check for non-linearities. Table 11 shows the factor levels that were chosen for each factor for the screening design.

Table 11: List of the low (−), center (0) and high (+) levels of each factor examined in the fractional factorial screening design.

	w_{PMAAm} / wt%	**$w_{\mathrm{NaHCO_3}}$ / wt%**	**w_{NaCl} / wt%**	**w_{EtOH} / wt%**	**$\overline{M}_{\mathrm{n,th}}$ / kDa**
−	0.25	0.1	0.4	15	26.7
0	1.125	0.2	0.6	20	40.3
+	2.0	0.3	0.8	25	53.9

Notice that the ranges of w_{PMAAm} and w_{EtOH} are slightly narrower than in the previous study (presented in Figure 33, section 5.1.3). This is due to the fact that the range of $\overline{M}_{\mathrm{n,th}}$ is, in turn, significantly wider and examines higher values which did not allow for w_{EtOH} values above 25 wt% as the PTT would then, most likely, lie above the detectable temperature of around 80 °C (ethanol begins to boil). The factor ranges of the salt concentrations $w_{\mathrm{NaHCO_3}}$ and w_{NaCl} (0.1−0.3 wt% and 0.4−0.8 wt%, respectively) were relatively narrow. However, their respective concentrations in human blood serum approximately lie in the middle of these ranges. The influences of $w_{\mathrm{NaHCO_3}}$ and w_{NaCl} will thus provide a viable prevision of how the solution behavior of PMAAm might chance in an environment containing relatively high salt concentrations (such as in biomedical applications or in switchable filtration devices filtrating saltwater).

After completion of the screening design (for the experimental plan, see Table A7, Appendix), some effects immediately stand out when looking at the normal plot of effects (Figure 39). As expected, w_{EtOH}, w_{PMAAm} and $\overline{M}_{\mathrm{n,th}}$ exert strong positive effects (red symbols) on the PTT. The effects of $w_{\mathrm{NaHCO_3}}$ and w_{NaCl} are less imposing as they only deviate slightly from the line of normally distributed, seemingly insignificant effects. Additionally, a negative effect (blue symbols) of a 2FI between $\overline{M}_{\mathrm{n,th}}$ and w_{PMAAm} appears to be significant as well.

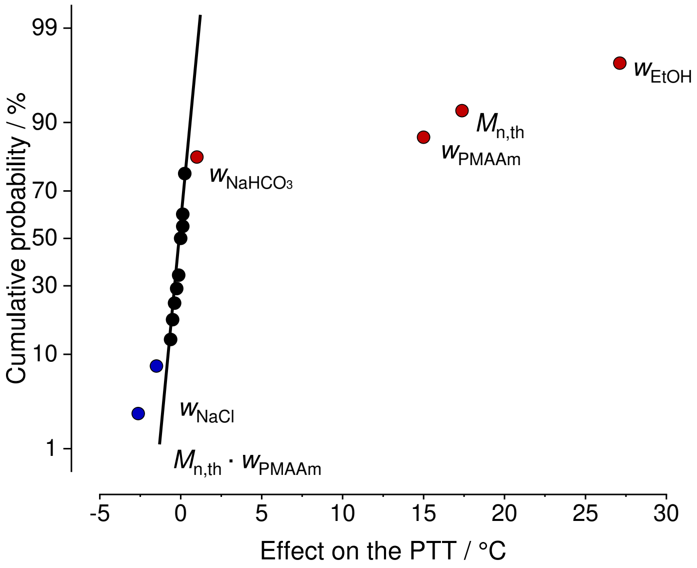

Figure 39: Normal probability plot of the factor and interaction effects on the PTT of PMAAm in different mixtures of water and ethanol. The seemingly insignificant effects are normally distributed and thus arrange linearly as indicated by the black line. The seemingly positive (red symbols) and negative (blue symbols) effects deviate from that line.

The ANOVA table as well as the fit statistics of the performed fractional factorial screening design is shown in Table 12. Apparently, all effects suggested by the normal probability plot in Figure 39 are, in fact, significant (respective p-values < 0.05). The ANOVA also implies that no significant effect was missed as the lack of fit is insignificant (p-value > 0.05).

Table 12: ANOVA table as well as fit statistics for the performed fractional factorial screening design.

Source	**SS**	**df**	**Mean Square**	**F-value**	**p-value**	**Fit Statistics**	
Model	5091.19	6	848.53	1965.42	< 0.0001	R^2	0.9989
w_{PMAAm}	900.00	1	900.00	2084.63	< 0.0001	R^2_{adj}	0.9984
$w_{\mathrm{NaHCO_3}}$	4.00	1	4.00	9.27	0.0094	R^2_{pred}	0.9971
w_{NaCl}	9.00	1	9.00	20.85	0.0005		
w_{EtOH}	2943.06	1	2943.06	6816.89	< 0.0001		
$\overline{M}_{\mathrm{n,th}}$	1207.56	1	1207.56	2797.03	< 0.0001		
$\overline{M}_{\mathrm{n,th}} \cdot w_{\mathrm{PMAAm}}$	27.56	1	27.56	63.84	< 0.0001		
Curvature	55.01	1	55.01	127.42	< 0.0001		
Residuals	5.61	13	0.4317				
Lack of Fit	3.81	9	0.4236	0.9414	0.5713		
Pure Error	1.80	4	0.4500				
Cor Total	5151.9	20					

Although the fit statistics imply great predictability and no signs of over-fitting, no accurate prediction model can be generated. This is due to the fact that non-linear effects are detected (curvature p-value < 0.05) which this screening design cannot unambiguously assign to the factors (as described in section 3.4.2.4) – an RSM design is required.

6.2.3 RSM Modelling: Execution of a Box-Behnken Design

The chosen RSM design was a Box-Behnken design (for design geometry see Figure 36, section 6.1.2) as it avoids “extreme” combinations of factor levels that could lead to run unfeasibility (*e.g.*, w_{PMAAm}^{+}, $\overline{M}_{\mathrm{n,th}}^{+}$, w_{EtOH}^{+} could lead to a PTT above the boiling point of ethanol). The experimental plan of the Box-Behnken design can be taken from Table A8 (Appendix).

After all required runs were executed, the following prediction model was established *via* polynomial regression and is shown in equation (23).

$$\begin{aligned}\mathrm{PTT}\,/\,^{\circ}\mathrm{C} = 46.0 + 7.4\, w_{\mathrm{PMAAm}} - 1.1\, w_{\mathrm{NaCl}} + 13.7\, w_{\mathrm{EtOH}} + 7.6\, \overline{M}_{\mathrm{n,th}} \\ - 3.3\, w_{\mathrm{PMAAm}}^{2} + 2.4\, w_{\mathrm{EtOH}}^{2} - 2.0\, \overline{M}_{\mathrm{n,th}}^{2}\end{aligned} \tag{23}$$

The ANOVA table as well as the fit statistics (see Table A9, Appendix) imply that the prediction model is valid: all model terms are significant (p-value < 0.05), the lack of fit (p-value > 0.05) suggests that no significant model terms have been missed and the fit statistics reveal no sign of potential over-fitting. On top of that, the diagnostic plots (see Figure A19, Appendix) reveal that the model can be trusted. Although the model is trustworthy, two major deviations from the screening results immediately catch the eye: the Box-Behnken design assesses $w_{\mathrm{NaHCO_3}}$ and the 2FI $\overline{M}_{\mathrm{n,th}} \cdot w_{\mathrm{PMAAm}}$ to be insignificant. This irritating observation was, most likely, caused by a combination of two conditions. Due to its design geometry, a Box Behnken design is particularly sensitive towards quadratic effects, however, less so for main and especially interaction effects. If, on top of that, these effects are very small – such as the two effects that were found significant in the screening – they can, thus, sometimes be missed. An FC-CCD, on the contrary, has markedly higher sensitivity when it comes to finding interaction effects. Apparently, a more suitable design than the Box-Behnken would have been the better choice.

Nonetheless, the stronger effects, of course, will not disappear below the "detection limit" of the Box-Behnken design. Figure 40 shows the prediction plots for each of the four significant factors (all other factors than the one illustrated are set to their midlevel, respective prediction equations are provided as well). The dashed green lines illustrate the 95 % prediction intervals. Once again, the high potential for academic research becomes apparent as the impact of each factor is resolved individually. As already observed in earlier experiments, graph A shows that the PTT increases with increasing concentration of PMAAm (*i.e.*, w_{PMAAm}). This appears plausible as with increasing w_{PMAAm}-values, each proton donor and acceptor of the amide functionality in the PMAAm side chains has an increased likelihood of meeting its counterpart. As a consequence, also intermolecular polymer–polymer interactions become increasingly relevant. The slope of the PTT-course, however, deceases with w_{PMAAm} (due to the negative quadratic term) as the PTT draws closer to the critical maximum temperature (*i.e.*, the UCST).

A similar PTT-course is observed in graph D which shows the prediction of the $\overline{M}_{\mathrm{n,th}}$-influence. According to the solution theory of Flory, Huggins and Staverman, the combinatorial mixing entropy – which is the driving force of UCST-type PTs – of the polymer decreases with increasing chain length.[34] Hence, the temperature at which the stabilizing effects of the polymer–polymer interactions are overpowered (according to equation (1)) will increase.

The influence of the ethanol content on the PTT (graph C) is also rather expected: as it is a non-solvent for PMAAm, increasing w_{EtOH} -values will markedly reduce PMAAm solubility – and thus increase the UCST-type PT. In fact, the PTT appears to increase exponentially with w_{EtOH} (fitted accurately with a negative quadratic predictor).

Graph B, shows the very weak influence of the NaCl-concentration on the PTT. Within the observed ranges from 0.4–0.8 wt%, the PTT only decreases by about 2 °C. As, in general, anions exert much stronger influence on polymer solubility as cations, it appears likely that chloride acts as a chaotropic agent.[123] As such, it may reduce the loss of entropy resulting from the hydrophobic hydration of the PMAAm backbone. This, in turn, increases the PMAAm solubility and thus lowers the UCST-type PT. It seems that both anions with the highest concentration in human blood serum (HCO_3^- and Cl^-) only possess very minor influence on the UCST-type PTTof PMAAm in water/ethanol mixtures. Apparently, PMAAm is more robust towards ionic surroundings than what most other UCST-type polymers are usually credited for.

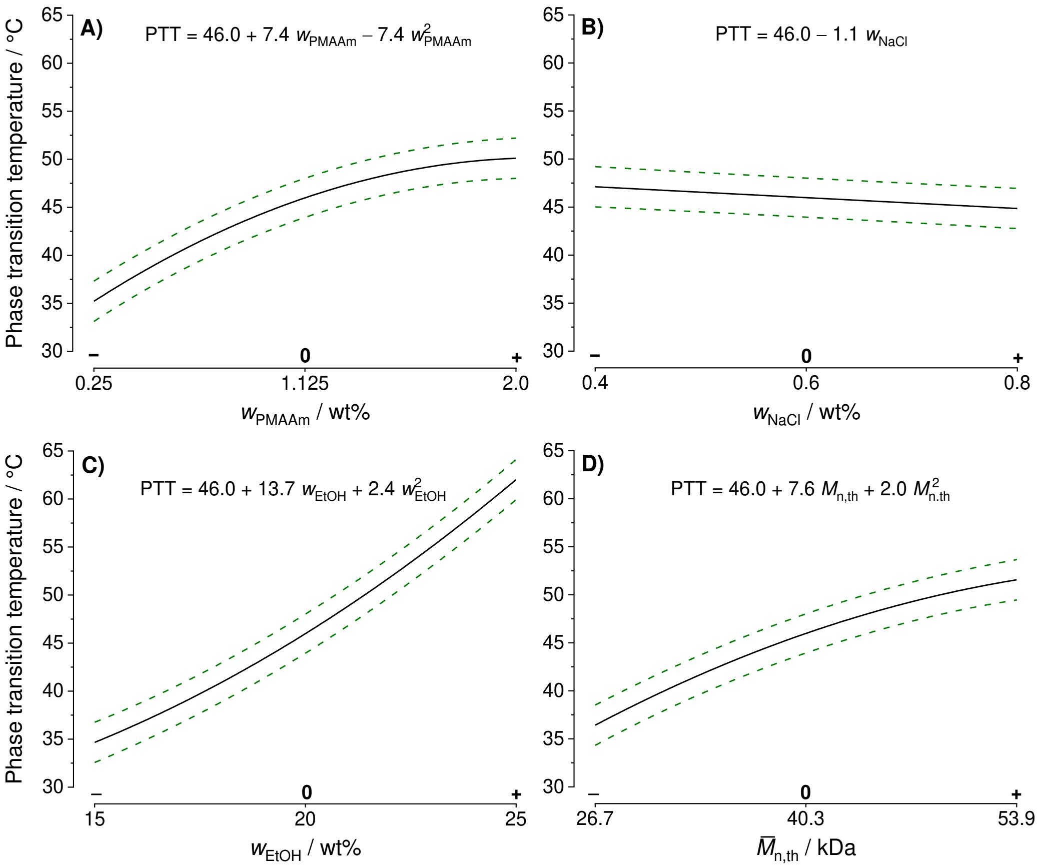

Figure 40: Prediction plots of the relationship between the response (PTT) and the individual factors (A: w_{PMAAm}, B: w_{NaCl}, C: w_{EtOH}, D: $\overline{M}_{n,th}$). In each graph, all but the predicted factors are set to their respective midlevel resulting in markedly shortened (and thus simplified) coded prediction equations which are additionally provided. The 95 % prediction intervals are illustrated by the green dashed lines.

To sum things up, the established PTT-model allows for precise adjustment of the transition temperature and – what might be even more interesting – thorough qualitative understanding of each factor's effect.

6.2.4 Conclusion

The investigation of the UCST-type PTT of PMAAm solutions in different water/ethanol mixtures *via* RSM, once again, showed the great potential of DoE when it comes to academic research purposes. The established PTT-prediction model allows the PTT to be adjusted precisely depending on the scientist's demand. On top of that, the prediction model facilitates great knowledge generation as the influence of each factor (within the respective chosen factor range) on the PTT is revealed individually.

Still, this first DoE represented a learning curve – especially when it comes to plan efficiency. As mentioned before, the Box-Behnken design has its flaws when it comes to detection of weak interaction effects. Instead, an FC-CCD may have been the superior design. Although the FC-CCD necessitates runs at more “extreme” conditions (remember that the runs are located at the cube vertices as opposed to a Box-Behnken design, see Figure 20), the design is more sensitive towards FIs and, in this specific case, would have boasted another great advantage: due to the great resemblance of the experimental geometry between the performed fractional factorial screening design and the FC-CCD, simple augmentation of the screening design with the required axial points would have sufficed. This way, the screening design would have been transformed into a sophisticated RSM design saving a lot of experimental effort. Obviously, hindsight is twenty-twenty, yet, this goes to show how important the choice of design can turn out to be.

7 Generation of “Smart” UCST-Materials

Potential applications of “smart” polymeric materials for drug delivery systems or switchable filtration devices rely on microphase separation of a “smart” block that is covalently bound to another block that does not respond equally to the stimulus. Hence, architectures like diblock copolymers are of great interest. This section will describe the challenges of preparing diblock copolymers with one UCST-type block as well as the limits of characterization methods due to issues with polymer solubility (section 7.1). *via* PISA stable dispersions with PMAAm as stabilizing block could be synthesized *via* heterogenous RAFT polymerization (section 7.2). On top of that, some obtained dispersions were thoroughly investigated *via* temperature-dependent DLS measurements in order to investigate potential “smartness” of the self-assembled particles (section 7.3). Therein, analytical difficulties and potential sources of error (section 7.3.2) as well as first insights into potential effects of confinement – *i.e.*, spatial constraints of the “smart” block and proximity to typical membrane majority forming blocks – are discussed (see section 7.3.3).

7.1 Challenges of Diblock Copolymer (In-)Solubility

Due to the high polarity and the pronounced inter- and intramolecular interactions of PMAAm, it is – to the best of the author’s knowledge – exclusively soluble in water. Although PNAGA is (merely) soluble in DMSO, it seems fair to conclude that UCST-type polymers are not soluble in a great spectrum of different solvents. If attached to another block, this can complicate characterization methods like ^{1}H NMR spectroscopy and especially SEC. “Smart” membranes with switchable pore sizes, for instance, require a comparably hydrophobic matrix forming block like PS or PMMA to provide a solid and tough support for the filtration device. The amphiphilicity of a diblock copolymer consisting of a UCST block and a block of PS or PMMA is way too high – *i.e,* their solubility parameters are too different – for a solvent (or solvent mixture) to dissolve both blocks which is a necessity for most routinely applied characterization methods.

Interestingly, however, even the combination of PMAAm with highly water soluble blocks like PEG or poly(*N*,*N*-dimethyl acrylamide) (PDMA) allowed for no

SEC analyses as the respective isolated polymers were insoluble in water (and in every other solvent or solvent mixture which made the diblock copolymers rather useless). Apparently, the solubility of the PMAAm block was drastically reduced by attachment to another block. This might be due to the loss of one carboxylic end group potentially elevating the UCST-type PTT resulting in heterogenous systems. Even at higher temperatures (vigorous and long stirring at 80 °C mixtures of the diblock copolymer and water remained heterogenous which made SEC analysis impossible). Just like SEC analysis, successful preparation of “smart” membranes with switchable pore size usually requires that all polymer components are dissolved simultaneously. With the necessity of a hydrophobic matrix block, it follows that switchable filtration devices will, most likely, not be obtainable using PMAAm as the “smart” UCST block.

Nonetheless, the chain extension of PMAAm with styrene *via* heterogenous RAFT polymerizations can generate highly interesting, potentially “smart” materials as well. The following sections will present the results of chain extension with styrene (emulsion polymerization) and methyl methacrylate (dispersion polymerization) as well as the solution behavior of the resulting block copolymers which are formed by PISA.

7.2 Chain Extension of PMAAm *via* PISA

Being aware that SEC analysis of the diblock copolymer resulting from chain extension of PMAAm will not be feasible, it was of particular importance to utilize a PMAAm-macroRAFT agent with sufficient chain end fidelity. As the RAFT polymerization of MAAm was already priorly optimized *via* DoE (see section 6.1), certain polymerization targets were applied which, in theory, should lead to high chain end livingness:

1. Minimize T: Lower rates of thermal trithiocarbonate decomposition
2. Minimize R_I: Fewer initiator derived radicals imply fewer dead chains
3. Minimize $Đ$: Although not necessarily connected,[125] low $Đ$-values typically imply good polymerization control and thus higher livingness

A fitting polymerization suggested by the DoE-Software (DesignExpert) was conducted (T = 75 °C, t = 357 min °C, R_M = 500 °C, R_I = 0.025 °C and w_s = 20 wt%) yielding a PMAAm$^{12.0}$-sample (Table 13 shows the respective experimental data).

Table 13 Experimental and analytical data of the thermally initiated RAFT polymerization of MAAm using CTCA as RAFT agent (75 °C for 357 min, R_M = 500, R_I = 0.025, w_s = 20 wt%).

Sample Code[a]	**R_M**[b]	**t / min**	**Conversion**[c] **/ %**	**$\overline{M}_{n,th}$**[c] **/ kDa**	**$\overline{M}_{n,app}$**[d] **/ kDa**	**$Đ$**[d]
PMAAm$^{12.0}$	500	357	27.5	12.0	6.12	1.17

[a]Superscripts represent $\overline{M}_{n,th}$. [b]R_M equals the ratio of initial concentrations of MAAm and CTCA. [c]Quantities determined *via* ^{1}H NMR spectroscopy and referencing to DMF. [d]Measured by SEC at 50 °Cin an 0.1 M $NaNO_3$ aqueous (Milli-Q quality) solution with an added 0.05 wt% of NaN_3. Measured by SEC against PEG standards.

Through simple chain extension with further MAAm repeating units and subsequent SEC analysis it was obvious that PMAAm$^{12.0}$ offered sufficient livingness (see Figure A20, Appendix) for the building of diblock copolymers *via* chain extension with styrene and MMA.

7.2.1 Synthesis of PMAAm-*b*-PS: A RAFT Emulsion Polymerization

In order to synthesize PMAAm-*b*-PS, a photoiniferter RAFT emulsion polymerization was conducted in water (T = 80 °C, t = 300 min °C, R_M = 1000 °C and w_s = 10 wt%) using PMAAm$^{12.0}$ as macroRAFT agent (the respective polymerization scheme is illustrated in Figure 41). Light initiation was achieved via a high-intensity UV-LED lamp (OmniCure AC450, emission maximum at 384 nm, 10 mW cm^{-2}) which has been reported to successfully facilitate chain extension of polyacrylamides with styrene by Lauterbach *et al.*[66]

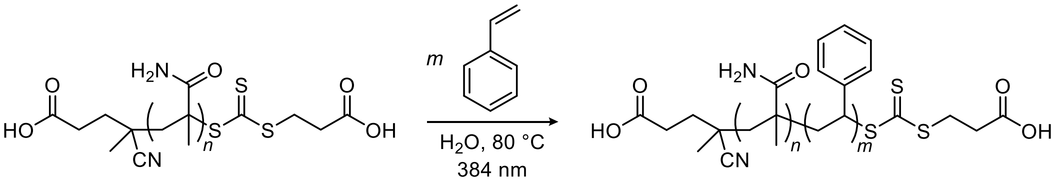

Figure 41: Photoiniferter RAFT emulsion polymerization of styrene in pure water using PMAAm$^{12.0}$ as macroRAFT agent.

Unfortunately, the RAFT agent did not sufficiently stabilize the initial polymerization mixture. Even after prolonged, vigorous stirring, no stable emulsion was obtainable and the mixture would visibly phase separate within a matter of minutes. This is caused by the rather polar RAFT agent which carries carboxylic groups at both chain ends which drastically reduces its ability to stabilize styrene droplets.[66] This phase separation leads to a new problem: until PISA facilitates a stabilized emulsion, standard laboratory procedures to obtain kinetic studies will be impossible as the samples taken *via* syringe are not representative of the whole polymerization (leading to strongly fluctuating or even negative conversions). The only method for reliable determination of the styrene conversion *via* NMR was to shake the glass vial intensely, immediately remove the screw-cap of the glass vial and remove a sample *via* Pasteur pipette and using deuterated DMSO to flush the whole sample (sucked up by capillary forces) into an NMR tube.

Applying this procedure, a short full factorial (2^3) DoE-screening was performed investigating the factors t, R_M and w_S on the conversion of styrene p at a constant polymerization temperature of 80 °C and light intensity of 10 mW cm^{-2} (emission maximum at 384 nm). Although such a short design will not suffice for complete modelling of all relations (such as presented in section 6.1), significant main or interaction effects will be revealed. The factor ranges of t, R_M and w_S were set at 100−300 min, 300−1000 and 10.0−20.0 wt%, respectively. Table 14 shows the ordered experimental plan as well as the obtained conversion of styrene.

Table 14: Two-level fractional factorial screening design (2^3) investigating the influences of t, R_M and w_S on the conversion of styrene p during chain extension of PMAAm$^{12.0}$.

Run	**Factors**			**Response**
	t / min	**R_M**	**w_S / wt%**	**p^a / %**
1	100	1000	10	38.0
2	300	1000	20	57.3
3	100	1000	20	5.9
4	100	300	10	37.7
5	300	300	20	36.0
6	100	300	20	15.5
7	300	1000	10	76.2
8	300	300	10	55.1

[a] Determined *via* ^{1}H NMR spectroscopy and referencing to DMF.

After performing the eight runs (in randomized order), four significant effects were obtained, as indicated by the normal plot in Figure 42 (respective p-values from the ANOVA as well as the relevant fit statistics can be found in Table A10, Appendix). As indicated by the strong positive (red circle) and negative (blue circle) effects, of t and w_s, respectively, the ANOVA confirms that both main effects are significant (p-value < 0.05). While the conversion of styrene will rise with increasing values of t for obvious reasons, the explanation of the negative effect of w_s is less straightforward. It could, however, be explained by aggravated stabilization of the emulsion (a similar phenomenon was found by Lauterbach *et al.*).[66]

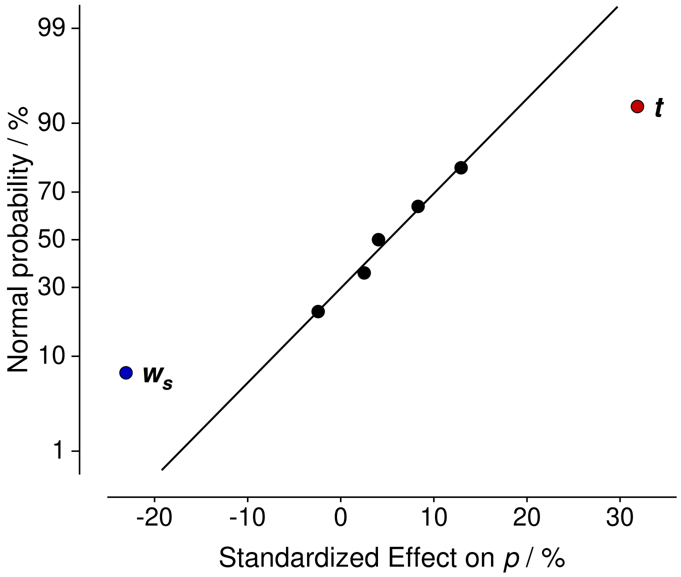

Figure 42: Normal plot of the main and interaction effects of the conducted two-level fractional factorial screening design (2^3) investigating the influences of t, R_M and w_s on the conversion of styrene p during chain extension of PMAAm$^{12.0}$.

The performed kinetic studies allowed for successful synthesis of PMAAm-*b*-PS which was also indicated visually by increasing turbidity over the reaction time. However, as strong macroscopic coagulation was observed, it is (amongst other hypotheses) possible that the polymerization boasts relatively low control over molecular weight and dispersity.[126–128] It was hence decided to switch from styrene to MMA – another monomer commonly used for the preparation of "smart" membranes.[129,130] The route to the synthesis of PMAAm-*b*-PMMA will be described in the following section.

7.2.2 Synthesis of PMAAm-*b*-PMMA *via* RAFT Dispersion Polymerization

Rather than performing another RAFT emulsion polymerization, chain extension of PMAAm$^{12.0}$ with MMA was conducted *via* dispersion polymerization. This procedure is feasible as MMA exhibits significantly increased solubility in water compared to styrene. Especially in cosolvent mixtures with water, the solubility of MMA – which is required in RAFT dispersion polymerizations – is significantly enhanced.[131] However, facilitating the desired component solubilities for a UCST-type macroRAFT agent is a delicate matter. While the cosolvent content should be high enough to dissolve MMA, the cosolvent mixture needs to remain sufficiently polar to dissolve PMAAm. As was already shown in section 5.2.3 (Figure 33) the solubility of PMAAm also greatly depends on its weight content w_{PMAAm} in the solution. By lowering the w_{S} to 5 wt% (compared to 10 wt% in the RAFT emulsion polymerization of styrene), ideal macroRAFT as well as monomer solubility – while trying to maintain maximum water content – was achieved in a water/ethanol mixture (75/25, *w*/*w*). Having "solved" these solubility-challenges, a photoiniferter surfactant-free RAFT dispersion polymerization using PMAAm$^{12.0}$ as macroRAFT agent was conducted. The respective reaction scheme is shown in Figure 43.

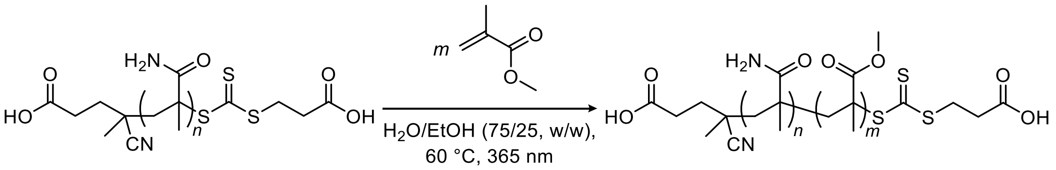

Figure 43: Photoiniferter RAFT dispersion polymerization of MMA in a water/ethanol mixture (75/25, *w*/*w*) using PMAAm$^{12.0}$ as macroRAFT agent.

The polymerization was conducted at varying reaction temperatures (60 °C and 80 °C) and R_{M}-values (400 and 1000). As MMA results in a similarly reactive growing species as MAAm that is propagating significantly quicker than a styrene growing species, the lower-intensity UV light source (365 nm, 0.38 mW cm^{-2}) that was already successfully applied for the MAAm homopolymerization was utilized. The respective conversion-time courses are illustrated in Figure 44. Graph A shows two kinetic studies performed at 60 °C (with varying R_{M}-value, green circles: 1000, black circles: 400) while graph B shows a kinetic study conducted at a polymerization temperature of 80 °C (dispersion stemming from the highlighted, orbited data points will be thoroughly investigated *via* DLS in section 7.3). The conducted kinetic studies allow for certain conclusions: all polymerizations facilitate high polymerization rates yielding conversions of up to 98 % within around 2 hours. Just like the photoiniferter homopolymerization of PMAAm (see section 5.2.2), the R_M-value appears to exert no drastic influence on the rate of polymerization. At 60 °C both polymerizations yield around 80 % conversion within around 2 hours. Elevating the reaction temperature by 20 °C, on the other hand, facilitates quicker polymerization rates as expected by Arrhenius’ law.

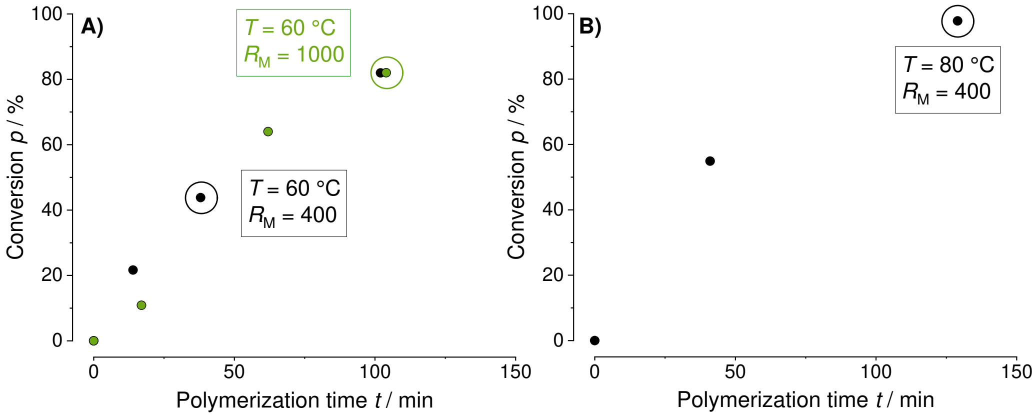

Figure 44: Kinetic studies of the photoiniferter surfactant-free RAFT dispersion polymerization of MMA using $\text{PMAAm}^{12.0}$ as macroRAFT agent. The dispersion samples stemming from highlighted, orbited data points are investigated *via* DLS section 7.3. Graph A) Two polymerizations at a reaction temperature of 60 °C with differing R_M-values (green circles: 1000, black circles: 400). Graph B) Kinetic study was performed at 80 °C.

In contrast to the chain extensions with styrene via emulsion polymerization, dispersion polymerizations with MMA did not exhibit any sign of pronounced coagulation. Compared to PS in water, PMMA in water/ethanol (75/25, *w*/*w*) is significantly less incompatible. This may explain the absence of coagulation of the PMAAm-*b*-PMMA-particles as no lowering of surface tension appears to be necessary. This is a clear success for UCST-type stabilized PISA processes and was achieved by simply switching from styrene to MMA.

As isolation of the diblock copolymer led to a glassy, insoluble and thus unusable solid, formation of potentially “smart” membranes with switchable pore sizes will not be possible *via* this route. Nonetheless, temperature-dependent DLS investigations of the obtained, self-assembled particles can provide interesting insights into the UCST-type solution behavior if PMAAm. Also, changes of the solution behavior may allow for conclusions concerning the changes of thermoresponsivity when switching from the UCST-homopolymer to a UCST-block in a self-assembled morphology. The dispersion samples which were subject to these DLS investigations, as well as their respective experimental and analytical data are listed in Table 15.

Table 15: The three PMAAm-*b*-PMMA-dispersions that were taken from the kinetic studies and were subject to thorough investigations *via* DLS. Experimental and analytical data is additionally provided.

Sample Code[a]	***T*/ °C**	***t* / min**	**R_M**[b]	**w_s / wt%**	**Conversion**[c] **/ %**
$PMAAm^{12.0}$-*b*-$PMMA^{17.5}$	60	62	400	5	27.5
$PMAAm^{12.0}$-*b*-$PMMA^{82.0}$	60	104	1000	5	82.0
$PMAAm^{12.0}$-*b*-$PMMA^{37.7}$	80	129	400	5	97.8

[a]Superscripts represent $\bar{M}_{n,th}$ of the respective blocks. [b]R_M equals the ratio of initial concentrations of MAAm and CTCA. [c]Quantities determined *via* ^{1}H NMR spectroscopy and referencing to DMF.

7.3 Solution Behavior of PMAAm-*b*-PMMA-Dispersions

In order to investigate the UCST-type behavior of the diblock copolymers, thorough analyses *via* DLS were conducted. The results will be presented in the following sections showcasing potential thermoresponsive behavior of the obtained, self-assembled particles in pure water. Specifications of polymer weight fractions will coherently refer only to the PMAAm content. This way, dispersions with different conversion of MMA can be diluted equally (a detailed explanation is provided in section 8.3.3.1).

7.3.1 Solution Behavior of PMAAm-*b*-PMMA in Pure Water

Similar to the PMAAm homopolymer, PMAAm-*b*-PMMA shows no sign of thermoresponsivity in pure water as can be seen in Figure 45 which plots the R_h-values versus the solution temperature. The intensity correlation function indicated only one particle species with an R_h-value of approximately 60 nm. Cooling of the solution (which was initially tempered to 70 °C) down to 6 °C (blue circles) showed no changes of particle size. Apparently, the stabilizing $PMAAm^{12.0}$ block is not thermoresponsive in pure water.

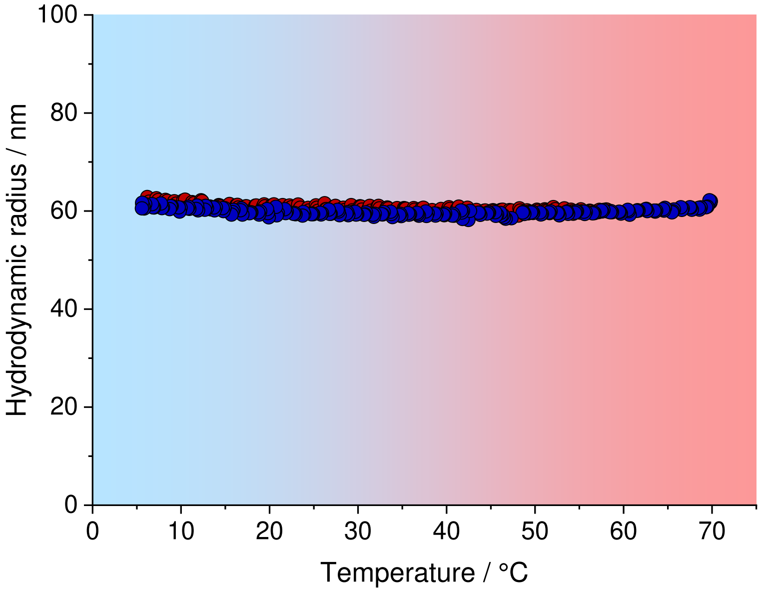

Figure 45. Temperature-dependent R_h-evolution of a 0.05 wt% aqueous solution of PMAAm$^{12.0}$-*b*-PMMA$^{82.0}$. The measurement was started at 70 °C and cooled down to around 6 °C (blue circles). Afterwards, the solution was reheated to 70 °C (red circles). The colored background indicates the temperature transition from high (red) to low (blue) and serves as a guide to the eye.

As the homopolymer PMAAm shows UCST-type solution behavior in water/ethanol mixtures, the PMAAm-*b*-PMMA-dispersions were analyzed in the same media. However, as the dispersions showed a thermosensitive rather then a -response UCST-type behavior (as shown in section 7.3.3). In contrast to thermoresponsivity, thermosensitivity usually leads to nonoccurrence of macroscopic agglomeration and, relating thereto, smaller changes of the particle size. As a less pronounced observed effect, for obvious reasons, is more prone to systematical error, a new challenge concerning data-accuracy arose which will be addressed in the following section.

7.3.2 The Influence of Polymer Solution Viscosity on DLS Analyses

Through the efforts of Albert Einstein, Marian Smoluchowski, William Sutherland and George Stokes in the early parts of the 20th century, the famous and often referred to "Stokes–Einstein" equation was developed.[132–134] This equation links the R_h with the diffusion coefficient D for spherical particles in solution with respect to solution temperature T and solution viscosity η according to equation (24).

$$R_\mathrm{h} = \frac{k_\mathrm{B} T}{6\pi\, \eta\, D} \tag{24}$$

Exactly this mathematical relation is being applied when the obtained experimental data from DLS measurements are being transferred into R_h-values (the theory behind the quantification of the diffusion coefficient D is not part of this work and it is thus referred to a more detailed textbook).[31] It becomes evident that for a conversion of D into R_h also the temperature and the viscosity of the solution have to be as accurate as possible. While the former quantity is usually easily accessible through high-precision thermostats, the viscosity is not as straight forward. Especially in temperature-dependent DLS measurements which facilitate the observation of the R_h-evolution with temperature, the exact η-values are required. While databases usually provide the viscosity-values for most pure solvents, things are not as clear with cosolvent mixtures.

In this work, for instance, the UCST-type PTs of PMAAm in different water/ethanol mixtures were investigated. Fortunately, Khattab *et al.* published viscosity-values of certain water/ethanol mixtures.[135] The widespread empirical correlation of a solvent viscosity with temperature by a two-parameter exponential thus allowed for fitting of the solvent mixtures' literature data (see section 10.5.2, Appendix).[136] However, the accuracy of these literature data may be questionable: if, for instance, their published dynamic viscosities of a water/ethanol mixture (83/17, *w*/*w*) are plotted versus the temperature (see graph A of Figure 46), it becomes apparent that the two data points at higher temperatures deviate from the expected exponential decrease. At this point, the decision whether these points will be included in the viscosity-predicting fit has to be made. As indicated by graph A of Figure 46, the resulting two fits are rather different and should deviate even more strongly upon extrapolation. In order to see if this fit-deviation can cause error for investigations of macroscopic PTs, graph B shows an exemplary macroscopic UCST-type PT of a thermoresponsive homopolymer (similar to the studies of section 5.2.3). Herein, the colored circles (blue circles denote the cooling and red symbols the reheating process) stem from Fit 1 while Fit 2 leads to the R_h-values which are illustrated by white circles. Apparently, the systematical error of the literature viscosity-values does not lead to significant error when investigating macroscopic PTs which occur rapidly within a narrow temperature-interval.

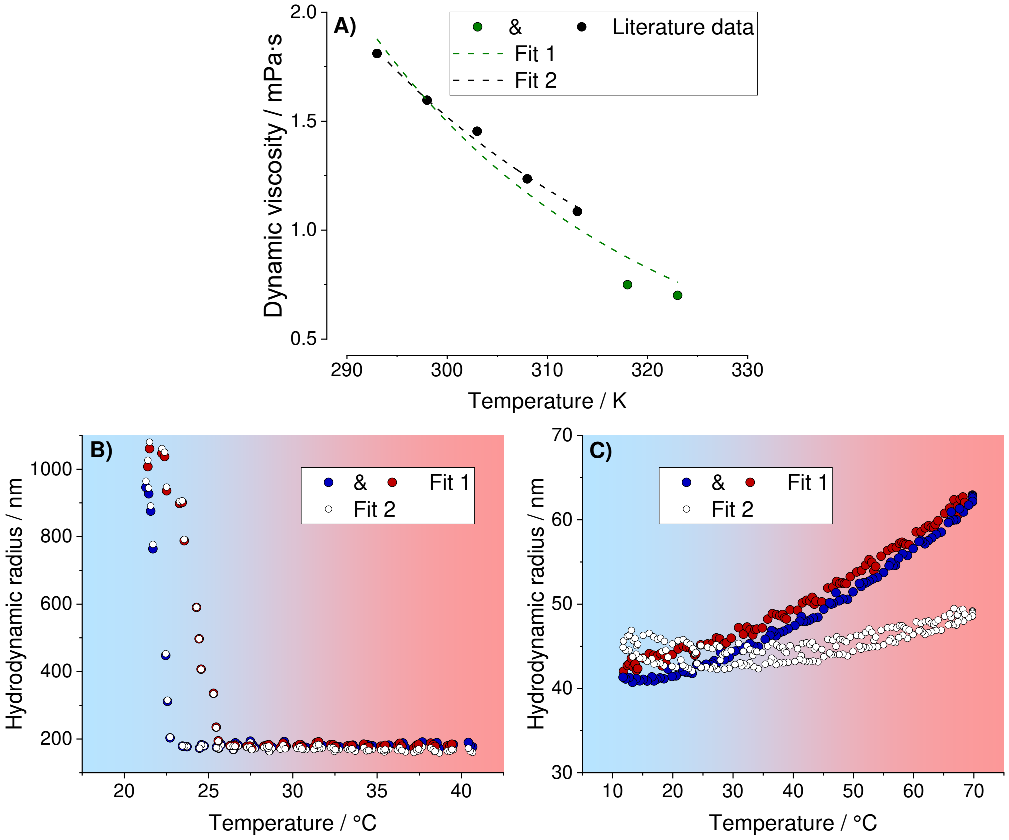

Figure 46: Graph A) Experimental temperature-dependent viscosity data of a water/ethanol mixture (83/17,w/*w*) taken from literature.[135] The two data points at higher temperature (green circles) appear to deviate from the expected exponential decrease of viscosity versus temperature. Depending on their fit-in- or exclusion, the resulting predicted viscosity values can show strong deviations – particularly upon extrapolation. Graph B) When observing an (exemplary) macroscopic PT which occurs rapidly within a narrow temperature-interval, the difference resulting from viscosity prediction *via* Fit 1 (colored circles) or Fit 2 (white circles) are negligible. Graph C) When examining (exemplary) thermosensitive solution behavior, the choice of either Fit 1 or Fit 2 might lead to wholly different interpretation of the obtained results.

If, however, no distinct PT of a thermoresponsive homopolymer, but thermosensitive behavior of block copolymers which typically only shows slight and gradual R_h-changes over a broad temperature range is investigated, things can look very different: graph C of Figure 46 shows an exemplary measurement of a thermosensitive block copolymer which shows a gradual, yet reversible, particle-shrinkage upon cooling (colored circles) when the value of R_h is determined *via* the viscosities predicted by Fit 1. When, in contrast, Fit 2 is applied, the R_h-evolution of both heating and cooling cycle (white symbols) will lead to a wholly different interpretation of the obtained results. Apparently, trustworthy investigations of thermosensitive behavior in cosolvent mixtures *via* DLS require particularly precise estimations of the solvent viscosity.

As a consequence, own viscosity measurements were conducted using a rheometer. Herein, a Couette element was used for rotational sheer dependent viscosity measurements (see section 8.3.4) at different temperatures for different water/ethanol mixtures. These measurements were conducted from 10 °C up to 70 °C in 5 °C-steps. At each temperature step, the viscosity was measured with different shear rates (100–500 s^{-1}) as is exemplarily displayed for a water/ethanol mixture (83/17, *w*/*w*) in Graph A of Figure 47. Within the observed shear rate interval, the mixture appears to be ideally viscous at low (blue circles) and at high (red circles) temperatures as all viscosity courses are parallel to the x-axis. The resulting experimental viscosity values for each temperature step are determined by averaging all viscosity values within a shear rate interval in which the liquid behaves as Newtonian (constant viscosities are obtained). Graph B shows the viscosity versus temperature of the same water/ethanol mixture (83/17, *w*/*w*). The same measurement was repeated with another water/ethanol mixture (92/8, *w*/*w*, Graph C). Both data sets allow for much more precise fitting producing superiorly reliable viscosity parameters (which are provided for both mixtures and will be used for viscosity predictions in the following). The high accuracy of this measurement is underlined by graph D which compares the obtained experimental viscosity data (black circles) from viscosity measurements of pure water (Milli-Q quality) with literature data.[137] The accuracy (never higher than (± 0.01 mPa·s) is, in fact, remarkable underlining the trustworthiness of the fit predictions.

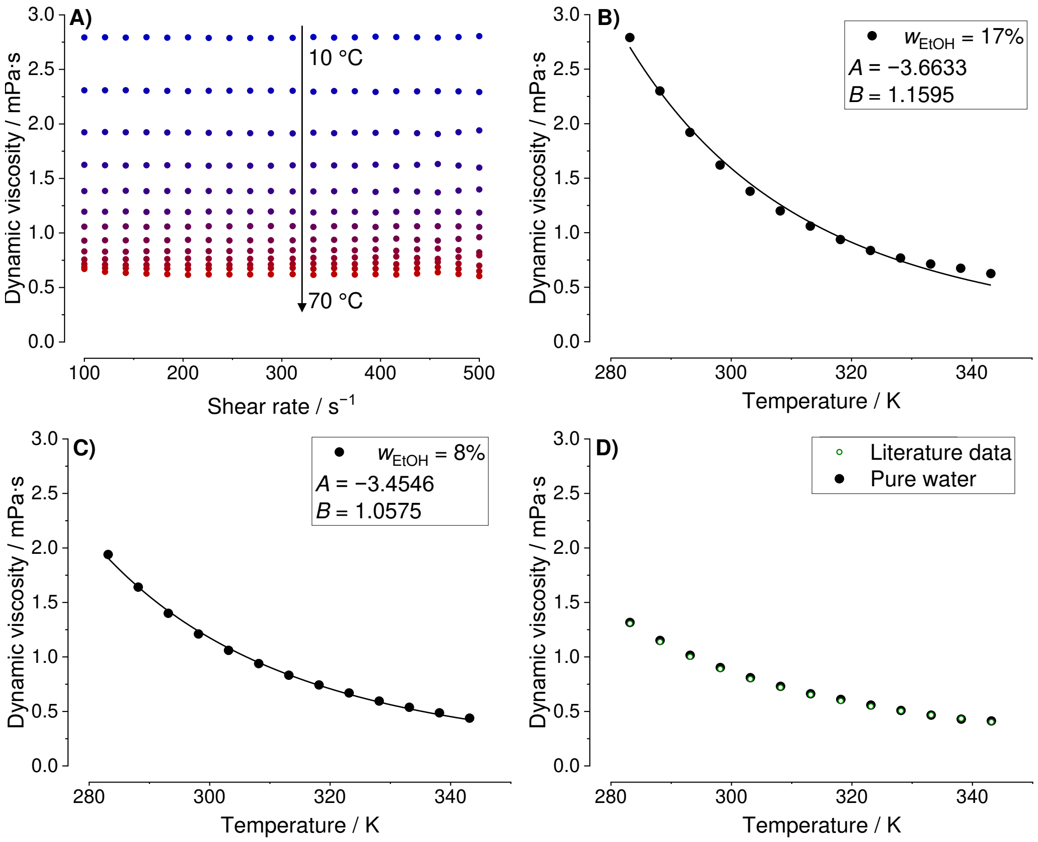

Figure 47: Graph A) Obtained viscosity-values of a water/ethanol mixture (83/17, *w*/*w*) versus different shear rates for different temperatures (10 °C to 70 °C, 5 °C-steps). The increasing temperature is indicated by the color gradient from blue (cold) to red (warm). Graph B) Viscosity average derived from constant viscosity-shear-rate-intervals for each temperature of a water/ethanol mixture (83/17, *w*/*w*) as well as the fit-derived viscosity parameters A and B. Graph C) Viscosity averages of a water/ethanol mixture (92/8, *w*/*w*) versus the temperature as well as the fit-derived viscosity parameters A and B. Graph D) Viscosity averages (black circles) of pure water (Milli-Q quality) versus the temperature. The measurement seems to facilitate great accuracy as is indicated by the conformance with the literature data (green, unfilled circles).[137]

The next section will present the results from temperature-dependent DLS analysis of the solution behavior of PMAAm-*b*-PMMA in two different water/ethanol mixtures (83/17 and 92/8, *w*/*w*) using the newly generated fits as viscosity predictors.

7.3.3 Solution Behavior of PMAAm-*b*-PMMA-Dispersions in Water/Ethanol Mixutures

The three PMAAm-*b*-PMMA-dispersions listed in Table 15 were suspended in the two water/ethanol mixtures (92/8 and 83/17, *w*/*w*) and thoroughly investigated *via* DLS. Herein, not only the influence of the content of non-solvent (ethanol) was investigated but also the influence of particle concentration by diluting the dispersion to PMAAm weight contents of 0.01 wt% and 0.001 wt% (dilution procedure is shown in section 8.3.3.1). Since RAFT dispersion polymerizations were all conducted at low solid concentrations ($w_s = 5$ %, see Table 15) formation of spherical micelles is likely. Future investigations via image generating transmission electron microscopy might, nonetheless, be highly interesting.[138]

Through temperature-dependent DLS measurements, potential UCST-type solution behavior of the self-assembled particles can be monitored. Figure 48 plots the R_h-evolutions of the PMAAm$^{12.0}$-*b*-PMMA$^{82.0}$-dispersion upon cooling from 70 °C to approximately 10 °C (blue circles) and reheating back to 70 °C (red symbols) depending on the ethanol weight content and the weight fraction of the PMAAm block. When looking at graph A, the observed solution behavior of the 0.01 wt% dispersion containing 8 wt% ethanol is rather remarkable: in contrast to the distinct and macroscopic PT of the thermoresponsive PMAAm-homopolymer (see section 5.2.3), the self-assembled particles with the stabilizing PMAAm-blocks appear to rather show a thermosensitive behavior. Upon cooling of the 70 °C solution, the R_h of the particles first decreases from around 67 nm to 53 nm (at 20–25 °C) before increasing to approximately 57 nm again. Apparently, at such low temperatures (approximately 10 °C) no equilibrated state could be obtained sufficiently quick as indicated by the hysteresis upon reheating which yields a rather unique “Swoosh”-shaped evolution. Further dilution of the dispersion to a PMAAm weight content of 0.001 wt% while keeping the ethanol weight fraction constant (graph B) results in a congruent evolution. In contrast to the PMAAm-homopolymer, the thermosensitive UCST-type solution behavior of the self-assembled particles seems to be unaffected by the particle concentration. This observation is, in fact, less surprising since the effective, local concentration of the particle-stabilizing PMAAm chains will not be affected if the particle concentration in the analyzed dispersion is changed (as long as the concentration stays above the critical micelle concentration).

Elevation of the ethanol weight fraction to 17 wt%, once again, produces highly similar shapes which are illustrated in graphs C and D (note that these R_h-values are computed with viscosity-predictions derived from another fit). The higher ethanol concentrations seem to lead to a minor contraction of the particles as implied by overall slightly lower R_h-values. Additionally, it appears that the obtained thermosensitivity is slightly more pronounced at higher ethanol contents as indicated by stronger R_h-growth upon cooling from 30 °C to 10 °C.

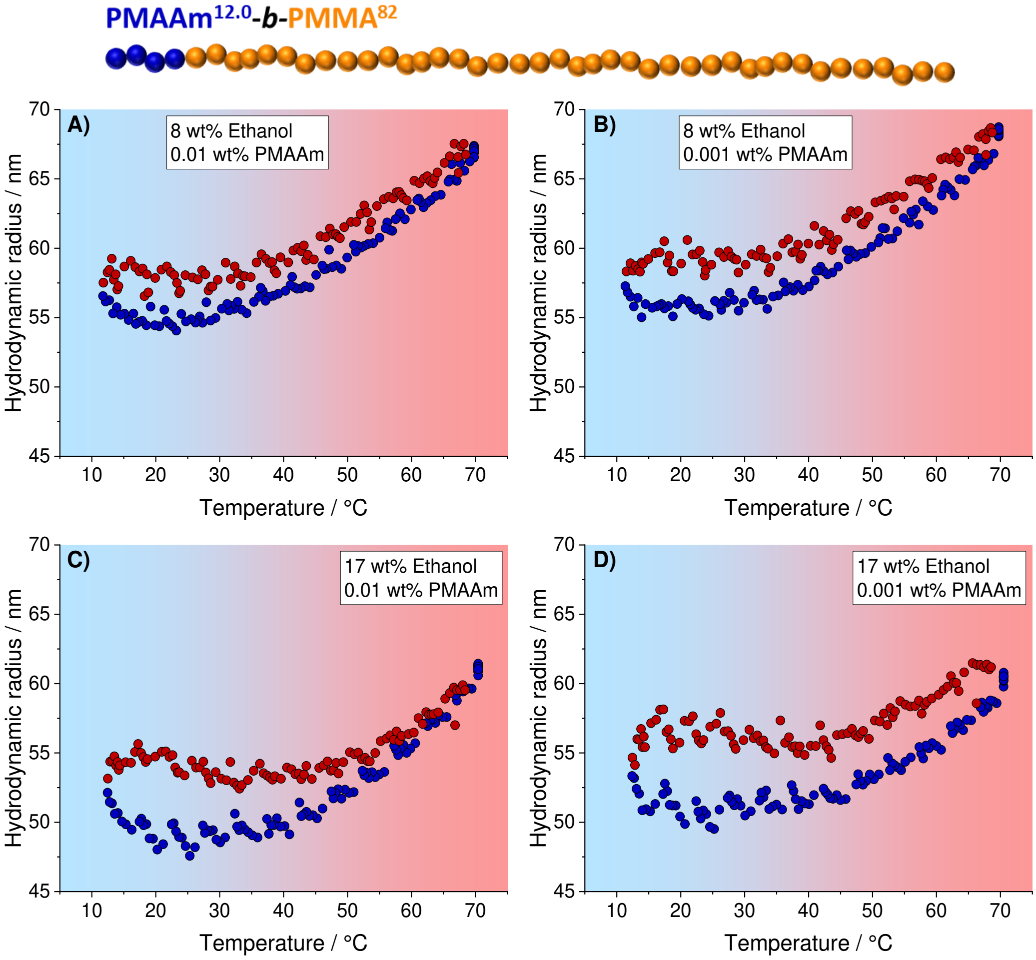

Figure 48: Temperature-dependent R_h-evolutions of PMAAm$^{12.0}$-*b*-PMMA$^{82.0}$-dispersions with different weight fractions of the PMAAm block and different ethanol weight content. The temperature-dependent DLS measurements were started at 70 °C and cooled down to approximately 10 °C (blue circles). Afterwards, the solution was reheated to 70 °C (red circles). The intensity correlation function implies only one particle species. The colored background indicates the temperature transition from high (red) to low (blue) and serves as a guide to the eye.

Undoubtedly, this “Swoosh”-shaped solution behavior is quite remarkable. A possible explanation approach is illustrated in Figure 49: heating of the particles – most likely micelles – at the local R_h-minimum at around 20−30 °C will lead to increased solubility of the particle-stabilizing PMAAm-blocks and thus a swelling with H_2O-molecules. This UCST-type swelling appears gradual as the effective, local concentration of the stabilizing PMAAm-blocks is not constant due to the inevitability of particle curvature. Similar, yet reversed, solution behavior was already obtained for thermosensitive LCST-type diblock copolymers.[66,139]

The second R_h-increase, this time upon cooling, might be similar to typical macroscopic UCST-type PTs: strong HB between the PMAAm side groups lead to formation of bigger aggregates. In contrast to the homopolymer, however, this aggregation does not lead to macroscopic phase separation into large, precipitating agglomerates. In fact, only small aggregates seem to be formed and, apparently, not every dispersed particle participates in such coalitions. While this might answer the question why the particles show an R_h-increase upon cooling from approximately 30 °C to 10 °C, it certainly provides no sufficient explanation for another question: why does the particle aggregation stop and why are no larger, precipitating agglomerates formed? A possible explanation for a similar phenomenon was already established by Xu *et al.*[140] If, as in the examined system, the outer chain ends of the stabilizing block all carry a carboxylic group from the original leaving group radical (red circles in Figure 49), the steric hindrance of bulky carboxyl hydration shells as well as strong repulsive forces between a minor fraction of carboxylate-groups can impede formation of larger aggregates.

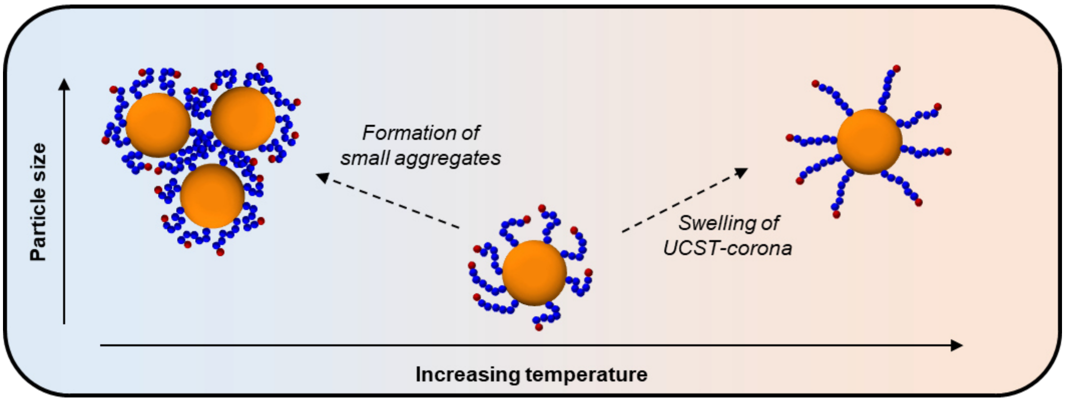

Figure 49: Explanatory approach for the observed “Swoosh”-shaped solution behavior of PMAAm-*b*-PMMA-dispersions. The PMMA-core (orange sphere) of the particles is stabilized by the PMAAm-blocks (blue chains) which carry a carboxyl group (red sphere) at their chain ends.

Analogous DLS investigations were performed for different dispersions of PMAAm$^{12.0}$-*b*-PMMA$^{17.5}$. The respective R_h-evolutions are shown in Figure 50. The observed peculiar solution behavior and trends remain the same. Due to the notedly shorter PMMA-block, however, the observed particles – presumably micelles – are smaller with the R_h-values being slightly lower (approximately 2–5 nm) compared to the particles of the PMAAm$^{12.0}$-*b*-PMMA$^{82.0}$-dispersions (the courses are shifted “downwards” to slightly lower R_h-values).

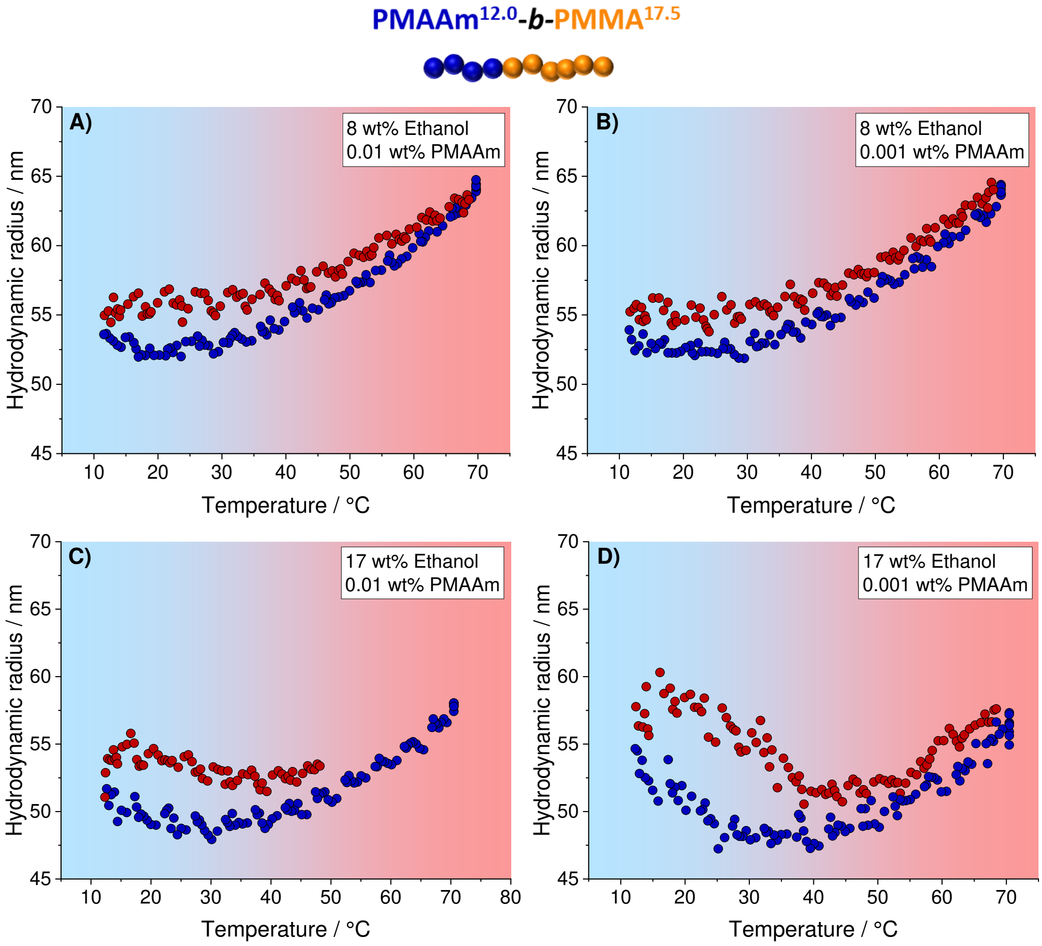

Figure 50: Temperature-dependent R_h-evolutions of PMAAm$^{12.0}$-*b*-PMMA$^{17.5}$-dispersions with varying weight fractions of the PMAAm block and ethanol. The measurements were started at 70 °C and cooled down to approximately 10 °C (blue circles). Then, the solution was reheated to 70 °C (red circles). The intensity correlation function implies only one particle species. The colored background indicates the temperature transition from high (red) to low (blue) and serves as a guide to the eye.

A more drastic difference is observed for the PMAAm$^{12.0}$-*b*-PMMA$^{37.7}$-dispersions (respective R_h-evolutions are displayed in Figure 51): compared with the dispersions in Figure 49 and Figure 50, the observed R_h-values are around twice as high reaching values above 100 nm. This will, most likely, be due to the elevated polymerization temperature – PMAAm$^{12.0}$-*b*-PMMA$^{37.7}$ was synthesized at 80 °C instead of 60 °C (see Table 15) – which constituted the only major synthetic deviation from the other two diblock copolymers. As the cosolvent ethanol is a potential plasticizer for PMMA, it seems plausible that 80 °C might lie above the PMMA-block glass transition temperature. This way, instead of a glassy and rigid core which impedes particle fusion, a softer core with more mobile chains could potentially allow for transition from spherical micelles into worm-like structures or even vesicles.[141] It has to me mentioned, however, that investigations *via* transmission electron microscopy will need to be conducted in order to prove these rather speculative explanation approaches.

Regardless of the morphology, however, it is remarkable that the particles of the PMAAm$^{12.0}$-*b*-PMMA$^{37.7}$-dispersions show almost congruent R_h-courses as the other two diblock copolymer dispersions which consist of notedly smaller particles. As the density of the stabilizing particle shell increases with core size (due to lowering curvature), this congruence is, in fact, rather striking. Apparently, the curvature-dependent shell density – which can be understood as a form of confinement – exerts no significant influence on the overall solution behavior of the PMAAm (shell forming) block. Although it may be too early to jump to conclusions for potential membrane applications, it might be a first hint that UCST-type thermoresponsive behavior of a pore forming block could – under the right circumstances – be unaffected by the pore sizes. Despite the fact this work found diblock copolymers with PMAAm unsuitable for membrane preparation, these results might be first evidences for the potential of alternative UCST polymers for future application in “smart” membranes.

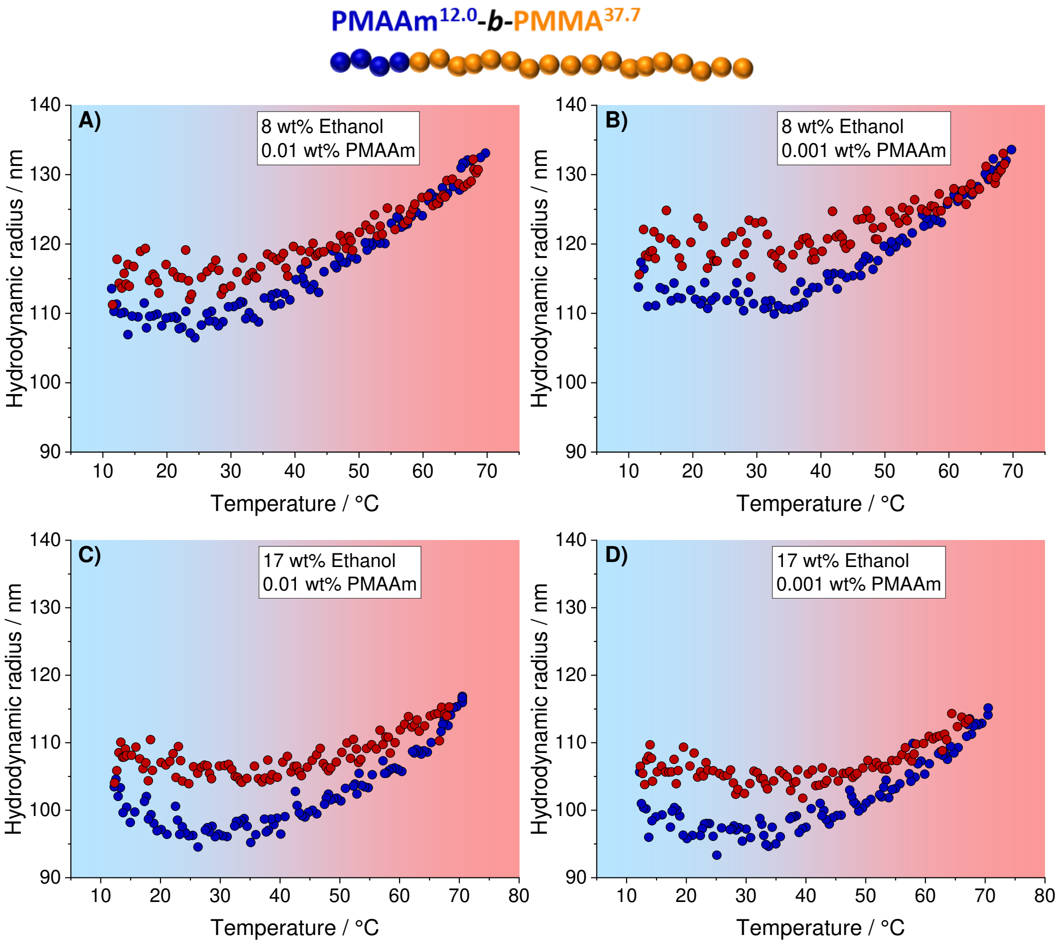

Figure 51: Temperature-dependent R_h-evolutions of PMAAm$^{12.0}$-*b*-PMMA$^{37.7}$-dispersions with varying weight fractions ethanol and different PMAAm-block-weight content. The temperature-series were started at 70 °C and cooled down to around 10 °C (blue circles). Subsequently, the solutions were reheated to 70 °C (red circles). The colored background indicates the temperature transition from high (red) to low (blue) and serves as a guide to the eye.

7.4 Conclusion

Clearly, chain extension of the UCST polymer PMAAm is accompanied by certain difficulties. Without exception, chain extension of PMAAm led to diblock copolymers that could – once isolated – not fully be redissolved in any solvent which impeded characterization *via* SEC. Unfortunately, this also applies for the diblock copolymers PMAAm-*b*-PS and PMAAm-*b*-PMMA. The author must hence conclude that membrane preparation via *conventional* routes – which necessitates complete solution of the whole polymer – will most likely not be feasible utilizing PMAAm when a majority component block such as PS or PMMA is required.

Nonetheless, the PMAAm-*b*-PMMA-dispersions obtained from surfactant-free RAFT dispersion polymerization allowed for several other conclusions concerning UCST-type solution behavior. In contrast to the distinct and macroscopic UCST-type PT of PMAAm homopolymers observed in water/ethanol mixtures, the dispersed particles of PMAAm-*b*-PMMA show only small and gradual temperature-induced R_h-growth upon cooling. Larger, macroscopic and precipitating agglomerates are never formed, most likely due to repulsion of the carboxylic end groups of the particle-stabilizing PMAAm blocks. In fact, due to UCST-type swelling of the PMAAm-shell, the thermosensitive particles showed a rather unique “Swoosh”-type solution behavior. Despite having an impact on the shell-density, the particle size does not affect the PMAAm-shell’s thermoresponse – the observed R_h-courses are almost congruent. Future investigations of the influence of PMAAm block length and polymerization temperature accompanied by in-depth analysis via transmission electron microscopy might provide further insights into the peculiar UCST-type solution behavior.

Although PMAAm itself will, most likely, not be successfully applied as a pore-forming, “smart” block in a membrane, these results suggests that UCST-“smartness” polymers might potentially constitute promising alternatives to LCST-polymers in the future.

8 Experimental Section

8.1 Materials

The RAFT agents CTCA and CPDT (Sigma Aldrich, 95 %) were stored at 4 °C and used as received. CTCPA was synthesized according to the published synthesis from McCormick and stored at the same temperature.[142] The applied solvents water (Milli-Q quality, resistivity > 18.2M Ωcm^{-1}), acetone (Sigma Aldrich, 99.5 %), DMF (VWR, GPR Rectapure, 99.5 %), DMSO (Grüssing, 99.5 %), ethanol (VWR, 99.8 %), methanol (Acros Organics, 99.9 %), dichloromethane (Acros Organics, 99.9 %, anhydrous), diethyl ether (Sigma Alrich, ≥ 99.7 %, anhydrous) were stored at room temperature. MAAm was dried *in vacuo* for 24 h and stored under nitrogen atmosphere. Styrene (Sigma Aldrich, ≥ 99 %, contains 4-*tert*-butylcatechol as stabilizier) and MMA (Sigma Aldrich, 99 %, contains ≥ 30 ppm monomethyl ether hydroquinone as inhibitor) were filtered over a column of basic alumina (Brockmann I, Sigma Aldrich, ≥ 98 %) prior to use. The chemicals glycinamide hydrochloride (Sigma Aldrich, 98 %), acryloyl chloride (ABCR, 96 %, contains phenothiazine as stabilizer) and ACVA (Sigma Aldrich, ≥ 98 %) were stored at 4 °C and used as received.

8.2 Syntheses

8.2.1 Synthesis of NAGA

The synthesis of NAGA was adapted from Agarwal *et al.* and slightly altered:[42]

Potassium carbonate (32.5 g, 226 mmol, 2.0 eq) and glycinamide hydrochloride (12.5 g, 113 mmol, 1.0 eq) were dissolved in ultrapure water (66 mL, Milli-Q quality, resistivity > 18.2M Ωcm^{-1}) and cooled to 0 °C. Subsequently, a solution of acryloyl chloride (9.22 mL, 113 mmol, 1.0 eq) and diethylether (130 mL) were added dropwise over a period of 30 min while stirring vigorously. The turbid suspension was then stirred at room temperature for 2 h. In the next step, the diethylether and water were removed by rotary evaporation at 40 °C. The crude product was then extracted by four stirring cycles with warm acetone (40 °C, 250 mL, 10 min stirring). The combined organic phases were filtered and the acetone was removed by rotary evaporation. Afterwards, the white crude product was dissolved in the minimal required amount of methanol and dichloromethane (1/4, *v*/*v*) and filtered over a short column chromatography ($d = 6$ cm, 200 g of silica, porosity 60 Angström, 0.063–0.2 mm mesh size, R_f (NAGA) = 0.40, potassium salts and potassium acrylate remain on column). The organic solvents were removed by rotary evaporation at 40 °C and the crude product was suspended with methanol (100 mL) and heated to reflux once. The hot slightly turbid suspension was quickly passed through a preheated filter and the NAGA was recrystallized by tempering the completely clear and homogenous solution to −30 °C overnight. The highly pure, colorless and elongated NAGA crystals were filtrated, washed with −30 °C cold methanol and dried in vacuum overnight. In combination with a second recrystallization crop, 10.4 g of NAGA were obtained (71.8 % yield).

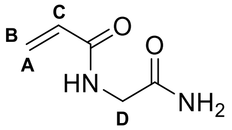

Melting point from DSC (heating- and cooling rate: 10 K min^{-1}): 144 °C. ^{1}H NMR (500 MHz, DMSO): δ / ppm = 6.31 (dd, 1H, H_A), 6.09 (dd, 1H, H_B), 5.59 (dd, 1H, H_C), 3.72 (d, 2H, H_D).

8.2.2 RAFT Polymerizations

For optimal reproducibility of RAFT polymerizations, this work specifies the reactant concentrations of the conducted polymerizations in weight percentages of the reaction solution. R_M, R_I and w_s fully suffice for unambiguous specification of the reaction solution. The weight content of the solids (monomer, RAFT agent and initiator) w_s precludes the internal standard which typically amounted to an extra 5 wt% of the whole reaction solution.

Unless explicitly stated otherwise, the RAFT polymerizations were performed in 10 mL screw-capped glass vials (LabSolute, 12 mL) sealed with bored polypropylene caps and butyl/polytetrafluoroethylene septa (LabSolute, ND15, 1.6 mm).

8.2.2.1 Photoiniferter RAFT Polymerization of NAGA

A typical photoiniferter RAFT solution homopolymerization of NAGA was carried out as follows:

A solution of NAGA (1.11 g, 8.67 mmol, $R_M = 100$), CPDT (30.0 mg, 86.8 µmol), DMF (285 mg, 5 wt% of whole reaction solution) and DMSO (4.56 g) was prepared and homogenized ($R_M = 100$, $w_s = 20$ wt%). A small sample was removed for NMR referencing. The solution was then purged with N_2 for 10 min at room temperature and heated to 70 °C. The solution was then irradiated with an LED-light source (445 nm, 1.4 mW cm^{-2}, intensity measured with a S120UV photodiode sensor head by Thorlabs) and stirred vigorously. After 85 min, the homopolymerization was quenched by turning off the light source, rapid cooling the reaction solution to 0 °C and exposure to oxygen. Another sample was removed for NMR analysis. Subsequently, the solution was precipitated in ice-cold methanol (100 mL), filtered and dried in vacuum. The polymer solid was again dissolved in 5 mL DMSO and the precipitation procedure was repeated. PNAGA$^{7.89}$ was obtained as a yellow, vitreous solid. $p = 59$ %, $\overline{M}_{\mathrm{n,th}} = 7.89$ kDa, $\overline{M}_{\mathrm{n,app}} = 15.0$ kDa (PMMA calibration), $Đ = 1.23$.

^{1}H NMR (500 MHz, DMSO): δ / ppm = 8.90–6.80 (m, $\mathrm{H_{A+A'}}$), 4.20–3.10 (m, $\mathrm{H_B}$), 2.30–1.75 (m, $\mathrm{H_C}$), 1.75–0.95 (m, $\mathrm{H_D}$); 0.89 (t, 3H, $\mathrm{H_E}$)^{1}H NMR spectrum displayed in the Appendix, Figure A3.

8.2.2.2 Photoiniferter RAFT Polymerization of MAAm

A typical photoiniferter RAFT polymerization of MAAm – which were all performed with a w_s of 15 wt% – with an exemplary R_M-value of 400 was conducted as follows:

MAAm (1.11 g, 13.0 mmol, $R_M = 400$), CTCA (10.0 mg, 34.8 µmol) and the internal standard DMF (0.155 g, for conversion determination) were dissolved in Milli-Q water (6.32 mL). A small sample was removed after homogenization for NMR referencing and the reaction solution was purged by bubbling with nitrogen for 15 min at 0 °C. Then, the reaction solution was vividly stirred (approximately 600 rpm) and heated to 70 °C. Initiation was achieved by irradiation with a 365 nm lamp of a Herolab UV – 15S/L (0.38 mW cm^{-2}; light intensity was successfully measured and pre-set with a S120UV photodiode sensor head by Thorlabs). The polymerization was quenched after 300 min by rapid cooling to 0 °C and exposure to air. Another sample was taken for NMR analysis and the solution was precipitated dropwise in 600 mL of ice-cold acetone. The precipitate was filtrated and dried *in vacuo* for 24 h at room temperature. This precipitation procedure was repeated twice in order to ensure quantitative removal of residual monomer. PMAAm was obtained as a yellowish powder. Monomer conversion = 49.5 %. Theoretical number average molecular weight ($\overline{M}_{\mathrm{n,th}}$) = 16.0 kDa. SEC: $\overline{M}_{\mathrm{n,app}}$ = 6.39 kDa (calibration with PEG), $Đ$ = 1.18.

8.2.2.3 Thermal RAFT Polymerization of MAAm

The thermal RAFT polymerization of MAAm was performed with a fixed solvent mass of 3.000 g of H_2O (Milli-Q quality). A typical exemplary polymerization (R_M = 350, R_I = 0.0625, w_s = 15 wt%) was conducted as follows:

MAAm (533 mg, 6.26 mmol, R_M = 350) and CTCA (5.6 mg, 18 µmol) were dissolved in water (Milli-Q quality). ACVA (31 µg, 1.12 µmol, R_I = 0.0625) was supplemented *via* Eppendorf Multipette E3 which transferred the required volume from an ACVA solution (10.0 mg mL^{-1}) in DMF into the mixture. Since DMF serves as internal standard for determination of the monomer conversion *via* ^{1}H NMR spectroscopy, more DMF was added to facilitate a 5 wt% DMF content (in terms of total mass of the final reaction mixture). Subsequently, the mixture was homogenized by stirring vigorously and a small sample was removed for NMR referencing. As neither the MAAm nor the DMF signal are affected by subsequent N_2-bubbling solution purging by N_2-bubbling for 10 min at 0 °C could easily be conducted after sample removal. The reaction solution was stirred (600 rpm) at a polymerization temperature of 80 °C for 260 min and was quenched by rapid cooling to 0 °C and exposure to air. Another sample was taken for NMR analysis and the solution was precipitated by dropwise addition into 60 mL of ice-cold acetone. The precipitate was filtrated and dried *in vacuo* for 24 h at room temperature. PMAAm was obtained as a yellowish powder.

Monomer conversion = 42.7 %. Theoretical number average molecular weight ($\overline{M}_{\mathrm{n,th}}$) = 12.8 kDa. SEC: $\overline{M}_{\mathrm{n,app}}$ = 6.20 kDa (calibration with PEG), $Đ$ = 1.18.

8.2.2.4 RAFT Emulsion Polymerization of PMAAm-*b*-PS

A typical surfactant-free photoiniferter RAFT emulsion polymerization of styrene for the synthesis of PMAAm-*b*-PS was conducted as follows (T = 80 °C, t = 300 min °C, R_M = 1000 °C and w_s = 10 wt%):

PMAAm$^{12.0}$ (17.9 mg, 1.49 µmol) was dissolved in 1.0 g of Milli-Q water. Then, styrene (171 µL, 1.49 mmol, R_M = 1000) and the internal standard DMF (91.8 µL) were added to the solution. The heterogenous mixture was vigorously shaken, the screw-cap was removed and a reference NMR-sample was taken quickly by Pasteur pipette (the sample was then flushed directly into an NMR tube with deuterated

DMSO). Subsequently, the mixture was tempered to 0 °C and purged with N_2 for 5 min. Then, the reaction solution was vividly stirred (1000 rpm) and heated to 80 °C. Initiation was achieved *via* irradiation with a UV-LED lamp (OmniCure AC450, emission maximum at 384 nm, 10 mW cm^{-2}, light intensity was with an S120UV photodiode sensor head by Thorlabs). The polymerization was quenched after 300 min by rapid cooling to 0 °C and exposure to air and another NMR sample was taken for the determination of the styrene conversion. Monomer conversion = 76.2 %.

8.2.2.5 RAFT Dispersion Polymerization of PMAAm-*b*-PMMA

The surfactant-free photoiniferter RAFT dispersion polymerizations of MMA for the synthesis of PMAAm-*b*-PMMA were conducted in a cosolvent mixture of water and ethanol (75/25, *w*/*w*, T = 60 °C, t = 62 min °C, R_M = 400 °C and w_s = 5 wt%. A typical polymerization was performed as follows:

PMAAm$^{12.0}$ (38.5.0 mg, 3.21 µmol) was dissolved in 2.37 g of Milli-Q water. Then, ethanol (793 mg) and MMA (0.128 g, 1.28 mmol, R_M = 400) and the internal standard DMF (0.0830 g) were added to the solution. After homogenization, a small sample was removed for NMR referencing. Then, the reaction solution was purged by bubbling with nitrogen for 10 min at 0 °C. Subsequently, the reaction solution was vividly stirred (approximately 600 rpm) and heated to 60 °C. Initiation was achieved by irradiation with a 365 nm lamp of a Herolab UV – 15S/L (0.38 mW cm^{-2}; light intensity was with a S120UV photodiode sensor head by Thorlabs). The polymerization was quenched after 62 min by rapid cooling to 0 °C and exposure to air and another sample was taken for NMR analysis. Monomer conversion = 43.8 %.

8.3 Analytics

8.3.1 Nuclear Magnetic Resonance Spectroscopy

^{1}H NMR measurements were performed with a Bruker AVANCE I 500 MHz spectrometer. Spectra were recorded at a temperature of 300 K with 64 scans per spectrum and a delay of three seconds.

The sample concentration was approximately 10 mg mL^{-1} for all measurements. In order to determine the monomer conversion DMF was typically added as internal standard and the DMF/monomer integral ratios before the polymerization and at a given polymerization time were compared (see Figure A1 as well as equations (A1) and (A2) in section 10.1 of the Appendix). Deuterium oxide (D_2O) was used as solvent for the RAFT homopolymerizations of MAAm. DMSO-*d*6 was utilized for RAFT homopolymerizations of NAGA as well as all heterogenous RAFT polymerizations.

8.3.2 Visual Turbidimetry

Visual turbidimetry is a highly reliable and easily feasible method for determination of the PTT. A typical visual turbidimetry for the PTT-determination of a PMAAm solution in a water/ethanol mixture (1.00 wt%, 75/25, *w*/*w*) was conducted as follows:

PMAAm (16.0 mg) was dissolved in 1180 µL of Milli-Q water under vigorous stirring. Next, 508 µL of ethanol were added to the solution which immediately turned turbid. Subsequently, it was quickly heated in a water bath until the mixture turned into a homogeneous solution. The water bath was then cooled down gradually and the temperature of the polymer solution was monitored by a Voltcraft PL-120-T1 thermometer (0.1 °C accuracy). The PTT was defined as the temperature at the first sign of turbidity upon cooling. Each measurement was repeated twice. Cooling was performed at room temperature with a rate of approximately 0.5 °C min^{-1}, while the heating rate was approximately 1 °C min^{-1}.

8.3.3 Dynamic Light Scattering

Thermoresponsive solution behavior of PMAAm in water/ethanol mixtures was analyzed *via* DLS. The measurements were performed using an ALV/CGS-3 Compact Goniometer-system with an ALV/LSE-5003 Multiple Tau Digital Correlator (V.1.5.6) in combination with a JDS Uniphase 1145/P laser (He–Ne, 632.8 nm, 22 mW) and the ALV Digital Correlator Software 3.0. A typical temperature dependent measurement was conducted as follows:

The polymer solution was prepared in a quartz glass vial (analogous to the procedure of the visual turbidimetry) and placed into a measurement cell filled with toluene which was tempered by a Julabo F25 thermostat (tempering with a water/ethylene glycol mixture enabling a temperature accuracy of 0.01 °C). Measurements could be conducted as soon as the polymer solution reached the targeted starting temperature as thermal equilibration was achieved within seconds (this can be seen in section 10.5.1, Appendix). The temperature ranges were set from approximately 10 °C above the CP (which was priorly determined *via* visual turbidimetry) to around 2–5 °C below the CP. Each measurement was performed for 60 s with six measurements per temperature step of 1 °C. The ΔT – *i.e.* the maximum temperature difference of the toluene bath to the targeted temperature, before the first of the six measurements is started – was set to 1.0 °C. This rather high value markedly shortens the heating and cooling cycles thus impeding agglomerate precipitation and, additionally, allows for high resolution of the temperature range as six different temperatures per temperature step are examined. Analysis of all measurements was conducted with a program written by Felix Lauterbach which is based on a cumulant approach up to the third order cumulant.[1] If more than one exponential decay was obtained (implying more than one particle species), the relative particle fractions were determined directly *via* the intensity autocorrelation function and are thus depending on the scattering intensity of each species. The author refers to this as unweighted quantities. The refractive indices for pure water and the different applied ethanol weight fractions were taken from reported literature tabulated values.[143]

8.3.3.1 Preparation of PMAAm-Diblock Copolymer Dispersions for DLS

Specifications of polymer weight fractions will coherently refer only to the PMAAm content: if, for example, a dispersion polymerization which contains 1.00 wt% of PMAAm as macroRAFT agent is extended with MMA or styrene, a resulting dispersion will have to be diluted with water (or water/ethanol mixture) by 1:100 (*w*/*w*, change of dispersion density is neglected) to obtain 0.01 wt% of PMAAm – independent of the second block chain length. Neglecting dead chains, this way, each diluted dispersion will contain equal number of macromolecules (the weight fraction of the whole diblock copolymer, however, will vary depending on the molecular weight of the second block).

If, in contrast, the author had chosen to refer to the weight percentage of the whole diblock copolymer, different chain lengths of PMMA or PS would necessitate different dilutions and would lead to different numbers of macromolecules.

If the PMAAm weight content of the initial, homogenous reaction solution (prior to the chain extension *via* dispersion polymerization) amounted to 1.0 wt%, a typical DLS solution of the resulting PMAAm-*b*-PMMA-dispersion in a water/ethanol mixture (92/8, *w*/*w*) with a PMAAm content of 0.01 wt% was prepared by suspending 20 µL of the dispersion in 1819 µL of water and 203 µL of ethanol.

8.3.3.2 Correction of Viscosity of Cosolvent Mixtures for Temperature-Dependent DLS Measurements

As can be taken from 10.5.2 (Appendix), where a detailed description on the correction of solvent-viscosity with temperature is provided, the software uses an exponential fit to calculate the viscosity at a given temperature based on only two values: viscosity parameter A and viscosity parameter B. Using literature viscosity-values for different mixtures of water and ethanol at different temperature, the viscosity of cosolvent mixtures can be fitted.[135] These fits were used for the R_h-determinations of the macroscopic UCST-type PTs of the PMAAm solutions presented in section 5.2.3. The thermosensitive solution behavior of the PMAAm-diblock copolymers require more accurate viscosity predictions. These were achieved by own viscosity-measurements *via* a modular compact rheometer (section 8.3.4) facilitating more accurate and trustworthy experimental viscosity-results which, in turn, allowed for more accurate fit-predictions.

8.3.4 Rheometry

The viscosity measurements were conducted *via* Couette flow measurements utilizing a rotational rheometer (MCR 502, Anton Paar GmBH, Graz, Austria) using a double gap cylinder measuring system (ISO 3219-2, DG26.7). The measured solution was tempered by a Peltier plate with 0.01 °C accuracy. Temperature-dependent viscosity measurements were conducted as follows: the measuring system was tempered to the lowest measuring temperature of 10 °C. Then, the homogenized solution (approximately 4.0 mL) was added into the gap between the walls of the measuring cylinder. As soon as the solution was tempered to the pre-set temperature of the measuring system, the measuring bob is lowered and immersed into the measuring cylinder (distance between measuring bob and cylinder was set to 0 mm). Through the extrusion of the solvent by the bob immersion, the filling level increases and starts to fill the collecting vessel on top of the inner cylinder. In order to facilitate the necessary standardized filling level, excess solvent was removed by emptying this collecting vessel *via* syringe (which was stuck through a whole on top of the measuring bob).

The first measurement was automatically started as soon as the solution was tempered within ± 0.01 °C of the desired temperature and kept within this temperature-interval for 180 s. The sheer rate was continuously increased from 100 s^{-1} to 500 s^{-1} (each shear rate-derived viscosity value was measured for 20 s at constant shear rate).

8.3.5 Size Exclusion Chromatography

SEC-analysis of PMAAm was conducted on a PSS Agilent Technologies 1260 Infinity system utilizing a SUPREMA column system consisting of a precolumn (8 mm × 50 mm, particle size: 5 µm) and three analytical columns (column 1: 8 mm× 300 mm, particle size: 5 µm, mesh size: 1000 Å; column 2: 8 mm × 300 mm, particle size: 5 µm, mesh size: 1000 Å; column 3: 8 mm × 300 mm, particle size: 5 µm, mesh size: 30 Å). All columns were always kept at a constant temperature of 50 °C. A 0.1 M $NaNO_3$ aqueous (Milli-Q quality) solution with an added 0.05 wt% NaN_3 served as eluent while concentrations of PMAAm varied between 1–2 mg mL^{-1}. The measurements were conducted at a flow rate of 1 mL min^{-1} applying an isocratic PSS SECcurity pump and ethylene glycol (20 µL per 100 mL of solvent) as internal standard. PEG was used as reference and the PSS SECcurity Differential-Refractometer-Detector was operated at 50 °C. Subsequent data analysis was performed with the software WinGPC UniChrom V8.10.

SEC-analysis of PNAGA was conducted on a PSS Agilent Technologies 1260 Infinity system utilizing a column system consisting of a precolumn (8 mm × 50 mm) and three analytical columns (column 1: 8 mm× 300 mm, mesh size: 1000 Å; column 2: 8 mm × 300 mm, mesh size: 1000 Å; column 3: 8 mm × 300 mm, mesh size: 30 Å). All columns were always kept at a constant temperature of 50 °C. A 0.1 M LiCl solution in *N*,*N*-dimethylacetamide served as eluent while concentrations of PMAAm varied between 1−2 mg mL^{-1}. The measurements were conducted at a flow rate of 0.8 mL min^{-1} applying an isocratic PSS SECcurity pump and methyl benzoate (20 µL per 100 mL of solvent) as internal standard. PMMA was used as reference and the PSS SECcurity Differential-Refractometer-Detector was operated at 50 °C. Subsequent data analysis was, again, performed with the software WinGPC UniChrom V8.10.

8.3.6 Differential Scanning Calorimetry

The DSC measurement of NAGA was conducted using a Netzsch DSC 204 F1 Phoenix and aluminum crucibles with pierced lids (V = 40 µL). The mass of NAGA inside these crucibles amounted to 3–5 mg. Three heating-cooling cycles from 80 °C to 180 °C were conducted with a heating rate of 10 °C $min^{-1}$and against empty aluminum crucibles with pierced lid as reference (baseline correction was additionally performed).

9 References

[1] F. Lauterbach, Advances in RAFT Polymerization Process Design and Analysis, University of Hamburg, **2020**.

[2] G. Vicente, A. Coteron, M. Martinez, J. Aracil, *Ind. Crops Prod.* **1998**, *8*, 29–35.

[3] V. A. Sakkas, M. A. Islam, C. Stalikas, T. A. Albanis, *J. Hazard. Mater.* **2010**, *175*, 33–44.

[4] M. Destarac, *Polym. Chem.* **2018**, *9*, 4947–4967.

[5] W. A. Braunecker, K. Matyjaszewski, *Prog. Polym. Sci.* **2007**, *32*, 93–146.

[6] G. Moad, *Polym. Chem.* **2017**, *8*, 177–219.

[7] V. Jitchum, S. Perrier, *Macromolecules* **2007**, *40*, 1408–1412.

[8] G. Moad, E. Rizzardo, S. H. Thang, *Aust. J. Chem.* **2012**, *65*, 985–1076.

[9] M. Destarac, *Polym. Rev.* **2011**, *51*, 163–187.

[10] G. Moad, *J. Polym. Sci. Part A Polym. Chem.* **2019**, *57*, 216–227.

[11] A. Favier, M. T. Charreyre, *Macromol. Rapid Commun.* **2006**, *27*, 653–692.

[12] A. Bordat, T. Boissenot, J. Nicolas, N. Tsapis, *Adv. Drug Deliv. Rev.* **2019**, *138*, 167–192.

[13] H. Wei, S. X. Cheng, X. Z. Zhang, R. X. Zhuo, *Prog. Polym. Sci.* **2009**, *34*, 893–910.

[14] M. Karimi, P. Sahandi Zangabad, A. Ghasemi, M. Amiri, M. Bahrami, H. Malekzad, H. Ghahramanzadeh Asl, Z. Mahdieh, M. Bozorgomid, A. Ghasemi, et al., *ACS Appl. Mater. Interfaces* **2016**, *8*, 21107–21133.

[15] R. M. P. da Silva, J. F. Mano, R. L. Reis, *Trends Biotechnol.* **2007**, *25*, 577–583.

[16] T. Aoki, K. Nakamura, K. Sanui, N. Ogata, A. Kikuchi, T. Okano, Y. Sakurai, *Polym. J.* **1999**, *31*, 1185.

[17] M. C. LeMieux, S. Peleshanko, K. D. Anderson, V. V. Tsukruk, *Langmuir* **2007**, *23*, 265–273.

[18] U. Farooq, L. Upadhyaya, A. Shakeel, G. Martinez, M. Semsarilar, *J. Memb. Sci.* **2020**, *611*, 118181.

[19] I. Oral, V. Abetz, *Macromol. Rapid Commun.* **2021**, *42*, 2000746.

[20] A. Rubio, G. Desnos, M. Semsarilar, *Macromol. Chem. Phys.* **2018**, *219*, 1800351.

[21] M. M. Rahman, *Macromol. Rapid Commun.* **2021**, *42*, 1–12.

[22] H. Hamedi, T. Brinkmann, *Chem. Eng. J. Adv.* **2022**, *10*, 100249.

[23] J. Seuring, S. Agarwal, *ACS Macro Lett.* **2013**, *2*, 597–600.

[24] W. Li, L. Huang, X. Ying, Y. Jian, Y. Hong, F. Hu, Y. Du, *Angew. Chemie*

2015, *127*, 3169–3174.
[25] W. Li, L. Huang, X. Ying, Y. Jian, Y. Hong, F. Hu, Y. Du, *Angew. Chem. Int. Ed.* **2015**, *54*, 3126–3131.
[26] L. Hui, S. Qin, L. Yang, *ACS Biomater. Sci. Eng.* **2016**, *2*, 2127–2132.
[27] J. Seuring, F. M. Bayer, K. Huber, S. Agarwal, *Macromolecules* **2012**, *45*, 374–384.
[28] J. Seuring, S. Agarwal, *Macromolecules* **2012**, *45*, 3910–3918.
[29] Z. Zhang, H. Li, S. Kasmi, S. Van Herck, K. Deswarte, B. N. Lambrecht, R. Hoogenboom, L. Nuhn, B. G. De Geest, *Angew. Chemie - Int. Ed.* **2019**, *58*, 7866–7872.
[30] S. Agarwal, J. Seuring, *Macromol. Rapid Commun.* **2012**, *33*, 1898–1920.
[31] P. C. Hiemenz, T. P. Lodge, *Polymer Chemistry*, CRC Press, Boca Raton, **2021**.
[32] D. N. Schulz, D. G. Peiffer, P. K. Agarwal, J. Larabee, J. J. Kaladas, L. Soni, B. Handwerker, R. T. Garner, *Polymer (Guildf).* **1986**, *27*, 1734–1742.
[33] M. B. Huglin, M. A. Radwan, *Polym. Int.* **1991**, *26*, 97–104.
[34] P. J. Flory, *J. Chem. Phys.* **1941**, *9*, 660–661.
[35] A. J. Staverman, J. H. Van Santen, *Recl. Trav. Chim. Pays-Bas* **1941**, *60*, 640.
[36] P. J. Flory, *J. Chem. Phys.* **1941**, *10*, 51.
[37] M. L. Huggins, *Ann. N. Y. Acad. Sci.* **1942**, *43*, 1.
[38] M. L. Huggins, *J. Chem. Phys.* **1941**, *9*, 440.
[39] S. Glatzel, A. Laschewsky, J. F. Lutz, *Macromolecules* **2011**, *44*, 413–415.
[40] V. Mishra, S. H. Jung, H. M. Jeong, H. Il Lee, *Polym. Chem.* **2014**, *5*, 2411–2416.
[41] Z. Xu, W. Liu, *Chem. Commun.* **2018**, *54*, 10540–10553.
[42] J. Seuring, S. Agarwal, *Macromol. Rapid Commun.* **2010**, *211*, 2109–2117.
[43] F. Liu, J. Seuring, S. Agarwal, *J. Polym. Sci. Part A-1 Polym. Chem.* **2012**, *50*, 4920–4928.
[44] J. Niskanen, H. Tenhu, *Polym. Chem.* **2017**, *8*, 220–232.
[45] J. Zhou, H. Yao, J. Ma, *Polym. Chem.* **2018**, *9*, 2532–2561.
[46] S. li Chen, P. fei Shi, W. qing Zhang, *Chinese J. Polym. Sci. (English Ed.* **2017**, *35*, 455–479.
[47] J. T. Sun, C. Y. Hong, C. Y. Pan, *Polym. Chem.* **2013**, *4*, 873–881.
[48] M. Semsarilar, V. Abetz, *Macromol. Chem. Phys.* **2021**, *222*, 2000311.
[49] S. Perrier, *Macromolecules* **2017**, *50*, 7433–7447.
[50] A. D. Jenkins, R. F. T. Stepto, P. Kratochvíl, U. W. Suter, *Pure Appl. Chem.* **1996**, *68*, 2287–2311.
[51] D. J. Keddie, *Chem. Soc. Rev.* **2014**, *43*, 496–505.
[52] G. Gody, R. Barbey, M. Danial, S. Perrier, *Polym. Chem.* **2015**, *6*, 1502–1511.

[53] P. A. J. M. De Jongh, A. Mortiboy, G. S. Sulley, M. R. Bennett, A. Anastasaki, P. Wilson, D. M. Haddleton, K. Kempe, *ACS Macro Lett.* **2016**, *5*, 321–325.

[54] A. Guinaudeau, S. Mazières, D. J. Wilson, M. Destarac, *Polym. Chem.* **2012**, *3*, 81–84.

[55] W. Bai, L. Zhang, R. Bai, G. Zhang, *Macromol. Rapid Commun.* **2008**, *29*, 562–566.

[56] Z. Liu, G. Zhang, W. Lu, Y. Huang, J. Zhang, T. Chen, *Polym. Chem.* **2015**, *6*, 6129–6132.

[57] J. Yeow, C. Boyer, *Adv. Sci.* **2017**, *4*, 1700137.

[58] S. Shanmugam, C. Boyer, *J. Am. Chem. Soc.* **2015**, *137*, 9988–9999.

[59] J. Xu, C. Fu, S. Shanmugam, C. J. Hawker, G. Moad, C. Boyer, *Angew. Chemie* **2017**, *129*, 8496–8503.

[60] J. Xu, K. Jung, A. Atme, S. Shanmugam, C. Boyer, *J. Am. Chem. Soc.* **2014**, *136*, 5508–5519.

[61] F. Lorandi, M. Fantin, S. Shanmugam, Y. Wang, A. A. Isse, A. Gennaro, K. Matyjaszewski, *Macromolecules* **2019**, *52*, 1479–1488.

[62] Y. Wang, M. Fantin, S. Park, E. Gottlieb, L. Fu, K. Matyjaszewski, *Macromolecules* **2017**, *50*, 7872–7879.

[63] M. Hartlieb, *Macromol. Rapid Commun.* **2022**, *43*, 2100514.

[64] T. Otsu, M. Yoshida, *Die Makromol. Chemie. Rapid Commun.* **1982**, *3*, 127–132.

[65] K. Jung, C. Boyer, P. B. Zetterlund, *Polym. Chem.* **2017**, *8*, 3965–3970.

[66] F. Lauterbach, V. Abetz, *Soft Matter* **2020**, *16*, 2321.

[67] F. Lauterbach, M. Rubens, V. Abetz, T. Junkers, *Angew. Chemie - Int. Ed.* **2018**, *57*, 14260–14264.

[68] J. Xu, V. Abetz, *Macromol. Rapid Commun.* **2021**, *42*, DOI 10.1002/marc.202000648.

[69] T. Eckert, V. Abetz, *J. Polym. Sci.* **2020**, *58*, 3050–3060.

[70] C. Barner-Kowollik, *Handbook of RAFT Polymerization*, Wiley, Weinheim, **2008**.

[71] F. Huo, X. Wang, Y. Zhang, X. Zhang, J. Xu, W. Zhang, *Macromol. Chem. Phys.* **2013**, *214*, 902–911.

[72] F. D'Agosto, J. Rieger, M. Lansalot, *Angew. Chemie - Int. Ed.* **2020**, *59*, 8368–8392.

[73] R. G. Gilbert, S. W. Prescott, W. Smulders, M. J. Monteiro, M. J. Ballard, E. Rizzardo, *Am. Chem. Soc. Polym. Prepr. Div. Polym. Chem.* **2002**, *43*, 130–131.

[74] J. K. Oh, *J. Polym. Sci. Part A Polym. Chem.* **2008**, *46*, 6983.

[75] X. Wang, Z. An, *Macromol. Rapid Commun.* **2019**, *40*, 1800325.

[76] I. A. Maxwell, B. R. Morrison, D. H. Napper, R. G. Gilbert, *Macromolecules* **1991**, *24*, 1629–1640.

[77] J. A. Selekman, J. Qiu, K. Tran, J. Stevens, V. Rosso, E. Simmons, Y. Xiao, J. Janey, *Annu. Rev. Chem. Biomol. Eng.* **2017**, *8*, 525–547.

[78] L. Ilzarbe, E. Viles, M. J. Álvarez, M. Tanco, *Qual. Reliab. Eng. Int.* **2008**, *24*, 417–428.

[79] C. Grant, A. C. da Silva Damas Pinto, H. P. Lui, J. M. Woodley, F. Baganz, *Biotechnol. Bioeng.* **2012**, *109*, 2179–2189.

[80] T. A. Shear, F. Lin, L. N. Zakharov, D. W. Johnson, *Angew. Chemie - Int. Ed.* **2020**, *59*, 1496–1500.

[81] N. R. Domagalski, B. C. Mack, J. E. Tabora, *Org. Process Res. Dev.* **2015**, *19*, 1667–1682.

[82] D. Lendrem, M. Owen, S. Godbert, *Org. Process Res. Dev.* **2001**, *5*, 324–327.

[83] S. A. Weissman, N. G. Anderson, *Org. Process Res. Dev.* **2015**, *19*, 1605–1633.

[84] R. Leardi, *Anal. Chim. Acta* **2009**, *652*, 161–172.

[85] M. J. Anderson, P. J. Whitcomb, *DOE Simplified*, CRC Press, Boca Raton, **2007**.

[86] R. Myers, D. Montgomery, C. Anderson-Cook, *Response Surface Methodology*, Wiley, New Yersey, **2016**.

[87] K. Siebertz, T. Hochkirchen, D. van Bebber, *Statistische Versuchsplanung*, Springer Verlag, Berlin, **2017**.

[88] P. Goos, B. Jones, *Optimal Design of Experiments*, John Wiley & Sons Ltd, Chichester, **2011**.

[89] M. J. Anderson, P. J. Whitcomb, *RSM Simplified*, CRC Press, Boca Raton, **2017**.

[90] H. B. Mann, *Analysis and Design of Experiments*, Dover Publications, New York, **1949**.

[91] B. R. Clarke, *Linear Models: The Theory and Application of Analysis of Variance*, Wiley, New Jersey, **2008**.

[92] C. Hirotsu, *Advanced Analysis of Variance*, Wiley, New Jersey, **2017**.

[93] M. Lovric, *International Encyclopedia of Statistical Science*, Springer Verlag, New York, **2011**.

[94] T. Sakai, *Laboratory Experiments in Information Retrieval*, Springer, Singapore, **2018**.

[95] D. M. Allen, *Technometrics* **1971**, *13*, 469–475.

[96] M. E. Fox, F. C. Szoka, J. M. J. Fréchet, *Acc. Chem. Res.* **2009**, *42*, 1141–1151.

[97] H. Hatakeyama, A. Kikuchi, M. Yamato, T. Okano, *Biomaterials* **2007**, *28*, 3632–3643.

[98] R. A. Mulvenna, J. L. Weidman, B. Jing, J. A. Pople, Y. Zhu, B. W. Boudouris, W. A. Phillip, *J. Memb. Sci.* **2014**, *470*, 246–256.

[99] J. L. Poole, S. Donahue, D. Wilson, Y. M. Li, Q. Zhang, Y. Gu, R. Ferebee,

Z. Lu, R. M. Dorin, L. F. Hancock, et al., *Macromol. Rapid Commun.* **2017**, *38*, 1–6.

[100] A. Jung, S. Rangou, C. Abetz, V. Filiz, V. Abetz, *Macromol. Mater. Eng.* **2012**, *297*, 790–798.

[101] M. Radjabian, V. Abetz, *Prog. Polym. Sci.* **2020**, *102*, 101219.

[102] L. Upadhyaya, M. Semsarilar, R. Fernández-Pacheco, G. Martinez, R. Mallada, I. M. Coelhoso, C. A. M. Portugal, J. G. Crespo, A. Deratani, D. Quemener, *Polym. Chem.* **2017**, *8*, 605–614.

[103] U. Farooq, L. Upadhyaya, A. Shakeel, G. Martinez, M. Semsarilar, *J. Memb. Sci.* **2020**, *611*, 118181.

[104] A. Asadujjaman, B. Kent, A. Bertin, *Soft Matter* **2017**, *13*, 658–669.

[105] W. Sun, Z. An, P. Wu, *Macromolecules* **2017**, *50*, 2175–2182.

[106] B. A. Pineda-Contreras, F. Liu, S. Agarwal, *J. Polym. Sci. Part A Polym. Chem.* **2014**, *52*, 1878–1884.

[107] S. Glatzel, N. Badi, M. Päch, A. Laschewsky, J. F. Lutz, *Chem. Commun.* **2010**, *46*, 4517–4519.

[108] O. F. Olaj, P. Vana, M. Zoder, *Macromolecules* **2002**, *35*, 1208–1214.

[109] J. P. A. Heuts, G. T. Russell, *Eur. Polym. J.* **2006**, *42*, 3–20.

[110] T. G. McKenzie, Q. Fu, E. H. H. Wong, D. E. Dunstan, G. G. Qiao, *Macromolecules* **2015**, *48*, 3864–3872.

[111] T. G. McKenzie, Q. Fu, M. Uchiyama, K. Satoh, J. Xu, C. Boyer, M. Kamigaito, G. G. Qiao, *Adv. Sci.* **2016**, *3*, 1–9.

[112] T. G. McKenzie, L. P. M. Da Costa, Q. Fu, D. E. Dunstan, G. G. Qiao, *Polym. Chem.* **2016**, *7*, 4246–4253.

[113] B. A. Pineda-Contreras, H. Schmalz, S. Agarwal, *Polym. Chem.* **2016**, *7*, 1979–1986.

[114] G. Muller, *Polym. Bull.* **1981**, *5*, 31–37.

[115] H. Kheradmand, J. Franqois, *Polymer (Guildf).* **1988**, *29*, 860–870.

[116] G. T. Russell, *Aust. J. Chem.* **2002**, *55*, 399–414.

[117] Y. Zhou, Z. Zhang, A. Postma, G. Moad, *Polym. Chem.* **2019**, *10*, 3284–3287.

[118] J. Xu, J. He, *Macromolecules* **2006**, *39*, 3753–3759.

[119] M. Z. Bekanova, N. K. Neumolotov, A. D. Jablanović, A. V. Plutalova, E. V. Chernikova, Y. V. Kudryavtsev, *Polym. Degrad. Stab.* **2019**, *164*, 18–27.

[120] A. Baroutaji, M. D. Gilchrist, D. Smyth, A. G. Olabi, *Thin-Walled Struct.* **2015**, *86*, 121–131.

[121] Y. Zhang, S. Furyk, L. B. Sagle, Y. Cho, D. E. Bergbreiter, P. S. Cremer, *J. Phys. Chem. C* **2007**, *111*, 8916–8924.

[122] S. Eggers, B. Fischer, V. Abetz, *Macromol. Chem. Phys.* **2016**, *217*, 735–747.

[123] Y. Zhang, S. Furyk, D. E. Bergbreiter, P. S. Cremer, *J. Am. Chem. Soc.*

2005, *127*, 14505–14510.
[124] T. Y. Nguyen, C. G. Liew, H. Liu, *PLoS One* **2013**, *8*, e76547.
[125] M. H. Stenzel, C. Barner-Kowollik, *Mater. Horizons* **2016**, *3*, 471–477.
[126] R. Wei, Y. Luo, P. Xu, *J. Polym. Sci. Part A Polym. Chem.* **2011**, *49*, 2980–2989.
[127] M. Chenal, L. Bouteiller, J. Rieger, *Polym. Chem.* **2013**, *4*, 752–762.
[128] K. Nieswandt, P. Georgopanos, M. Held, E. Sperling, V. Abetz, *Polymers (Basel).* **2022**, *14*, 62.
[129] X. Wang, J. Yu, G. Sun, B. Ding, *Mater. Today* **2016**, *19*, 403–414.
[130] J. J. Li, Y. N. Zhou, Z. H. Luo, *ACS Appl. Mater. Interfaces* **2015**, *7*, 19643–19650.
[131] P. Samatha, N. Krishnamurti, *J. Appl. Polym. Sci.* **1997**, *66*, 1419–1423.
[132] A. Einstein, *Nuovo Cim.* **1905**, *19*, 371.
[133] W. Sutherland, *London, Edinburgh, Dublin Philos. Mag. J. Sci.* **1905**, *9*, 781–785.
[134] M. von Smoluchowski, *Ann. d. Phys.* **1906**, *326*, 756.
[135] I. S. Khattab, F. Bandarkar, M. A. A. Fakhree, A. Jouyban, *Korean J. Chem. Eng.* **2012**, *29*, 812–817.
[136] C. V. Raman, *Nature* **1923**, *111*, 532–533.
[137] J. Kestin, M. Sokolov, W. A. Wakeham, *J. Phys. Chem. Ref. Data* **1978**, *7*, 941–948.
[138] S. L. Canning, G. N. Smith, S. P. Armes, *Macromolecules* **2016**, *49*, 1985–2001.
[139] S. Eggers, V. Abetz, *Polymers (Basel).* **2017**, *9*, 668.
[140] J. Xu, V. Abetz, *Soft Matter* **2022**, *18*, 2082.
[141] C. Liu, C. Y. Hong, C. Y. Pan, *Polym. Chem.* **2020**, *11*, 3673–3689.
[142] X. Xu, A. E. Smith, S. E. Kirkland, C. L. McCormick, *Macromolecules* **2008**, *41*, 8429–8435.
[143] T. A. Scott, *J. Phys. Chem.* **1946**, *50*, 406–412.

10 Appendix

10.1 Determination of Monomer Conversion *via* ^{1}H NMR Spectroscopy

This section provides information on the general procedure of monomer conversion determination *via* ^{1}H NMR spectroscopy for all conducted RAFT polymerizations. Figure A1 exemplary shows two ^{1}H NMR spectra of a MAAm homopolymerization in water (measured in D_2O). The proton signals that are relevant for conversion determination are assigned. While the top spectrum derives from the reaction solution after a given polymerization time, the bottom spectrum represents the initial reaction solution prior to the start of the polymerization (which is indicated by the "0" in the indices of the signals). When the integral of the DMF signal is normalized, the relevant monomer signal integrals can be easily compared and the monomer conversion p can be computed as follows:

$$p = 1 - \frac{I_{\mathbf{A'}} + I_{\mathbf{B'}}}{I_{\mathbf{A_0}} + I_{\mathbf{B_0}}}. \tag{A1}$$

Applying the determined monomer conversion, the theoretical number average molecular weight can be calculated according to equation (A2):

$$\overline{M}_{\mathrm{n,th}} = \frac{p\,[\mathrm{MAAm}]_0 M_{\mathrm{MAAm}}}{[\mathrm{CTCA}]_0} + M_{\mathrm{CTCA}} = p\,R_{\mathrm{M}}\,M_{\mathrm{MAAm}} + M_{\mathrm{CTCA}}\,. \tag{A2}$$

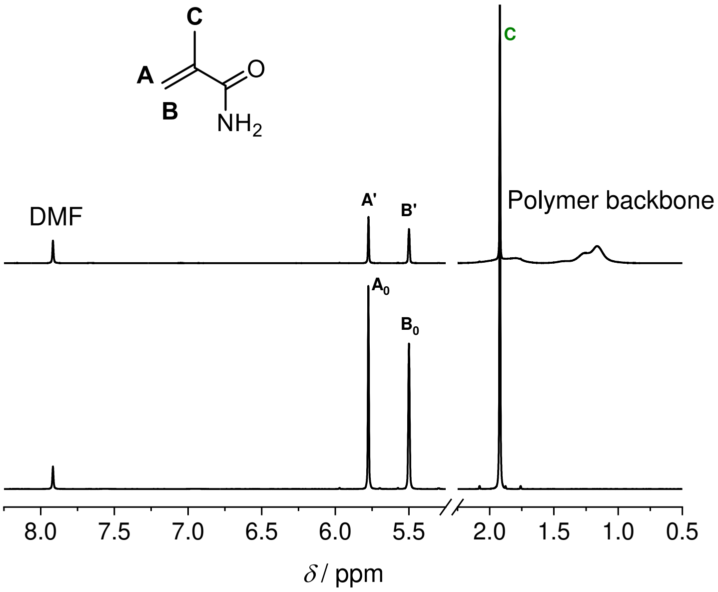

Figure A1: Display of the relevant parts of two ^{1}H NMR spectra for the determination of the monomer conversion of the homopolymerization of MAAm. Top: Spectra of polymerization solution after a given polymerization time. Bottom: Spectra of initial polymerization solution prior to initiation.

10.2 Photoiniferter RAFT Polymerization of NAGA

In Figure A2 part A, the conversion of the photoiniferter RAFT polymerization of NAGA using CPDT as RAFT agent is plotted versus the reaction time. Part B shows the elution chromatogram of the last kinetic sample taken after > 200 min.

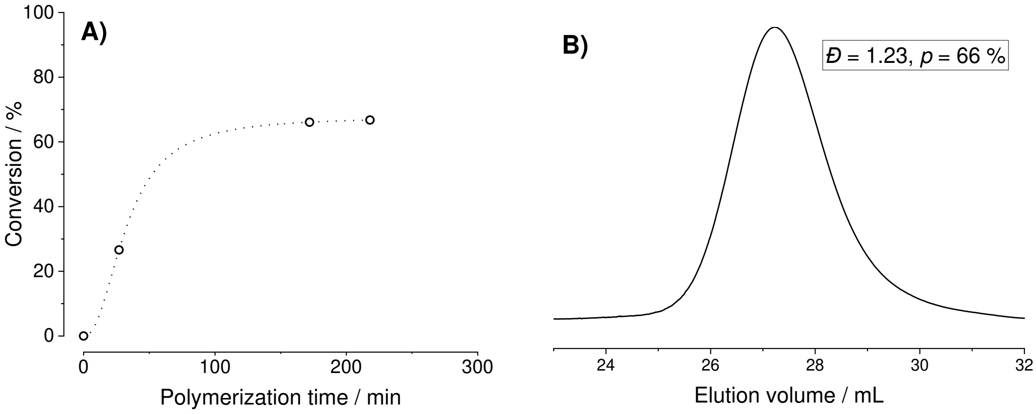

Figure A2: Graph A) Kinetic study of the photoiniferter RAFT polymerization of NAGA using CPDT as RAFT agent. Graph B) Elution chromatogram of the last kinetic sample.

In Figure A3, the ^{1}H NMR spectrum of a PNAGA homopolymer in DMSO-*d*6 is displayed and the relevant signals are assigned.

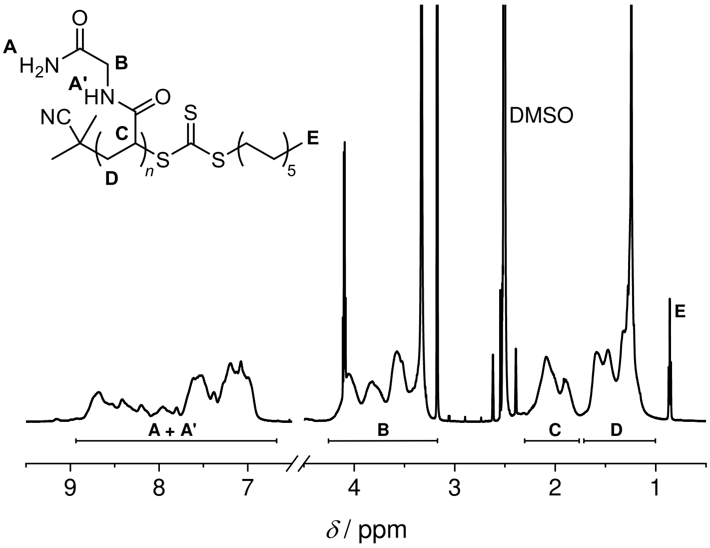

Figure A3: ^{1}H NMR spectrum of PNAGA in DMSO as well as assignment of the relevant signals.

10.3 RAFT Polymerization of MAAm using CTCPA as RAFT Agent

In the following, the kinetic studies as well as the elugrams from SEC experimentation of thermal RAFT polymerizations of MAAm using CTCPA as RAFT agent in three different water/cosolvent mixtures are presented. All polymerizations were conducted thermally with the azo-initiator ACVA at a reaction temperature of 75 °C ($R_M \equiv [\text{MAAm}]_0/[\text{CTCPA}]_0 = 500$, $[\text{CTCPA}]_0/[\text{ACVA}]_0 = 10$, $w_S = 15$ wt%). All polymerizations were homogenous throughout the whole reaction.

10.3.1 Cosolvent Mixture: H_2O/DMF

Figure A4 shows the monomer conversion versus the reaction time of the RAFT polymerization of MAAm in the cosolvent mixture H_2O/DMF (7/3, *w*/*w*). Although low conversion-values are obtained (Figure A4, graph A), the polymerization seems to be uncontrolled as the elugrams from SEC (graph B) are very broad (*Đ*-values greater than 1.8) and asymmetrical.

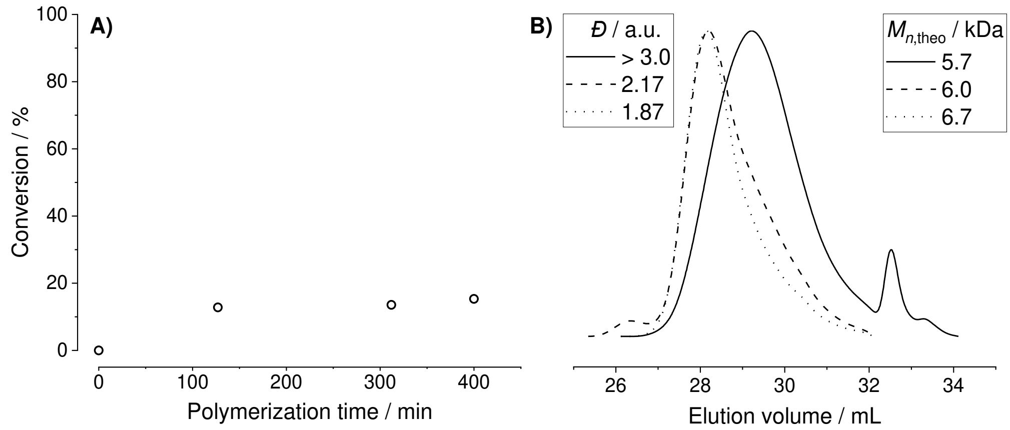

Figure A4: Graph A) Conversion versus polymerization time for the RAFT polymerization of MAAm in the cosolvent mixture H_2O/DMF (7/3, *w*/*w*) using CTCPA as RAFT agent. Graph B) Elution chromatograms of the three respective samples.

10.3.2 Cosolvent Mixture: H_2O/Ethanol

The monomer conversion versus the reaction time (graph A) as well as the evolution of elution chromatograms (graph B) of the thermal RAFT polymerizations of MAAm using CTCPA as RAFT in water/ethanol (8/2, *w*/*w*) is shown in Figure

A5. Again, the polymerization proceeds rather slowly. Also, the SEC traces are extremely broad ($Đ$ > 2.0) and do not shift to lower elution volumes with increasing $\overline{M}_{\mathrm{n,th}}$ which clearly proves the absence of polymerization control.

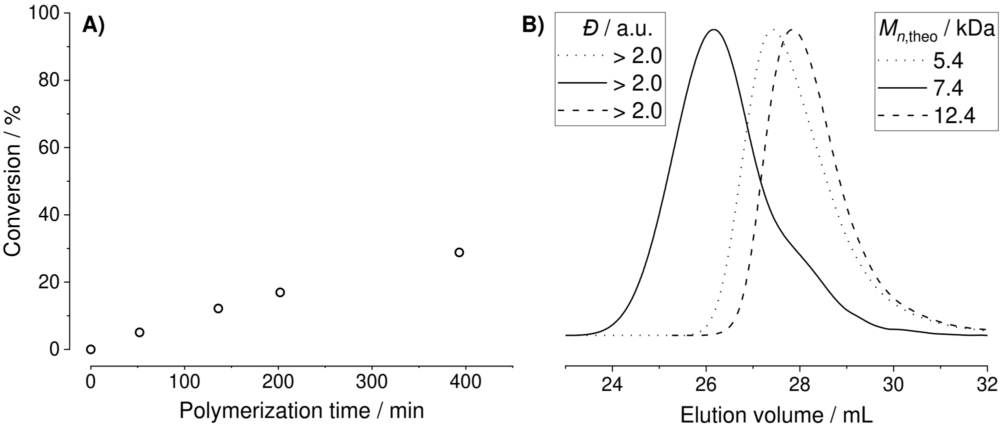

Figure A5: Graph A) Conversion–reaction time plot for the thermal RAFT polymerization of MAAm using CTCPA as RAFT agent in a cosolvent mixture of water/ethanol (8/2, *w*/*w*). Graph B) Display of SEC traces at different monomer conversions.

10.3.3 Cosolvent Mixture: H2O/Dioxane

The plot of monomer conversion versus polymerization time (graph A) and the SEC traces (graph B) for the thermal RAFT polymerization of MAAm using CTCPA as RAFT agent are illustrated in Figure A6. Just like in the cosolvent mixtures water/ethanol and water/dioxane, the rate of polymerization appears to be comparably slow with just about 20 % conversion after over 5 h. Moreover, the SEC traces are extremely broad which is a clear indication of a poorly controlled RAFT polymerization. CTCPA seems to be incapable of controlling the polymerization of MAAm.

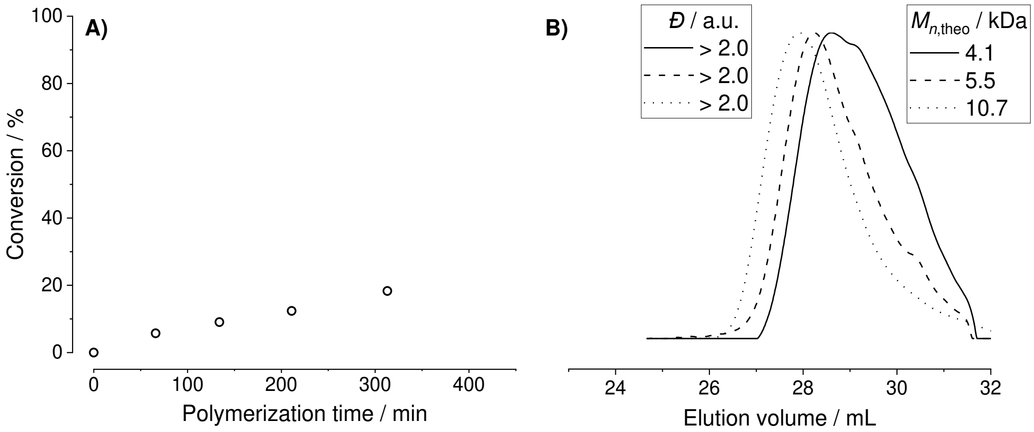

Figure A6: Graph A) Plot of the monomer conversion versus the polymerization time for the thermal RAFT polymerization of MAAm using CTCPA as RAFT agent in a cosolvent mixture of water/dioxane (65/35, *w*/*w*). Graph B) Display of the SEC traces throughout the polymerization.

10.4 Photoiniferter RAFT Polymerization of MAAm

Using CTCA as RAFT agent, well-controlled photoiniferter RAFT polymerizations of MAAm were performed in aqueous solution utilizing UV-light. In the following, kinetic studies regarding the effect of temperature, as well as SEC analyses are presented.

10.4.1 Effect of Temperature on the Polymerization Rate

In order to assess the influence of temperature on the polymerization rate, the polymerization was conducted at both 60 °C and 70 °C (R_M, $w_s = 15$ wt%, 0.38 mW cm^{-2}). Evidently, the polymerization rate is significantly lower at 60 °C which coincides with expectations associated to Arrhenius law.

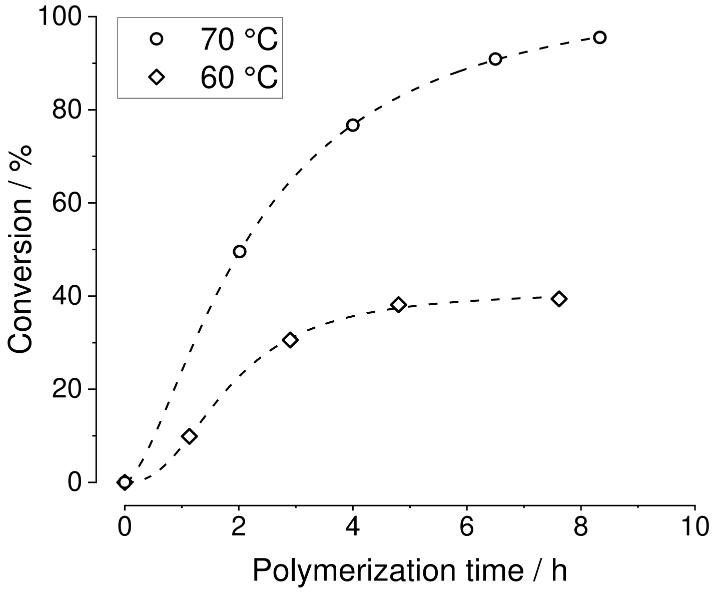

Figure A7: Monomer conversion versus the polymerization time for the photoiniferter RAFT polymerization of MAAm using CTCA as RAFT agent (R_M, $w_s = 15$ wt%, 0.38 mW cm^{-2}) at different reaction temperatures.

10.4.2 SEC Analyses

The kinetic studies presented in section 5.2.2 were also analyzed *via* SEC. Figure A8 illustrates the evolution of the SEC traces with conversion (which is directly proportional to $\overline{M}_{n,th}$). All kinetic studies show imply a well-controlled polymerization as the SEC traces reliably shift towards lower elution volumes with increasing values of $\overline{M}_{\mathrm{n,th}}$. Also, the traces appear rather symmetrically and narrow ($Đ < 1.20$). With increasing conversion and increasing R_{M}-values, however, termination events appear to accumulate causing the distributions to broaden and the values of $Đ$ to increase markedly ($Đ > 1.7$). Another factor that can contribute to the broadening of SEC traces is the gradual decomposition of the thrithiocarbonate moiety of the RAFT agent over time which will be addressed in the following section 10.4.3.

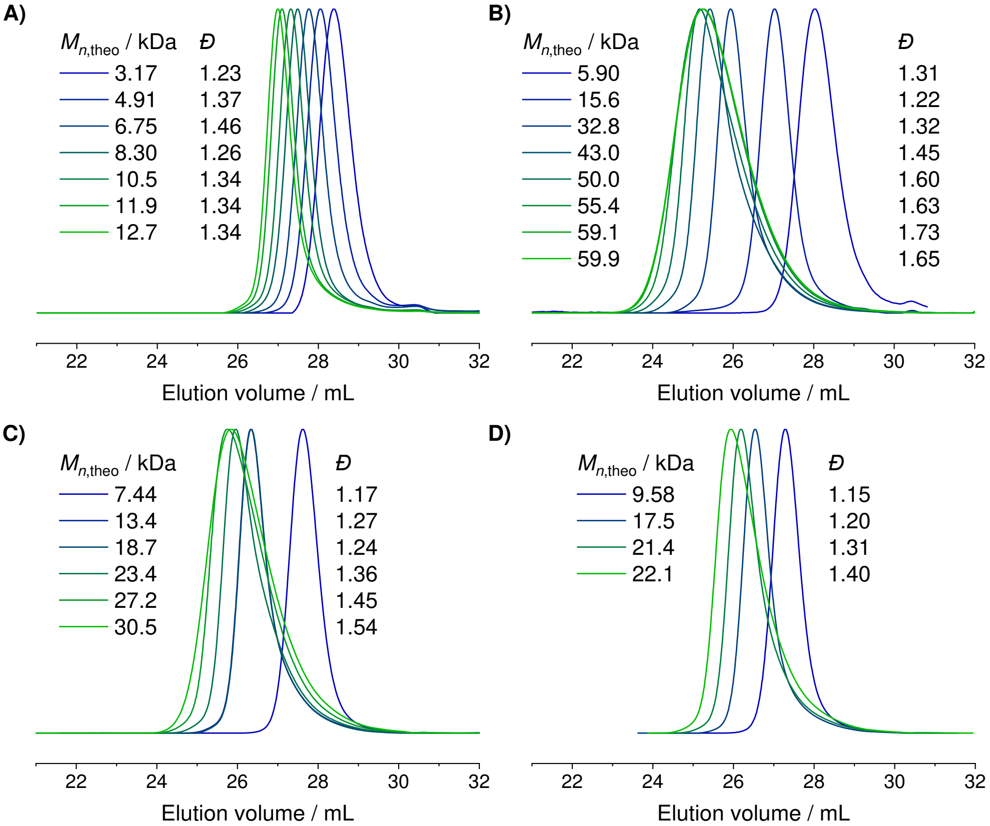

Figure A8: Evolution of SEC traces with increasing theoretical number-averaged molecular weight ($\overline{M}_{\mathrm{n,th}}$) of the photoiniferter RAFT polymerization of MAAm using CTCA as RAFT agent (70 °C, $w_{\mathrm{s}} = 15$ wt%). Graph A) $R_{\mathrm{M}} = 200$, 0.38 mW cm^{-2}. Graph B) $R_{\mathrm{M}} = 800$, 0.38 mW cm^{-2}. Graph C) $R_{\mathrm{M}} = 400$, 0.61 mW cm^{-2}. Graph D) $R_{\mathrm{M}} = 400$, 0.30 mW cm^{-2}.

The two polymers PMAAm$^{11.7}$ and PMAAm$^{20.1}$ were synthesized (for experimental and analytical data see Table 5) on a larger scale for subsequent analyses of solution behavior *via* DLS. The SEC measurements of both polymer samples is displayed in Figure A9.

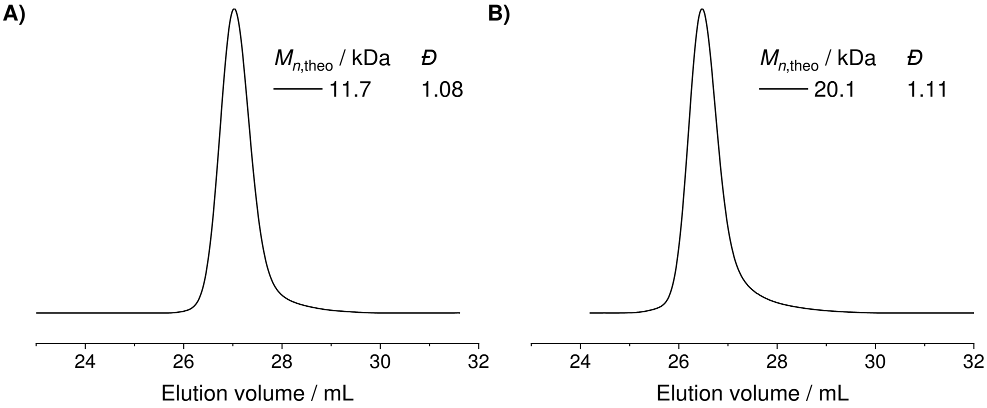

Figure A9: SEC traces of PMAAm$^{11.7}$ (graph A) and PMAAm$^{20.1}$ (graph B).

10.4.3 Photolytic Decomposition of CTCA

RAFT agents are well-known to be able to decompose under light irradiation, which can significantly affect the molecular weight distribution of the obtained polymer.[112] These irreversible decompositions also significantly limit the chain end fidelity of the obtained polymer.

The inclination of CTCA for irreversible decomposition under UV-light irradiation and the optimized polymerization conditions ($DP_{\text{max}} = 400$, 0.38 mW cm^{-2}, 70 °C) were tested. A solution containing 52.1 mg of CTCA, 0.291 g of water and 0.243 g of DMF as internal standard was prepared. The solution was purged with N_2 for 10 minutes at 0 °C and a reference sample was removed for NMR analysis. Subsequently, the solution was irradiated with 0.38 mW cm^{-2} and stirred it at 70 °C for 9 hours. Every three hours, a sample was taken for NMR spectroscopy and the integral of the methylene group proton signal at 4.04 ppm (in D_2O) was monitored. This triplet derives from the methylene group protons of the stabilizing group directly adjacent to the trithiocarbonate moiety. As decomposition turns this stabilizing group into a primary thiol, the methylene proton signal shifts high field and can be used for determination of the degree of decomposition (by referencing this signal to the internal standard DMF, in analogous fashion as the monomer conversion is computed in section 10.1).

Figure A10 illustrates the course of the degree of CTCA-decomposition over 9 hours. No decomposition is observable within the first three hours, however, 4 %

of CTCA decompose within hours 3–6 and additional 10 % will decompose within the hours 6–9. As polymer chains without the trithiocarbonate moiety can no longer participate in the RAFT equilibrium and cease to propagate, the molecular weight distribution broadens. This explains the observed broadening of the SEC traces.

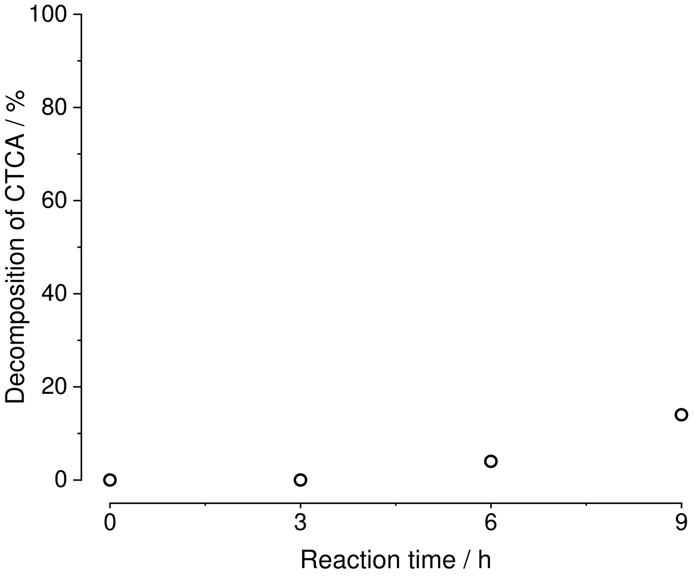

Figure A10: Course of the degree of photolytic decomposition of CTCA over time at 70 °C in aqueous solution.

10.5 Dynamic Light Scattering

10.5.1 Thermal equilibration of PMAAm solutions in water/ethanol mixtures

Prior to the start of a temperature-dependent DLS measurement, it is – for purposes of reproducibility and comparability – always important to facilitate a thermally equilibrated state of the polymer solution. As examination of UCST-type PTs are (at least in this work) started at elevated temperatures above the PT, this is not as big a problem as with LCST-type PT which are usually started below the PTT – especially since most temperature-dependent DLS experiments were started at 70 °C. Nonetheless, the speed of thermal equilibration of a 0.25 wt% PMAAm$^{20.1}$ solution in a water/ethanol (75/25, *w*/*w*) mixture at a temperature of 40 °C (which was the lowest starting temperature for all temperature-dependent DLS experiments conducted in this work) was tested. The polymer solution was quickly heated (< 3 min) above its PTT of 31 °C (see Figure 33) and quickly placed in the toluene bath of the DLS measurement cell (preheated to 40 °C). The DLS measurement was instantly started and the solution was repeatedly analyzed at 40 °C over a time-period of almost 4 h (see graph A, Figure A11). It is shown, that the R_h-value remains constant over the whole analysis. Also the relative scattering intensities of both particle species – unimers and aggregates – remains constant as implied by the unchanged symbol area. The polymer solution appears to be thermally equilibrated almost instantly – even at a comparably low temperature of 40 °C. This conclusion is further supported by graph B which displays the count rate of the first measurement (which was excluded in graph A) versus the time. It shows a continuously decreasing average of the fluctuating count rate which indicates that thermal equilibration – in this case most likely partial redissolution of polymer aggregates into unimer species – is actually only a matter of seconds.

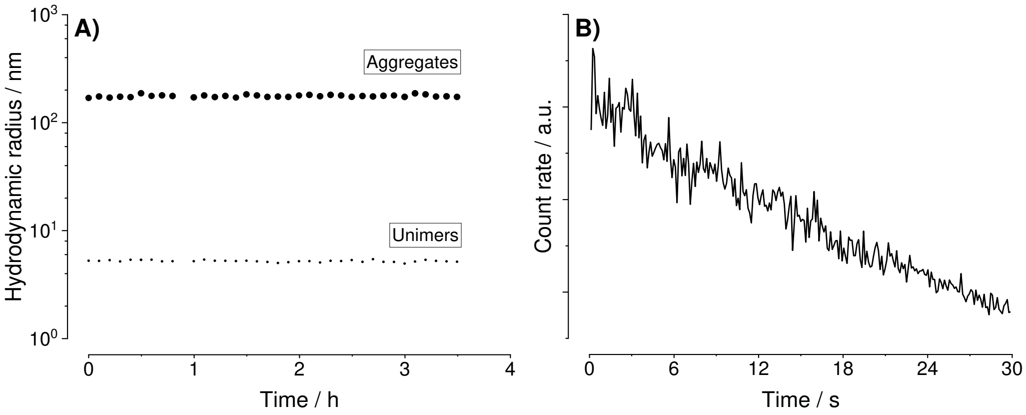

Figure A11: Graph A) Evolution of the R_h of both unimer and aggregate species a 0.25 wt% PMAAm$^{20.1}$ solution in a water/ethanol (75/25, *w*/*w*) mixture at 40 °C over a course of almost 4 h. The area of the symbols represents the relative scattering intensity of the particular species. Graph B) Display of the count rate of the first measurement versus the measuring time. Thermal equilibration at 40 °C is achieved within seconds.

10.5.2 Viscosity-Corrections for Water/Ethanol Mixtures

In order to facilitate precise estimations for the viscosity-changes with temperature, the experimental viscosity values at different temperatures can be fitted using the following equation:

$$\eta = 10^{A + B\,{}^{1000}\!/_{T}}. \tag{A3}$$

With the two viscosity parameters *A* and *B*, the ALV Digital Correlator Software 3.0 provides a temperature-dependent estimate for the viscosity. Although experimental data for the temperature-dependent viscosity of different water/ethanol mixtures is limited, Khattab *et al.* provided data for some mixtures (92/8, 83/17; 75/25, 65/35, *w*/*w*).[135] The respective experimental data, the applied fit according to equation (A3) as well as the obtained viscosity parameters are shown in Figure A12: Temperature-dependent viscosity-data (black circles) for different water/ethanol mixtures. The exponential fit (black line) delivers the mixture-specific viscosity parameters *A* and *B*.

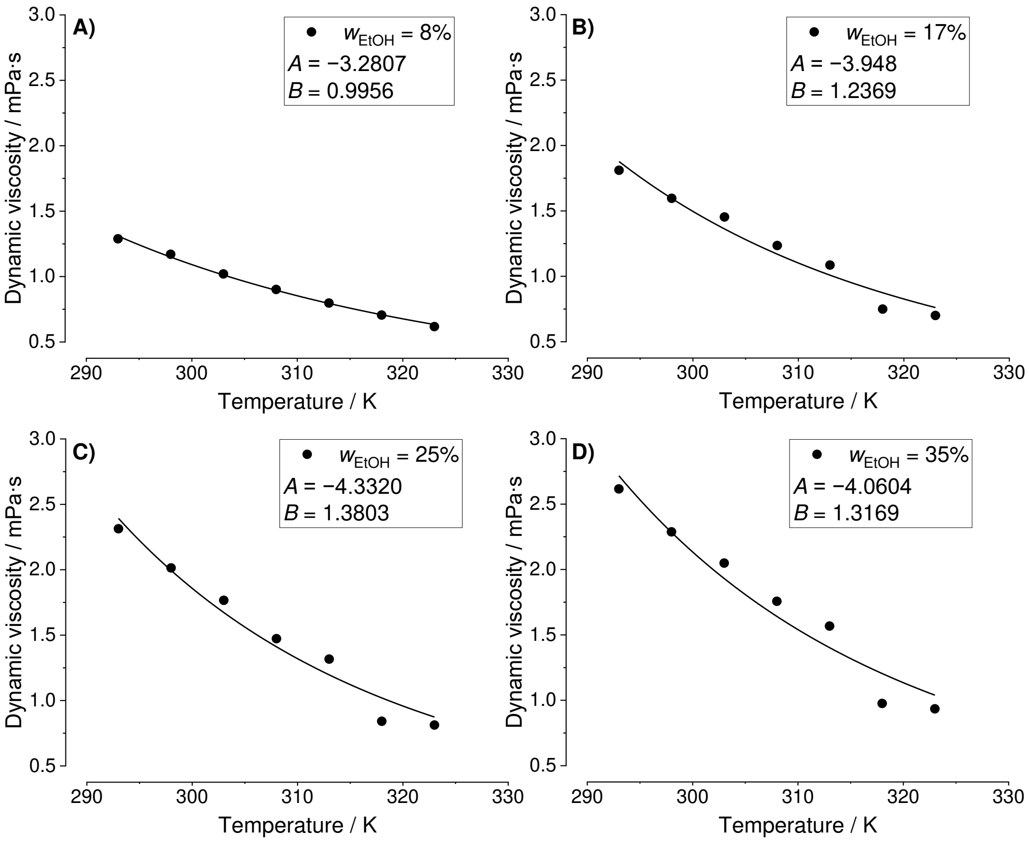

Figure A12: Temperature-dependent viscosity-data (black circles) for different water/ethanol mixtures. The exponential fit (black line) delivers the mixture-specific viscosity parameters *A* and *B*.[135]

If, however, instead of a drastic thermoresponsive PT, a thermosensitive behavior is obtained, the influence of η is way more decisive. Hence, the author conducted his own viscosity measurements of different water/ethanol mixtures within a temperatures range of 10–70 °C. These were conducted *via* a rheometer using a Couette element and measuring the viscosity of a (co-)solvent at different shear rates and at different temperatures. These results are shown in the main part of this work (see Figure 47, section 7.3.3).

10.6 Design of Experiments

In the following, supplementary information regarding the performed experimental designs of this work will be provided.

10.6.1 True Optimization of a RAFT Polymerization

This section will provide the supplementary data regarding the step-by-step guide for an optimization of a RAFT polymerization which is presented in section 6.1.

10.6.1.1 Screening: Expelling the Insignificant Factors

The four factors $\boldsymbol{m}_{\mathbf{H_2O}}$, $\boldsymbol{w}_{\mathbf{DMF}}$, $\boldsymbol{v}_{\mathbf{S}}$ and $\boldsymbol{t}_{\mathbf{N_2}}$ were found to be insignificant after completion of the two-level fractional factorial (shown in Table 6) and subsequent ANOVA. The ANOVA tables for all four monitored responses ($\boldsymbol{p}$, $\overline{\boldsymbol{M}}_{\mathbf{n,th}}$, $\boldsymbol{Đ}$ and $\overline{\boldsymbol{M}}_{\mathbf{n,app}}$) is shown in Table A1.

Table A1: ANOVA tables for the responses $\boldsymbol{p}$, $\overline{\boldsymbol{M}}_{\mathbf{n,th}}$, $\boldsymbol{Đ}$ and $\overline{\boldsymbol{M}}_{\mathbf{n,app}}$. No effect was significant, while all lack of fit were insignificant (p-values all above 0.05).

Source	Sum of Squares	df	Mean Square	F-value	p-value
Model of $\boldsymbol{p}$	0.0000	0			
Curvature	6.41	1	6.41	1.45	0.2557
Residual	44.08	10	4.41		
Lack of Fit	35.18	7	5.03	1.69	0.3593
Pure Error	8.90	3	2.97		
Cor Total	50.49	11			
Model of $\overline{\boldsymbol{M}}_{\mathbf{n,th}}$	0.0000	0			
Curvature	0.8817	1	0.8817	2.71	0.1304
Residual	3.25	10	0.3248		
Lack of Fit	2.80	7	0.4000	2.68	0.2246
Pure Error	0.4475	3	0.1492		
Cor Total	4.13	11			
Model of $\boldsymbol{Đ}$	0.0000	0			
Curvature	0.0001	1	0.0001	0.1743	0.6851
Residual	0.0038	10	0.0004		
Lack of Fit	0.0023	7	0.0003	0.6828	0.6957

Source	Sum of Squares	df	Mean Square	F-value	p-value
Pure Error	0.0015	3	0.0005		
Cor Total	0.0039	11			
Model of $\overline{M}_{\mathrm{n,app}}$					
Curvature	0.6337	1	0.6337	3.02	0.1127
Residual	2.10	10	0.2096		
Lack of Fit	1.15	7	0.1641	0.5196	0.7859
Pure Error	0.9475	3	0.3158		
Cor Total	2.73	11			

10.6.1.2 Preparation prior to RSM: Performing Preliminary Tests

In order to assure the feasibility of every run that needs to be conducted in the later RSM design, appropriate preliminary tests were conducted. Herein, a kinetic study (shown in graph A of Figure A13) of the RAFT polymerization of MAAm was performed ($\boldsymbol{T}$ = 75 °C, $\boldsymbol{R}_{\mathrm{M}}$ = 500, $\boldsymbol{R}_{\mathrm{I}}$ = 0.025, $\boldsymbol{w}_{\mathrm{s}}$ = 10 wt%). As the limiting factor for the feasibility was the permeation limit of the GPC, this combination of factor levels needs to be checked prior to execution of the FC-CCD as it will most likely result in the lowest obtained response. As indicated by the conversion values, however, after 2 h easily enough conversion is obtained to ensure a reliable response from SEC analysis (graph B).

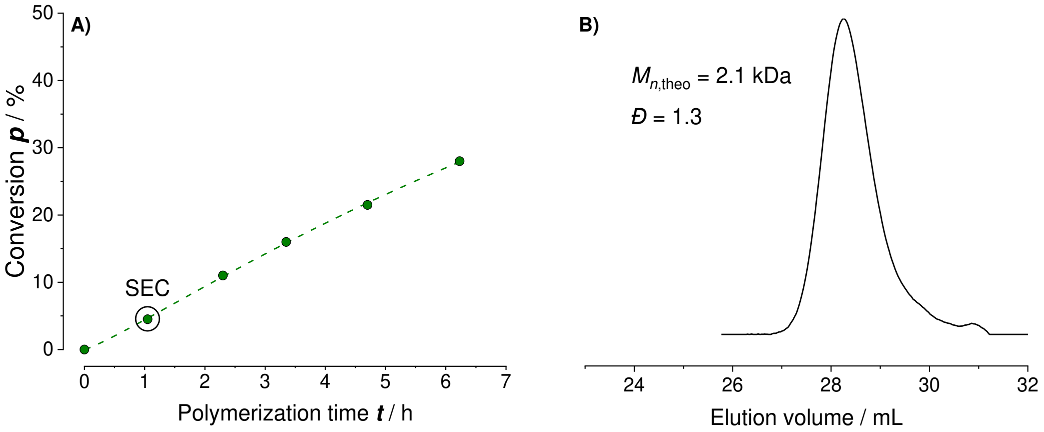

Figure A13: Graph A) Conversion time course of a RAFT polymerization of MAAm (**T** = 75 °C, **R_I** = 0.025, **w_S** = 10°wt%) serving as a preliminary test for the succeeding FC-CCD. Graph B) Elution chromatogram from SEC analysis of the sample after around 1 h polymerization time (highlighted with black circle in graph A). Sufficiently high conversions are obtained, at the latest, after 2 h.

10.6.1.3 Execution of the RSM Design

The FC-CCD plan was executed in random order to minimize potential time-lurking influences. For purposes of clarity, the experimental plan is shown in ordered form (non-randomized) in Table A2 together with all actual (*i.e.*, “uncoded”) factor levels as well as measured responses.

Table A2: Standard order of the executed FC-CCD. Display of all acutal factor levels as well as measured responses.

Run	**T / °C**	**t / min**	**R_M**	**R_I**	**w_S**	**p^a / %**	**$\bar{M}_{n,th}{}^a$ / kDa**	**$Đ^b$**	**$\bar{M}_{n,app}{}^b$ / kDa**
1	75	120	200	0.025	10	10.5	2.1	1.29	3.2
2	85	120	200	0.025	10	18.2	3.4	1.38	5.4
3	75	400	200	0.025	10	36.6	6.4	1.22	3.7
4	85	400	200	0.025	10	40.2	7.2	1.45	4.6
5	75	120	500	0.025	10	8.4	3.9	1.3	2.2
6	85	120	500	0.025	10	12	5	1.45	8.7
7	75	400	500	0.025	10	22.2	9.8	1.29	4.6
8	85	400	500	0.025	10	26.2	11	1.45	6.0
9	75	120	200	0.1	10	25.6	4.7	1.3	6.3
10	85	120	200	0.1	10	39.8	7.1	1.22	3.0
11	75	400	200	0.1	10	59.9	10.5	1.24	10
12	85	400	200	0.1	10	62.6	11	1.33	7.3

Run	T / °C	t / min	R_M	R_I	w_s	p^a / %	$\bar{M}_{n,th}{}^a$ / kDa	$Đ^b$	$\bar{M}_{n,app}{}^b$ / kDa
13	75	120	500	0.1	10	18.5	7.9	1.34	3.4
14	85	120	500	0.1	10	26	10.9	1.28	3.8
15	75	400	500	0.1	10	43.4	19.6	1.24	6.5
16	85	400	500	0.1	10	44.7	19.3	1.35	4.2
17	75	120	200	0.025	20	19.1	3.6	1.21	6.4
18	85	120	200	0.025	20	24.8	4.5	1.22	6.1
19	75	400	200	0.025	20	48.3	8.5	1.23	3.8
20	85	400	200	0.025	20	52.6	9.2	1.36	5.1
21	75	120	500	0.025	20	8.4	3.9	1.25	5.7
22	85	120	500	0.025	20	17.3	7.7	1.26	5.2
23	75	400	500	0.025	20	36.8	16	1.25	3.4
24	85	400	500	0.025	20	36.5	15.8	1.35	5.4
25	75	120	200	0.1	20	31.2	5.6	1.16	6.4
26	85	120	200	0.1	20	51.5	9.1	1.23	8.4
27	75	400	200	0.1	20	75.6	13.2	1.25	3.4
28	85	400	200	0.1	20	74	12.8	1.33	7.3
29	75	120	500	0.1	20	22	9.7	1.19	4.8
30	85	120	500	0.1	20	36.1	15.7	1.25	6.3
31	75	400	500	0.1	20	55.1	23.8	1.23	5.0
32	85	400	500	0.1	20	57.1	25.1	1.38	2.3
33	75	260	350	0.0625	15	36.4	11	1.21	7.7
34	85	260	350	0.0625	15	43.8	13.4	1.27	4.2
35	80	120	350	0.0625	15	23.8	7.4	1.25	5.3
36	80	400	350	0.0625	15	52	15.8	1.29	2.8
37	80	260	200	0.0625	15	52.2	9.2	1.24	6.8
38	80	260	500	0.0625	15	37.4	16.2	1.26	6.3
39	80	260	350	0.025	15	28.8	9.2	1.27	7.6
40	80	260	350	0.1	15	49.8	15.2	1.25	9.5
41	80	260	350	0.0625	10	36.7	11.2	1.27	8.4
42	80	260	350	0.0625	20	47.6	14.3	1.24	4.9
43	80	260	350	0.0625	15	40	12.2	1.26	5.0
44	80	260	350	0.0625	15	42.7	13	1.31	4.5
45	80	260	350	0.0625	15	43	13.1	1.26	4.4
46	80	260	350	0.0625	15	41.7	12.7	1.25	5.6
47	80	260	350	0.0625	15	42.7	12.8	1.28	2.5
48	80	260	350	0.0625	15	41.8	12.8	1.24	6.3
49	80	260	350	0.0625	15	44	13.2	1.27	7.3
50	80	260	350	0.0625	15	42.9	12.8	1.25	6.2

[a] Determined *via* ^{1}H NMR spectroscopy and referencing to DMF. [b]Measured by SEC at 50 °C in an 0.1 M $NaNO_3$ aqueous (Milli-Q quality) solution with an added 0.05 wt% NaN_3 and calibration with PEG.

10.6.1.4 Prediction Models: ANOVA, Fit Statistics and Diagnostic Tools

In the following subsections, the prediction models of $\boldsymbol{p}$, $\boldsymbol{\overline{M}}_{\mathbf{n,th}}$, $\boldsymbol{Đ}$ and $\boldsymbol{\overline{M}}_{\mathbf{n,app}}$ (equations (A4)–(A7)) together with the respective ANOVA tables and fit statistics (Table A3–Table A6) as well as the diagnostic plots (Figure A14–Figure A17) from the performed RSM design for the optimization of a RAFT polymerization will be shown individually. The implications of these subsection will be presented jointly in the last subsection (10.6.1.4.5) in order to avoid redundancies.

10.6.1.4.1 The Monomer Conversion **p**

Equation (A4) shows the prediction equation for ***p***:

$$\boldsymbol{p}\,/\,\% = 42.3 + 3.10\,T + 12.7\,t - 6.31\,R_\mathrm{M} + 9.59\,R_\mathrm{I} + 4.78\,w_\mathrm{s} - 2.06\,T\,t + 0.719\,T\,R_\mathrm{I} + 0.275\,T\,w_\mathrm{s} - 1.74\,t\,R_\mathrm{M} + 1.28\,t\,R_\mathrm{I} + 1.52\,t\,w_\mathrm{s} - 1.09\,R_\mathrm{M}\,R_\mathrm{I} - 2.08\,T^2 - 4.28\,t^2 + 2.62\,R_\mathrm{M}^2 - 2.88\,R_\mathrm{I}^2 - 1.17\,T\,t\,R_\mathrm{I} - 0.725\,T\,t\,w_s \quad \text{(A4)}$$

The ANOVA table as well as the fit statistics for the prediction model of ***p*** are shown in Table A3.

Table A3: ANOVA for the prediction model of ***p*** as well as the relevant fit statistics.

Source	Sum of Squares	df	Mean Square	F-value	p-value	Fit Statistics	
Model of *p*	11977.37	18	665.41	242.12	< 0.0001	R^2	0.9929
T	326.74	1	326.74	118.89	< 0.0001	R^2_adj	0.9888
t	5453.42	1	5453.42	1984.33	< 0.0001	R^2_pred	0.9780
R_M	1354.50	1	1354.50	492.86	< 0.0001		
R_I	3125.76	1	3125.76	1137.37	< 0.0001		
w_s	776.65	1	776.65	282.60	< 0.0001		
$T\,t$	136.13	1	136.13	49.53	< 0.0001		
$T\,R_\mathrm{I}$	16.53	1	16.53	6.02	0.0200		
$T\,w_\mathrm{s}$	2.42	1	2.42	0.8806	0.3553		
$t\,R_\mathrm{M}$	97.30	1	97.30	35.40	< 0.0001		
$t\,R_\mathrm{I}$	52.53	1	52.53	19.11	0.0001		
$t\,w_\mathrm{s}$	74.42	1	74.42	27.08	< 0.0001		
$R_\mathrm{M}\,R_\mathrm{I}$	37.84	1	37.84	13.77	0.0008		
T^2	11.29	1	11.29	4.11	0.0514		
t^2	47.90	1	47.90	17.43	0.0002		
R_M^2	18.05	1	18.05	6.57	0.0155		
R_I^2	21.67	1	21.67	7.88	0.0086		
$T\,t\,R_\mathrm{I}$	43.71	1	43.71	15.91	0.0004		
$T\,t\,w_\mathrm{s}$	16.82	1	16.82	6.12	0.0190		
Residual	85.20	31	2.75				
Lack of Fit	75.26	24	3.14	2.21	0.1416		
Pure Error	9.94	7	1.42				
Cor Total	12062.56	49					

The normal probability plot of residuals (graph A), the residuals versus predicted plot (graph B) as well as the residuals versus runs plot (graph C) are displayed in Figure A14.

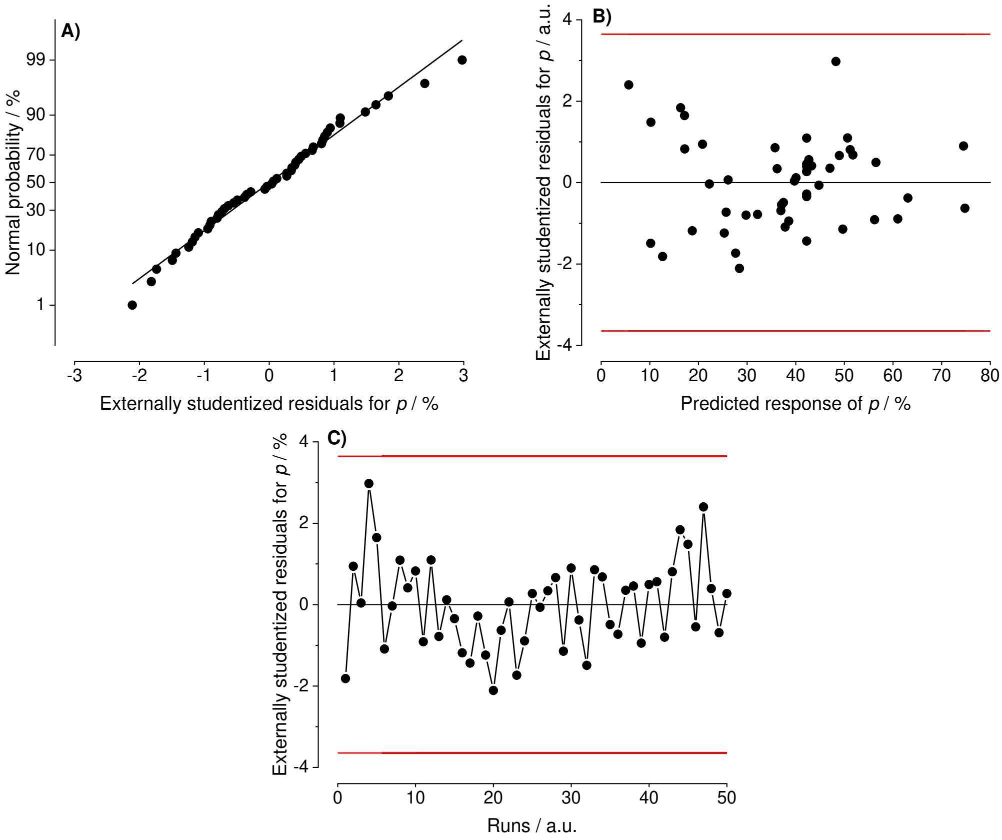

Figure A14: Diagnostic plots for the prediction model of $\boldsymbol{p}$. Graph A) Normal probability plot of residuals. Graph B) Residuals (externally studentized) versus the predicted response. Graph C) Residuals versus run plot. The red lines of plots A and B signify the Bonferroni-corrected confidence limits.

10.6.1.4.2 The Theoretical Number-Averaged Molecular Weight $\overline{\mathbf{M}}_{\mathbf{n,th}}$

The prediction equation for $\overline{\boldsymbol{M}}_{\mathbf{n,th}}$ is shown in equation (A5). As $\overline{\boldsymbol{M}}_{\mathbf{n,th}}$ is proportional to $\boldsymbol{p}$, it comes at no surprise that the models consist of similar terms.

$$\begin{gathered}\overline{\boldsymbol{M}}_{\mathbf{n,app}} \,/\, \mathrm{kDa} = 12.8 + 0.824\ T + 3.61\ t - 2.74\ R_\mathrm{M} + 2.76\ R_\mathrm{I} + 1.40\ w_\mathrm{s} - 0.575\ T\,t + 0.200\ T \\ R_\mathrm{I} + 0.175\ T\,w_\mathrm{s} - 1.16\ t\,R_\mathrm{M} + 0.463\ t\,R_\mathrm{I} + 463\ t\,w_\mathrm{s} - 0.931\ R_\mathrm{M}\,R_\mathrm{I} - 0.650\ T^2 - 1.25\ t^2 \\ - 0.150\ R_\mathrm{M}^2 - 0.650\ R_\mathrm{I}^2 - 0.288\ T\,t\,R_\mathrm{I} - 0.225\ T\,t\,w_s\end{gathered} \tag{A5}$$

The respective ANOVA table for the prediction model of $\overline{\boldsymbol{M}}_{\mathbf{n,th}}$ is provided in Table A4 together with the respective fit statistics.

Table A4: ANOVA for the prediction model of $\boldsymbol{\overline{M}_{\mathrm{n,th}}}$ as well as the relevant fit statistics.

Source	Sum of Squares	df	Mean Square	F-value	p-value	Fit Statistics	
Model of $\overline{M}_{\mathrm{n,th}}$	1219.14	18	67.73	90.64	< 0.0001	R^2	0.9814
T	23.06	1	23.06	30.86	< 0.0001	R^2_{adj}	0.9705
t	443.52	1	443.52	593.54	< 0.0001	R^2_{pred}	0.9379
R_{M}	255.48	1	255.48	341.89	< 0.0001		
R_{I}	259.88	1	259.88	347.78	< 0.0001		
w_{s}	66.36	1	66.36	88.81	< 0.0001		
$T\,t$	10.58	1	10.58	14.16	0.0007		
$T\,R_{\mathrm{I}}$	1.28	1	1.28	1.71	0.2002		
$T\,w_{\mathrm{s}}$	0.9800	1	0.9800	1.31	0.2609		
$t\,R_{\mathrm{M}}$	42.78	1	42.78	57.25	< 0.0001		
$t\,R_{\mathrm{I}}$	6.85	1	6.85	9.16	0.0049		
$t\,w_{\mathrm{s}}$	6.85	1	6.85	9.16	0.0049		
$R_{\mathrm{M}}\,R_{\mathrm{I}}$	27.75	1	27.75	37.14	< 0.0001		
T^2	1.11	1	1.11	1.48	0.2330		
t^2	4.09	1	4.09	5.47	0.0259		
R_{M}^2	0.0586	1	0.0586	0.0784	0.7813		
R_{I}^2	1.11	1	1.11	1.48	0.2330		
$T\,t\,R_{\mathrm{I}}$	2.64	1	2.64	3.54	0.0693		
$T\,t\,w_{\mathrm{s}}$	1.62	1	1.62	2.17	0.1510		
Residual	23.16	31	0.7473				
Lack of Fit	22.51	24	0.9379	10.02	0.0021		
Pure Error	0.6550	7	0.0936				
Cor Total	1242.31	49					

Figure A15 illustrates the normal probability plot of residuals (graph A), the residuals versus predicted plot (graph B) as well as the residuals versus runs plot (graph C).

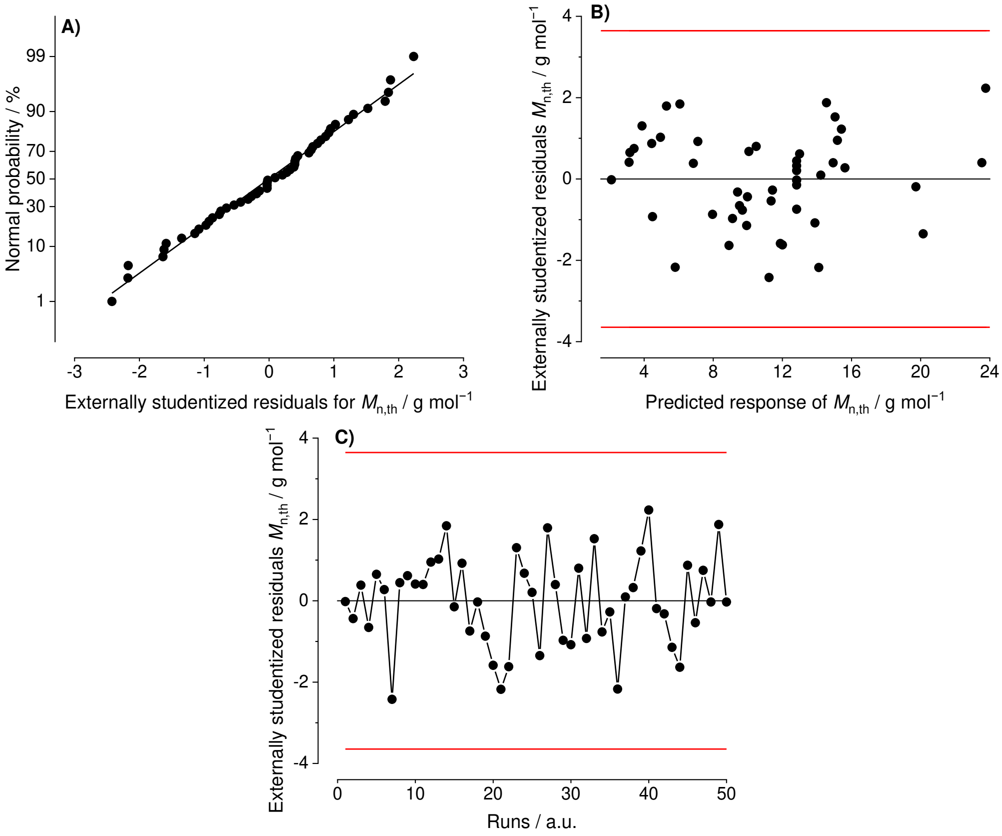

Figure A15: Diagnostic plots for the prediction model of $\overline{\boldsymbol{M}}_{\mathbf{n,th}}$. Graph A) Normal probability plot of residuals. Graph B) Residuals (externally studentized) versus the predicted response. Graph C) Residuals versus run plot. The red lines of plots A and B signify the Bonferroni-corrected confidence limits.

10.6.1.4.3 The Apparent Number-Averaged Molecular Weight $\overline{\mathbf{M}}_{\mathbf{n,app}}$

The prediction equation of $\overline{\boldsymbol{M}}_{\mathbf{n,app}}$ is presented in (A6).

$$\overline{\boldsymbol{M}}_{\mathbf{n,app}} \text{ / kDa} = 6.23 + 0.259\, T + 1.25\, t - 1.06\, R_{\mathrm{M}} + 0.927\, R_{\mathrm{I}} + 0.488\, w_{\mathrm{s}} - 0.259\, T\, t + 0.209\, T\, R_{\mathrm{M}} + 0.053\, T\, w_{\mathrm{s}} + 0.453\, t\, R_{\mathrm{M}} + 0.109\, t\, R_{\mathrm{I}} + 0.322\, t\, w_{\mathrm{s}} + 0.278\, R_{\mathrm{M}}\, R_{\mathrm{I}} + 0.278\, R_{\mathrm{M}}\, w_s + 0.047\, R_{\mathrm{I}}\, w_s - 0.366\, T^2 - 0.766\, t^2 - 0.134\, T\, t\, w_s - 0.303\, t\, R_{\mathrm{I}}\, w_s \tag{A6}$$

Table A5 shows the ANOVA table of the $\overline{\boldsymbol{M}}_{\mathbf{n,app}}$-prediction equation as well as the respective fit statistics.

Table A5: ANOVA for the prediction model of $\bar{M}_{\mathrm{n,app}}$ as well as the relevant fit statistics.

Source	**Sum of Squares**	**df**	**Mean Square**	**F-value**	**p-value**	**Fit Statistics**	
Model $\bar{M}_{\mathrm{n,app}}$	166.10	18	9.23	67.92	< 0.0001	R^2	0.9814
T	2.28	1	2.28	16.76	0.0003	R^2_{adj}	0.9705
t	53.38	1	53.38	392.83	< 0.0001	R^2_{pred}	0.9379
R_{M}	37.91	1	37.91	278.98	< 0.0001		
R_{I}	29.18	1	29.18	214.78	< 0.0001		
w_{s}	8.10	1	8.10	59.65	< 0.0001		
$T\,t$	2.15	1	2.15	15.84	0.0004		
$T\,R_{\mathrm{M}}$	1.40	1	1.40	10.32	0.0031		
$T\,w_{\mathrm{s}}$	0.0903	1	0.0903	0.6647	0.4211		
$t\,R_{\mathrm{M}}$	6.57	1	6.57	48.36	< 0.0001		
$t\,R_{\mathrm{I}}$	0.3828	1	0.3828	2.82	0.1033		
$t\,w_{\mathrm{s}}$	3.32	1	3.32	24.40	< 0.0001		
$R_{\mathrm{M}}\,R_{\mathrm{I}}$	2.48	1	2.48	18.22	0.0002		
$R_{\mathrm{M}}\,w_{\mathrm{s}}$	2.48	1	2.48	18.22	0.0002		
$R_{\mathrm{I}}\,w_{\mathrm{s}}$	0.0703	1	0.0703	0.5175	0.4773		
T^2	0.4855	1	0.4855	3.57	0.0681		
t^2	2.13	1	2.13	15.67	0.0004		
$T\,t\,w_{\mathrm{s}}$	0.5778	1	0.5778	4.25	0.0477		
$t\,R_{\mathrm{I}}\,w_{\mathrm{s}}$	2.94	1	2.94	21.64	< 0.0001		
Residuals	4.21	31	0.1359				
Lack of Fit	4.02	24	0.1674	6.01	0.0103		
Pure Error	0.1950	7	0.0279				
Cor Total	170.32	49					

Figure A16 shows three graphs for the model diganostics: the normal probability plot of residuals (graph A), the residuals versus predicted plot (graph B) as well as the residuals versus runs plot (graph C).

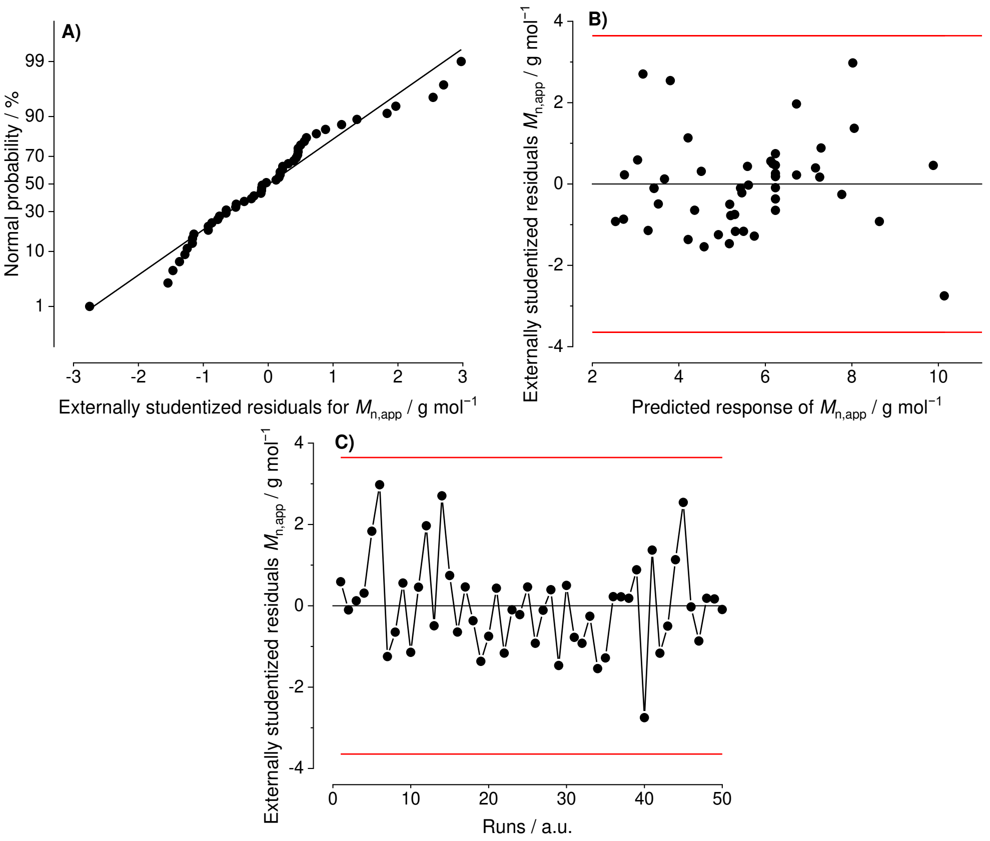

Figure A16: Diagnostic plots for the prediction model of $\overline{\boldsymbol{M}}_{\mathbf{n,app}}$. Graph A) Normal probability plot of residuals. Graph B) Residuals (externally studentized) versus the predicted response. Graph C) Residuals versus run plot. The red lines of plots A and B signify the Bonferroni-corrected confidence limits.

10.6.1.4.4 The Dispersity Đ

The prediction model for ***Đ*** is shown in equation (A7).

$$\boldsymbol{Đ} = 1.26 + 0.04\,T + 0.0194\,t + 0.0135\,R_{\mathrm{M}} - 0.0194\,R_{\mathrm{I}} - 0.0297\,w_{\mathrm{s}} + 0.025\,T\,t - 0.0144\,T\,R_{\mathrm{I}} - 0.0025\,T\,w_{\mathrm{s}} + 0.0188\,t\,w_{\mathrm{s}} + 0.0131\,R_{\mathrm{I}}\,w_{\mathrm{s}} + 0.0307\,t^{2} + 0.0212\,t\,R_{\mathrm{I}}\,w_{s} \tag{A7}$$

The ANOVA table as well as the fit statistics for the prediction model of ***Đ*** are shown in Table A6.

Table A6: ANOVA for the prediction model of ***Đ*** as well as the relevant fit statistics.

Source	**Sum of Squares**	**df**	**Mean Square**	**F-value**	**p-value**	**Fit Statistics**	
Model of *Đ*	0.1845	12	0.0154	34.03	< 0.0001	R^2	0.9169
T	0.0544	1	0.0544	120.37	< 0.0001	R^2_{adj}	0.8900
t	0.0128	1	0.0128	28.35	< 0.0001	R^2_{pred}	0.8347
R_M	0.0062	1	0.0062	13.77	0.0007		
R_I	0.0128	1	0.0128	28.35	< 0.0001		
w_s	0.0300	1	0.0300	66.39	< 0.0001		
$T\,t$	0.0200	1	0.0200	44.25	< 0.0001		
$T\,R_I$	0.0066	1	0.0066	14.63	0.0005		
$T\,w_s$	0.0002	1	0.0002	0.4425	0.5100		
$t\,w_s$	0.0113	1	0.0113	24.89	< 0.0001		
$R_I\,w_s$	0.0055	1	0.0055	12.20	0.0013		
t^2	0.0103	1	0.0103	22.69	< 0.0001		
$T\,R_I\,w_s$	0.0144	1	0.0144	31.97	< 0.0001		
Residual	0.0167	37	0.0005				
Lack of Fit	0.0133	30	0.0004	0.9142	0.6080		
Pure Error	0.0034	7	0.0005				
Cor Total	0.2013	49					

Figure A17 illustrates the normal probability plot of residuals (graph A), the residuals versus predicted plot (graph B) as well as the residuals versus runs plot (graph C).

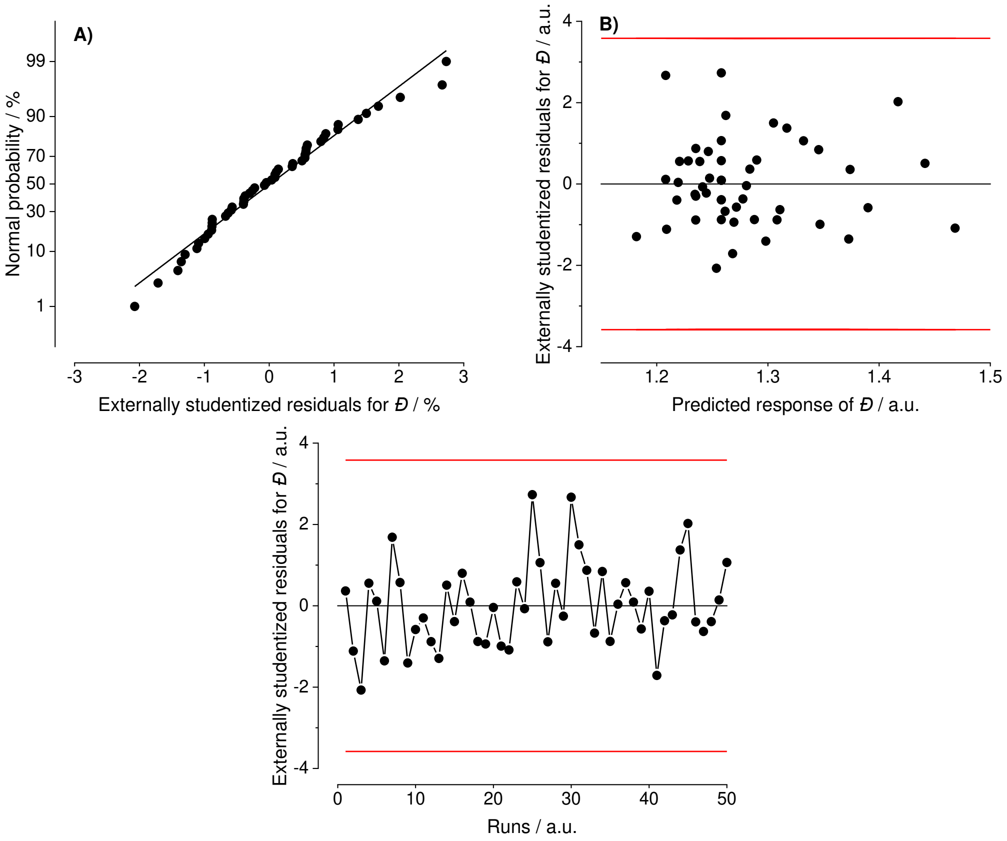

Figure A17: Diagnostic plots for the prediction model of ***Đ***. Graph A) Normal probability plot of residuals. Graph B) Residuals (externally studentized) versus the predicted response. Graph C) Residuals versus run plot. The red lines of plots A and B signify the Bonferroni-corrected confidence limits.

10.6.1.4.5Conclusions from the ANOVAs, Fit Statistics and Diagnostic Plots

As all prediction models allow for similar conclusions, this section will present them jointly. All ANOVAs show that the included model terms are significant (p-value < 0.05). In some cases, insignificant terms are added to the model to maintain model hierarchy.[85] The fit statistics show no sign of potential over-fitting and imply high prediction accuracy for all prediction models.

The diagnostic plots imply normality of the residuals and show no outlier (as no data point is located outside the Bonferroni-corrected confidence limits). Also, the residual variance appears to be homogenous over the whole predictive space of each equation implying homoscedasticity. The residuals versus runs plot, furthermore, do not reveal any time-lurking effect. The FC-CCD successfully generated highly informative and accurate prediction models for each individual response.

10.6.2 Decomposition of the Thermal Initiator ACVA

The activation Energy $E_{\mathrm{act.}}$ of the decomposition of racemic ACVA amounts to 132.2 kJ mol^{-1} and the pre-exponential factor A has a value of $4.76 \cdot 10^{15}$ s^{-1}.[117] According to Arrhenius' law (equation (A8)), the decomposition rate coefficient k_{d} at 85 °C obtains a value of:

$$k_{\mathrm{d}} = A \exp\left({}^{-E_{\mathrm{act.}}}\!/_{\mathrm{R}T}\right) = 2.489 \cdot 10^{-4}\mathrm{s}^{-1}. \tag{A8}$$

After 260 min at 85 °C in aqueous solution, 98 % of the initial ACVA concentration $[\mathrm{I}]_0$ has decomposed according to equation (A9):

$$1 - {}^{[\mathrm{I}]}\!/_{[\mathrm{I}]_0} = 1 - \exp(-k_{\mathrm{d}}\, t) = 0.98 \tag{A9}$$

10.6.3 Advanced PTT-Analysis of PMAAm Solutions

In the following, supplementary information regarding the investigation of the PMAAm solution behavior *via* experimental design will be provided.

10.6.3.1 Polymer Synthesis

The examined polymers were supposed to obtain higher molecular weights than in previous investigations. Thus, the photoiniferter RAFT solution polymerization using CTCA as RAFT agent and water as solvent was conducted with an R_{M} of 1000 (T = 70 °C, 0.38 mW cm^{-2}, w_{s} = 15 wt%). In order to obtain three polymer samples with equidistant $\overline{M}_{\mathrm{n,th}}$-values, a kinetic study was performed (see unfilled circles in graph A of Figure A18). After knowing the conversion-time course, the polymerization was repeated on a larger scale aiming for three polymer samples (green cirlces) with conversions that produce equidistant $\overline{M}_{\mathrm{n,th}}$-values. The elugrams from these three polymer samples are shown in graph B.

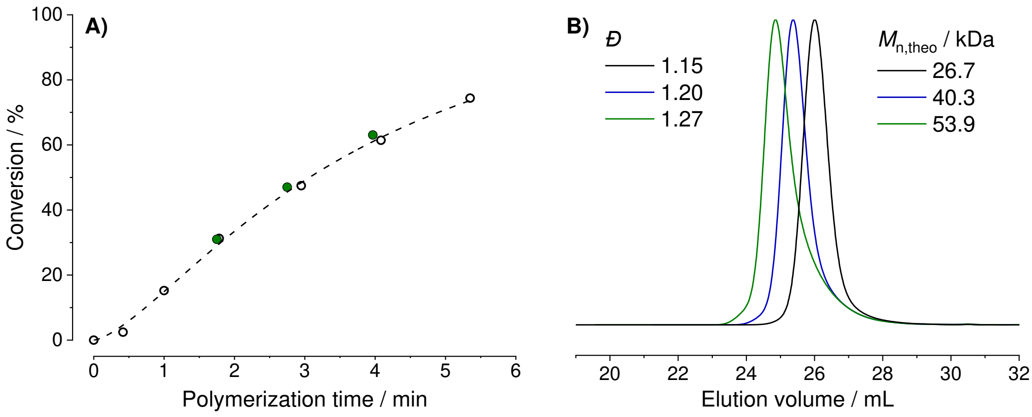

Figure A18: Graph A) Kinetic study (unfilled circles) of a photoiniferter RAFT polymerization of MAAm ($T = 70$ °C, $R_M = 1000$, 0.38 mW cm^{-2}, $w_s = 15$ wt%). The green symbols stem from a succeeding larger scaled polymerization that yielded sufficient amounts of polymer samples for the experimental design. Graph B) SEC derived elugrams of the three larger-scaled RAFT polymerization samples. The three $\bar{M}_{n,th}$-values are equidistant which is a requirement for investigation of the factor $\bar{M}_{n,th}$ in a design including center points.

10.6.3.2 The Screening

The experimental plan (in standard order) with the actual values of the factors and the observed response – the PTT – is shown in Table A7.

Table A7: Standard order experimental plan of the fractional factorial design (2^{5-1}, resolution V) for the screening of the factors.

Run	**Factors**					**Response**
	w_{PMAAm} / **wt%**	w_{NaHCO_3} / **wt%**	w_{NaCl} / **wt%**	w_{EtOH} / **wt%**	$\bar{M}_{n,th}$[a] / **kDa**	**PTT**[b] **/ °C**
1	0.25	0.1	0.4	15	53.9	31.5
2	2	0.1	0.4	15	26.7	29.5
3	0.25	0.3	0.4	15	26.7	12.5
4	2	0.3	0.4	15	53.9	46
5	0.25	0.1	0.8	15	26.7	11.5
6	2	0.1	0.8	15	53.9	43.5
7	0.25	0.3	0.8	15	53.9	31.5
8	2	0.3	0.8	15	26.7	29.5
9	0.25	0.1	0.4	25	26.7	39.5
10	2	0.1	0.4	25	53.9	71.5

Run	**Factors**					**Response**
	w_{PMAAm} / **wt%**	$w_{\mathrm{NaHCO_3}}$ / **wt%**	w_{NaCl} / **wt%**	w_{EtOH} / **wt%**	$\bar{M}_{\mathrm{n,th}}$[a] / **kDa**	**PTT**[b] **/ °C**
11	0.25	0.3	0.4	25	53.9	61
12	2	0.3	0.4	25	26.7	58.5
13	0.25	0.1	0.8	25	53.9	58
14	2	0.1	0.8	25	26.7	55
15	0.25	0.3	0.8	25	26.7	38.5
16	2	0.3	0.8	25	53.9	70.5
17	1.125	0.2	0.6	20	40.3	47.5
18	1.125	0.2	0.6	20	40.3	46
19	1.125	0.2	0.6	20	40.3	47.5
20	1.125	0.2	0.6	20	40.3	46.5
21	1.125	0.2	0.6	20	40.3	46.5

[a] Determined *via* ^{1}H NMR spectroscopy and referencing to DMF. [b] Measured *via* visual turbidimetry.

10.6.3.3 The Box-Behnken Design

The executed experimental plan of the Box-Behnken design with the actual factor levels for each run as well as the observed PTT of the respective PMAAm solution is shown in Table A8.

Table A8: Standard order experimental plan of the Box-Behnken design showing the actual factor levels as well as the observed response (the PTT of the respective PMAAm solution) for each individual run.

Run	w_{PMAAm} / **wt%**	$w_{\mathrm{NaHCO_3}}$ / **wt%**	w_{NaCl} / **wt%**	w_{EtOH} / **wt%**	$\bar{M}_{\mathrm{n,th}}$[a] / **kDa**	**PTT**[b] / **°C**
1	0.25	0.1	0.6	20	40.3	36.1
2	2	0.1	0.6	20	40.3	50
3	0.25	0.3	0.6	20	40.3	33.1
4	2	0.3	0.6	20	40.3	50.4
5	1.125	0.2	0.4	15	40.3	36.8
6	1.125	0.2	0.8	15	40.3	33.5
7	1.125	0.2	0.4	25	40.3	63
8	1.125	0.2	0.8	25	40.3	60.2
9	1.125	0.1	0.6	20	26.7	36.3
10	1.125	0.3	0.6	20	26.7	35.9
11	1.125	0.1	0.6	20	53.9	51.6

Run	w_{PMAAm} / **wt%**	$w_{\mathrm{NaHCO_3}}$ / **wt%**	w_{NaCl} / **wt%**	w_{EtOH} / **wt%**	$\bar{M}_{\mathrm{n,th}}$[a] / **kDa**	**PTT**[b] / **°C**
12	1.125	0.3	0.6	20	53.9	51.3
13	0.25	0.2	0.4	20	40.3	34.8
14	2	0.2	0.4	20	40.3	51
15	0.25	0.2	0.8	20	40.3	34.8
16	2	0.2	0.8	20	40.3	49.8
17	1.125	0.2	0.6	15	26.7	26.3
18	1.125	0.2	0.6	25	26.7	52.4
19	1.125	0.2	0.6	15	53.9	41.1
20	1.125	0.2	0.6	25	53.9	65.9
21	1.125	0.1	0.4	20	40.3	47.6
22	1.125	0.3	0.4	20	40.3	47.5
23	1.125	0.1	0.8	20	40.3	44.8
24	1.125	0.3	0.8	20	40.3	45.1
25	0.25	0.2	0.6	15	40.3	21.7
26	2	0.2	0.6	15	40.3	38.3
27	0.25	0.2	0.6	25	40.3	52.2
28	2	0.2	0.6	25	40.3	66.8
29	1.125	0.2	0.4	20	26.7	36.6
30	1.125	0.2	0.8	20	26.7	34.7
31	1.125	0.2	0.4	20	53.9	53.3
32	1.125	0.2	0.8	20	53.9	49.6
33	0.25	0.2	0.6	20	26.7	26.9
34	2	0.2	0.6	20	26.7	40.4
35	0.25	0.2	0.6	20	53.9	42.9
36	2	0.2	0.6	20	53.9	54.9
37	1.125	0.1	0.6	15	40.3	35.1
38	1.125	0.3	0.6	15	40.3	33.9
39	1.125	0.1	0.6	25	40.3	62.4
40	1.125	0.3	0.6	25	40.3	62.7
41	1.125	0.2	0.6	20	40.3	46.9
42	1.125	0.2	0.6	20	40.3	46.4
43	1.125	0.2	0.6	20	40.3	45.2
44	1.125	0.2	0.6	20	40.3	46.4
45	1.125	0.2	0.6	20	40.3	45.1
46	1.125	0.2	0.6	20	40.3	46.4

[a] Determined *via* ^{1}H NMR spectroscopy and referencing to DMF. [b] Measured *via* visual turbidimetry.

Equation (A4) shows the prediction equation for the **PPT**:

$$\begin{aligned}\textbf{PTT} / ^{\circ}\mathrm{C} = 46.0 + 7.4\, w_{\mathrm{PMAAm}} - 1.13\, w_{\mathrm{NaCl}} + 13.7\, w_{\mathrm{EtOH}} + 7.6\, \overline{M}_{\mathrm{n,th}} \\ - 3.3\, w^{2}_{\mathrm{PMAAm}} + 2.36\, w^{2}_{\mathrm{EtOH}} - 1.99\, \overline{M}^{2}_{\mathrm{n,th}}\end{aligned} \tag{A10}$$

The ANOVA table as well as the fit statistics for the prediction model of the **PTT** are shown in Table A9. The curvature that was detected in the screening was successfully attributed to the specific factors. The lack of fit is insignificant which implies that not significant model terms are missing from the prediction equation. Also, the excellent fit statistic indicate that the model was not overfit and new data can be accurately predicted.

Table A9: ANOVA for the prediction model of **PTT** as well as the relevant fit statistics.

Source	**Sum of Squares**	**df**	**Mean Square**	**F-value**	**p-value**	**Fit Statistics**	
Model	5051.56	7	721.65	765.29	< 0.0001	R^2	0.9930
w_{PMAAm}	886.55	1	886.55	940.17	< 0.0001	R^2_{adj}	0.9917
w_{NaCl}	20.48	1	20.48	21.71	< 0.0001	R^2_{pred}	0.9888
w_{EtOH}	2994.83	1	2994.83	3175.95	< 0.0001		
$\overline{M}_{\mathrm{n,th}}$	916.58	1	916.58	972.01	< 0.0001		
w^{2}_{PMAAm}	108.98	1	108.98	115.57	< 0.0001		
w^{2}_{EtOH}	55.16	1	55.16	58.49	< 0.0001		
$\overline{M}^{2}_{\mathrm{n,th}}$	39.04	1	39.04	41.40	< 0.0001		
Residuals	35.83	38	0.9430				
Lack of Fit	33.12	33	1.00	1.85	0.2560		
Pure Error	2.71	5	0.5427				
Cor Total	5087.39	45					

The normal probability plot of residuals (graph A), the residuals versus predicted plot (graph B) as well as the residuals versus runs plot (graph C) are displayed in Figure A19. It shows that the residuals are normally distributed and neither show a sign of heteroscedasticity nor of an outlier. Additionally, no time-lurking effect is implied by the residuals versus runs plot.

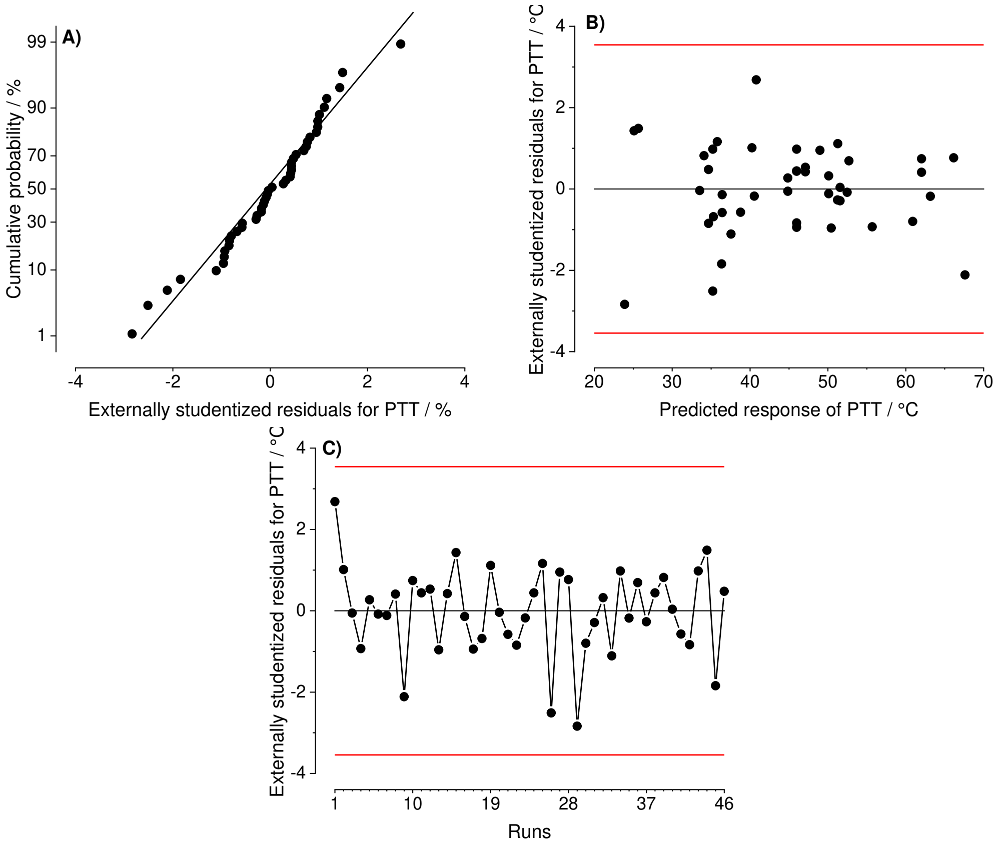

Figure A19: Diagnostic plots for the prediction model of **PTT**. Graph A) Normal probability plot of residuals. Graph B) Residuals (externally studentized) versus the predicted response. Graph C) Residuals versus run plot. The red lines of plots A and B signify the Bonferroni-corrected confidence limits.

10.7 Chain Extensions of PMAAm

10.7.1 Investigation of the Livingness of PMAAm

A fitting polymerization suggested by the DoE-Software (DesignExpert) was conducted ($T = 75$ °C, $t = 357$ min °C, $R_\mathrm{M} = 500$ °C, $R_\mathrm{I} = 0.025$ °C and $w_\mathrm{s} = 20$ wt%) yielding PMAAm$^{12.0}$ (for experimental data see Table 13). In order to investigate the polymer's chain end livingness, the isolated polymer was used as a macroRAFT agent and extended with further MAAm units ($T = 75$ °C, $t = 250$ min °C, $R_\mathrm{M} = 500$ °C, $R_\mathrm{I} = 0.1$ °C and $w_\mathrm{s} = 20$ wt%) which lead to a PMAAm$^{29.4}$-sample that was extended by an $\overline{M}_\mathrm{n,th}$-value of 17.4 kDa. The SEC traces from both polymer samples are shown in Figure A20 which shows that PMAAm$^{12.0}$ boasts reasonable chain end livingness making it suitable for chain extension for the building of diblock copolymers.

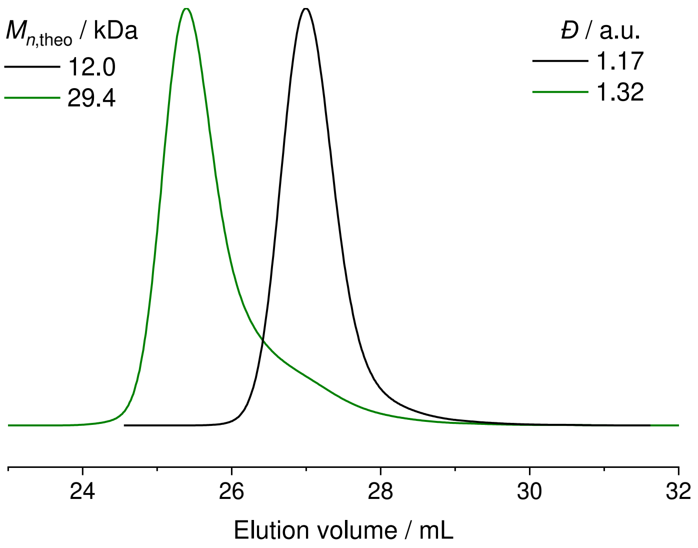

Figure A20: SEC traces of PMAAm$^{12\text{-}0}$ and PMAAm$^{29.4}$.

10.7.2 RAFT Emulsion Polymerization of Styrene

For first kinetic insights on the polymerization kinetics of the chain extension of PMAAm$^{12.0}$ with styrene *via* surfactant-free RAFT emulsion polymerization a two-level fractional factorial screening design (2^3) investigating the influences of t, R_M and w_s on the conversion of styrene p was conducted. The ANOVA as well as the fit statistics are shown in Table A10. Clearly, both t and w_s exert a significant main effect on p.

Table A10: ANOVA for a two-level fractional factorial screening design (2^3) investigating the influences of t, R_M and w_s on the conversion of styrene p.

Source	**Sum of Squares**	**df**	**Mean Square**	**F-value**	**p-value**	**Fit Statistics**	
Model	0.3095	2	0.1548	14.61	0.0082	R^2	0.8539
t	0.2032	1	0.2032	19.18	0.0072	R^2_{adj}	0.7954
w_s	0.1063	1	0.1063	10.04	0.0249	R^2_{pre}	0.6260
Residual	0.0530	5	0.0106				
Cor Total	0.3625	7					

10.8 Used Hazardous Substances According to GHS

substance	symbol	hazard statements	precautionary statements
acetone (Merck, 99 %)		EUH066, 225, 319, 336	210, 233, 240, 241, 242, 243, 264, 280, 303+361+353, 305+351+338, 337+313, 370+378, 403+235, 501
acryloyl chloride (ABCR, 96 %)		EUH014, EUH208, 225, 302, 314, 330	280, 301+330+331, 305+351+338, 310, 501
activated basic aluminum oxide (≥ 98 %, Brockmann I, Sigma Aldrich)		222, 229, 319, 336	210, 251, 305+351+338, 405, 410+412, 501
4,4’-azobis(4-cyanopentanoic acid) (Aldrich, 98 %)		228, 302	210, 240, 241, 280, 301+312, 501
chloroform-d_1 (Euriso-Top. 99.8 %)		302, 315, 350, 373	201, 202, 260, 264, 280, 281, 301+312, 305+352, 308,313, 321, 330, 332,313, 362, 405, 501
2-cyano-2-propyl dodecyl trithiocarbonate (ABCR, 97 %)		302	—
deuterium oxide (Deutero, 99.9 %)	—	—	—
dichloromethane (Acros, 99.9 %)		351	201, 202, 281, 308+313, 405, 501
diethyl ether		EUH019, EUH066 224, 302, 336	210, 233, 240, 241, 301+312, 403+233

substance	symbol	hazard statements	precautionary statements
N,*N*-dimethylformamide (VWR, 99.5 %)		312, 319, 332, 360d	201, 202, 261, 264, 380, 381, 302+352, 304+340, 305+351+338, 308+313, 312+ 322, 337+313, 363, 405, 501
dimethylsulfoxide	—	—	—
1,4-dioxane (Grüssing, 99 %)		EUH019, EUH066, 225, 319, 335, 351	201, 202, 210, 240, 241, 242, 243, 261, 264, 280, 281, 303+361+353, 304+340, 305+351+338, 308+313, 312, 337+313, 370+378, 403+233, 403+235, 405, 501
ethanol (VWR, 99.8 %)		225	210, 233, 240, 241, 242, 243, 280, 303+361+353, 370+378, 403+235, 501
n-hexane (VWR, 95 %)		225, 304, 315, 336, 361f, 373, 411	201, 202, 210, 233, 240, 241, 242, 243, 260, 264, 273, 280, 281, 301+310, 302+352, 303+361+353, 303+313, 370+378, 391, 403+235, 405, 501

substance	symbol	hazard statements	precautionary statements
isoprene (Acros, 99 %)		224, 341, 350, 412	201, 202, 210, 233, 240, 241, 242, 243, 273, 280, 281, 303+361+353, 308+313, 370+378, 403+235, 405, 501
magnesium sulfate (Grüssing, 99 %)	—	—	—
methacrylamide		302, 319, 335, 371, 373	260, 264, 270, 301+312, 305+351+338, 308+311
methanol		225, 301+311+331, 370	210, 233, 280, 301+310, 303+361+353, 304+340+311
methyl methacrylate		225, 315, 317, 335	210, 233, 240, 241, 280, 303+361+353
silica gel (Macherey Nagel, 100 %)		373	260, 314, 501
sodium hydrogen carbonate (Grüssing, 99 %)	—	—	—

substance	symbol	hazard statements	precautionary statements
styrene (Acros, 99 %)		226, 315, 319, 332, 361d, 372	201, 202, 210, 233, 240, 241, 242, 243, 260, 264, 280, 281, 305+352, 303+361+353, 304+340, 305+351+338, 308+313, 321, 330, 332+313, 337+313, 370+378, 403+233, 403+235, 405, 501

Danksagung

In den ziemlich exakt dreieinhalb Jahren meiner Promotion hat sich die Reihe an Menschen, denen ich dankbar bin, stetig verlängert. Besonderer Dank gilt hierbei natürlich Volker Abetz, der nicht nur meine Promotion, sondern auch wichtige Teile meines Studiums betreut hat und dabei stets seiner unterstützenden und besonnenen Art treu geblieben ist. In meinem zweiten „Promotionsleben“ als HZG/Hereon-Mitarbeiter durfte ich dazu noch unter Maryam Radjabians Leitung forschen, die mir ebenfalls viele hilfreiche fachliche Ratschläge in den monatlichen Meetings mitgeben konnte – vielen Dank! Im Zuge dieses zweiten Promotionslebens möchte ich mich außerdem noch für die finanzielle Unterstützung durch das kollaborative Projekt der Helmholtz Gesellschaft und der Russian Science Foundation (HRSF 0075) danken. Auch Ilona Zillich und Sigi, die mir immer wieder zur Seite gesprungen sind, möchte ich herzlich danken.

Herrn Horst Weller danke ich für das Bereitstellen des Zweitgutachtens dieser Arbeit und für den damit verbundenen Zeitaufwand. Mein Dank gilt außerdem Christoph Wutz, der mir äußerst hilfsbereit zahlreiche Fragen zur Polymer-NMR beantworten konnte. Darüber hinaus sei auch den Service-Abteilungen der Chemiefakultät, wie der NMR- und MS-Abteilung sowie der Werkstatt für die zahlreichen Messungen und Baukunstwerke gedankt.

Im Rahmen meines DoE-Projekts hatte ich außerdem das Vergnügen mit zwei Statistikern aus Kassel zusammenzuarbeiten. Danke Olli und Piet für eure Hilfe, die launigen Skype-Sessions und die tausend Fragen, die ihr mir beantwortet habt – es hat mir großen Spaß gemacht.

Die Arbeit in der Arbeitsgruppe Abetz hat mir große Freude bereitet. Mein Dank gilt meinen zahlreichen Mitarbeiter:innen Alex, Elaine, Birgit, Andreas, Taida, Sigi und Ulf für Hilfe im Labor, angemessenen gelegentlichen Tadel für Schusseligkeit und nette Gespräche im Sozialraum. Maggie, JC, Martin, Sascha, Maria, Philipp, Felix, Stephan und Niklas möchte ich für die zahlreichen Messungen – sei es GPC, DLS, TEM, DMA, etc. – danken.

Ich danke meinen Bürogenossen Philipp und Jingcong für eure Geduld mit meiner nicht-Ansprechbarkeit, wenn ich konzentriert bin. PL, vielleicht bleibst du ja mein Schatten. Wir hörn voneinander! 😉 JC, dir wünsche ich nur das Allerbeste für die Zukunft, die ja vermutlich in China liegen wird. Ich hoffe du wirst die Zeit bei uns in guter Erinnerung behalten und vielleicht kannst du ja auch den Tennisschläger mal wieder ausgraben. Vielleicht besuche ich dich ja sogar schon bald!

Danke auch an meine Freunde drüben im Nachbarbüro. Sascha, vielen Dank für deine Hilfsbereitschaft und deine liebenswerte und authentische Art. Mach dein Ding, reg dich nicht so auf und lass mal von dir hören! Maria und Sabrina, euch noch eine schöne Zeit an der Grindelallee! Viel Durchhaltevermögen am TEM wünsche ich, genau wie einen ruhigen Wurfarm. Zielt auf das Viererfeld „12, 9, 14, 11“. Hier habt ihr die 26 Punkte sicher!

Ich danke Iklima dafür, Iklima zu sein. Du bist wirklich einfach die coolste! Ich bin super dankbar, in dir eine Freundin gefunden zu haben, mir der ich über alles reden kann und die verrückterweise einfach alle meine Interessen (okay, bis auf Tennis) teilt. Wehe du änderst dich da unten in Karlsruhe. Danke auch an Siraphat für die mentale Unterstützung als ich vor dem Telefonat mit dem zukünftigen Arbeitgeber doch ein klein wenig nervös war.

Danke Stephan, danke Felix danke Niklas, danke Steffen, danke Betti für all die schönen Momente, die regelmäßigen (aber dennoch zu seltenen) Treffen, für die Warcraft-Sessions und und und. Ich werde mich auch immer an die intensiven Tennisstunden mit dir, Felix, in Hollenstedt erinnern. Schade, dass es jetzt nicht mehr so oft möglich ist, dir einen 6:0-Satz einzuschenken, aber ehrlicherweise kriege ich dadurch auch selber nicht mehr ständig auf die Mütze!

Ich möchte außerdem all meinen Praktikant:innen danken. Mir hat es mit euch immer Spaß gemacht und ich hoffe ich konnte euch ein wenig mitgeben. In Florian habe ich ja sogar einen klasse Nachfolger rekrutieren können. Verrückterweise wirst du sogar auf meinem Platz sitzen – ich schenke dir hiermit meinen Bürokühlschrank!

Ich möchte außerdem nochmal ausdrücklich Felix und Steffen danken. Zu dir, Steffen, habe ich immer aufgeschaut und ich habe eine Menge von dir gelernt. Danke, dass du meine tausenden Fragen beantwortet hast. Das Kicken damals in der Halle werde ich auch in positiver Erinnerung behalten. Ich habe Nils wütendes Verfolgungsschnaufen noch in den Ohren. Mit dir, Felix, verbindet mich zwar ein anderer Sport, aber du hast mir ebenso viel geholfen. Deine Hilfsbereitschaft ist absolut bemerkenswert! Danke für alles habibi.

Ich kann mich außerdem sehr glücklich schätzen, neben meines tollen Arbeitsumfelds noch weitere wichtige Menschen in meinem Leben zu haben. Neben meinen Freunden aus Schul- oder Unizeiten, vom Tennis oder Fußball, habe ich das große Glück jederzeit von meiner Familie und Maike unterstützt worden zu sein. Danke für alles und auf viele weitere gemeinsame Tage.

11 Eidesstattliche Versicherung

Hiermit versichere ich an Eides statt, die vorliegende Dissertation selbst verfasst und keine anderen als die angegebenen Hilfsmittel benutzt zu haben. Die eingereichte schriftliche Fassung entspricht der auf dem elektronischen Speichermedium. Ich versichere, dass diese Dissertation nicht in einem früheren Promotionsverfahren eingereicht wurde.

24.07.2022